AN ABSTRACT OF THE THESIS OF

Jai-Ho Oh for the degree of Doctor of Philosophy in Atmospheric Sciences presented on May 2, 1989.

Title: Physically-Based General Circulation Model Parameterization of Clouds and Their Radiative Interaction

Redacted for privacy

Abstract approved:___

Michael E. Schlesinger

A physically-based parameterization of clouds and their radiative interactions has been developed for a multilayer atmospheric general circulation model. The main purpose of this development is to enable the evaluation of cloud optical depth feedback, a feedback of potential importance for greenhouse-gas-induced climate change.

In the cloud-radiation parameterization, cloud water is a prognostic variable; fractional cloud amount is predicted semi-prognostically; stratiform and cumuloform clouds can coexist in a vertical atmospheric column; clouds can exist either as liquid water, ice or mixed liquid water-ice clouds; the solar spectrum is subdivided into three bands, two for Rayleigh scattering and ozone absorption, and one for water vapor absorption which is further subdivided into six intervals for the k-distribution method; multiple scattering is calculated by the two-stream, delta-Eddington method; the longwave spectrum is divided into four regions based on the absorbers; the radiative properties of clouds depend on their predicted cloud liquid water and ice amounts; and the vertical distribution of clouds is considered to have maximum overlap for contiguous cloud layers and random overlap for noncontiguous cloud layers.

The parameters for the stratiform-cloud parameterization and the values chosen are: (1) the characteristic time for the evaporation of cloud water, τ = 50 minutes; (2) the autoconversion rate of cloud water into precipitation, a = $(3600\text{ s})^{-1}$; (3) the threshold relative humidity of the environment at which condensation can begin, U_{00} = 0; and (4) the threshold cloud water above which precipitation can begin, $m_{c,w}$ = 0.5×10^{-4} g/g for water clouds; $m_{c,i}$ = $0.4\times I_c(T_c)$ for ice clouds, where $I_c(T_c)$ are the values given by Heymsfield and Platt (1984) as a function of the cloud temperature T_c; $m_{c,i}$ = $1.2\times I_c(T_c)$ for ice clouds formed from an antecedent cumuloform cloud. The parameters for the cumuloform-cloud parameterization and the values chosen are: (1) the characteristic time for the evaporation of cloud water, τ = 50 minutes; (2) the parameter in the diagnostic equation for the cloudiness in terms of the mass flux at the base of the detrainment layer, α = 10; and (3) the conversion rate of cloud water into precipitation, C_0 = 0.002 m^{-1}. In addition, two radiation parameters were determined: (1) the mass absorption coefficient of cumuloform ice clouds, $a_0^{\uparrow,\downarrow}$ = 0.096; and the multiple-scattering asymmetry factor for cumuloform clouds, g = 0.85.

An evaluation of the performance of the model shows that the cloud-radiation parameterization is capable of successfully simulating many features of the observed cloud cover, the vertically integrated cloud water, precipitation, and the earth's radiation budget at the top of the atmosphere. The model is less successful in reproducing the cloud optical depths as given by the International Satellite Could Climatology Project observations. This apparent contradiction suggests that these optical depth observations may not be useful in validating a cloud-radiation parameterization. The comparison of the simulated and observed climates also shows that the cloud parameterization is deficient in its reproduction of the subtropical stratocumulus clouds. To rectify this deficiency it is necessary to develop a model for stratocumulus clouds in the cloud-radiation parameterization.

Physically-Based General Circulation Model Parameterization of Clouds and Their Radiative Interaction

by

Jai-Ho Oh

A THESIS

submitted to

Oregon State University

in partial fulfillment of
the requirements for the
degree of

Doctor of Philosophy

Completed May 2, 1989
Commencement June 1989

APPROVED:

Redacted for privacy

Professor of Atmospheric Sciences in charge of major

Redacted for privacy

Chairman of Department of Atmospheric Sciences

Redacted for privacy

Dean of Graduate School

Date thesis is presented_____May 2, 1989

ACKNOWLEDGEMENTS

This success of this research can be attributed in large part to the guidance of my advisor, Michael E. Schlesinger. Without his dedication, patience, and understanding, this research would not have been completed.

I am most appreciative of the interest evinced in my thesis by other members of my doctoral committee, including Professors T.B. Brown, J.A. Coakley, J.W. Deardorff, and S.K. Esbensen. I am also grateful to Drs. J.-F. Geleyn, W. J. Wiscombe, and M.-D. Chou for allowing the use of their numerical algorithm and the line-by-line absorption data. I would also like to thank to Dr. Y.-J. Han for his encouragement during the course of this research.

It is with pleasure that I acknowledge the help I have received from my fellow students and colleagues, particularly D. Vickers for his programming assistance, X.-J. Jiang and E.-X. Fu for many their helpful discussions, and W. McMechan for his editing. Finally, I would also like to thank my wife, Sung-Hi, for her support, patience, and understanding during the period of my graduate program at Oregon State University.

Table of Contents

Table of Contents/continued

List of Figures

List of Figures/continued

viii

List of Figures/continued

List of Figures/continued

List of Tables

List of Figures in Appendices

List of Figures in Appendices/continued

List of Figures in Appendices/continued

List of Tables in Appendices

PHYSICALLY-BASED GENERAL CIRCULATION MODEL PARAMETERIZATION OF CLOUDS AND THEIR RADIATIVE INTERACTION

1. INTRODUCTION

Clouds play several important roles in maintaining present climate (Arakawa, 1975), including cooling the earth-atmosphere system through their radiative effects (Ramanathan *et al.*, 1989). They may also play an important role in "greenhouse" gas-induced climatic changes (Schlesinger and Mitchell, 1985, 1987; Roeckner *et al.*, 1987; Schlesinger, 1988a,b,c, and 1989). Consequently, to be able to use mathematical climate models to correctly simulate the present climate and potential climate changes requires a physically-based parameterization of clouds and their radiative interactions. However, in terms of cloud microphysics and their influence on the optical properties of clouds, the treatment of clouds in contemporary atmospheric general circulation models (AGCMs) is quite rudimentary (Rutledge and Schlesinger, 1985). Attempts have been made to improve the treatment of clouds in AGCMs by making the cloud water content a prognostic quantity (Sundqvist, 1978, 1988; Roeckner *et al.*, 1987; Smith, 1988), but parameterization for inclusion of both stratiform and cumuloform clouds, or liquid water, ice and mixed-phase clouds, have not been developed. Because the radiative interactions of these different types of clouds have not been included in AGCMs, it has not been possible to accurately simulate cloud optical depth feedback, which is potentially important to greenhouse gas-induced climatic changes (Schlesinger, 1988b,c). Therefore, the objective of investigation has been the development of a physically-based AGCM parameterization of clouds and their radiative interactions. In large part, the purpose of this development is to enable the evaluation of cloud optical depth feedback.

Recently, global satellite observations, including International Satellite Could Climatology Project (ISCCP, Rossow *et al.*, 1985), NIMBUS-7/ERBE (Jacobowitz *et al.*, 1984; Hwang *et al.*, 1988; Susskind *et al.* 1987), the ERB of NOAA-9 and ERBS (Kyle *et al.*,1989), and SMMR data (Njoku and Swanson, 1983), in which the earth radiation budget and the cloud liquid

water were accurately measured with the satellites radiometers, have encouraged the development of physical cloud-radiation parameterization and provided the observational data, e.g., the planetary albedo, outgoing longwave radiation at the top of the atmosphere, cloud-top pressure and temperature, cloud optical depth, and vertically accumulated cloud liquid water amounts, to test and validate the physically-based cloud-radiation parameterizations. Moreover, the ICRCCM (Luther *et al.*, 1988), in which the calculated radiative fluxes in a model under given atmospheric conditions are compared to those of other precise models, including line-by-line models, has provided the opportunity of improving the current, relatively-crude AGCM radiation scheme.

Chapter 2 is a review of recent investigations that have been directed at broadening "our understanding" of the impact of clouds on climate, and vice versa, as well as the development of a more physically-based cloud-radiation parameterization. The nature of the physically-based cloud parameterization, in which cloud water is calculated prognostically and fractional cloudiness is predicted semi-prognostically, is described in Chapter 3. The new radiation scheme associated with comprehensive cloud parameterization is described in Chapter 4. This radiation scheme is designed to provide fractional cloud cover feedback by allowing calculation of both the cloud part flux and the clear part flux within the same grid box. In addition, the radiation parameterization is designed to generate cloud optical depth feedback by the calculation of cloud radiative properties from cloud optical depths obtained from the cloud liquid water content. The latter is one of the prognostic variables considered in the Oregon State University (OSU) multilayer atmospheric GCM and is discussed in Chapter 3. An approach to the development and testing of the cloud-radiation parameterization is described in Chapter 5. For this purpose, the OSU multilayer atmospheric GCM has been developed (see Appendix A). In Chapter 6, the cloud-radiation parameterization for the OSU multilayer AGCM is evaluated, comparing it with data drawn from the prior global satellite observations cited above, as well as Jaeger's (1976) precipitation data. Chapter 7 presents a summary of the evaluations of the physically-based cloud-radiation parameterization and suggestions for further research.

2. BACKGROUND

Clouds play a major role in determining the atmospheric general circulation and climate of the Earth. As described by Arakawa (1975), the most important processes are:

1) the coupling of dynamical and hydrological processes through the heat of condensation and vaporization (evaporation), and the vertical redistribution of heat and momentum;

2) the coupling of radiative and dynamical-hydrological processes through the reflection, absorption and emission of radiation;

3) the coupling of hydrological processes in the atmosphere and at the surface through precipitation; and

4) the coupling between the atmosphere and ground through modification of the radiative and turbulent transfers at the surface.

However, most of the current climate models cannot simulate all of the these processes. In particular, the coupling between radiative and dynamical-hydrological processes through time-dependent fractional cloudiness and its optical properties has been ignored or has been prefixed in most of the general circulation models.

In recent years a number of the studies of the role of clouds in the maintenance and change of climate have been performed with radiative-convective models (RCMs) and general circulation models (GCMs). The first RCM cloud study was conducted by Manabe and Strickler (1964), and subsequent studies have been carried out by Manabe and Wetherald (1967), Augustsson and Ramanathan (1977), Reck (1979a,b), Wang and Stone (1980), Hansen *et al.* (1981), Hummel and Reck (1981), Hunt (1981), Stephens and Webster (1981), Wang *et al.* (1981), Charlock (1981, 1982), Hummel (1982), and Somerville and Remer (1984). Recently, Schlesinger (1985) reviewed these studies and characterized their results in terms of

the cloud feedback, f, on the surface air temperature change, ΔT_s, as expressed by

$$\Delta T_s = \frac{(\Delta T_s)_0}{1-f} , \tag{2.1}$$

where

$$(\Delta T_s)_0 = G_0 \, \Delta R_T \tag{2.2}$$

in the absence of any feedback, is the surface air temperature change induced by the change in the net radiation at the tropopause, ΔR_T, and the gain (output/input) of the climate system, G_0. Cloud feedback can occur from changes in cloud altitude, fractional cloudiness and cloud optical depth.

Three cloud altitude treatments have been used in an RCM, namely, those for fixed cloud altitude (FCA), fixed cloud pressure (FCP) and fixed cloud temperature (FCT). Fixed cloud altitude and fixed cloud pressure have frequently been regarded as synonymous factors, though this is certainly not the case. For FCA, cloud temperature increases by the same amount as the surface temperature and there is no feedback, whereas for FCP, the cloud temperature increases less than the surface temperature. Thus, to achieve equilibrium, surface temperature warming coupled to FCP must be greater than with FCA. Therefore, FCP is a positive feedback process for which, however, insufficient information exists for the quantitative evaluation of f_{CA}. For FCT, cloud temperature does not change with a change in surface temperature; hence, surface temperature warming must be even greater than that for FCP in order to achieve equilibrium. From the OSU RCM the FCT feedback, f_{CA} is 0.261, in comparison to a range of 0.168 to 0.203 from another RCM, which in turn was compared with the FCP case. Thus, a reasonable f_{CA} range is perhaps 0.15 to 0.30 (Schlesinger, 1985).

The feedback due to changes in cloud cover, A_c, is in part dependent upon the quantity

$$\delta = -\frac{S_0}{4}\frac{\partial\, \alpha_p}{\partial\, A_c} - \frac{\partial\, R_0}{\partial\, A_c}\,,$$

(2.3)

which is dependent upon the competing effects of changes in the planetary albedo, α_p, and in the net upward longwave flux at the top of the atmosphere, R_0. An analysis of several RCM studies (Schlesinger, 1985) shows that $\delta \cong -100$ Wm^{-2} for low clouds, $\delta \cong -50$ Wm^{-2} for middle clouds, and $\delta \cong 5\text{-}80$ Wm^{-2} for high clouds, with the latter generally increasing with cloud emissivity. Thus, for the case $dA_c/dT_s > 0$, low and middle clouds contribute to a positive cloud cover feedback, f_{CC}, while the contribution of high clouds is negative. The sign of these contributions reverses for $dA_c/dT_s < 0$. In the case of doubled CO_2, a single RCM study of cloud cover feedback provided a positive f_{CC} value, but was negative in case of a 2% solar constant (S_0) increase. These seemingly contradictory findings can be understood on the basis of the changes in the vertical cloud cover profile, which demonstrate that the vertical integral of $\delta\Delta A_c$ determines the sign and magnitude of the cloud cover feedback. Because of this effect, cloud altitude feedback is subsumed in cloud cover feedback.

The feedback due to changes in cloud optical depth, τ_c , is in part dependent upon the quantity

$$\phi = -\frac{S_0}{4}\frac{\partial\, \alpha_p}{\partial\, \tau_c} - \frac{\partial\, R_0}{\partial\, \tau_c}\,,$$

(2.4)

which in turn is dependent upon the competing albedo and longwave effects. For black clouds, $\partial R_0/\partial\tau_c = 0$ and $\phi < 0$. For non-black clouds, $\partial R_0/\partial\tau_c < 0$, and ϕ is either positive or negative. Thus, for the case $d\tau_c/dT_s > 0$, low and middle clouds negatively contribute to the cloud optical depth feedback, f_{OD}, and the contribution of high clouds can be either positive or negative. The sign of these contributions reverses for $d\tau_c/dT_s < 0$. An RCM study by Charlock (1981) of a single cloud layer found a negative f_{OD} value of -0.427. A second study (Wang $et\ al.$, 1981) found that for doubled CO_2, f_{OD} was essentially zero, but was negative in the case of a 2% solar constant increase. This latter finding is similar to those cited above for

cloud cover feedback, indicated that the cloud optical depth feedback is dependent upon the vertical integral of $d\tau_c / dT_s$ throughout the atmosphere.

More recently, Somerville and Remer (1984) found that at $f_{OD} \cong -1.05$ to -1.32, cloud optical depth feedback is strongly negative. If this is true, then the warming of the Earth's surface simulated by GCMs for CO_2 doubling should be reduced by approximately 50% since none of existing models include cloud optical depth feedback (Schlesinger and Mitchell, 1985). On the other hand, Liou (1986) reported a positive f_{OD} value, which indicates that the inclusion of cloud optical depth feedback in GCMs would increase their simulation of CO_2-induced warming. Clearly, this uncertainty about the sign and magnitude of cloud optical depth feedback is one of the major uncertainties in projecting climatic changes induced by changes in the concentrations of CO_2 and other trace gases in the Earth's atmosphere.

A number of GCM sensitivity studies have been conducted which indicate that uncertainties about cloud feedback impact our capability of simulating the present climate. Schneider *et al.* (1978) performed a series of National Center for Atmospheric Research GCM experiments (in the month of January) in which changes of 2^0C were imposed on the prescribed sea surface temperature (SST), either globally or in zonal strips. Statistically significant changes were found in the global and local low cloudiness. The former provided a sign opposite to that of the change in global SST, while the latter provided a sign that was dependent upon the vertical velocity sign in the zone of SST change.

Wetherald and Manabe (1980) used a simplified non-global and non-seasonal version of a Geophysical Fluid Dynamics Laboratory (GFDL) atmospheric GCM with swamp ocean model (i.e., an ocean with zero heat capacity and no currents) to investigate the influence of cloud cover variations on the climatic sensitivity to solar constant increases of 2, 4 and 6%. In response to these increases, model cloudiness decreased in the upper and middle troposphere at most latitudes and increased in the lower stratosphere and near the Earth's surface, particularly in the higher latitudes. At 50^0 latitude, total cloudiness increased in the direction of the poles and decreased in the equatorial direction, thus providing only a small change in area-mean cloudiness. This low-latitude decrease of

cloudiness led to an increase in both absorbed solar and outgoing longwave radiation, while the high-latitude increase of cloudiness provided an inverse reaction. The result of this local compensation between solar and longwave radiation was a low degree of change in area-mean radiation as a response to solar constant-induced changes in cloudiness.

Recently, Wetherald and Manabe (1986) used the same GCM to re-examine the influence of interactive cloud cover on the climate sensitivity. First, they compared previously obtained data on cloud changes induced by a 6% increase in solar constant (Wetherald and Manabe, 1980), to cloud changes induced by a quadrupling of the CO_2 concentration (Manabe and Wetherald, 1980). Second, CO_2-induced changes in cloudiness were simulated by a global version of a GFDL atmospheric GCM with a fixed-depth mixed layer ocean model for both non-seasonal (annual-mean) and seasonally-varying solar insolation. These comparisons revealed cloud pattern changes with following similarities: 1) a decrease in cloud amount in the moist, convectively-active regions in the tropics and middle latitudes; 2) an increase in cloud amount in the stable region near the Earth's surface in middle and high latitudes; 3) an increase in cloud amount in the lower stratosphere of the middle and high latitudes; and 4) a decrease in cloud amount in the middle and upper troposphere for nearly all latitudes. However, in contrast to their earlier studies (Wetherald and Manabe, 1980; Manabe and Wetherald, 1980) of the non-global, non-seasonal model, the solar and longwave radiative effects of changes in cloudiness failed to compensate for each other in the global model with seasonally-varying insolation. Thus, when the cloud cover feedback process was incorporated in the global, seasonal model, its sensitivity to CO_2-inducing warming increased 30%. Their conclusion was that the difference in the magnitude of changes in cloudiness between the global, seasonal and the non-global, non-seasonal models may be responsible for the difference in model sensitivity.

Hunt (1982) used the United Kingdom Meteorological Office GCM to investigate the effects of prescribed changes of the model's cloud base and optical properties (absorptivity and transmissivity) for surface flux, temperature, and precipitation. Because the prescribed sea surface temperatures could not be changed for these experiments, Hunt restricted

attention to the land and ice areas and found statistically significant changes in several zonal mean quantities, including surface solar and longwave fluxes, precipitation and evaporation, and atmospheric temperatures, in response to changes in the cloud optical properties.

The results of investigation conducted by Schneider *et al.* (1978), Wetherald and Manabe (1986), and Hunt (1982) suggest that the feedback between cloud cover and surface temperature could produce significant errors in the simulation of sea surface temperature for present climate by a coupled atmosphere/ocean (A/O) GCM. Indeed, this hypothesis is supported by the recent simulations of the present climate by the Oregon State University A/O GCM (Gates *et al.*, 1985; Han *et al.*, 1985). In particular, the model simulated warmer-than-observed sea surface temperatures in the eastern Pacific and Southern oceans, apparently due to excessive solar radiation at the sea surface attributed to model underestimates of the stratocumulus cloud cover over the eastern Pacific and to incorrect optical properties for the clouds over the Southern ocean.

Two additional studies using atmospheric GCMs with prescribed sea surface temperatures investigated the influence of clouds on present climate simulations. Meleshko and Wetherald (1981) performed two simulations for the month of July with a GFDL atmospheric GCM. The first was for fixed clouds prescribed from an observed geographical distribution, and the second was for fixed clouds prescribed everywhere equal to the zonal mean of observed cloud distribution. The incorporation in the model of the geographical cloud distribution rather than a zonal mean cloud distribution produced: 1) marked changes in the net radiation flux at the top of the atmosphere and in the surface radiation budget; 2) decreases in continental surface temperatures due to the reduced cloud cover; 3) surface pressure decreases over the continents and increases over the oceans; and 4) substantial changes in precipitation rates, intensifying the arid and semi-arid climate conditions for several continental regions. In a similar study for the month of August, Shukla and Sud (1981) performed two simulations with the Goddard Laboratory for Atmospheric Sciences atmospheric GCM. The first simulated time-dependent clouds predicted by the model, and the second simulated time-independent clouds prescribed on the basis of time-dependent cloud simulation statistics. The

study determined that time-independent clouds act as a longitudinally-asymmetric heat source for enhancement of generation of eddy available potential energy and its conversion to eddy kinetic energy. Furthermore, the fixed clouds in the model caused a large increase in maritime evaporation and precipitation, even though the sea surface temperature was unchanged from the simulation with variable clouds. This effect amplified both the planetary-scale stationary waves and the synoptic-scale transient disturbances, leading Shukla and Sud (1981) to conclude that cloud-radiation feedback must be adequately parameterized in numerical experiments designed to simulate the mean climate and/or to examine the sensitivity of GCM's to changes in external boundary conditions or internal atmospheric constituents (such as aerosols and CO_2) and their feedback effects.

The parameterization of clouds and radiation in seven contemporary atmospheric GCMs was recently reviewed by Rutledge and Schlesinger (1985). In these models, non-convective cloud predictions consist of their initiation when large-scale relative humidity exceeds a threshold value in a stably stratified atmosphere. Excess moisture above this threshold value is condensed out immediately to form precipitation. Convective clouds are parameterized either by a moist adiabatic adjustment or by a model of an ensemble of cumulus clouds. Therefore, both non-convective and convective clouds are purely diagnostic quantities. In addition, the radiative properties of these clouds are prescribed on the basis of altitude, generally in low, middle and high cloud categories. From the viewpoint cloud physics, the cloud parameterization used in GCMs are only crude approximations of the detailed cloud microphysical mechanisms which produce clouds and precipitation (Rutledge and Schlesinger, 1985). Furthermore, cloud/radiation parameterization do not include the dependence of optical properties on the microphysical properties of clouds, such as the cloud liquid water. However, during the last decade there have been a few efforts to develop more physically-based cloud/radiation parameterization for GCMs.

At present there are two approaches to prediction of fractional cloud cover. The first is a diagnostic approach in which the fractional cloud cover is predicted empirically from large-scale variables, while the cloud

optical properties are prescribed or calculated separately, based upon assumed variation in cloud water content (Slingo, 1980, 1987). The disadvantage of this statistical scheme is that clouds are largely separated from the rest of the model. Clouds has only radiative interaction. The second method is a prognostic approach in which cloud water content is predicted as the result of application of a conservation equation. Sundqvist (1978) developed a parameterization for stratiform clouds in which cloud liquid water is a prognostic variable governed by a continuity equation, which included such cloud microphysics as the formation and evaporation of cloud liquid water and rain drops.

Sundqvist (1981) tested his parameterization on non-convective clouds by performing a five-day numerical weather prediction with the European Centre for Medium Range Weather Forecasts (ECMWF) model. However, the model's radiative scheme was not included and the only interaction between large-scale cloudiness and the flow field was through the release of latent heat.

Roeckner and Schlese (1985) tested the Sundqvist (1978) stratiform water cloud parameterization with interactive radiation in a perpetual-January integration with the three-layer Hamburg University GCM for the northern hemisphere. It was found that: 1) advection and turbulent diffusion of cloud liquid water were negligible compared to the microphysical terms, 2) the simulated cloud liquid water content was in reasonable agreement with currently available observations, 3) simulated low-level cloudiness was less than observed in low latitudes and greater than observed in high latitudes, and 4) zonally-averaged Earth radiation budgets could be simulated within the range of observational errors.

Roads *et al.* (1984) also developed parameterization for stratiform clouds in which cloud water is a prognostic variable. The source term for large-scale cloud water is condensation, occurring only when the relative humidity exceeds 100%, and the sink terms include evaporation and conversion of cloud water to precipitation. This condensation formulation is more easily understood from the viewpoint of cloud physics than that provided by Sundqvist (1978, 1981), while the conversion formulation has one fewer free parameter. Parameterization of the optical properties of clouds was employed in their test of the parameterization within a two-

dimensional model using prescribed winds.

Charlock and Ramanathan (1985) investigated the effects of variable cloud optical properties on January climates simulated with the NCAR GCM. In this study, cloud optical properties were dependent upon cloud liquid water content, which was determined diagnostically from the condensed water vapor based upon the assumption of one-hour cloud lifetime. The model albedos with the interactive cloud optics were found to be in rough agreement with satellite observations, first as were the simulated cloud radiation sensitivity parameters. Furthermore, systematic regional differences between the GCM-simulated albedos, with and without interactive cloud optics were found with large asymmetries in the interactive cloud-water. The investigators concluded that "it seems that the hydrological cycles of GCMs are sufficiently realistic to warrant a more physically based . . . treatment of cloud microphysical and radiative processes."

Recently, Harshvardhan et al. (1989) examined the earth radiation budget and the fractional cloud cover in the UCLA/GLA GCM (Randall et al., 1988), including cloud optical depth feedback in the study. However, the fractional cloud cover of a grid in the UCLA/GLA GCM is either 0 or 1. Furthermore, the optical depth used for determination of the cloud optical properties was not directly related to cloud liquid water content, which is not simulated in the model, but was calculated from cloud layer temperature and pressure thickness. For this model, the simulated global mean cloudiness was greater then that observed with either the ISCCP or by Susskind et al. (1987), and the meridional structure of the cloud cover was poorly simulated. The simulated zonally-averaged fractional cloud cover significantly exceeds observations a) in tropics and northern hemisphere midlatitudes for January and b) in subtropics for July, while it was significantly underestimated in tropics during July. Moreover, the vertical location of the simulated tropical clouds was much higher than that in the ISCCP either January or July. As expected, the simulated planetary albedo and outgoing longwave radiation were somewhat underestimated compared to the NIMBUS-7 data since these radiation budget terms relate directly to the performance of cloud simulation. As noted by the investigators, these disagreements in the simulated earth

radiation budget and cloud cover may be caused by deficiencies in the parameterization of the fractional cloud cover, in which no fractional cloud cover feedback is allowed, or the lack of cloud water content for determination of cloud optical depths.

At nearly the same time, Smith (1988) introduced a prognostic equation for the cloud water (the stratiform clouds only) into the Meteorological Office 11-layer AGCM (Slingo, 1985). However, cloud radiative properties were fixed within the model. Thus, the cloud optical depth feedback was not allowed.

Finally, Cess and Potter (1987) intercompared the cloud radiative forcing (CF) of six GCMs, comparing these results with those from a comparison of the CF of the OSU/LLNL model (Cess et al., 1985) and the GOES observations (Minnis and Harrison, 1984). Cloud radiative forcing is defined as the impact of clouds on the Earth radiation budget at the top of the atmosphere, or the impact on

$$N = S - R,$$

where N is the net radiation,

      S the solar radiation and

      R the terrestrial longwave radiation.

Thus,

$$CF(N) = CF(S) - CF(R),$$

where CF(S) = S(total) - S(clear),

      CF(R) = R(total) - R(clear), and

      total = indicates the clear plus cloudy conditions.

For their intercomparison of the six GCMs, Cess and Potter (1987) found that CF(N) < 0, indicating that cloud forcing tends to cool the climate, with values range from -2 to -34 Wm^{-2} in January and from +1 to -27 Wm^{-2} in July. This cooling tendency is due to the dominance of solar CF over the warming due to the longwave CF, with values of CF(S) = -45 to -74 Wm^{-2} and CF(R) = -23 to -55 Wm^{-2} in January and CF(S) = -52 to -69 Wm^{-2} and CF(R) = -39 to -53 Wm^{-2} in July. Although two different methods were used in the compared GCMs for CF computation, and several of the GCMs did

not have a diurnal cycle, neither of these differences explain the differences in the CFs among the models. Furthermore, the comparison between the OSU/LLNL GCM and the GOES observations indicated that there was reasonable agreement between the simulated S and R and the observations, (i.e., errors of 10 and 6 Wm^{-2}, respectively), there were respectively, errors of -46 and -40 Wm^{-2} for the overcast S and R components. The agreement between simulated and observed S and R was fortuitously achieved when the overcast S and R errors compensated for the errors of the simulated cloud amounts, which included an underestimation of the GOES observed cloudiness. These model and observational CF results led Cess and Potter to conclude that "these comparisons certainly emphasize the need for improving our understanding as to how to model the impact of clouds upon climate within a GCM."

Recently, Ramanathan et al. (1989), based on the april (1985) data from the Earth Radiation Budget Satellite (ERBS) and the National Oceanic and Atmospheric Administration satellite (NOAA-9), reported negative net cloud forcing is negative with shortwave forcing of -44.5 Wm^{-2} and longwave forcing of 31.3 Wm^{-2}. Their conclusion was that the size of observed net cloud forcing is about four times as large as the expected value of radiative forcing from a doubling of CO_2.

As reviewed above, the role of clouds, for not only maintaining the present climate but also predicting the climate change, has been emphasized (Shukla and Sud, 1981; Tiedtke, 1984; Charlock and Ramanathan, 1985). However, it has not been clearly understood due to the lack of physical parameterization in the GCMs to simulate the cloud-radiation interaction and the lack of adequate global observations. Recently, global satellite observations (e.g., Rossow et al., 1985; Kyle et al., 1985, 1989; Ramanathan et al., 1989) and attempts of the development of physically-based cloud-radiation parameterization for GCMs (e.g., Sundqvist, 1978, 1988; Slingo, 1980, 1987; Harshvardhan et al. 1989; Smith, 1988) encourage us to develop a comprehensive physically-based cloud-radiation parameterization for better understanding of the role of the clouds in maintaining the present climate or changing of the climate related to increase of the greenhouse gases.

3. PARAMETERIZATION OF CLOUDS AND PRECIPITATION

In the earlier version of the OSU multilayer AGCM (Schlesinger and Oh, 1987) as well as in the the OSU two-level AGCM (Ghan *et al.*, 1982), large-scale condensation occurs only when the relative humidity exceeds 100% and the excess moisture of the saturated value of the mixing ratio is precipitated. This precipitated water continues to evaporate until the lower layers become saturated. However, convective precipitation, assumed to be the difference in the water vapor mixing ratio of the model atmosphere prior to and following convection, does not evaporate at all. Whenever large-scale condensation or convection occurs, the fractional cloud cover is assumed to be 1. Thus, the above schemes make no allowance for fractional cloud cover feedback or cloud optical feedback.

At present there are two approaches to the prediction of the fractional cloud cover of stratiform clouds. In the statistical approach, fractional cloud cover is predicted empirically from large-scale variables (Slingo, 1980). By this scheme the model clouds have no interactions with other processes (Arakawa, 1975) except radiative process and the cloud optical properties must be prescribed or calculated separately, based upon cloud water content assumptions (Slingo, 1987). Therefore, only fractional cloud cover feedback is allowed. The second approach is prognostic, involving the prediction of cloud water content from application of a conservation equation encompassing such cloud microphysics as the formation and evaporation of cloud liquid water and rain drops. This scheme allows for the prediction of cloud liquid water content, fractional cloud cover, and then, cloud optical properties, even though more computation time is required. Thus, the prognostic approach encompasses cloud optical depth feedback, as well as fractional cloud cover feedback.

Sundqvist (1978) developed a parameterization for stratiform clouds in which the prognostic variable, cloud liquid water, is governed by a continuity equation. Cloud water is lost due to evaporation in the cloud-

free portion of a grid box and by conversion to precipitation. The evaporation of precipitation falling in sub-saturated air is also parameterized, as is the fractional cloudiness which is closely dependent upon the prescribed relative humidity at which condensation can occur. Non-convective and convective clouds are treated as mutually exclusive considerations with the by-pass of large-scale cloudiness parameterization if a grid box is convectively unstable.

There are three commonly-used penetrating convective schemes for large-scale models. In a review, Tiedtke (1988) noted that the convective adjustment scheme (Manabe *et al.*, 1965, Kurihara, 1973; Betts and Miller, 1984) is relatively simple and fast. However, this scheme is not based on a physical concept, has unrealistic criteria and profiles, and may not be suitable for GCMs. The Kuo scheme (Kuo, 1965, 1974) offers a simple physical concept, with a closure assumption supported by tropical observations. This scheme has been successfully applied under a variety of conditions. However, Kuo's assumption that the environment is heated by mixing of cloud air and environmental air is unrealistic. In turn, the Arakawa and Schubert (1974) scheme provides a clear concept of the interaction of convection and the environment, but at the same time is complex and computationally expensive.

The OSU multilayer AGCM cloud and precipitation parameterization, a modification of the Sundqvist (1978, 1988) scheme for the stratiform clouds and Arakawa and Schubert (1974) and Lord (1978) for cumuloform clouds, has been designed for the prognostic evaluation of cloud water. Fractional cloudiness is calculated diagnostically and cloud optical properties are dependent upon the amount of the cloud water. Thus, the proposed cloud scheme allows both fractional cloud cover feedback and cloud optical depth feedback. In this parameterization, large-scale condensation can occur even though the relative humidity is less than 100 percent. The cloud liquid water generated by large-scale condensation remains in the cloud until it exceeds the threshold value. Cumuloform clouds generate cloud water and precipitation as a function of convective mass flux. The remaining cloud water can be evaporated to the environment. Moreover, the model allows for the evaporation of precipitation from both stratiform and cumuloform clouds below the cloud

base. Fractional cloudiness is calculated from the relative humidity and cloud mass flux.

3.1. Stratiform Clouds and Large-Scale Precipitation

The parameterization of stratiform clouds and large-scale precipitation for the OSU multilayer AGCM is based on Sundqvist's (1978, 1988), but with a different treatment for cloud microphysics. The Sundqvist's parameterization is summarized in section 3.1.1. Then, in section 3.1.2, the design of the new stratiform clouds and precipitation parameterization is introduced with the difference from the Sundqvist's.

3.1.1. Sundqvist's stratiform condensation and fractional cloudiness parameterization

A schematic diagram of Sundqvist's (1978, 1988) stratiform cloud model is shown in Fig. 3.1. A GCM grid box with horizontal and vertical dimensions, respectively, Δs and Δz, has the fractional cloudiness b (0 to 1), [based on the assumption that it fills the vertical extent of the GCM layer.] Inside the cloud (denoted by a circumflex), the relative humidity U is assumed to be equal to the saturation value $U_s = 1$, the liquid water mixing ratio is $\hat{m}$, the rate of condensation per unit mass of air is $\hat{Q}$, and the rate of precipitation is $\hat{P}$. In clear air, the relative humidity is U_0, precipitation falling from above partially evaporates at rate E_r, and cloud liquid water evaporates at the rate $\hat{E}_c$. The average grid box values of the condensation quantities are

$$Q = b \hat{Q}, \tag{3.1}$$

$$m = b \hat{m}, \tag{3.2}$$

and

$$P = b \hat{P}. \tag{3.3}$$
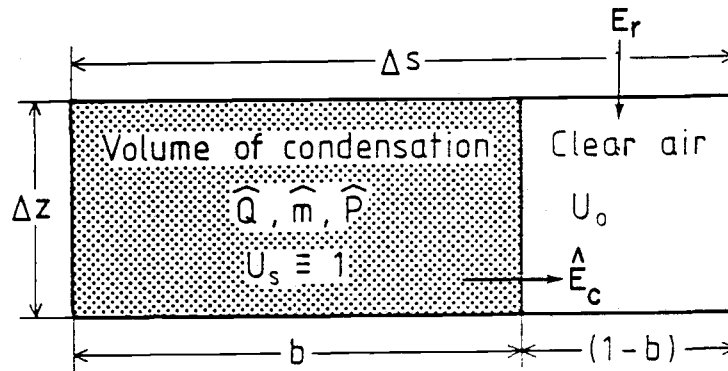
Fig. 3.1. Schematic diagram of Sundqvist's stratiform cloud model (from
Sundqvist, 1988).

The large-scale prognostic equations for a GCM grid box are

$$\frac{\partial T}{\partial t} = A_T + \frac{L}{c_p} Q - \frac{L}{c_p} (E_r + E_c) \,, \tag{3.4}$$

$$\frac{\partial q}{\partial t} = A_q - Q + E_r + E_c \,, \tag{3.5}$$

and

$$\frac{\partial m}{\partial t} = A_m + Q - P - E_c \,, \tag{3.6}$$

where the A terms denote tendencies from all processes other than
condensation. In these equations the only unknown term on the right-
hand side is Q. Using the definition of relative humidity,

$$U = \frac{q}{q_s (T,p)} \,, \tag{3.7}$$

where q is the water vapor mixing ratio, and

$$q_s(T,p) \cong \varepsilon \frac{e_s(T)}{p} \tag{3.8}$$

is the saturation mixing ratio at temperature T and pressure p, with $\varepsilon =$ 0.622 and $e_s(T)$, the saturation vapor pressure satisfies the Clausius-Clapeyron equation:

$$\frac{\partial \ln e_s}{\partial T} = \frac{\varepsilon L}{R_d T^2}, \tag{3.9}$$

where L and R_d are, respectively, the latent heat of condensation and the gas constant. The following equation is then obtained:

$$\frac{1}{q} \frac{\partial q}{\partial t} = \frac{1}{U} \frac{\partial U}{\partial t} + \frac{\varepsilon L}{R_d T^2} \frac{\partial T}{\partial t} - \frac{1}{p} \frac{\partial p}{\partial t}. \tag{3.10}$$

Combining Eq. (3.10) with Eqs. (3.4) and (3.5) (excluding the evaporation terms since E_c is not a grid-scale source of condensate and precipitation does not evaporate within the cloud) and solving for Q, the result is

$$Q = \frac{M - q_s \frac{\partial U}{\partial t}}{1 + U S_q}, \tag{3.11}$$

where

$$M = A_q - U \frac{c_p}{L} S_q A_T + U q_s \frac{1}{p} \frac{\partial p}{\partial t} \tag{3.12}$$

and

$$S_q = \frac{\varepsilon L^2}{R_d c_p} \frac{q_s}{T^2}. \tag{3.13}$$

In Eq. (3.11), the term $\partial U/\partial t$ can be expressed in terms of $\partial b/\partial t$ and $\partial U_0/\partial t$ as follows. The grid-averaged mixing ratio can be written as

$$q = b\,q_s + (1-b)\,q_0\,, \tag{3.14}$$

where q_0 is the clear part mixing ratio. Hence, dividing by q_s and using Eq. (3.7),

$$U = b\,U_s + (1-b)\,U_0\,. \tag{3.15}$$

Then,

$$\frac{\partial U}{\partial t} = (U_s - U_0)\,\frac{\partial b}{\partial t} + (1-b)\,\frac{\partial U_0}{\partial t}\,. \tag{3.16}$$

Substituting Eq. (3.16) into Eq. (3.11) gives

$$Q = \frac{\left\{ M - q_s\left[(U_s - U_0)\,\frac{\partial b}{\partial t} + (1-b)\,\frac{\partial U_0}{\partial t} \right] \right\}}{1 + U\,S_q}\,. \tag{3.17}$$

To close the parameterization, expressions must be provided for $\partial U_0/\partial t$ and $\partial b/\partial t$. First, as shown in Fig. 3.2, [it is assumed that $M + E_r$ is partitioned between clear and cloudy air in the proportions, respectively, $(1-b)$ and b, and that the clear component acts to increase both b and q_0 as

$$(1-b)\,\frac{\partial q_0}{\partial t} + [(q_s + \hat{m}) - q_0]\,\frac{\partial b}{\partial t} = (1-b)\,(M + \bar{E}_r)\,, \tag{3.18}$$

where $\bar{E}_r = E_r\,/\,(1-b)$.] The first term in the left-hand side of Eq. (3.18) represents the moistening of the clear area, while the second term represents the horizontal cloud expansion in a GCM grid box. The right-hand side of Eq. (3.18) represents the convergence of moisture in the clear part and the evaporation within the clear part of rain from the layer above. Then, using

$$\frac{\partial q_0}{\partial t} \cong q_s\,\frac{\partial U_0}{\partial t}\,, \tag{3.19}$$

Eq. (3.18) becomes

$$q_s (1-b) \frac{\partial U_0}{\partial t} + [(q_s + \hat{m}) - q_0] \frac{\partial b}{\partial t} = (1-b)(M + \bar{E}_r).$$

(3.20)
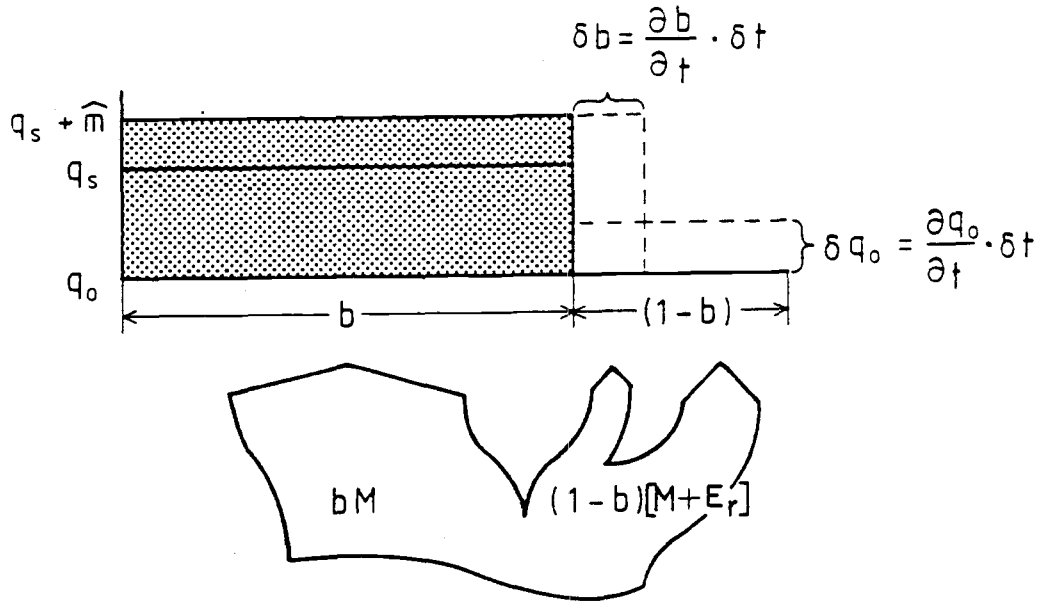
Fig. 3.2. Use of moisture convergence in the Sundqvist stratiform cloud model (from Sundqvist, 1988).

Second, [it is assumed that $U_0 = F(b)$ and, for purpose of simplicity,

$$U_0 = U_{00} + b (U_s - U_{00}),$$

(3.21)

where U_{00} is a prescribed threshold relative humidity at which condensation can begin.] This expression satisfies the consistency condition $U_0(1) = U_s$. Then, it follows that

$$\frac{\partial U_0}{\partial t} = (U_s - U_{00}) \frac{\partial b}{\partial t} .$$

(3.22)

Substituting Eq. (3.22) into Eq. (3.20), and solving for $\partial b/\partial t$,

$$\frac{\partial b}{\partial t} = \frac{(1-b)(M+E_r)}{\hat{m} + q_s [(1-b)(U_s - U_{00}) + U_s - U_0]} ,$$

(3.23)

and from Eq. (3.22),

$$\frac{\partial U_0}{\partial t} = (U_s - U_{00}) \left\{ \frac{(1-b)(M+E_r)}{\hat{m} + q_s [(1-b)(U_s - U_{00}) + U_s - U_0]} \right\} .$$

(3.24)

Finally, substituting Eqs. (3.23) and (3.24) into Eq. (3.17), and using Eq. (3.21), the following is obtained:

$$Q = \left(\frac{1}{1 + U S_q} \right) \left\{ M - q_s \left[\frac{2(1-b)^2 (U_s - U_{00})}{\hat{m} + 2 q_s (1-b)(U_s - U_{00})} (M + \bar{E}_r) \right] \right\} .$$

(3.25)

The fractional cloudiness b may then be expressed in terms of U by the substitution of Eq. (3.21) into Eq. (3.15) to obtain

$$b = \begin{cases} 1 - \sqrt{\dfrac{U_s - U}{U_s - U_{00}}} & \text{for } Q > 0 \\[2em] 0 & \text{for } Q = 0 . \end{cases}$$

(3.26)

The cloud microphysical quantities, $\hat{P}$, E_r and $\hat{E}_c$ are parameterized as follows:

$$\hat{P} = c_0 \, \hat{m} \, \{1 - \exp[-(\hat{m}/m_r)^2]\} ,$$

(3.27)

where c_0^{-1} is a characteristic time for conversion of cloud droplets into precipitation drops and m_r is the cloud water content at which the release of precipitation begins to be efficient (for $\hat{m} < m_r$, $\hat{P}$ is small and the condensed water mainly increases the cloud water content);

$$E_r = k_E (U_s - U) (1 - b) \hat{P}^{1/2} , \tag{3.28}$$

where k_E is an evaporation coefficient and b is the fractional cloudiness. $\hat{E}_c$ is allowed to take place only when cloud water is advected into a grid square where no condensation is taking place. In such cases [all the advected cloud water is assumed to evaporate instantly.]

3.1.2. Parameterization of stratiform cloud, precipitation, and fractional cloudiness for the OSU multilayer AGCM

The OSU multilayer AGCM parameterization of stratiform clouds is based on Sundqvist's (1978, 1988) work. However, it differs in the treatment of cloud microphysics related to the source and sink of cloud liquid water. The differences are listed below, following description of the parameterization.

The conservation equations for thermodynamic energy, water vapor, and cloud water for an AGCM gridbox in layer ℓ are, respectively,

$$\frac{\partial T_\ell}{\partial t} = (A_T)_\ell + \frac{L}{c_p} Q_\ell - \frac{L}{c_p} (E_r)_\ell - \frac{L}{c_p} (E_c)_\ell , \tag{3.29}$$

$$\frac{\partial q_\ell}{\partial t} = (A_q)_\ell - Q_\ell + (E_r)_\ell + (E_c)_\ell , \tag{3.30}$$

and

$$\frac{\partial m_\ell}{\partial t} = (A_m)_\ell + Q_\ell - P_\ell - (E_c)_\ell . \tag{3.31}$$

Here only horizontal advection is allowed for the cloud liquid water. To

insure that the horizontal cloud liquid water flux does not remove more liquid water from any point in time Δt, than exists, the cloud liquid water flux is constrained in the same manner as for the moisture flux (for details, see Ghan *et al.*, 1982).

The last three processes are parameterized independently. Assuming that A_T, A_q, and A_m are known, the condensation term Q is the only unknown term in Eqs. (3.29) through (3.31). However unlikely in Sundqvist (1988), the evaporation is not included in calculation of condensation, in order to maintain consistency between the budget equation inside the cloud and outside the cloud. Condensation can be obtained by considering the generation of cloud liquid water. Total condensation is the sum of the increase of cloud liquid water within the cloud and the condensation associated with the horizontal expansion of the cloud. This results in

$$Q = \frac{1}{1 + U S_q}\left(b\,M + \hat{m}\,\frac{\partial b}{\partial t}\right).$$

(3.32)

In Eq. (3.32), the first term on the right-hand side represents the increase of cloud liquid water content by condensation inside the cloud and the second term represents the expansion of the cloud by condensation from outside the cloud. Then, from Eqs. (3.17) and (3.32),

$$b\,M + \hat{m}\,\frac{\partial b}{\partial t} = M - \left[q_s\,(1-b)\,\frac{\partial U_0}{\partial t} + (q_s - q_0)\,\frac{\partial b}{\partial t}\right]$$

(3.33)

or

$$q_s\,(1-b)\,\frac{\partial U_0}{\partial t} + [(q_s + \hat{m}) - q_0]\,\frac{\partial b}{\partial t} = (1-b)\,M\,.$$

(3.34)

This equation is identical to Eq. (3.20) without evaporation, which must be obtained from the clear part. Thus, to be consistent, the condensation in the layer ℓ is written without evaporation as in Eq. (3.25):

$$Q_\ell = \frac{M_\ell}{1 + U_\ell \, (S_q)_\ell} \left[1 - \frac{(1 - b_\ell) \, B_\ell}{\dfrac{m_\ell}{b_\ell} + B_\ell} \right],$$

(3.35)

where

$$B_\ell = 2 \, (q_s)_\ell \, (1 - b_\ell) \, (U_s - U_{00}) \, ,$$

(3.36)

and, from Eqs. (3.12) and (3.13), respectively,

$$M_\ell = (A_q)_\ell - U_\ell \, \frac{c_p}{L} \, (S_q)_\ell \, (A_T)_\ell + U_\ell \, (q_s)_\ell \left[\frac{1}{p_\ell} \frac{\partial p_\ell}{\partial t} \right]$$

(3.37)

and

$$(S_q)_\ell = \frac{\varepsilon \, L^2 \, (q_s)_\ell}{R_d \, c_p \, T_\ell^2} \, .$$

(3.38)

[The evaporation of cloud water is assumed to be in the form

$$(\hat{E}_c)_\ell = \left(\frac{U_s - U_\ell}{\tau} \right) \hat{m}_\ell \, ,$$

or in the grid-averaged form

$$(E_c)_\ell = \left(\frac{U_s - U_\ell}{\tau} \right) m_\ell \, ,$$

(3.39)

where τ is an empirical parameter.] Figure 3.3 shows the relationship between the e-folding time, τ_e [$= \tau/(U_s - U)$], for different values of U in the case, $\tau = 0.05$ hour. The cloud liquid water can be advected into a cloud-free grid square and may exist without clouds. To prevent this case, [if there is no cloud it is assumed that cloud liquid water is evaporated instantly.]

Precipitation of cloud water occurs in two basic processes, including the autoconversion of cloud water to rain water due to coalescence and the collection of cloud droplets by rain droplets. However, for the GCM, the
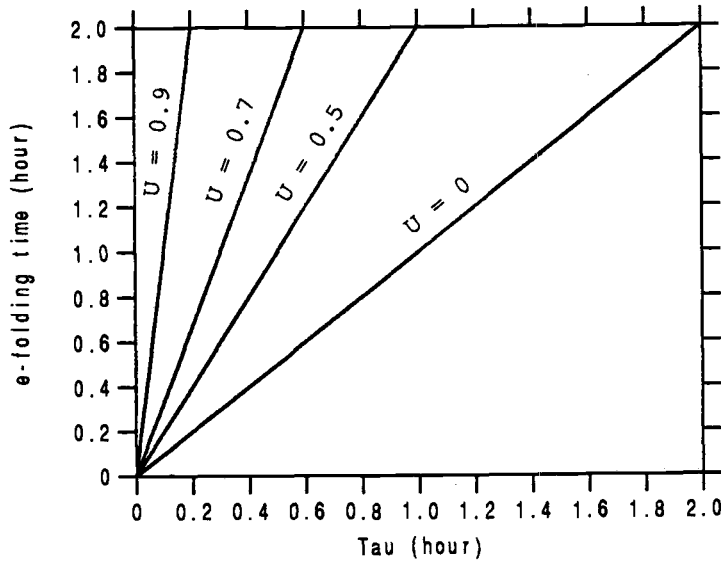
Fig. 3.3 The e-folding time of the evaporation of the cloud liquid water for different U values of environment.

precipitation process is treated as simply as possible. [It is assumed that all cloud water in excess of a threshold value is precipitated in a manner similar to the autoconversion process introduced by Kessler (1969).] The autoconversion of cloud water is parameterized as follows:

$$\hat{P}_\ell = \begin{cases} a\,(\hat{m}_\ell - m_c)\,, & \text{for } \hat{m}_\ell > m_c \\ \\ 0\,, & \text{for } \hat{m}_\ell \le m_c \end{cases}$$

or for grid-averaged autoconversion of cloud water,

$$P_\ell = \begin{cases} a\,(m_\ell - b_\ell\,m_c)\,, & \text{for } \hat{m}_\ell > m_c \\ \\ 0\,, & \text{for } \hat{m}_\ell \le m_c\,, \end{cases} \tag{3.40}$$

where a is a rate coefficient, b_ℓ is the fractional cloudiness of layer ℓ, and m_c is the mass threshold value for the conversion. The values of a and m_c are chosen as

$$a = \frac{1}{3600} \, s^{-1}$$

(3.41)

in order that the excess cloud liquid water above the threshold value of the cloud can be precipitated. As shown in Fig. 3.4, the threshold value for precipitation is given as

$$m_c = \begin{cases} 1 \times 10^{-4} \text{ g/g}, & \text{for } T \geq 0^\circ C, \\ (1 \times 10^{-4})(1 - R_T) + I_c \, R_T & \text{for } T_i < T < 0^\circ C, \\ I_c, & \text{for } T \leq T_i, \end{cases}$$

(3.42)

in which $T \geq 0^\circ C$ is from Rutledge and Schlesinger (1985) and the observational study of Heymsfield and Platt (1984), in which the mean ice content of cirrus was given in unit of g/m^3. In Eq. (3.42), T_i is the critical temperature of the ice cloud and R_T is the ratio for a linear combination of the threshold value of the mixed phase cloud,

$$R_T = \frac{273.1 - T}{273.1 - T_i},$$

(3.43)

and I_c is the ice threshold value in units of g/g from the mean ice content of cirrus (Heymsfield and Platt, 1984) and the air density of U.S. Standard atmosphere (U.S. Committee on Extension to the Standard Atmosphere, 1976).

The evaporation rate of rain below the cloud in layer ℓ, in which the fractional cloudiness is b, is taken from Schlesinger et $al.$ (1988) as

$$(E_r)_\ell = 10 \left(\frac{g}{\pi \, \Delta_\ell \sigma} \right)(1 - b_\ell) \, C_{RM} \, (R_{\ell-1/2})^{\alpha_{RM}} \, \Psi(z_{\ell-1/2} - z_{\ell+1/2}),$$

(3.44)
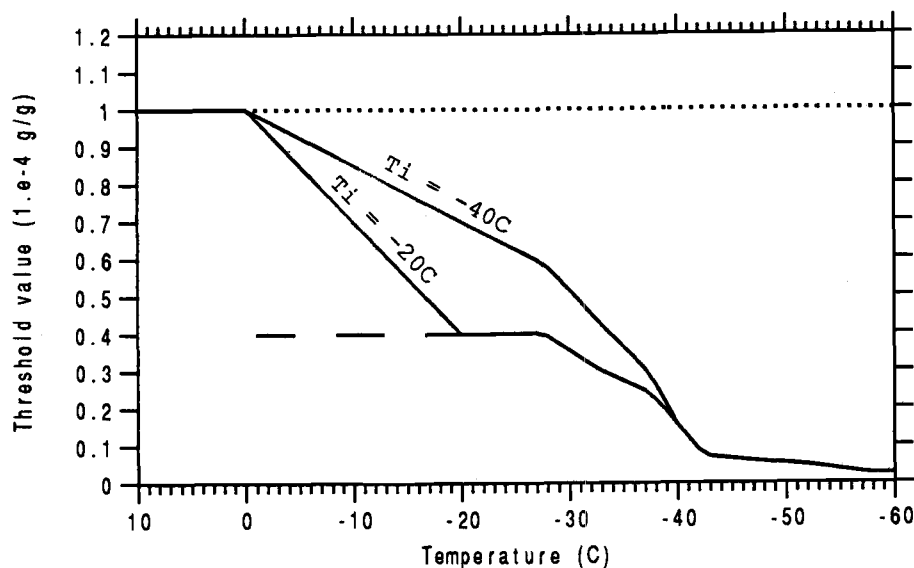
Fig. 3.4 Temperature dependence of threshold value for stratiform cloud. The solid line is for the mixed phase cloud, the dotted line is for the liquid water cloud, and the dashed line is for the ice cloud (I_c).

where $R_{\ell\text{-}1/2}$ is the grid-averaged precipitation rate from the layer above in units of mm/h. It follows, then, that

$$C_{RM} = 2.63 \times 10^{-2} \, [(\text{mm/h})^{1-\alpha_{RM}} \, \text{mm}^3/\text{s}] , \tag{3.45}$$

$$\alpha_{RM} = 0.606 , \tag{3.46}$$

and

$$\Psi(z_{\ell-1/2} - z_{\ell+1/2}) = \int_{z_{\ell+1/2}}^{z_{\ell-1/2}} \left(\frac{1-S}{K_1 + K_2}\right)_\ell dz$$

$$= \frac{1-S_\ell}{(K_1 + K_2)_\ell} (z_{\ell-1/2} - z_{\ell+1/2}) \tag{3.47}$$

where S is the layer saturation ratio (Schlesinger *et al.*, 1988). From Eq. (3.47),

$$K_1 = \frac{L^2 \rho_m}{k R_v T^2} \tag{3.48}$$

and

$$K_2 = \frac{R_v T \rho_m}{D_w e_s(T)} \tag{3.49}$$

where ρ_m is the density of liquid water, k is the thermal conductivity of air, D_w is the diffusivity of water vapor in the air, and R_v is the gas constant for water vapor.

Fractional cloudiness, as shown in Fig. 3.5 for non-zero condensation, is defined by Eq. (3.26) as

$$b_\ell = 1 - \sqrt{\frac{U_s - U_\ell}{U_s - U_{00}}}, \qquad \text{for } Q > 0 \text{ and } m_\ell > 0 , \tag{3.50}$$

where the constraints $Q > 0$ and $m_\ell > 0$ are imposed on the solution. [For other conditions, it is assumed that

$$b_\ell = \begin{cases} \tilde{b}_\ell , & \text{for } Q = 0 \text{ and } m_\ell > 0 , \\ \\ 0, & \text{otherwise} , \end{cases} \tag{3.51}$$

where $\tilde{b}_\ell$ is the fractional cloudiness of the previous time-step of the time marching procedure of the model.] If there is no condensation ($Q = 0$), fractional cloudiness retains the same value as long as the cloud liquid water exists.

With autoconversion and evaporation terms, the large-scale precipitation rate in units of [mm/hr] at the bottom of the cloud layer ℓ is

$$R_{\ell+1/2} = R_{\ell-1/2} + \frac{1}{10\left(\dfrac{g}{\pi \Delta_\ell \sigma}\right)} [P_\ell - (E_r)_\ell] . \tag{3.52}$$
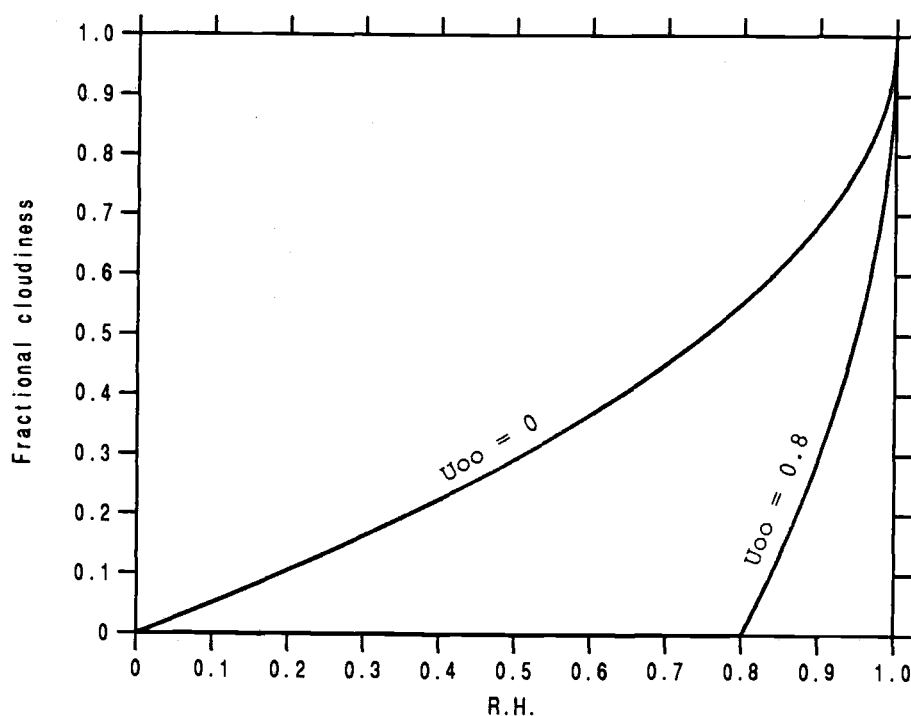
Fig. 3.5 Relationship between the relative humidity and fractional cloudiness for $U_{00} = 0$ and 0.8.

[In Eq. (3.52) the cloud overlap is ignored for the sake of simplicity.]

The principal differences of this parameterization from that of Sundqvist (1978, 1988) are:

1) The evaporation in the clear part of a GCM gridbox of rain from layers above is not included in the calculation of Q, in order to maintain consistency between the budget equations for water inside the cloud and outside the cloud.

2) The evaporation (sublimation) of cloud liquid water (ice) is calculated regardless of whether or not there is condensation, and the evaporation rate depends on the cloud water content and the

saturation ratio of environment.

3) The fractional cloud cover remains until the cloud water either evaporates completely or condensation reoccurs.

4) The autoconversion of cloud water to precipitation is parameterized in a manner similar to that of Kessler (1969).

5) The evaporation rate of rain is calculated according to Schlesinger *et al.* (1988).

A schematic diagram of the physical procedure for stratiform cloud calculation is shown in Fig. 3.6 with a comparison to Sundqvist's (1988). The major difference lies in the treatment of existing cloudiness when there is no condensation ($U \leq U_{00}$ or $M \leq 0$). In the Sundqvist parameterization the fractional cloud cover is set to 0 and advected cloud liquid water is evaporated instantly. Furthermore, Sundqvist did not allow evaporation of cloud liquid with condensation. In the proposed parameterization, fractional cloudiness retains the same value until the cloud liquid water is completely evaporated, after which b is set to 0 as in Eq. (3.51). And evaporation is allowed whether or not there is condensation.
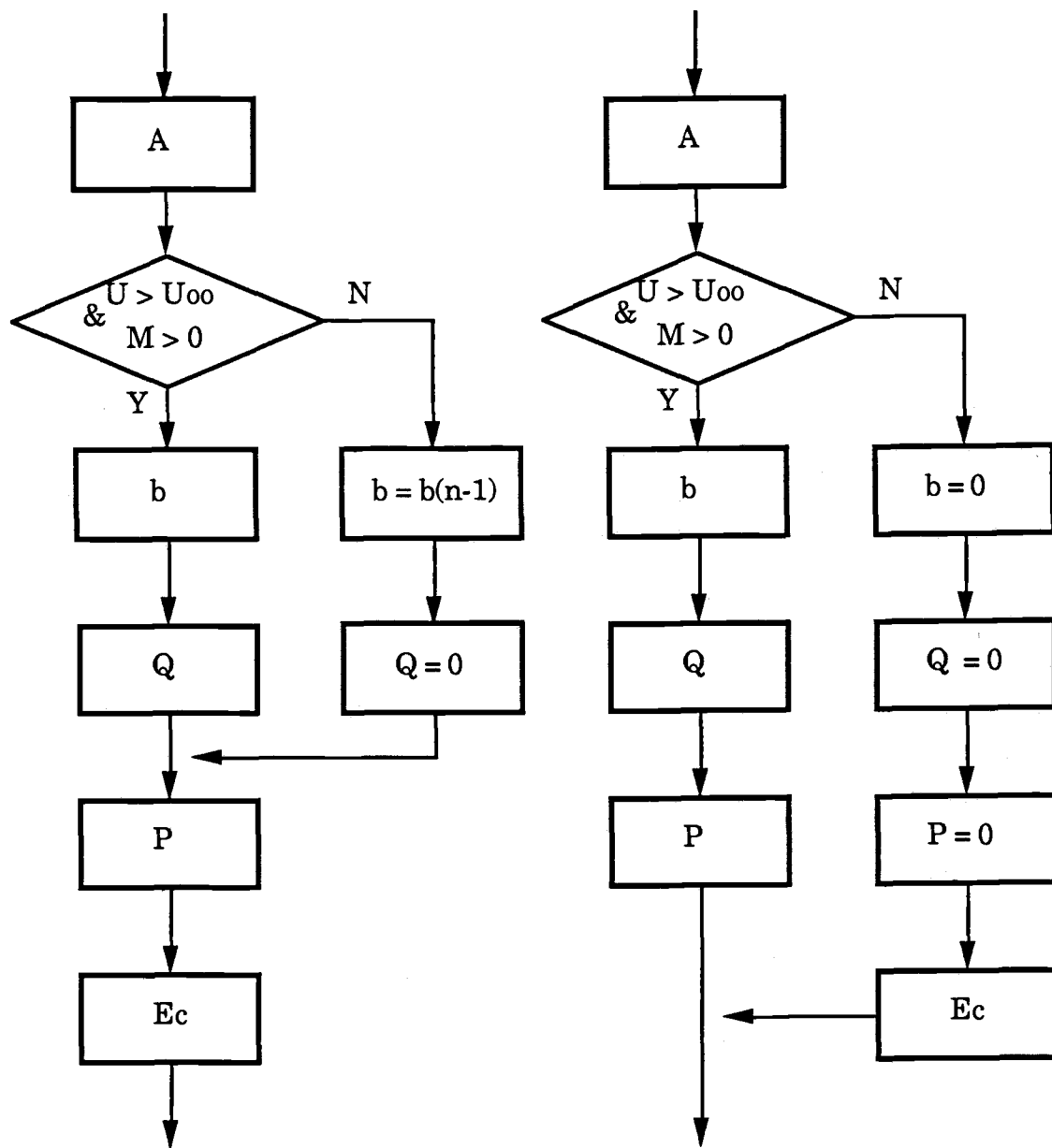
OSU multilayer AGCM   Sundqvist's parameterization

Fig. 3.6. Schematic diagram of physical procedure in stratiform cloud parameterization.

3.2. Cumuloform Clouds and Convective Precipitation

3.2.1. Static variables for convection

[It is assumed that the air in the cloud is saturated.] Then,

$$q_c \approx q^*(T_c, p) . \tag{3.53}$$

Neglecting the effect of the pressure difference between the cloud and the environment on q^*, Eq. (3.53) can be written as

$$q_c \approx q^* + \frac{1}{c_p} \left(\frac{\partial q^*}{\partial T} \right)_p (s_c - s) , \tag{3.54}$$

where the variables subscripted with c are cloud variables. Then,

$$s_c - s \approx \frac{1}{1 + \gamma} (h_c - h^*) \tag{3.55}$$

and

$$q_c - q^* \approx \frac{\gamma}{1 + \gamma} \frac{1}{L} (h_c - h^*) , \tag{3.56}$$

where

$$\gamma \equiv \frac{L}{c_p} \left(\frac{\partial q^*}{\partial T} \right) ,$$

$h \ (= c_p T + gz + Lq)$ is the moist static energy, and h^* is the saturated value of h.

3.2.2. Mid-level convection

If $h_{\ell+1} > h_\ell^*$, an air parcel rising from the layer $\ell+1$ will experience positive buoyancy if the air parcel becomes saturated in the layer ℓ. [It is assumed that this buoyancy results in the mid-level convection. Two stages of convection are assumed: (1) the mature stage when the cloud has a positive buoyancy, followed by cloud mass flux, and (2) the dissipating stage, when the cloud no longer has positive buoyancy, and then, has no cloud mass flux. During the dissipating stage the cloud is nonprecipitating and it decays by evaporation or the sublimation of cloud water into the environment.]

3.2.2.1. Cloud water budget

[Assuming that there is no storage in the cloud at the entrainment layer and only storage of cloud water at the detrainment layer (i.e., consistent with stratiform clouds),] the cloud total water and liquid water budgets for this type of convection during the mature stage can be written as

$$[b \, \hat{M}_c \, (q_c + \hat{m})]_{\ell+1/2} = [(1-b) \, \hat{M}_e \, q]_{\ell+1}$$

$$- b_\ell \, (\hat{M}_c)_\ell \, C_0 \, (z_{\ell+1/2} - z_{\ell+1}) \, \hat{m}_{\ell+1/2} \qquad (3.57)$$

for the entrainment layer, and as

$$\frac{\pi \, \delta_\ell \sigma}{g} \frac{\partial}{\partial t} \, [b \, (q_c + \hat{m})]_\ell = [b \, \hat{M}_c \, (q_c + \hat{m})]_{\ell+1/2} - b_\ell \, (\hat{M}_c)_\ell \, (q_c)_\ell$$

$$- b_\ell \, (\hat{M}_c)_\ell \, C_0 \, (z_\ell - z_{\ell+1/2}) \, \hat{m}_\ell - \frac{\pi \, \delta_\ell \sigma}{g} \, (E_c)_\ell \qquad (3.58)$$

for the detrainment layer, where $\hat{m}$ is cloud water content, $\hat{M}_c$ is the mass

flux inside cloud, $\hat{M}_e$ is the environmental mass flux due to convection, $(E_c)_\ell$ is the evaporation of cloud water, and $(q_c)_\ell$ is taken from Eq. (3.56) as

$$(q_c) = q^* + \frac{\gamma}{1+\gamma} \frac{1}{L} [(h_c) - h^*] .$$

(3.59)

In Eqs. (3.57) and (3.58), C_0 is the autoconversion coefficient for convective precipitation. The moist static energy at the cloud top, h_c, is defined as

$$(h_c)_\ell = (h_c)_{\ell+1/2} = h_{\ell+1}$$

(3.60)

for the conservation of moist static energy. For the conservation of mass, the mass flux of both cloud and environment can be written as

$$b M_c = (1-b) M_e = M_{\ell+1/2} ,$$

(3.61)

where $M_{\ell+1/2}$ is the area weighted mass flux, as shown in Fig. 3.7 (see section 3.2.2.5 for the determination of this mass flux).
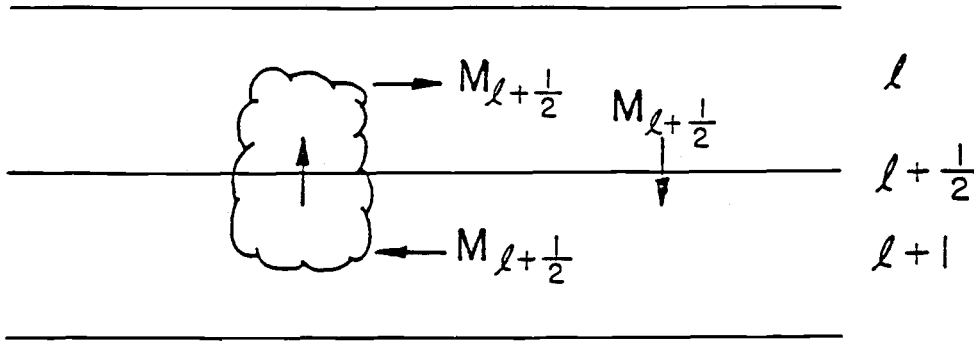
Fig. 3.7. Schematic diagram for mid-level convection. $M_{\ell+1/2}$ is mass flux at level $\ell+1/2$.

Substituting Eq. (3.61) into Eqs. (3.57) and (3.58), the results are

$$M_{\ell+1/2} [q_c + \hat{m}]_{\ell+1/2} = M_{\ell+1/2} q_{\ell+1} - M_{\ell+1/2} C_0 (z_{\ell+1/2} - z_{\ell+1}) \hat{m}_{\ell+1/2}$$

(3.62)

for the entrainment layer and

$$\frac{\pi \delta_\ell \sigma}{g} \frac{\partial}{\partial t} [b (q_c + \hat{m})]_\ell = M_{\ell+1/2} [q_c + \hat{m}]_{\ell+1/2} - M_{\ell+1/2} (q_c)_\ell$$

$$- M_{\ell+1/2} C_0 (z_\ell - z_{\ell+1/2}) \hat{m}_\ell - \frac{\pi \delta_\ell \sigma}{g} (E_c)_\ell \qquad (3.63)$$

for the detrainment layer.

In the entrainment layer the cloud water budget is trivial since it is assumed that after precipitation all cloud water is moved to the next layer above. However, at the detrainment layer the cloud water budget can be written from Eq. (3.63), based upon the assumption that the only storage in the cloud is cloud water. Therefore,

$$\frac{\partial}{\partial t} (q_c) = 0 , \qquad (3.64)$$

and then,

$$\frac{\pi \delta_\ell \sigma}{g} \frac{\partial m_\ell}{\partial t} = M_{\ell+1/2} [q_c + \hat{m}]_{\ell+1/2} - M_{\ell+1/2} (q_c)_\ell$$

$$- M_{\ell+1/2} C_0 (z_\ell - z_{\ell+1/2}) \hat{m}_\ell - \frac{\pi \delta_\ell \sigma}{g} (E_c)_\ell . \qquad (3.65)$$

The cloud water budget is computed in three steps, based upon the following cloud water mixing ratio definition:

$\tilde{m}$ = the value before precipitation and evaporation

$\check{m}$ = the value after precipitation and before evaporation .

Entrainment layer:

From Eq. (3.62), representing cloud water prior to precipitation, $\tilde{m}$ can be written as

$$\tilde{m}_{\ell+1/2} = q_{\ell+1} - (q_c)_{\ell+1/2} . \qquad (3.66)$$

Then, when precipitation is taken into account, the cloud water is

$$\breve{m}_{\ell+1/2} = \tilde{m}_{\ell+1/2} - C_0\,(z_{\ell+1/2} - z_{\ell+1})\,\breve{m}_{\ell+1/2}$$

$$= \frac{\tilde{m}_{\ell+1/2}}{1 + C_0\,(z_{\ell+1/2} - z_{\ell+1})} \tag{3.67}$$

and the autoconversion rate to precipitation in units of g/g, $P_{\ell+1}$ is

$$P_{\ell+1} = M_{\ell+1/2}\,(\tilde{m}_{\ell+1/2} - \breve{m}_{\ell+1/2})\,. \tag{3.68}$$

Detrainment layer:

From Eq. (3.63), $\tilde{m}$ can be written as

$$\tilde{m}_{\ell} = (q_c + \hat{m})_{\ell+1/2} - (q_c)_{\ell}\,. \tag{3.69}$$

Then, when precipitation is taken into account, the cloud water is

$$\breve{m}_{\ell} = \tilde{m}_{\ell} - C_0\,(z_{\ell} - z_{\ell+1/2})\,\breve{m}_{\ell}$$

$$= \frac{\tilde{m}_{\ell}}{1 + C_0\,(z_{\ell} - z_{\ell+1/2})} \tag{3.70}$$

and the autoconversion rate to precipitation in units of g/g, P_{ℓ} is

$$P_{\ell} = M_{\ell+1/2}\,(\tilde{m}_{\ell} - \breve{m}_{\ell})\,. \tag{3.71}$$

Following precipitation, the evaporation of cloud water has been taken into account as

$$(E_c)_{\ell} = -\frac{(U_s - U_{\ell})}{\tau}\,\breve{m}_{\ell}\,, \tag{3.72}$$

where τ is chosen the same as in section 3.1.2.

During the dissipating stage, $M_{\ell+1/2} = 0$, the cloud consists only of its detrainment shield, in which [it is assumed that the fractional cloudiness, b_ℓ (defined in following section) remains at maximum value during the mature stage. It is also assumed that the cloud is nonprecipitating and decays only by evaporation or the sublimation of cloud water into the environment.] Thus, from Eq. (3.65), with $M_{\ell+1/2} = 0$,

$$\frac{\partial\, m_\ell}{\partial t} = -\frac{(U_s - U_\ell)}{\tau}\, m_\ell\,. \qquad (3.73)$$

3.2.2.2. Environmental moisture, energy and momentum budgets

[Based upon the assumption of the conservation of energy and momentum for this type of convection,] the environmental moisture, energy, and momentum budgets for layers ℓ and $\ell+1$ can be written as

$$\frac{\pi\,\delta_\ell\sigma}{g}\,\frac{\partial\, q_\ell}{\partial t} = M_{\ell+1/2}\,[(q_c)_\ell - \hat{q}_{\ell+1/2}] + \frac{\pi\,\delta_\ell\sigma}{g}\,[(E_r)_\ell + (E_c)_\ell]\,, \qquad (3.74)$$

$$\frac{\pi\,\delta_{\ell+1}\sigma}{g}\,\frac{\partial\, q_{\ell+1}}{\partial t} = M_{\ell+1/2}\,[\,\hat{q}_{\ell+1/2} - q_{\ell+1}] + \frac{\pi\,\delta_{\ell+1}\sigma}{g}\,(E_r)_{\ell+1}\,, \qquad (3.75)$$

$$c_p\,\frac{\pi\,\delta_\ell\sigma}{g}\,\frac{\partial\, T_\ell}{\partial t} = M_{\ell+1/2}\,[(s_c)_\ell - \hat{s}_{\ell+1/2}] - L\,\frac{\pi\,\delta_\ell\sigma}{g}[(E_r)_\ell + (E_c)_\ell]\,, \qquad (3.76)$$

$$c_p\,\frac{\pi\,\delta_{\ell+1}\sigma}{g}\,\frac{\partial\, T_{\ell+1}}{\partial t} = M_{\ell+1/2}\,[\hat{s}_{\ell+1/2} - s_{\ell+1}] - L\,\frac{\pi\,\delta_{\ell+1}\sigma}{g}\,(E_r)_{\ell+1}\,, \qquad (3.77)$$

$$\frac{\pi\,\delta_\ell\sigma}{g}\,\frac{\partial\, V_\ell}{\partial t} = M_{\ell+1/2}\,[(V_c)_\ell - \hat{V}_{\ell+1/2}]\,, \qquad (3.78)$$

and

$$\frac{\pi \, \delta_{\ell+1} \sigma}{g} \cdot \frac{\partial \mathbf{V}_{\ell+1}}{\partial t} = M_{\ell+1/2} \, [\hat{\mathbf{V}}_{\ell+1/2} - \mathbf{V}_{\ell+1}] \, , \tag{3.79}$$

where $\pi \, \delta_\ell \sigma / g$ is the mass of layer ℓ per unit area, E_r is the evaporating rate from precipitation of this convection type from the layer above, and (s_c) and $(\mathbf{V}_c)$ are the grid-averaged dry static energy defined by Eq. (3.55) and the momentum of the detrained cloud air in layer ℓ as

$$(s_c)_\ell = s + \frac{1}{1+\gamma_\ell} \, [(h_c)_\ell - h_\ell^*] \, , \tag{3.80}$$

and by the conservation of momentum as

$$(\mathbf{V}_c)_\ell = \mathbf{V}_{\ell+1} \, . \tag{3.81}$$

Moreover, the variables at the half-integer level, $\hat{(\,)}$, are defined as

$$\hat{q}_{\ell+1/2} = \frac{1}{2} \, (q_\ell + q_{\ell+1}) \tag{3.82}$$

and

$$\hat{s}_{\ell+1/2} = c_p \, \hat{T}_{\ell+1/2} + g \, \hat{z}_{\ell+1/2} \, , \tag{3.83}$$

where

$$\hat{T}_{\ell+1/2} = \theta_{\ell+1} \, \hat{p}_{\ell+1/2} + \frac{\hat{p}_{\ell+1/2} - p_\ell}{p_{\ell+1} - p_\ell} \, p_{\ell+1} \, (\theta_\ell - \theta_{\ell+1}) \, , \tag{3.84}$$

with θ as the potential temperature and

$$\hat{\mathbf{V}}_{\ell+1/2} = \frac{1}{2} \, (\mathbf{V}_\ell + \mathbf{V}_{\ell+1}) \, . \tag{3.85}$$

3.2.2.3. Fractional cloudiness

The fractional cloudiness, b_ℓ, of the mid-level convection is defined as

$$b_\ell = \frac{\alpha\, M_{\ell+1/2}}{1 + \alpha\, M_{\ell+1/2}}\, U_\ell\,,$$

(3.86)

where α is an empirical parameter. This form is similar to that proposed by Sundqvist (1988) for cumuloform clouds and is based upon the following considerations: fractional cloudiness increases as the flux of the mass is detrained at level ℓ, but is constrained to be no larger than U_ℓ, a constraint arising from the definition of the grid-average relative humidity as $U = b\, U_s + (1 - b)\, U_0$ and the condition $U_0 > 0$. However, Equation (3.86) cannot be used as given since it entails the disappearance of the cloud as it passes from the mature stage, ($M_{\ell+1/2} > 0$), to the dissipating stage, $M_{\ell+1/2} = 0$. In contrast, in this study it is expected that the cloud will grow to its maximum extent in the mature stage, remaining at this size until the cloud water is depleted during the dissipating stage. Accordingly, Eq. (3.86) is modified to be

$$b_\ell = \max\left[\frac{\alpha\, M_{\ell+1/2}}{1 + \alpha\, M_{\ell+1/2}}\, U_\ell\,,\, \min(\tilde{b}_\ell\,,\, U_\ell)\right],$$

(3.87)

where $\tilde{b}_\ell$ is the fractional cloudiness of the previous time-step.

3.2.2.4. Evaporation of precipitation from the layer above

The evaporation of precipitation from the layer above is calculated in the same manner as for large-scale precipitation, i.e.,

$$(E_r)_\ell = (1 - b_\ell)\, (E_0)_\ell\, C_{RM}\, (R_{\ell-1/2})^{\alpha_{RM}}\, \Psi(z_{\ell-1/2} - z_{\ell+1/2})\,.$$

(3.88)

This is the same form expressed in Eq. (3.44), and the coefficients C_{RM} and α_{RM} are chosen to be the same as for stratiform precipitation. The grid-averaged precipitation in units of mm/h at the bottom of layer ℓ, $R_{\ell+1/2}$ can be written as

$$R_{\ell+1/2} = R_{\ell-1/2} + \Delta_\ell \sigma \left[\frac{\Delta_{\ell-1}\sigma}{\Delta_\ell \sigma} P_{\ell-1} + P_\ell - (E_r)_\ell \right],$$

(3.89)

where P_ℓ and $P_{\ell+1}$ are as defined in Eqs. (3.68) and (3.71).

3.2.2.5. Cloud mass flux

The mass flux, $M_{\ell+1/2}$, is obtained, [based upon the assumption of no cloud water loading and no evaporation from cloud water or from rain dropped from the layer above.] From the definition of moist static energy it can written as

$$\frac{\partial h_\ell^*}{\partial t} = c_p \frac{\partial T_\ell}{\partial t} + L \frac{\partial q_\ell^*}{\partial t}$$

$$= c_p \frac{\partial T_\ell}{\partial t} (1 + \gamma_\ell) .$$

(3.90)

Thus, Eq. (3.90) can be written as described in Eqs. (3.55) and (3.76), but without the evaporation term, as

$$\frac{\pi \delta_\ell \sigma}{g} \frac{\partial h_\ell^*}{\partial t} = M_{\ell+1/2} \left[h_{\ell+1} - h_\ell^* + (1 + \gamma_\ell)(s_\ell - \hat{s}_{\ell+1/2}) \right] .$$

(3.91)

Then, combining L with Eq. (3.75) combined with Eq. (3.77), without the evaporation term, gives

$$\frac{\pi \delta_{\ell+1} \sigma}{g} \frac{\partial h_{\ell+1}}{\partial t} = M_{\ell+1/2} (\hat{h}_{\ell+1/2} - h_{\ell+1}) .$$

(3.92)

Subtracting Eq. (3.91) from Eq. (3.92), the result is

$$\frac{\partial}{\partial t}(h_{\ell+1} - h_\ell^*)$$

$$= M_{\ell+1/2} \frac{g}{\pi} \left[\frac{\hat{h}_{\ell+1/2} - h_{\ell+1}}{\delta_{\ell+1}\sigma} - \frac{h_{\ell+1} - h_\ell^* + (1 + \gamma_\ell)(s_\ell - \hat{s}_{\ell+1/2})}{\delta_\ell\sigma} \right]$$

$$\equiv -\frac{h_{\ell+1} - h_\ell^*}{\tau_{con}} , \tag{3.93}$$

[here τ_{con} (= 1 hour) is an assumed e-folding time for the adjustment process.] Solving Eq. (3.93) for $M_{\ell+1/2}$ gives

$$M_{\ell+1/2} = \frac{\pi}{\tau_{con}\, g} \left[\frac{h_{\ell+1} - h_\ell^*}{\dfrac{h_{\ell+1} - h_\ell^* + (1 + \gamma_\ell)(s_\ell - \hat{s}_{\ell+1/2})}{\delta_\ell\sigma} - \dfrac{\hat{h}_{\ell+1/2} - h_{\ell+1}}{\delta_{\ell+1}\sigma}} \right] . \tag{3.94}$$

3.2.3. Penetrating convection

Penetrating convection is parameterized following Arakawa and Schubert (1974) and Lord (1978) with four differences; (1) the instability of the moisture static energy is used instead of the cloud work function; (2) the detrainment is not allowed for the cloud top layer; (3) the dissipating stage of clouds considered; (4) the fractional cloud cover is calculated diagnostically. In this parameterization, an ensemble of cumulus clouds, in which each sub-ensemble member or cloud type identified by the layer in which it reaches neutral buoyancy and detrainment occurs, is coexistent. A schematic of the ℓ'-th cloud type is shown in Fig. 3.8. In this representation, the penetrative convective clouds are given roots in the planetary boundary layer comprised of model layers LF+1 through L. The parameterization is developed in the following order: cloud mass budget, cloud moist static energy and momentum, determination of the cloud type parameter λ, environmental budgets for moisture, dry static energy and momentum, and the cloud base mass flux.
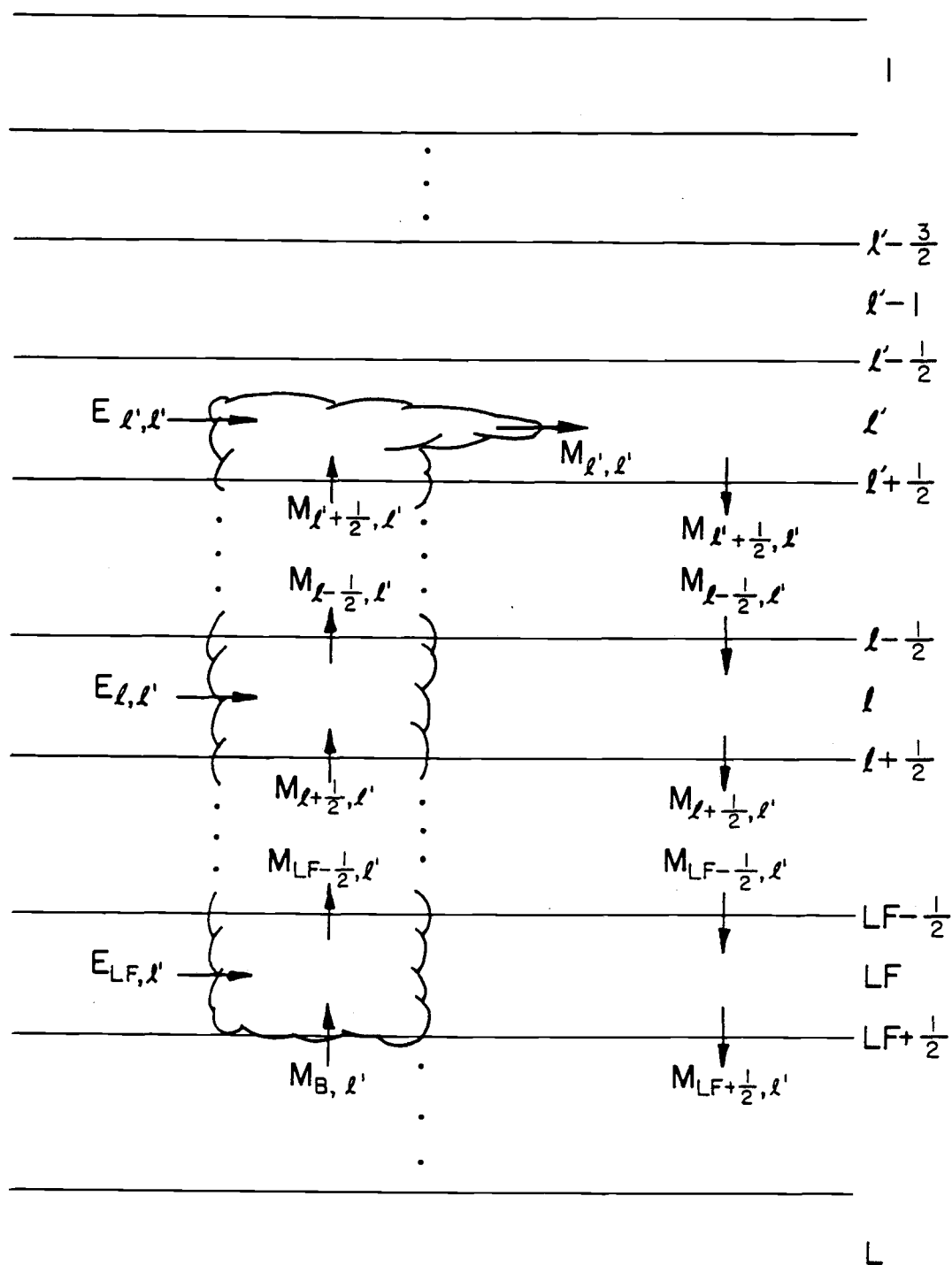
Fig. 3.8. Schematic vertical structure of ℓ'th penetrating convection cloud type. Here $M_{LF+1/2, \ell'} = M_{B, \ell'}$.

3.2.3.1. Cloud and environmental mass budgets

The mass flux in the cloud type ℓ' at the level k, $M_{k,\ell}$, is represented in terms of the cloud base flux, $M_{B,\ell'}$ as

$$M_{k,\ell'} = \eta_{k,\ell'} \, M_{B,\ell'} \, , \quad k = \ell', \ \ell'+1/2,\ldots,LF + 1/2 \, , \tag{3.95}$$

where

$$\eta_{k,\ell'} = \begin{cases} \exp\left[\lambda_{\ell'}\left(z_k - z_{LF+1/2}\right)\right], & \text{if } \ell' \leq k \leq LF+1/2 \\ \\ 0, & \text{if } k > \ell' \end{cases} \tag{3.96}$$

and $\eta > 0$ is a ratio of the mass flux at level k to the cloud base mass flux determined by the cloud type parameter (further description of this determination is provided in section 3.2.3.4). Note that

$$\eta_{LF+1/2,\ell'} = 1 \, . \tag{3.97}$$

[Assuming there is no mass storage in the clouds in the entrainment layers,] the entrainment $E_{\ell,\ell'}$ can be expressed as (see Fig. 3.8):

$$E_{\ell,\ell'} = \begin{cases} M_{\ell-1/2,\ell'} - M_{\ell+1/2,\ell'} \, , & \text{if } \ell'+1 \leq \ell \leq LF \\ \\ M_{\ell',\ell'} - M_{\ell+1/2,\ell'} \, , & \text{if } \ell = \ell' \end{cases} \tag{3.98}$$

or

$$E_{\ell,\ell'} = \begin{cases} \left(\eta_{\ell-1/2,\ell'} - \eta_{\ell+1/2,\ell'}\right) M_{B,\ell'} \, , & \text{if } \ell'+1 \leq \ell \leq LF \\ \\ \left(\eta_{\ell',\ell'} - \eta_{\ell'+1/2,\ell'}\right) M_{B,\ell'} \, , & \text{if } \ell = \ell' \end{cases} \tag{3.99}$$

by Eq. (3.95).

By above assumption, the area weighted mass flux at any level $k = \ell'+1/2, \ldots, LF+1/2$ in the environment, as given in Eq. (3.61), must be equal in magnitude and opposite in direction to that in the cloud at the same

level (see Fig. 3.8).

3.2.3.2. Sub-ensemble cloud water budget and fractional cloudiness

Similar to the mid-level convection parameterization described in section 3.2.2.1, the total cloud water budget with the area weighted mass flux for the cloud type ℓ' can be written in the form

$$\frac{\pi \, \delta_\ell \sigma}{g} \frac{\partial}{\partial t}[b \, (q_c + \hat{m})_{\ell,\ell'}]$$

$$= E_{\ell,\ell'} \, q_\ell + [M \, (q_c + \hat{m})]_{\ell+1/2,\ell'} - [M \, (q_c + \hat{m})]_{\ell-1/2,\ell'}$$

$$- M_{\ell-1/2,\ell'} \, C_0 \, \Delta_\ell z \, \hat{m}_{\ell-1/2,\ell'} \tag{3.100}$$

for the entrainment layers and

$$\frac{\pi \, \delta_{\ell'} \sigma}{g} \frac{\partial}{\partial t}[b \, (q_c + \hat{m})_{\ell',\ell'}]$$

$$= E_{\ell',\ell'} \, q_{\ell'} + [M \, (q_c + \hat{m})]_{\ell'+1/2,\ell'} - M_{\ell',\ell'} \, (q_c)_{\ell',\ell'}$$

$$- M_{\ell',\ell'} \, C_0 \, \Delta_{\ell'} z \, \hat{m}_{\ell',\ell'} - \frac{\pi \, \delta_{\ell'} \sigma}{g} \, (E_c)_{\ell',\ell'} \tag{3.101}$$

for the detrainment layer. In Eqs. (3.100) and (3.101), $q_{\ell'}$ is the environmental mixing ratio for the layer ℓ'; $\pi \, \delta_\ell \sigma/g$ is the mass per unit horizontal area of the layer ℓ, with $\Delta_\ell z$ its thickness; C_0 is the conversion rate of cloud water into precipitation per unit thickness of layer ℓ; and $(E_c)_{\ell',\ell'}$ is the evaporation rate of cloud water.

[Arakawa and Schubert (1974) assumed as a closure condition that

$$\frac{\partial}{\partial t}[b \, (q_c + \hat{m})]_{\ell,\ell'} = 0 \quad \text{for } \ell = \ell',...,LF , \tag{3.102}$$

where $(\hat{\ })$ is the cloud variable while $(\ )$ is the grid-averaged variable.] This

condition can be justified with respect to statistical cloud dynamics since, the cloud type ℓ' represents an ensemble average over the individual clouds that are: 1) in their growing stage and will eventually become neutrally buoyant in layer ℓ'; 2) in their mature stage and are detraining in layer ℓ'; and 3) in their dissipating stage, with a decaying detrainment anvil in layer ℓ' (see Fig. 3.9). The resulting ensemble average cloud is represented in Fig. 3.8. As an alternative, the ensemble average cloud can be interpreted as a time average over the life cycle of a single cloud in which the growing and dissipating stages are negligibly short; for this interpretation, all individual type ℓ' clouds are in a mature stage so long as they exist.

For the radiative effects of these cumuloform clouds, however, it is the mature and dissipating stages which are of greatest importance since the fractional cloudiness large only during these stages. Therefore, [it is assumed that only the growing stage is negligibly short,] that all individual type ℓ' clouds are in their mature stage when they detrain ($M_{\ell',\ell'} > 0$), and that they are subsequently in their dissipating stage when detrainment ceases ($M_{\ell',\ell'} = 0$).

Growing Stage   Mature Stage   Dissipating Stage
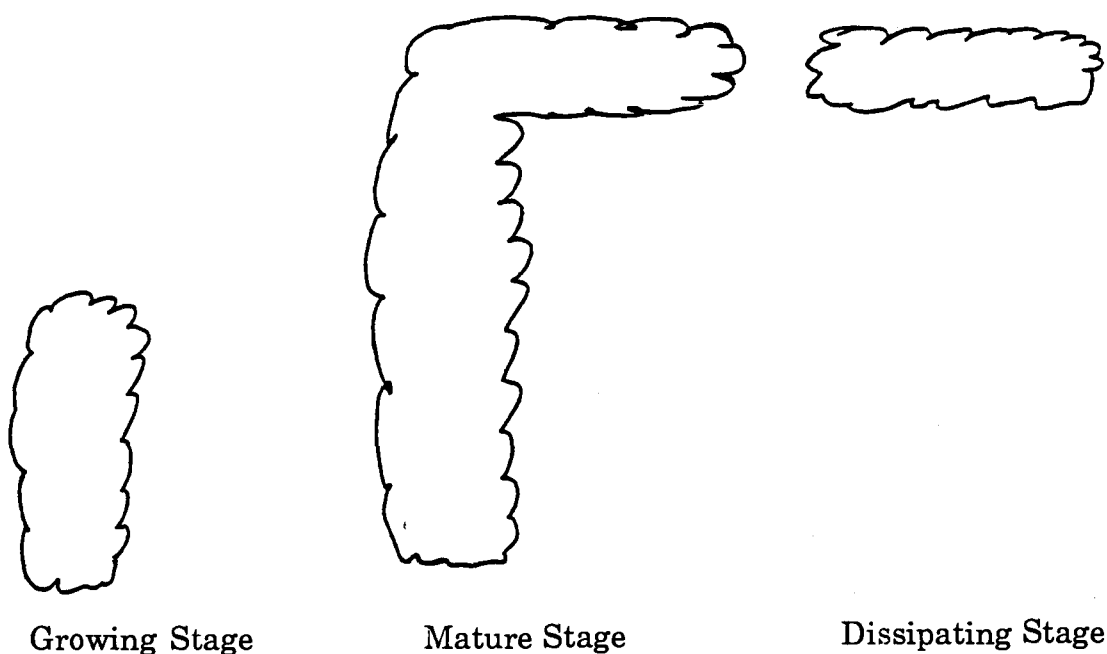
Fig. 3.9. Stages in the lifecycle of a convective cumuloform cloud.

The cloud water budget at the entrainment layers is trivial due to the closure assumption given for Eq. (3.102). However, the cloud water budget at the detrainment layer can be written from Eq. (3.101), based upon the assumption that cloud water is stored only as follows:

a. *Mature Stage:*

For the entrainment layers the ensemble average condition given in Eq. (3.102) is employed since $b_{\ell,\ell'}$ is small and the cloud is not radiatively significant. [For the radiation calculations it is assumed that $b_{\ell,\ell'} = 0$ for $\ell = \ell'+1,...,LF$.] Consequently, for these entrainment layers, Eqs. (3.100) and (3.102) are applied as follows

$$[M\,(q_c + \hat{m})]_{\ell-1/2,\ell'} = [M\,(q_c + \hat{m})]_{\ell+1/2,\ell'} + E_{\ell,\ell'}\, q_\ell$$
$$- M_{\ell-1/2,\ell'}\, C_0\, \Delta_\ell z\, \hat{m}_{\ell-1/2,\ell'}\, , \ \text{for } \ell = \ell'+1,...,LF \quad (3.103)$$

The calculation of $[M\,(q_c + \hat{m})]_{\ell-1/2,\ell'}$ from Eq. (3.103) proceeds sequentially upward from $\ell = LF$ to $\ell = \ell' + 1$, with the same definition of cloud water mixing ratios provided for the mid-level convection, i.e.,

$\tilde{m}$ = the value before precipitation and evaporation

$\check{m}$ = the value after precipitation and before evaporation .

First,
$$[M\,(q_c + \tilde{m})]_{\ell-1/2,\ell'} = M_{\ell-1/2,\ell'}\, (q_T)_{\ell-1/2,\ell'}\, , \quad (3.104)$$

is written, where $M_{\ell-1/2,\ell'}$ is known from the mass budget and $(q_T)_{\ell-1/2,\ell'}$ is the cloud total water, or condensate plus vapor, which can be determined from Eqs. (3.103) and (3.104). Second, two cases are distinguished on the basis of whether or not $(q_T)_{\ell-1/2,\ell'}$ exceeds the known saturation mixing ratio in the cloud type ℓ' at layer ℓ, $[q^*(T_c)]_{\ell-1/2,\ell'}$:

i) $\underline{(q_T)_{\ell-1/2,\ell'} < [q^*(T_c)]_{\ell-1/2,\ell'}}$

In this case, the cloud air in layer ℓ is not saturated; hence, the cloud water vapor equals the cloud total water,

$$(q_c)_{\ell-1/2,\ell'} = (q_T)_{\ell-1/2,\ell'} , \qquad (3.105)$$

the cloud water is zero,

$$\tilde{m}_{\ell-1/2,\ell'} = 0 , \qquad (3.106)$$

and the precipitation from layer ℓ is zero,

$$P_{\ell,\ell'} = 0 . \qquad (3.107)$$

ii) $\underline{(q_T)_{\ell-1/2,\ell'} \geq [q^*(T_c)]_{\ell-1/2,\ell'}}$

In this case, the cloud air in layer ℓ is saturated; hence, the cloud water vapor equals the saturation value in the cloud,

$$(q_c)_{\ell-1/2,\ell'} = [q^*(T_c)]_{\ell-1/2,\ell'} , \qquad (3.108)$$

and the cloud water, before precipitation is considered, is

$$\tilde{m}_{\ell-1/2,\ell'} = (q_T)_{\ell-1/2,\ell'} - (q_c)_{\ell-1/2,\ell'} . \qquad (3.109)$$

When precipitation is considered, the cloud water is

$$\begin{aligned}
\check{m}_{\ell-1/2,\ell'} &= \tilde{m}_{\ell-1/2,\ell'} - C_0 \, \Delta_\ell z \, \check{m}_{\ell-1/2,\ell'} \\
&= \frac{\tilde{m}_{\ell-1/2,\ell'}}{1 + C_0 \, \Delta_\ell z}
\end{aligned} \qquad (3.110)$$

and the precipitation rate is then

$$P_{\ell,\ell'} = M_{\ell-1/2,\ell'} \, (\tilde{m}_{\ell-1/2,\ell'} - \check{m}_{\ell-1/2,\ell'}) . \qquad (3.111)$$

The cloud total water finally carried to the level ℓ-1/2 is

$$(q_T)_{\ell-1/2,\ell'} = (q_c)_{\ell-1/2,\ell'} + \breve{m}_{\ell-1/2,\ell'} \, . \tag{3.112}$$

[For the detrainment layer, the closure condition given in Eq. (3.102) is replaced with the following assumed diagnostic relation for $b_{\ell',\ell'}$, similar to that given for the mid-level convection:

$$b_{\ell',\ell'} = \max\left[\frac{\alpha \, M_{\ell',\ell'}}{1 + \alpha \, M_{\ell',\ell'}} \, U_{\ell'} \, , \, \min(\tilde{b}_{\ell',\ell'} \, , \, U_{\ell'})\right], \tag{3.113}$$

where $\tilde{b}$ is the fractional cloudiness of the previous time-step.] With this closure condition, the cloud water budget can be written as

$$\frac{\pi \, \delta_{\ell'} \sigma}{g} \frac{\partial m_{\ell',\ell'}}{\partial t}$$

$$= E_{\ell',\ell'} \, q_{\ell'} + [M \, (q_c + \hat{m})]_{\ell'+1/2,\ell'} - M_{\ell',\ell'} \, (q_c)_{\ell',\ell'}$$

$$- M_{\ell',\ell'} \, C_0 \, \Delta_{\ell'} z \, \hat{m}_{\ell',\ell'} - \frac{\pi \, \delta_{\ell'} \sigma}{g} \, (E_c)_{\ell',\ell'} \, , \tag{3.114}$$

where $(q_c)_{\ell',\ell'}$ and $m_{\ell',\ell'}$ are calculated as follows.

The sub-ensemble water vapor mixing ratio at the cloud top (see Eq. (3.56)) is given in discrete form as

$$(q_c)_{\ell',\ell'} = (q^*)_{\ell',\ell'} - \frac{\gamma_{\ell'}}{1 + \gamma_{\ell'}} \frac{1}{L} [(h_c)_{\ell',\ell'} - h_{\ell'}^*] \, . \tag{3.115}$$

Then, the cloud water, $m_{\ell',\ell'}$, is calculated as described for the mid-level convection in section 3.2.2.1. First, cloud water prior to consideration of precipitation can be written as

$$\tilde{m}_{\ell',\ell'} = (q_T)_{\ell',\ell'} - (q_c)_{\ell',\ell'} , \qquad (3.116)$$

where $(q_T)_{\ell',\ell'}$ is from Eq. (3.114) without precipitation and evaporation, and $(q_c)_{\ell',\ell'}$ is from Eq. (3.115).

When precipitation is considered,

$$\check{m}_{\ell',\ell'} = \tilde{m}_{\ell',\ell'} - C_0 \, \Delta_{\ell'} z \, \check{m}_{\ell',\ell'} \qquad (3.117)$$

or

$$\check{m}_{\ell',\ell'} = \frac{\tilde{m}_{\ell',\ell'}}{1 + C_0 \, \Delta_{\ell'} z} . \qquad (3.118)$$

Following precipitation, the evaporation of cloud water is taken into account as,

$$(E_c)_{\ell',\ell'} = \left(\frac{U_s - U_{\ell'}}{\tau} \right) \check{m}_{\ell',\ell'} . \qquad (3.119)$$

b. *Dissipating stage:*

During the dissipating stage, $M_{\ell',\ell'} = 0$ and the cloud consists only of its detrainment shield, for which, [it is assumed that $b_{\ell',\ell'}$ remains at maximum value during the mature stage. It is further assumed that consistent with Eq. (3.111) the cloud is nonprecipitating, decaying only by evaporation or the sublimation of cloud water into the environment, as described for mid-level convection.] Thus, the cloud water equation is given by Eq. (3.114) with $M_{\ell',\ell'} = 0$ as

$$\frac{\partial m_{\ell',\ell'}}{\partial t} = - \left(\frac{U_s - U_{\ell'}}{\tau} \right) m_{\ell',\ell'} . \qquad (3.120)$$

If $M_{\ell',\ell'} > 0$ subsequently occurs, $m_{\ell',\ell'}$ is determined rom Eq. (3.114), starting from any residual $m_{\ell',\ell'}$, and the value of $b_{\ell',\ell'}$ is determined from

Eq. (3.113). This treatment of the dissipating stage and the reformation of the cumuloform cloud is identical to that for the dissipating stage ($Q = 0$) and the reformation ($Q > 0$) of the stratiform cloud given in the preceding section.

3.2.3.3. Cloud moist static energy and momentum

Again, based upon the assumption again that there is no storage of moist static energy in the cloud, using Eqs. (3.95) and (3.99) it can be written that

$$M_{LF-1/2,\ell'} \, (h_c)_{LF-1/2} = M_{B,\ell'} \, [h_M + (\eta_{LF-1/2,\ell'} - 1) \, h_{LF}]$$

$$\vdots$$

$$M_{\ell-1/2,\ell'} \, (h_c)_{\ell-1/2} = M_{\ell+1/2,\ell'} \, (h_c)_{\ell+1/2} + M_{B,\ell'} \, (\eta_{\ell-1/2,\ell'} - \eta_{\ell+1/2,\ell'}) \, h_\ell$$

$$\vdots$$

$$M_{\ell',\ell'} \, (h_c)_{\ell'} = M_{\ell'+1/2,\ell'} \, (h_c)_{\ell'+1/2} + M_{B,\ell'} \, (\eta_{\ell',\ell'} - \eta_{\ell'+1/2,\ell'}) \, h_{\ell'} \, , \qquad (3.121)$$

where h_c is the cloud moist static energy and h_M is the boundary layer moist static energy, defined in this study as

$$h_M = \frac{\displaystyle\sum_{\ell = LF+1}^{L} h_\ell \, \delta_\ell \sigma}{\displaystyle\sum_{\ell = LF+1}^{L} \delta_\ell \sigma} \, . \qquad (3.122)$$

From Eq. (3.121), the moist static energy in the cloud-top layer ℓ' can be obtained as

$$(h_c)_{\ell'} = \frac{1}{\eta_{\ell',\ell'}} [(\eta_{\ell',\ell'} - \eta_{\ell'+1/2,\ell'}) \, h_{\ell'} + (\eta_{\ell'+1/2,\ell'} - \eta_{\ell'+3/2,\ell'}) \, h_{\ell'+1}$$

$$+ \ldots + (\eta_{LF-1/2,\ell'} - 1) \, h_{LF} + h_M]$$

$$= \frac{1}{\eta_{\ell',\ell'}} [(\eta_{\ell',\ell'} \, h_{\ell'} + \eta_{\ell'+1/2,\ell'} \, (h_{\ell'+1} - h_{\ell'}) + \ldots$$

$$+ \eta_{LF-1/2,\ell'} \, (h_{LF} - h_{LF-1}) + (h_M - h_{LF})] \, . \tag{3.123}$$

Similarly, it may be found that

$$(V_c)_{\ell'} = \frac{1}{\eta_{\ell',\ell'}} [(\eta_{\ell',\ell'} \, \mathbf{V}_{\ell'} + \eta_{\ell'+1/2,\ell'} \, (\mathbf{V}_{\ell'+1} - \mathbf{V}_{\ell'}) + \ldots$$

$$+ \eta_{LF-1/2,\ell'} \, (\mathbf{V}_{LF} - \mathbf{V}_{LF-1}) + (\mathbf{V}_M - \mathbf{V}_{LF})] \, , \tag{3.124}$$

where

$$\mathbf{V}_M = \frac{\displaystyle\sum_{\ell=LF+1}^{L} \mathbf{V}_\ell \, \delta_\ell \sigma}{\displaystyle\sum_{\ell=LF+1}^{L} \delta_\ell \sigma} \, . \tag{3.125}$$

3.2.3.4. Determination of $\lambda_{\ell'}$

From the condition of neutral buoyancy at the detrainment level, $(h_c)_{\ell'} = h^*_{\ell'}$, Eq. (3.123) when combined with Eq. (3.96) gives

$$(h_{\ell'} - h^*_{\ell'}) \, \exp [\lambda_{\ell'} (z_{\ell'} - z_{LF+1/2})]$$

$$+ (h_{\ell'+1} - h_{\ell'}) \, \exp [\lambda_{\ell'} (z_{\ell'+1/2} - z_{LF+1/2})] + \ldots$$

$$+ (h_{LF} - h_{LF-1}) \, \exp [\lambda_{\ell'} (z_{LF-1/2} - z_{LF+1/2})] + (h_M - h_{LF})] = 0 \, . \tag{3.126}$$

This transcendental equation for $\lambda_{\ell'}$ differs from the polynomial equation used by Lord (1978). Eq. (3.126) is solved iteratively by the Newton-Raphson method, beginning with the solution, $\lambda_{\ell'}^{(o)}$, of the linearized form of Eq. (3.126):

$$\lambda_{\ell'}^{(o)} = (h_M - h_{LF}) / [(h_{\ell'}^* - h_{\ell'}) (z_{\ell'} - z_{LF+1/2})$$
$$- (h_{\ell'+1} - h_{\ell'}) (z_{\ell'+1/2} - z_{LF+1/2})$$
$$- \ldots - (h_{LF} - h_{LF-1}) (z_{LF-1/2} - z_{LF+1/2})] . \tag{3.127}$$

The iteration is continued until $[(h_c)_{\ell'} - h^*_{\ell'}]/c_p < 5 \times 10^{-3}$ K. [If the solution for $\lambda_{\ell'}$ is negative, then it is assumed that the cloud type ℓ' does not exist.] For computational reasons, $\lambda_{\ell'}$ is constrained to not exceed λ_{max}, defined as

$$\exp [\lambda_{max} (z_{\ell'} - z_{LF+1/2})] = 10^{10} . \tag{3.128}$$

3.2.3.5. Environmental budgets for moisture, dry static energy and momentum

The environmental budgets for moisture, dry static energy, and momentum (see Fig. 3.8) can be written for the detrainment layer ℓ' as

$$\frac{\pi \delta_{\ell'} \sigma}{g} \frac{\partial q_{\ell'}}{\partial t} = M_{\ell',\ell'} (q_c)_{\ell',\ell'} - M_{\ell'+1/2,\ell'} \hat{q}_{\ell'+1/2} - E_{\ell',\ell'} q_{\ell'} + \frac{\pi \delta_{\ell'} \sigma}{g} (E_c)_{\ell',\ell'} , \tag{3.129}$$

$$c_p \frac{\pi \delta_{\ell'} \sigma}{g} \frac{\partial T_{\ell'}}{\partial t} = M_{\ell',\ell'} (s_c)_{\ell'} - M_{\ell'+1/2,\ell'} \hat{s}_{\ell'+1/2} - E_{\ell',\ell'} s_{\ell'} - L \frac{\pi \delta_{\ell'} \sigma}{g} (E_c)_{\ell',\ell'} , \tag{3.130}$$

and

$$\frac{\pi \, \delta_{\ell'} \sigma}{g} \frac{\partial \mathbf{V}_{\ell'}}{\partial t} = M_{\ell',\ell'} \, (\mathbf{V}_c)_{\ell'} - M_{\ell'+1/2,\ell'} \, \hat{\mathbf{V}}_{\ell'+1/2} - E_{\ell',\ell'} \, \mathbf{V}_{\ell'} \, , \tag{3.131}$$

where $(q_c)_{\ell'}$, $(s_c)_{\ell'}$, $(\mathbf{V}_c)_{\ell'}$ are, respectively, the detrained cloud moisture, dry static energy, and momentum.

For the layers beneath the detrainment level and above the boundary layer the budgets are

$$\frac{\pi \, \delta_\ell \sigma}{g} \frac{\partial q_\ell}{\partial t} = M_{\ell-1/2,\ell'} \, \hat{q}_{\ell-1/2} - M_{\ell+1/2,\ell'} \, \hat{q}_{\ell+1/2} - E_{\ell,\ell'} \, q_\ell \, , \tag{3.132}$$

$$c_p \frac{\pi \, \delta_\ell \sigma}{g} \frac{\partial T_\ell}{\partial t} = M_{\ell-1/2,\ell'} \, \hat{s}_{\ell-1/2} - M_{\ell+1/2,\ell'} \, \hat{s}_{\ell+1/2} - E_{\ell,\ell'} \, s_\ell \tag{3.133}$$

and

$$\frac{\pi \, \delta_\ell \sigma}{g} \frac{\partial \mathbf{V}_\ell}{\partial t} = M_{\ell-1/2,\ell'} \, \hat{\mathbf{V}}_{\ell-1/2} - M_{\ell+1/2,\ell'} \, \hat{\mathbf{V}}_{\ell+1/2} - E_{\ell,\ell'} \, \mathbf{V}_\ell \, , \tag{3.134}$$

where $\ell = \ell'+1, \dots, LF$.

The budgets for the boundary layer are

$$\frac{\pi \, \delta_M \sigma}{g} \frac{\partial q_M}{\partial t} = M_{B,\ell'} \, (\hat{q}_{LF+1/2} - q_M) \, , \tag{3.135}$$

$$\frac{\pi \, \delta_M \sigma}{g} \frac{\partial h_M}{\partial t} = M_{B,\ell'} \, (\hat{h}_{LF+1/2} - h_M) \, , \tag{3.136}$$

and

$$\frac{\pi \, \delta_M \sigma}{g} \frac{\partial \mathbf{V}_M}{\partial t} = M_{B,\ell'} \, (\hat{\mathbf{V}}_{LF+1/2} - \mathbf{V}_M) \, , \tag{3.137}$$

where

$$q_M = \frac{1}{\delta_M \sigma} \sum_{\ell=LF+1}^{L} q_\ell \, \delta_\ell \sigma \tag{3.138}$$

and

$$\delta_M\sigma = \sum_{\ell=LF+1}^{L} \delta_\ell\sigma = 1 - \sigma_{LF+1/2} \,.$$

(3.139)

Substituting Eqs. (3.55), (3.56), (3.95) and (3.99) into Eqs.(3.129) through (3.134) gives

$$\frac{\pi\,\delta_{\ell'}\sigma}{g}\frac{\partial q_{\ell'}}{\partial t} = M_{B,\ell'}\{\eta_{\ell',\ell'}[(q_c)_{\ell',\ell'} - q_{\ell'}] + \eta_{\ell'+1/2,\ell'}(q_{\ell'} - \hat{q}_{\ell'+1/2})\}$$
$$+ \frac{\pi\,\delta_{\ell'}\sigma}{g}(E_c)_{\ell',\ell'} \,,$$

(3.140)

$$c_p\frac{\pi\,\delta_{\ell'}\sigma}{g}\frac{\partial T_{\ell'}}{\partial t} = M_{B,\ell'}\{\eta_{\ell',\ell'}[(s_c)_{\ell',\ell'} - s_{\ell'}] + \eta_{\ell'+1/2,\ell'}(s_{\ell'} - \hat{s}_{\ell'+1/2})\}$$
$$- L\frac{\pi\,\delta_{\ell'}\sigma}{g}(E_c)_{\ell',\ell'} \,,$$

(3.141)

and

$$\frac{\pi\,\delta_{\ell'}\sigma}{g}\frac{\partial \mathbf{V}_{\ell'}}{\partial t} = M_{B,\ell'}\{\eta_{\ell',\ell'}[(\mathbf{V}_c)_{\ell',\ell'} - \mathbf{V}_{\ell'}] + \eta_{\ell'+1/2,\ell'}(\mathbf{V}_{\ell'} - \hat{\mathbf{V}}_{\ell'+1/2})\} \,,$$

(3.142)

where $(q_c)_{\ell',\,\ell'}$ is defined iteratively by Eq. (3.115), and

$$\frac{\pi\,\delta_\ell\sigma}{g}\frac{\partial q_\ell}{\partial t} = M_{B,\ell'}[\eta_{\ell-1/2,\ell'}(\hat{q}_{\ell-1/2} - q_\ell) + \eta_{\ell+1/2,\ell'}(q_\ell - \hat{q}_{\ell+1/2})] \,,$$

(3.143)

$$c_p\frac{\pi\,\delta_\ell\sigma}{g}\frac{\partial T_\ell}{\partial t} = M_{B,\ell'}[\eta_{\ell-1/2,\ell'}(\hat{s}_{\ell-1/2} - s_\ell) + \eta_{\ell+1/2,\ell'}(s_\ell - \hat{s}_{\ell+1/2})] \,,$$

(3.144)

and

$$\frac{\pi\,\delta_\ell\sigma}{g}\frac{\partial \mathbf{V}_\ell}{\partial t} = M_{B,\ell'}[\eta_{\ell-1/2,\ell'}(\hat{\mathbf{V}}_{\ell+1/2} - \mathbf{V}_\ell) + \eta_{\ell+1/2,\ell'}(\mathbf{V}_\ell - \hat{\mathbf{V}}_{\ell+1/2})] \,,$$

(3.145)

where $\ell = \ell'+1, ..., LF$.

The changes in q_M, h_M and $\mathbf{V}_M$ due to all the sub-ensembles can be

obtained from Eqs. (3.135) though (3.137), respectively, as:

$$\frac{\pi \, \delta_M \sigma}{g} \frac{\partial q_M}{\partial t} = (\hat{q}_{LF+1/2} - q_M) \sum_{\ell'=1}^{LF} M_{B,\ell'},$$

(3.146)

$$\frac{\pi \, \delta_M \sigma}{g} \frac{\partial h_M}{\partial t} = (\hat{h}_{LF+1/2} - h_M) \sum_{\ell'=1}^{LF} M_{B,\ell'},$$

(3.147)

and

$$\frac{\pi \, \delta_M \sigma}{g} \frac{\partial \mathbf{V}_M}{\partial t} = (\hat{\mathbf{V}}_{LF+1/2} - \mathbf{V}_M) \sum_{\ell'=1}^{LF} M_{B,\ell'}.$$

(3.148)

From Eqs. (3.138), (3.122), (3.125), and (3.139):

$$\frac{\partial q_M}{\partial t} = \frac{1}{\delta_M \sigma} \sum_{\ell=LF+1}^{L} \frac{\partial q_\ell}{\partial t} \delta_\ell \sigma,$$

(3.149)

$$\frac{\partial h_M}{\partial t} = \frac{1}{\delta_M \sigma} \sum_{\ell=LF+1}^{L} \frac{\partial h_\ell}{\partial t} \delta_\ell \sigma,$$

(3.150)

and

$$\frac{\partial \mathbf{V}_M}{\partial t} = \frac{1}{\delta_M \sigma} \sum_{\ell=LF+1}^{L} \frac{\partial \mathbf{V}_\ell}{\partial t} \delta_\ell \sigma.$$

(3.151)

[For purpose of simplification, it is assumed that

$$\frac{\partial q_\ell}{\partial t} = \frac{\partial q_M}{\partial t},$$

(3.152)

$$\frac{\partial h_\ell}{\partial t} = \frac{\partial h_M}{\partial t} \, , \tag{3.153}$$

and

$$\frac{\partial \mathbf{V}_\ell}{\partial t} = \frac{\partial \mathbf{V}_M}{\partial t} , \tag{3.154}$$

where $\ell = LF+1,...,L.$] Clearly this assumption satisfies Eqs. (3.149) through (3.151). Finally, from the definition of h,

$$\frac{dT_\ell}{dt} = \frac{1}{C_p} \frac{dh_\ell}{dt} - \frac{L}{c_p} \frac{dq_\ell}{dt} \, , \quad \ell = LF+1,...,L \, . \tag{3.155}$$

3.2.3.6. Evaporation of convective precipitation in the boundary layer

The evaporation of convective rain in the boundary layers has been provided by the theoretical and observational study (Schlesinger *et al.* 1988) as

$$E_r = 10 \left(\frac{g}{\pi \, \Delta\sigma} \right) (1 - b) \, C_{RM} \, (R_0)^{\alpha_{RM}} \, \Psi(\bar{z}) \, , \tag{3.156}$$

where R_0 is the precipitation rate in units of mm/h and $\bar{z}$ is the distance below the cloud base. This is the same form given for stratiform precipitation, with the exception that [it is assumed that q rather than the saturation ratio S is constant], such that

$$q_\ell = q_M \, , \quad \ell = LF+1,...,L \, . \tag{3.157}$$

From Eq. (3.156),

$$\Psi(\bar{z}) = \frac{\bar{z} - \bar{\gamma} \ln (1 + \bar{z}/\bar{\gamma})}{K_1 + K_2} \, , \tag{3.158}$$

where C_{RM}, α_{RM}, K_1, and K_2 are as given previously in section 3.1.2 for large-scale precipitation, $\bar{\gamma}$ is given as

$$\bar{\gamma} = \frac{c_p}{g} \frac{q^*}{\left(\dfrac{\partial q^*}{\partial T}\right)}$$

(3.159)

at the cloud base, and R_0 is defined as

$$R_0 = \sum_{\ell'=1}^{LF} \left[\sum_{\ell=\ell'}^{LF} \left(\frac{\pi \Delta_\ell \sigma}{10\,g} \right) P_{\ell,\ell'} \right].$$

(3.160)

Or, from Eqs. (3.53), (3.110) and (3.111),

$$R_0 = \sum_{\ell'=1}^{LF} \left\{ \left[\sum_{\ell=\ell'+1}^{LF} \left(\frac{\pi \Delta_\ell \sigma}{10\,g} \right) M_{\ell-1/2,\ell'}\, C_0\, \Delta_\ell z\, \breve{m}_{\ell-1/2,\ell'} \right] + \left(\frac{\pi \Delta_{\ell'} \sigma}{10\,g} \right) M_{\ell',\ell'}\, C_0\, \Delta_{\ell'} z\, \breve{m}_{\ell',\ell'} \right\}.$$

(3.161)

The total evaporation at the clear part of the layer ℓ ($\ell = LF + 1,...,L$) is

$$(E_r)_\ell = (1 - b_\ell)\ (E_0)_\ell\ C_{RM}\ (R_0)^{\alpha_{RM}} \{\Psi(z_{\ell+1/2} - z_{LF+1/2}) - \Psi(z_{\ell-1/2} - z_{LF+1/2}\}.$$

(3.162)

Thus, the moisture change in the boundary layers due to the evaporation of convective precipitation can be written as

$$\frac{\partial q_\ell}{\partial t} = (E_r)_\ell\ ,\quad \ell = LF+1,...,L\ ,$$

(3.163)

and the associated temperature change is

$$\frac{dT_\ell}{dt} = -\frac{L}{c_p}\ (E_r)_\ell\ ,\quad \ell = LF+1,...,L\ .$$

(3.164)

3.2.3.7. Cloud base mass flux

[Similar to the procedure for mid-level convection, it is assumed that the instability for the penetrating convective cloud top ℓ', $h_M - h^*_{\ell'}$, is removed with an e-folding time, τ_{con} (= 1 hour),] that is,

$$\frac{1}{c_p} \frac{\partial}{\partial t} (h_M - h^*_{\ell'}) = - \frac{h_M - h^*_{\ell'}}{c_p \tau_{con}} , \quad 1 \le \ell' \le LF .$$

(3.165)

This closure assumption differs from that provided by Arakawa and Schubert (1974) and by Lord (1978). From Eq. (3.147),

$$\frac{1}{c_p} \frac{\partial h_M}{\partial t} = \frac{1}{c_p} \frac{g}{\pi \delta_M \sigma} (\hat{h}_{LF+1/2} - h_M) \sum_{\ell'=1}^{LF} M_{B,\ell'} .$$

(3.166)

[Assuming there is no cloud water loading,] the change of moist static energy can be expressed in term of static energy change as

$$\frac{\partial h^*}{\partial t} = \frac{\partial s}{\partial t} + L \frac{\partial q^*}{\partial t}$$

$$\cong c_p \frac{dT}{dt} (1 + \gamma) .$$

(3.167)

Then, from Eqs. (3.167), (3.141) and (3.144),

$$\frac{1}{c_p} \frac{\partial h^*_{\ell'}}{\partial t} = \frac{g}{c_p \pi \delta_{\ell'} \sigma} \{ [\eta_{\ell',\ell'} ((\mathbf{h_c})_{\ell',\ell'} - \mathbf{h}_{\ell'}) + \eta_{\ell'+1/2,\ell'} (1 + \gamma_{\ell'}) (s_{\ell'} - \hat{s}_{\ell'+1/2})] M_{B,\ell'}$$

$$+ (1 + \gamma_{\ell'}) \sum_{\ell=1}^{\ell'-1} [\eta_{\ell'-1/2,\ell} (\hat{s}_{\ell'-1/2} - s_{\ell'}) + \eta_{\ell'+1/2,\ell} (s_{\ell'} - \hat{s}_{\ell'+1/2})] M_{B,\ell} \} ,$$

(3.168)

where the first bracketed term is due to the cloud type ℓ' (the bold-faced term is zero due to a neutral buoyancy condition) and the second bracketed term is due to subsidence induced by all cloud types that detrain above the level ℓ'. Substituting Eqs. (3.166) and (3.168) into Eq. (3.165) gives

$$\sum_{\ell=1}^{LF} a_{\ell',\ell}\, M_{B,\ell} = B_{\ell'}\ , \quad \ell' = 1,...,L\ , \tag{3.169}$$

where

$$B_{\ell'} = -\frac{h_M - h_{\ell'}^*}{c_p\, \tau_{con}} \tag{3.170}$$

and

$$a_{\ell',\ell} = \begin{cases} \dfrac{1}{c_p}\dfrac{g}{\pi\,\delta_M\sigma}\,(\hat{h}_{LF+1/2} - h_M)\ , & \text{for } \ell = \ell' \\[2ex] \dfrac{1}{c_p}\dfrac{g}{\pi\,\delta_M\sigma}\,(\hat{h}_{LF+1/2} - h_M) - \dfrac{g}{c_p\,\pi\,\delta_{\ell'}\sigma}\,[\eta_{\ell',\ell'}\,(\,(h_c)_{\ell',\ell'} - h_{\ell'}) & \\[1ex] \quad + \eta_{\ell'+1/2,\ell'}\,(1 + \gamma_{\ell'})\,(s_{\ell'} - \hat{s}_{\ell'+1/2})]\ , & \text{for } \ell = \ell' \\[3ex] \dfrac{1}{c_p}\dfrac{g}{\pi\,\delta_M\sigma}\,(\hat{h}_{LF+1/2} - h_M) - (1 + \gamma_{\ell'})\dfrac{g}{c_p\,\pi\,\delta_{\ell'}\sigma} & \\[1ex] \quad [\eta_{\ell'-1/2,\ell}\,(\hat{s}_{\ell'-1/2} - s_{\ell'}) + \eta_{\ell'+1/2,\ell}\,(s_{\ell'} - \hat{s}_{\ell'+1/2})]\ , & \\[1ex] & \text{for } \ell < \ell'. \end{cases} \tag{3.171}$$

In general, $h_{LF+1/2} - h_M < 0$, $\hat{s}_{\ell'-1/2} - s_{\ell'} \geq 0$ and $s_{\ell'} - \hat{s}_{\ell'+1/2} \geq 0$. therefore $a_{\ell',\ell} < 0$ for $\ell', \ell = 1,...,$ LF.

The constraint

$$M_{B,\ell} \geq 0 \text{ for } \ell = 1,...,LF \tag{3.172}$$

must then be imposed on the solution of Eq. (3.169). However, as illustrated in Fig. 3.10 for the case LF = 2, it may not be possible to satisfy both Eqs. (3.169) and (3.172). Thus, additional constraints must be imposed to uniquely determine $M_{B,\ell}$. Since $-B_{\ell'} > 0$ is the large-scale forcing of the cloud type ℓ', while
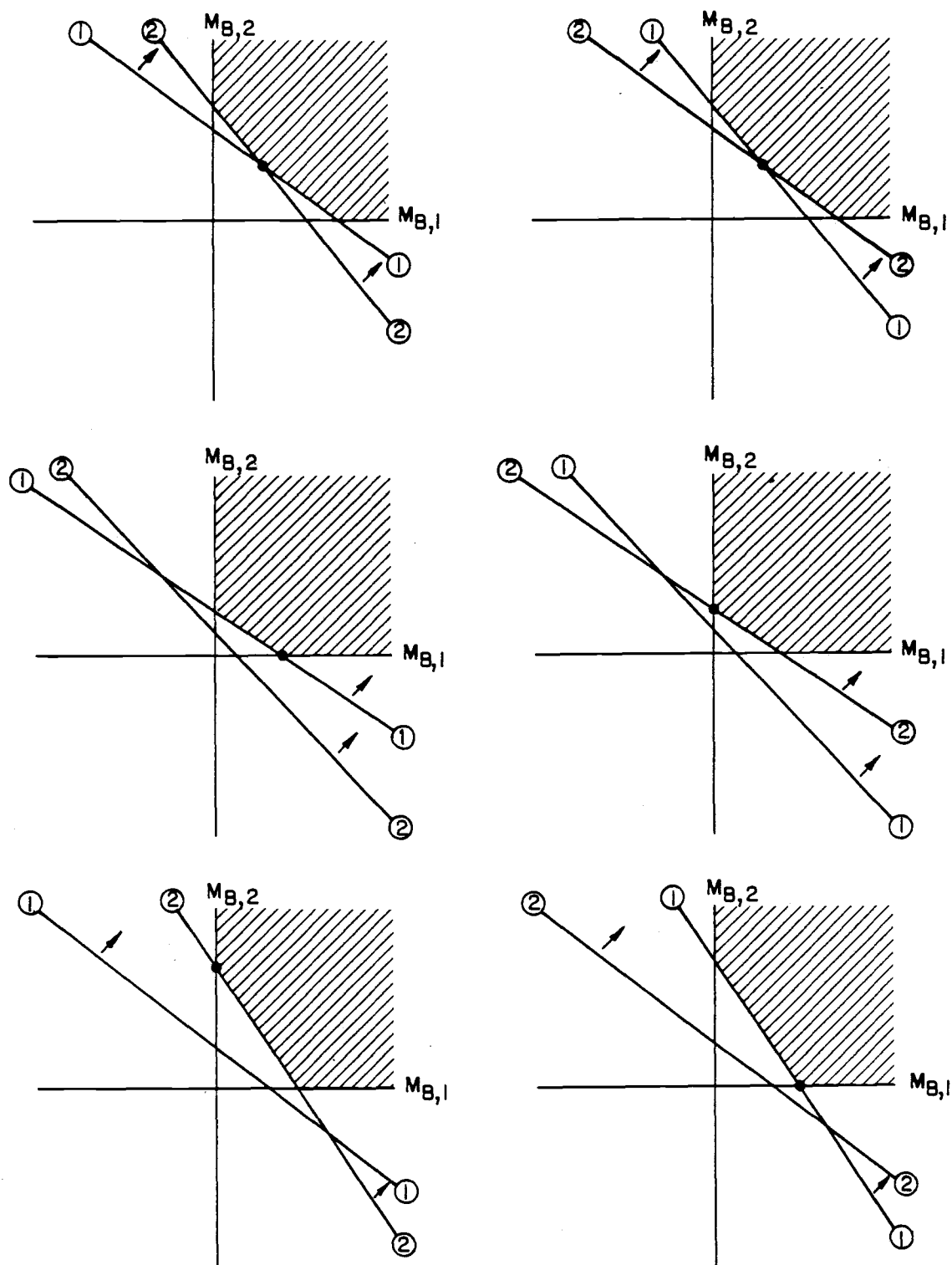
Fig. 3.10. Schematic representation of the determination of $M_{B,\ell}$ for the case where only two cloud types can exist.

$$\sum_{\ell=1}^{LF} a_{\ell',\ell} \, M_{B,\ell} < 0$$

$$(3.173)$$

is the stabilizing effect of the cloud ensemble on cloud type ℓ', it can be argued that when

$$B_{\ell'} = 0 \, , \, M_{B,\ell} > 0$$

$$(3.174)$$

and

$$B_{\ell'} < 0 \, , \, M_{B,\ell} = 0 \, .$$

$$(3.175)$$

The unique values of $M_{B,\ell}$ may be determined from these conditions as illustrated by the dots in each panel of Fig. 3.10.

To solve the linear programming problem Eqs. (3.174) and (3.175), it is cast in the generalized form whereby $M_{B,\ell}$ are determined from

$$\sum_{\ell=1}^{LF} a_{\ell',\ell} \, M_{B,\ell} - B_{\ell'} \leq 0 \, , \quad \ell' = 1,...,LF,$$

$$(3.176)$$

subject to the constraints given in Eq. (3.172) and such that a linear objective function Z is maximized. (Conditions for the Eqs. (3.176) and (3.172) are shown for the case LF=2 by the cross-hatching in Fig. 3.10.) The linear objective function is obtained by summing Eq. (3.176) over all cloud types:

$$Z' \equiv \sum_{\ell'=1}^{LF} \sum_{\ell=1}^{LF} a_{\ell',\ell} \, M_{B,\ell} - \sum_{\ell'=1}^{LF} B_{\ell'} \leq 0$$

$$= \sum_{\ell=1}^{LF} \left(\sum_{\ell'=1}^{LF} a_{\ell',\ell} \right) M_{B,\ell} - \sum_{\ell'=1}^{LF} B_{\ell'} \leq 0 \, .$$

$$(3.177)$$

$M_{B,\ell}$ are then determined such that Z' is maximized, i.e., is as close to zero

as possible. Since

$$- \sum_{\ell'=1}^{LF} B_{\ell'} > 0 \, ,$$

maximizing Z' is equivalent to maximizing the negative quantity

$$Z \equiv \sum_{\ell=1}^{LF} \left(\sum_{\ell'=1}^{LF} a_{\ell',\ell} \right) M_{B,\ell} \, .$$

$$(3.178)$$

The solutions given in Eqs. (3.176) and (3.172) for the maximization of Z do not always agree with the solutions given in Eqs. (3.174) and (3.175). This may be seen in Fig. 3.10. The solutions given in Eqs. (3.176) and (3.172) for the middle and bottom cases are independent of which curve lies farther from the origin in the first quadrant. This may be contrasted to the solutions given in Eqs. (3.174) and (3.175), as indicated by the filled circles. Thus, this stage of parameterization development, Eqs (3.176) and (3.173) supersede Eqs. (3.174) and (3.175). Finally, the values of $M_{B,\ell}$ are constrained to prevent the generation of negative mixing ratios in the convective layers.

3.2.3.8. Maximum value of cloud base mass flux

The environmental budget equations at the layer ℓ for the cloud type ℓ' can be written in the form

$$\zeta'(\ell) = \zeta(\ell) + \delta_{\ell'}[\zeta(\ell)] \, M_{B,\ell'} \, \Delta t \, ,$$

$$(3.179)$$

where $\delta_{\ell'}[\zeta(\ell)]$ refers to the change in the environmental variables, $\zeta(\ell)$, per unit mass flux of the sub-ensemble ℓ'. The cloud base mass flux has been reduced to prevent the generation of a negative value of q, e.g.,

$$\delta_{\ell'}[q(\ell)] \, M_{B,\ell'} \, \Delta t \leq - C \, q_{\ell'} \quad \text{if} \quad \delta_{\ell'}[q(\ell)] < 0 \, .$$

$$(3.180)$$

Solving Eq. (3.180) for $M_{B,\ell'} \, \Delta t$ gives

$$M_{B,\ell'} \Delta t \leq -\frac{C\, q_\ell}{\delta_{\ell'}[q(\ell)]} \,, \tag{3.181}$$

where C = 0.9 is an arbitrarily chosen constant, which allows 90 percent of q to be changed by the cloud type ℓ' mass flux. Then, from Eq. (3.143),

$$\delta_{\ell'}[q(\ell)] = \frac{g}{\pi\, \delta_\ell \sigma} \left[\eta_{\ell-1/2,\ell'}\, (\hat{q}_{\ell-1/2} - q_\ell) + \eta_{\ell+1/2,\ell'}\, (q_\ell - \hat{q}_{\ell+1/2}) \right] . \tag{3.182}$$

Note that the cloud base mass flux has been reduced to prevent overshooting at the cloud top layer, i.e.,

$$h_M \geq (h_{\ell'}^*)' = h_{\ell'}^* + (1 + \gamma_{\ell'})\, \delta(T_{\ell'})\, M_{B,\ell'}\, \Delta t \tag{3.183}$$

or

$$M_{B,\ell'} \Delta t \leq \frac{h_M - h_{\ell'}^*}{(1 + \gamma_{\ell'})\, \delta(T_{\ell'})} \,, \tag{3.184}$$

where

$$\delta(T_{\ell'}) = \frac{1}{c_p}\, \frac{g}{\pi\, \delta_{\ell'}\sigma} \left\{ \eta_{\ell',\ell'}\, [(s_c)_{\ell',\ell'} - s_{\ell'}] + \eta_{\ell'+1/2,\ell'}\, (s_{\ell'} - \hat{s}_{\ell'+1/2}) \right\} \tag{3.185}$$

is taken from Eq. (3.141), without evaporation of cloud water.

3.3. Combination of the Stratiform- and Cumuloform-Cloud Parameterizations

In nature, in an area as large as that of a contemporary GCM grid box, clouds formed by both convection and stratiform condensation can coexist, albeit not at the same horizontal location. Thus, it may be argued that a GCM grid box should be subdivided into the area of clear air, the area occupied by stratiform clouds and an area occupied by cumuloform clouds. This has not been done for this study since it would greatly complicate the

parameterizations of cloud and cloud-radiative interactions. Considering the primitive stage of contemporary cloud parameterizations (Rutledge and Schlesinger, 1985), the results would be unwarranted and premature. Consequently, the GCM grid box was subdivided only into areas of clear air and those occupied by either stratiform cloud or cumuloform clouds.

The identification of a cloud in layer ℓ as either a stratiform or cumuloform cloud is dependent upon the preceding cloud type, large-scale condensation, and the convective mass flux in the layer ℓ. A schematic diagram for cloud type decisions is given in Fig. 3.11. If there is a convective mass flux, then the cloud type is cumuloform regardless of whether the preceding cloud was stratiform or cumuloform. If there is large-scale condensation without convection, the cloud is stratiform. If nothing happens, the cloud keeps the preceding cloud type until completely evaporated.

3.4. Ice Clouds and Mixed Water-Ice Clouds

When the temperature within a cloud is below 0°C, a three-phase mixture of water vapor, supercooled liquid water, and ice can exist. The partitioning of cloud water between liquid and ice phases is a complex cloud microphysical problem. For example, Rutledge and Hobbs (1983), in their study of seeder-feeder clouds in warm frontal rainbands have shown that when a feeder cloud is considered in the absence of an overlying seeder cloud, liquid water and ice coexist. However, when combined seeder-feeder clouds are considered, only ice can exist. For a GCM it is impossible to perform detailed cloud microphysical calculations such as given by Rutledge and Hobbs (1983). Rather, the partitioning of the cloud water between the liquid and ice phases is parameterized.

One such parameterization would be to consider that the cloud water is entirely ice when the cloud temperature is below 0°C. This would in fact be a good parameterization for seeder-feeder clouds in warm frontal rainbands. However, this parameterization would be tantamount to considering every sub-zero cloud as a cirrus cloud. As this would likely result in an overestimation of the amount of cirrus clouds, thereby
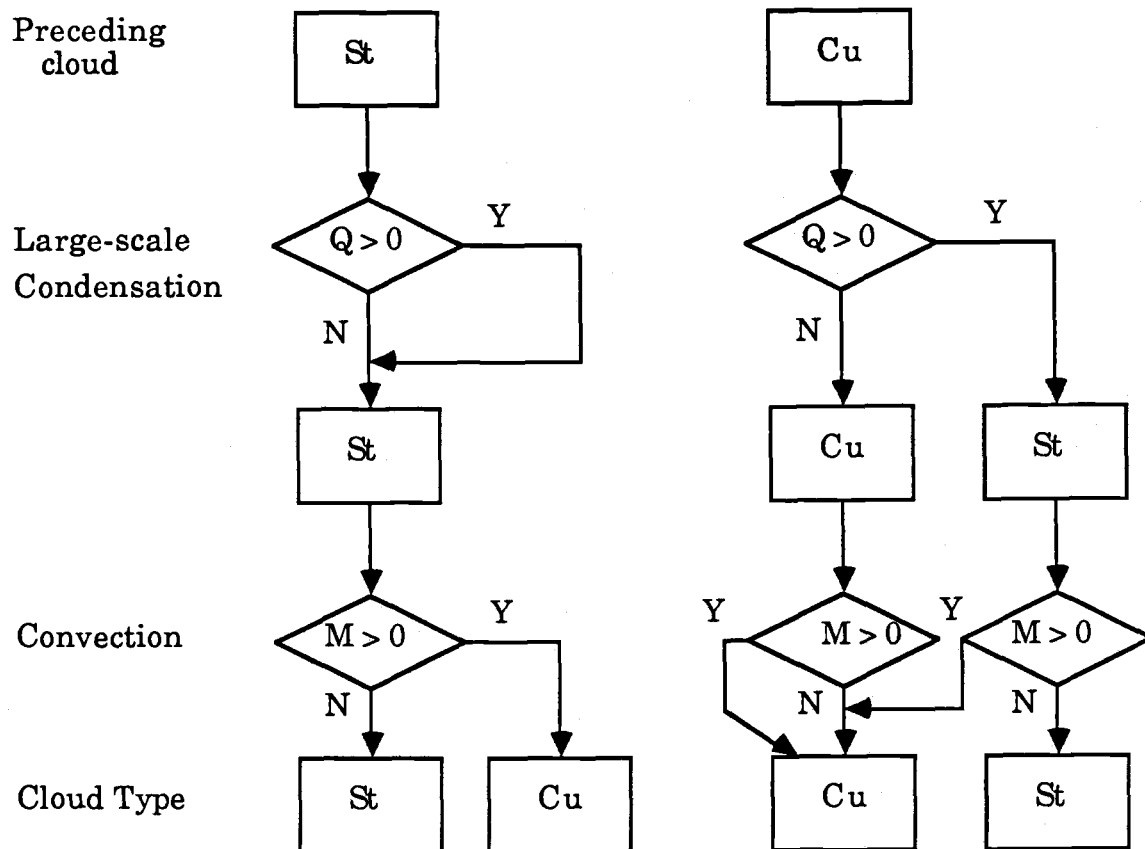
Fig. 3.11. Cloud type flow chart. Q is large-scale condensation, M is convective mass flux, St is stratiform cloud, and Cu is cumuloform cloud.

deleteriously affecting the calculation of radiation fields, an alternate parameterization has been adopted for this study.

[It is assumed in a statistical sense, averaged over all the sub-zero clouds, that the fraction of cloud water in the ice phase, f_i, is a function of only the cloud temperature subject to the conditions that $f_i = 0$ when $T > 0°C$ and $f_i = 1$ when $T < T_i$, where T_i is a temperature with a likely value between -20°C and -40°C. For simplification, it is assumed that f_i is a linear function of temperature between 0°C and T_i.] Thus,

$$\frac{m_i}{m_T} = f_i = \min\left[1, \max\left(0, \frac{273.1 - T}{273.1 - T_i}\right)\right], \tag{3.186}$$

where T is in degrees Kelvin and $m_T = m_i + m_w$ is the total cloud water given by the appropriate expressions in sections 3.1 and 3.2 for, respectively, stratiform and cumuloform clouds.

4. RADIATION PARAMETERIZATION

The radiation parameterization for the OSU multilayer AGCM is designed to allow the fractional cloud cover feedback by the calculation of both the cloud part and the clear part flux within the same grid box. This radiation parameterization has also been designed to allow the cloud optical depth feedback by the calculation of cloud radiative properties, which are obtained from cloud water content. In Chapter 3, cloud water was one of the prognostic variables considered.

The vertical distribution of model clouds is subdivided into individual cloud groups. Each group is comprised of an ensemble of contiguous cloud layers and each cloud group is separated from another by at least one cloud-free layer. The contiguous cloud layers within each group are considered to overlap each other vertically to the maximum extent possible, while the noncontiguous cloud groups are considered to randomly overlap each other in a vertical direction for both solar radiation and longwave radiation.

For accurate calculation of radiative forcing in the model atmosphere, the spectral ranges solar radiation and longwave radiation are divided into several subbands rather than the assumption of single and double bands, respectively, for longwave and solar radiation in the earlier version of the OSU multilayer AGCM (Schlesinger and Oh, 1987) as well as in the the OSU two-level AGCM (Ghan *et al.*, 1982). For solar radiation, the spectrum is subdivided into three frequency bands -- two for Rayleigh scattering and ozone absorption and one for water vapor absorption. The latter region is further subdivided into six intervals, in accordance with the water vapor absorption coefficients. For longwave radiation, the spectrum is divided into four regions based on the absorbers: water vapor band centers, water vapor band wings, CO_2, and O_3 bands.

The characteristics of the radiation scheme of the OSU multilayer AGCM are summarized in Tables 4.1 and 4.2. Detailed descriptions with

Table 4.1. Characteristics of the solar radiation parameterization for the
multilayer AGCM.

Process	Comments
(a) Clear sky	Calculation based on the two-stream delta-Eddington method employing 3 broad spectral intervals (0 - 0.44, 0.44 - 0.69, 0.69 - 3.85 µm)
Rayleigh scattering	Ghan (1986)
Gas absorption	
H_2O	6 k-distribution intervals
CO_2	Fouquart (1987)
O_3	Lacis and Hansen (1974)
(b) Cloudy sky	Maximum overlapping for contiguous cloudy layers and random overlapping for non-contiguous overlapping Geleyn (1977)
Droplet absorption	Treated explicitly via the two stream and scattering method. $\tilde{\omega}_0$[a] and δ[b] are determined by Stephens (1978) for non-ice clouds, and Starr and Cox (1985) for cirrus. g[c] is prescribed.

a. Single scattering albedo
b. Cloud optical depth
c. Asymmetric factor

Table 4.2. Characteristics of the longwave radiation parameterization for the multilayer AGCM.

Process	Comments
(a) Clear sky	Calculation based on the two-stream formula of the flux equations with parameterized optical depths. Pressure scaling is employed.
Gas absorption	
H_2O	Chou (1984) and Kneizys *et al.* (1983) 4 broad bands with e-type continuum (band centers, band wings, CO_2 overlap, O_3 overlap)
CO_2	Chou and Peng (1983)
O_3	Kneizys *et al.* (1983)
(b) Cloudy sky	Maximum overlapping for contiguous cloudy layers and random overlapping for non-contiguous overlapping
Scattering	Neglected
Droplet absorption	Emissivity formulation with mass absorption coefficients; Stephens (1978) for non-ice clouds Starr and Cox (1985) and Griffith *et al.* (1980) for non-tropical and tropical cirrus, respectively

performance reports for this radiation scheme under various sky conditions and comparison with other models (ICRCCM, Luther *et al.*, 1988) and observations (Ackerman and Cox, 1982; Ellingson and Serafino, 1984) are documented in Appendices B and C. This chapter describes briefly the parameterization of radiation of the OSU multilayer AGCM.

4.1. Solar Radiation

The absorption of solar radiation at the Earth's surface and in the atmosphere is the initial source of energy for the climate system. The major difficulty in computing the absorption of solar radiation is the correct incorporation of the effects of multiple scattering. King and Harshvardhan (1986) concluded that the two-stream/delta-Eddington method is the most suitable for use in general circulation models in which it is important to produce accurate computations of moderately thick cloud layers over a wide range of solar zenith angles. In this section, the design of a two-stream /delta-Eddington method for the OSU multilayer AGCM is described.

4.1.1. Radiative transfer equation

The azimuthally-independent, monochromatic radiative transfer equation is usually written in the form (Liou, 1980)

$$\mu \, \frac{dI(\delta,\mu)}{d\delta} = I(\delta,\mu) - \frac{\bar{\omega}_0}{2} \int_{-1}^{1} P(\mu,\mu') \, I(\delta,\mu') \, d\mu' - \frac{S_\infty}{4\pi} \, P(\mu,\mu_0) \exp(-\delta/\mu_0) \,,$$

(4.1)

where $I(\delta,\mu)$ is the radiance in the direction $\mu = \cos \zeta$ (ζ = zenith angle) through the level defined by the optical depth

$$\delta = \int_{z}^{\infty} k \, \rho \, dz \,;$$

(4.2)

and where S_∞ is the solar flux associated with the collimated beam

incident at direction μ_0 on the top of the atmosphere, P is the scattering phase function of the particle (i.e., air molecule or aerosol), and $\tilde{\omega}_0$ is the single scattering albedo.

To determine the atmosphere and the surface solar heating for a GCM requires the upward and downward fluxes, respectively, F^+ and F^-, given by

$$F^{\pm}(\delta) = \int_0^1 \mu \, I(\delta, \pm\mu) \, d\mu \, .$$

(4.3)

To determine these fluxes from Eq. (4.1), the evaluation of the integrals with respect to both μ' and μ, plus the integration of δ and ultimately the wavelength is required. Since the fluxes must be determined for thousands of grid points over the Earth's surface, and at many times each day, direct solution of Eqs. (4.1) and (4.3) is impractical. Therefore, to save computation time, the delta-Eddington approximation is used.

For delta-Eddington approximation of Eq. (4.1) the upward and downward hemispheres are first integrated to obtain the following flux equations (for details see Appendix B):

$$\frac{dF^+(\delta)}{d\delta} = \alpha_1 \, F^+(\delta) - \alpha_2 \, F^-(\delta) - \alpha_3 \, S(\delta)/\mu_0 \, ,$$

(4.4a)

$$\frac{dF^-(\delta)}{d\delta} = \alpha_2 \, F^+(\delta) - \alpha_1 \, F^-(\delta) + \alpha_4 \, S(\delta)/\mu_0 \, ,$$

(4.4b)

and

$$\frac{dS(\delta)}{d\delta} = -\frac{S(\delta)}{\mu_0} \, ,$$

(4.4c)

where S represents the direct downward solar radiation and the α_i coefficients are

$$\alpha_1 = \frac{1}{4} [7 - \tilde{\omega}_0' (4 + 3 g')] ,$$

$$\alpha_2 = -\frac{1}{4} [1 - \tilde{\omega}_0' (4 - 3 g')] ,$$

$$\alpha_3 = \frac{1}{4} (2 - 3 g' \mu_0) \tilde{\omega}_0'^2 ,$$

$$\alpha_4 = \tilde{\omega}_0' - \alpha_3 , \tag{4.5}$$

with

$$\delta \rightarrow \delta' = (1 - \tilde{\omega}_0 f) \delta ,$$

$$\tilde{\omega}_0 \rightarrow \tilde{\omega}_0' = (1 - f) \tilde{\omega}_0 / (1 - \tilde{\omega}_0 f) ,$$

$$g \rightarrow g' = g / (1 + g) . \tag{4.6}$$

In Eq. (4.6), g is the asymmetry factor and $f = g^2$ is the fractional scattering into the forward peak. To determine these coefficients, μ_0, δ, $\tilde{\omega}_0$ and g must be known and their calculations are presented in following sections.

4.1.2. Vertical discretization

In the atmosphere, solar radiation is absorbed by water vapor, ozone, carbon dioxide and clouds, and is scattered by air molecules (Rayleigh scattering) and clouds. However, the heating by ozone absorption below 200 mb is negligible, compared with the heating by water vapor absorption (Manabe and Strickler, 1964), and above 200 mb the amount of Rayleigh scattering is negligible since with decreasing pressure there is an exponential decrease. [Consequently, it may be assumed that above 200 mb there is stratospheric only ozone absorption, as shown schematically in Fig. 4.1, with no tropospheric ozone absorption (below 200 mb).] For the latter, there is Rayleigh scattering and scattering by clouds, as well as absorption by water vapor, carbon dioxide and clouds. Therefore, the two-stream/delta-Eddington approximation for multiple scattering with absorption, as described below, is applied only to the troposphere.

The troposphere is divided into L layers, as shown in Fig. 4.1. [Within each layer it is assumed that the α coefficients from Eq. (4.6) are constant.]

$$S_\infty \qquad R_\infty$$

$$\downarrow \qquad \uparrow$$

p=0 ————————————————————————————

Ozone absorption

$$S_1 \qquad R_1$$

$$\downarrow \qquad \uparrow$$

$\ell=1/2$ ———— Model top, $p = p_T \equiv 200\,mb,\ \dot\sigma \equiv 0$ ———— $\sigma_{1/2} = 0$

$\ell=1$

$\ell=11/2$ ———————————————————————————————

$\ell=2$

⋮

$\ell-1$

$\ell-1/2$ ——————————————————————————————— $\hat\sigma_{\ell-1/2}$

$\ell \qquad\qquad \delta_\ell,\ \tilde\omega_\ell,\ g$

$\ell+1/2$ ——————————————————————————————— $\hat\sigma_{\ell+1/2}$

$\ell+1$

⋮

$\ell=L-1$

$\ell=L-1/2$ ———————————————————————————

$\qquad\qquad\qquad\qquad\qquad\qquad\qquad\qquad S_{L+1} \uparrow R_{L+1}$

$\ell=L$ $\qquad\qquad\qquad\qquad\qquad\qquad\qquad\qquad \downarrow\ \uparrow$

$\ell=L+1/2$ ————————————————————————— $\hat\sigma_{L+1/2} = 1$

Earth's surface, $p = p_s,\ \dot\sigma = 0,$
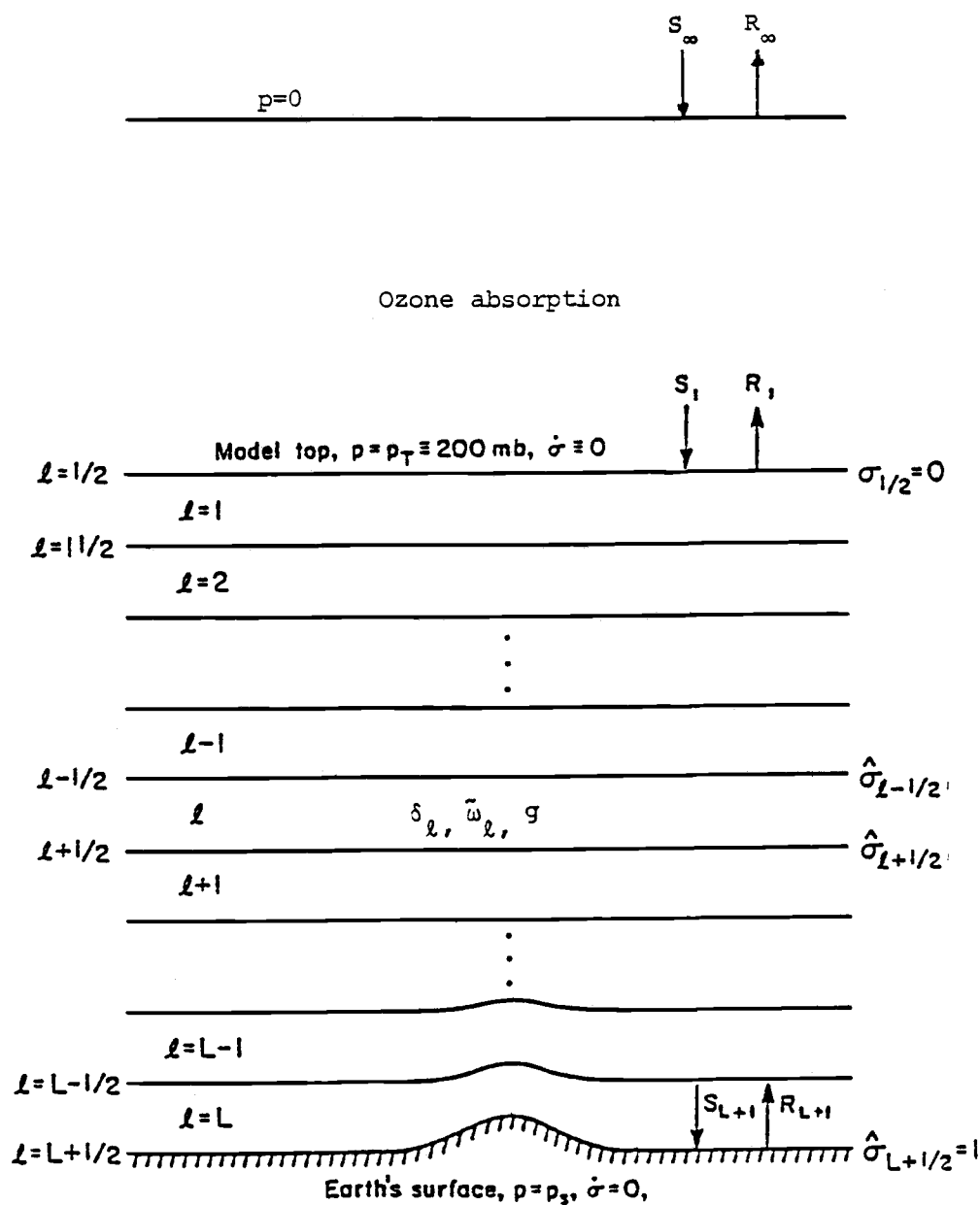
Fig. 4.1. Vertical indexing of a L-layer model. The model's layers are indexed by integers $\ell = 1, 2, ..., L$. The levels separating the layers are indexed by half-integers $\ell = 1/2, 3/2, ..., L+1/2$.

Each layer ℓ is then characterized by its optical depth, $\Delta\delta_\ell$, and its values for $\alpha_{1\ell}, \alpha_{2\ell}, \alpha_{3\ell}$ and $\alpha_{4\ell}$. From Geleyn and Hollingsworth (1979) Equations (4.4) can then be integrated analytically across each layer and the results expressed as

$$
\begin{bmatrix} S_b \\ F_b^- \\ F_t^+ \end{bmatrix}_\ell = \begin{bmatrix} a_1 & 0 & 0 \\ a_2 & a_4 & a_5 \\ a_3 & a_5 & a_4 \end{bmatrix}_\ell \cdot \begin{bmatrix} S_t \\ F_t^- \\ F_b^+ \end{bmatrix}_\ell .
$$

(4.7)

In Eq. (4.7), (S_b, F_b^-, F_t^+) and (S_t, F_t^-, F_b^+) are, respectively, the outgoing and incoming fluxes to the layer, with subscripts t and b denoting the top and bottom of the layer; a_1 is the transmission for the parallel beam, a_2 is the diffuse transmission for the parallel beam, a_3 is the diffuse reflection for the parallel beam, a_4 is the transmission for diffuse radiation, and a_5 is the reflection for diffuse radiation. The coefficients a_4 and a_5 appear in the expressions for both F_b^- and F_t^+ since it is not necessary to distinguish between layer optical properties for the upward and downward diffuse fluxes. The coefficients $a_{i\,\ell}$ (i = 1,5) are the analytical functions of $\Delta\delta_\ell$, $\alpha_{1\ell}$, $\alpha_{2\ell}$, $\alpha_{3\ell}$, $\alpha_{4\ell}$, and μ_o which are given in Appendix B.

For the computation of the a_i coefficients for all the L layers there are the 3L linear equations for 3L+3 unknown fluxes. This linear system is completed by three boundary conditions, namely $(S_t)_1$,

$$
(F_t^-)_1 = F^-(0) = 0
$$

(4.8)

at the top of the atmosphere, and

$$
(F_b^+)_L = F^+(\delta_s) = \alpha_s(\mu_0) S(\delta_s) + \tilde\alpha_s F^-(\delta_s)
$$

(4.9)

at the bottom of the atmosphere, where $\alpha_s(\mu_0)$ and $\tilde\alpha_s$ are, respectively, the surface albedos for the parallel and diffuse fluxes.

The 3L+3 linear system equations for the 3L+3 unknowns can then be written in matrix form as

$$
\mathbf{A} \vec{F} = \vec{S} ,
$$

(4.10)

where **A** is a band-structured matrix with all diagonal elements equal to one and other nonzero elements equal to $-a_{i\,\ell}$, $-\alpha_s(\mu_0)$ or $-\tilde{\alpha}_s$; $\vec{F}$ is the vector of the fluxes, consisting of the subvectors (S, F^-, F^+) appropriate to each layer, and S is the source vector with only one nonzero element equal to $\mu_0 S_\infty$.

[For fractional cloud cover, a maximum overlap (Geleyn and Hollingsworth, 1979) is assumed for vertically contiguous cloud layers and a random overlap (Manabe and Strickler, 1964) for vertically noncontiguous cloud layers (see Fig. 4.2).]
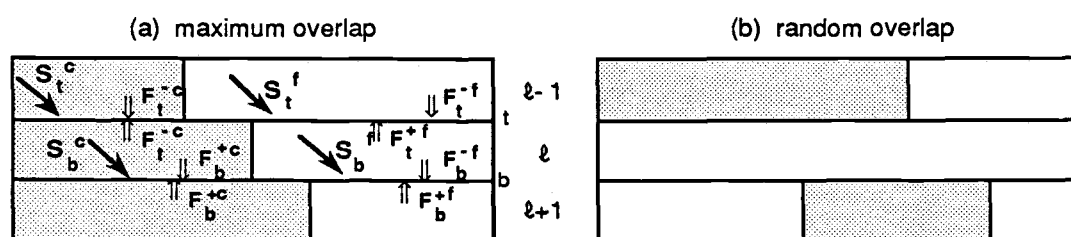
Fig. 4.2. Schematic representation of cloud geometry assuming: (a) maximum overlap and (b) random overlap.

4.1.3. Spectral discretization

Spectral solar irradiance is taken from Labs and Neckel (1970) for spectral intervals 0 - 0.33 µm and 1.2 - 4 µm, and from Neckel and Labs (1984) for the intervals 0.33 - 1.2 µm. The solar constant, S_∞ integrated with this spectrum from 0 to 4 µm, is 1362.3 W m^{-2}.

The major atmospheric absorbers are ozone in the stratosphere and water vapor in the troposphere. Ozone absorbs solar radiation effectively in the ultraviolet ($\lambda \leq 0.35$ µm) and visible range (0.5 µm $\leq \lambda \leq 0.7$ µm), while water vapor absorbs in the near-infrared range (0.7 µm $\leq \lambda \leq 4$ µm). Thus, the model the spectrum is subdivided into three frequency bands, two for wavelengths less than 0.69 µm and one for wavelengths greater

than 0.69 µm. The latter region is further subdivided into six intervals, in accordance with the water vapor absorption coefficient as described in Appendix B.

4.1.4. Layer optical properties

As noted in section 4.1.2, δ, $\tilde{\omega}_0$ and g must be determined for each layer in order to find the α_i and a_i coefficients. The calculation of these quantities is described below, first for the stratosphere and then for the troposphere.

4.1.4.1. Clear part of an atmospheric layer

a. *Rayleigh scattering*

The scattering optical thickness for the clear part of an atmospheric layer in the spectral interval $\lambda \leq 0.69$ µm is calculated by assuming that the atmosphere within the layer is homogeneous. This gives

$$\delta = \delta_{\ell,i} = \delta_{R,i}\, \delta\sigma_\ell, \qquad i = 1, 2, \tag{4.11}$$

where $\delta\sigma_\ell$ is the σ-thickness of layer ℓ and $\delta_{R,i}$ is the spectrally- averaged Rayleigh scattering optical depth, as shown in Appendix B.

The single scattering albedo for the Rayleigh scattering is

$$\tilde{\omega} = \tilde{\omega}_{\ell,i} = 1, \quad i = 1, 2, \tag{4.12}$$

and

$$g = 0, \tag{4.13}$$

because Rayleigh scattering is isotropic.

b. *Water vapor absorption*

Following Lacis and Hansen (1974), the water vapor absorptance A(u) is expressed in terms of a probability distribution p(k), where p(k) dk is the fraction of the incident flux that is associated with an absorption coefficient

between k and k + dk, for example

$$A(u) = \int p_k \, e^{-ku} \, dk$$

$$= \sum_n p(k_n) \, e^{-k_n u} \, \Delta k_n \, .$$

(4.14)

The values of the discrete probability distribution, $p(k_n) \, \Delta k_n$, and the absorption coefficients, k_n, are obtained to fit the line-by-line transmittivity given by Chou (1986) (see Appendix B).

The optical properties of each layer are specified by the absorption optical depth of the layer,

$$\delta = \delta_{\ell,n} = k_n w_\ell \, ,$$

(4.15)

where

$$w_\ell = u^*_{H_2O,\ell} \sec \zeta$$

(4.16)

is the effective water vapor amount in layer ℓ, with

$$u^*_{H_2O,\ell} = \frac{1}{g} \int_{p_{\ell-1/2}}^{p_{\ell+1/2}} q_\ell \left(\frac{p}{p_r} \right)^m dp \, ,$$

(4.17)

and by the single scattering albedo

$$\tilde{\omega}_{\ell,n} = 0 \, .$$

(4.18)

In Eq. (4.17) m and p_r are chosen to be 0.8 and 300 mb (Chou, 1986). [The vertical interpolation of q_ℓ is assumed in the same form given for longwave radiation (see Appendix C).]

c. *Ozone absorption*

Although the model's top is formally 200 mb, the stratosphere has been included in the radiative transfer parameterization. For the stratosphere, scattering is neglected and only the absorption of the downward direct solar radiation by ozone is included following Lacis and Hansen (1974).

Scattering in the stratosphere can be ignored since the amount of Rayleigh scattering is negligible. Thus,

$$\tilde{\omega}_0 = 0, \tag{4.19}$$

and δ can be calculated as

$$\delta = -\ln(1 - A_{O_3}). \tag{4.20}$$

d. *Carbon dioxide absorption*

CO_2 absorption is included for both the stratosphere, in which ozone is the principal absorber, and the troposphere, in which water vapor and clouds are the major absorbers of solar radiation. The transmittivity of CO_2 has been calculated based on the Fouquart (1987) parameterization by means of the Pade Approximation.

4.1.4.2. Cloudy part of an atmospheric layer

a. *Liquid water cloud*

The optical depth of a cloud layer comprised only of liquid water is calculated following Stephens (1978) as follows:

$$\log_{10}(\delta_\ell^{wc}) = \begin{cases} 0.2633 + 1.07095 \ln[\log_{10}(LWP_\ell)], \\ \qquad\qquad \text{for } \tilde{\omega}_0 = 1, \ \lambda \le 0.69 \ \mu m, \\ \\ 0.3492 + 1.6518 \ln[\log_{10}(LWP_\ell)], \\ \qquad\qquad \text{for } \tilde{\omega}_0 < 1, \ \lambda > 0.69 \ \mu m, \end{cases} \tag{4.21}$$

where LWP_ℓ is the liquid water path defined in Appendix B.

The cloud optical properties for wavelengths less than 0.69 μm are chosen as

$$\delta_{\ell,i} = \delta_\ell^{wc}, \tag{4.22}$$

$$\tilde{\omega}_{\ell,i} = \tilde{\omega}_{\ell,i}^{wc} = 1, \tag{4.23}$$

and

$$g_i^{wc} = 0.84 , \quad i = 1,2 ,$$

(4.24)

where i is the index for the wavelength interval. The asymmetry factor g has been chosen based on Cess *et al.* (1985).

The optical properties of clouds for wavelengths greater than 0.69 μm are

$$\delta_{\ell,n} = \delta_{\ell}^{wc} + k_n w_{\ell} ,$$

(4.25)

$$\tilde{\omega}_{\ell,n} = \text{the value from Stephens (1978)},$$

(4.26)

and

$$g_{\ell,n}^{wc} = \begin{cases} 0.76 & \text{for stratiform clouds ,} \\ \\ 0.85 & \text{for cumuloform clouds, } n = 1,...,6 , \end{cases}$$

(4.27)

where n is the index for $p(k_n)$ and δ_{ℓ}^{wc} is the optical depth due to cloud liquid water in ℓ-th layer. The asymmetry factor g is chosen following Cess *et al.* (1985) for the stratiform clouds and Stephens (1984) for the cumuloform clouds.

b. *Pure ice cloud (cirrus)*

Radiative properties for the cirrus clouds are parameterized following Starr and Cox (1985). The albedo and absorptance of the ice clouds are obtained from the relationship between α and ζ, and a and α as (for details, see Appendix B; Starr and Cox, 1985)

$$\alpha_{\ell} (\zeta) = (0.161 + 0.0117 \zeta + 0.386 \times 10^{-4} \zeta^2) \alpha_{\ell} (60°)$$
$$+ (0.914 - 0.0152 \zeta) [\alpha_{\ell} (60°)]^2$$

(4.28)

and

$$a_\ell (\zeta) = 1.01 \, a_\ell(35°) + 0.716 \, [\, a_\ell(35°)]^2$$
$$+ \{-0.246 \times 10^{-2} \, a_\ell(35°) + 0.765 \times 10^{-2} \, [a_\ell(35°)]^2\} \, \zeta$$
$$- 0.493 \times 10^{-3} \, [\, a_\ell(35°)]^2 \, \zeta^2 , \tag{4.29}$$

where

$$\alpha_\ell \, (\zeta = 60°) = 0.557 \, \varepsilon_\ell + 0.105 \, \varepsilon_\ell{}^2 \tag{4.30}$$

based on the results provided by Platt and Stephens (1980) and the theoretical results of Welch *et al.* (1980), as well as

$$a_\ell \, (\zeta = 35°) = 0.283 \, \alpha_\ell \, (\zeta = 35°) \tag{4.31}$$

from Starr and Cox (1985). In Eq. (4.30) the effective infrared flux emittance, ε_ℓ, of cirrus cloud is (Griffith *et al.*, 1980)

$$\varepsilon_\ell = 1 - \exp(-\beta \, \text{IWP}_\ell) , \tag{4.32}$$

where β is the effective infrared mass absorption coefficient and IWP is the ice water path. From Paltridge and Platt (1980), $\beta = 0.056 \text{ m}^2 \text{ g}^{-1}$ is chosen based on the observed flux profiles in cirrostratus clouds. Thus, the optical depth is

$$\delta_\ell^{ic} = -\ln[\, 1 - \alpha_\ell(\zeta) - a_\ell(\zeta)\,] \tag{4.33}$$

and the single-scattering albedo can be obtained from Stephens (1978). The optical properties (Cess *et al.*, 1985; Stephens, 1978) of a cirrus layer are then

$$\delta_{\ell,n} = \delta_\ell^{ic} + k_n \, w_\ell , \tag{4.34}$$

$$\tilde{\omega}_\ell = \begin{cases} 1, & \text{for } \lambda \le 0.69 \text{ μm,} \\[2ex] \text{the value from Stephens (1978), for } \lambda > 0.69 \text{ μm,} \end{cases} \tag{4.35}$$

and

$$g_\ell = g_\ell^{ic} = 0.82 . \tag{4.36}$$

c. *Mixed-phase clouds*

Many clouds consist of ice as well as liquid water. [To treat these mixed phase clouds, a linear combination of the radiative properties of liquid-water cloud and pure-ice cloud is assumed based on the ratio of the water path for each phase to the total water path.] Thus,

$$\delta_{\ell,n} = \delta_{\ell}^{wc} + \delta_{\ell}^{ic} + k_n w_{\ell} \,, \tag{4.37}$$

$$\tilde{\omega}_{\ell,n} = \gamma_{\ell} \, \tilde{\omega}_{\ell,n}^{wc} + (1 - \gamma_{\ell}) \, \tilde{\omega}_{\ell,n}^{ic} \,, \tag{4.38}$$

and

$$g_{\ell} = \begin{cases} 0.84 \;\; \text{for } \lambda < 0.69 \; \mu m \,, \\ \\ \gamma_{\ell} \, g_{\ell}^{wc} + (1 - \gamma_{\ell}) \, g_{\ell}^{ic} \;\; \text{for } \lambda \geq 0.69 \; \mu m \,, \end{cases} \tag{4.39}$$

where

$$\gamma_{\ell} = \frac{LWP_{\ell}}{LWP_{\ell} + IWP_{\ell}} \tag{4.40}$$

with g^{wc} and g^{ic} as given, respectively, in Eqs. (4.27) and (4.36).

4.1.5. Surface

The surface albedo, α_s, is considered for the different surface types, which are detailed in Table 6 of Appendix B. The surface albedo (α_s) for water is taken as 0.07 for the diffuse solar flux. For direct solar flux the albedo for water is obtained from the fit provided by Briegleb *et al.* (1986) from Payne's (1972) tabulated values, or

$$\alpha_s(\zeta) = \frac{0.026}{[(\cos \zeta)^{1.7} + 0.065]} + 0.15 \, (\cos \zeta - 0.1) \, (\cos \zeta - 0.5) \, (\cos \zeta - 1.0) \,. \tag{4.41}$$

4.2. Longwave Radiation

4.2.1. Basic equations

a. *Clear sky*

[Based upon the assumptions that the atmosphere is plane parallel, radiation is isotropic, and scattering by air molecules and aerosols is negligible, the frequency-integrated downward and upward fluxes of longwave radiation (Liou, 1980) at a level z can be expressed by

$$R_z^\downarrow = \int_0^\infty \pi B_\nu(T_z) \, d\nu + \int_{T_z}^0 dT \int_0^\infty \frac{d}{dT}[\pi B_\nu(T)] \, \tau_\nu(\Delta u) \, d\nu \tag{4.42}$$

and

$$R_z^\uparrow = \int_0^\infty \pi B_\nu(T_z) \, d\nu + \int_{T_z}^{T_g} dT \int_0^\infty \frac{d}{dT}[\pi B_\nu(T)] \, \tau_\nu(\Delta u) \, d\nu, \tag{4.43}$$

where ν is the frequency, $\pi B_\nu(T)$ is the blackbody flux emitted at temperature T, T_z is the temperature at level z, T_g is the temperature of the Earth's surface, τ_ν is the monochromatic transmission function, and $\Delta u = |u - u_z|$ where u and u_z are the absorber amounts at, respectively, the level of temperature T and level z.] The Eqs. (4.42) and (4.43) can be written in terms of the blackbody radiation (πB) and the fraction of spectral subintervals (f_j) (detailed derivation is provided in Appendix C) as

$$R_z^\downarrow = \pi B_z + \sum_{j=1}^J \int_{\pi B_z}^0 f_j(\pi B) \, \tau_j(\Delta u) \, d(\pi B) \tag{4.44}$$

and

$$R_z^\uparrow = \pi B_z + \sum_{j=1}^J \int_{\pi B_z}^{\pi B_g} f_j(\pi B) \, \tau_j(\Delta u) \, d(\pi B), \tag{4.45}$$

where

$$\pi B_g = \pi B(T_g) = \sigma T_g^4. \tag{4.46}$$

From Eq. (4.44), the vertically-discrete form of the downward flux at the bottom of layer ℓ (Fig. 4.1) can be written as

$$R^{\downarrow}_{\ell+1/2} = \pi B_{\ell+1/2} + \sum_{j=1}^{J} \sum_{\ell'=0}^{\ell} \int_{\pi B_{\ell+1/2}}^{\pi B_{\ell-1/2}} f_j(\pi B) \, \tau_j(|u - u_{\ell+1/2}|) \, d(\pi B)$$

$$= \pi B_{\ell+1/2} - \sum_{j=1}^{J} \sum_{\ell'=0}^{\ell} C^j_{\ell',\ell}$$

$$= \pi B_{\ell+1/2} - \sum_{\ell'=0}^{\ell} S_{\ell',\ell} , \tag{4.47}$$

where

$$C^j_{\ell',\ell} \equiv \int_{\pi B_{\ell+1/2}}^{\pi B_{\ell-1/2}} f_j(\pi B) \, \tau_j(|u - u_{\ell+1/2}|) \, d(\pi B) \tag{4.48}$$

represents the contribution of layer ℓ' to the flux at level $\ell+1/2$, including a nonzero contribution from $C^j_{0,\ell}$ when the model atmosphere is restricted to the troposphere. Then, with $\ell = 1/2$ corresponding to the tropopause,

$$S_{\ell',\ell} = \sum_{j=1}^{J} C^j_{\ell',\ell} . \tag{4.49}$$

Similarly, the upward flux at level $\ell+1/2$ can be written as

$$R^{\uparrow}_{\ell+1/2} = \pi B_{\ell+1/2} + \sum_{\ell'=\ell+1}^{L+1} S_{\ell',\ell} . \tag{4.50}$$

The trapezoidal rule is used to calculate the $C^j_{\ell',\ell}$, obtaining

$$
C^j_{0,\ell} = \begin{cases} 0, & \ell = 1/2 \text{ is the top of the atmosphere} \\[2mm] \dfrac{1}{2} f_j (\pi B_{1/2}) [\tau_j(|u_\infty - u_{\ell+1/2}|) + \tau_j(|u_{1/2} - u_{\ell+1/2}|)] \, \pi B_{1/2} \,, \\[2mm] & \ell = 1/2 \text{ is the tropopause} \end{cases}
$$

$$(4.51a)$$

$$
C^j_{\ell',\ell} = \frac{1}{2} [\, f_j(\pi B_{\ell'+1/2}) \, \tau_j(|u_{\ell'+1/2} - u_{\ell+1/2}|)
$$
$$
+ f_j(\pi B_{\ell'-1/2}) \, \tau_j(|u_{\ell'-1/2} - u_{\ell+1/2}|)] \, (\pi B_{\ell'+1/2} - \pi B_{\ell'-1/2}) \,,
$$
$$
1 \le \ell \le L \qquad (4.51b)
$$

and

$$
C^j_{L+1,\ell} = (\pi B_g - \pi B_{L+1/2}) \frac{1}{2} [f_j(\pi B_{L+1/2}) + f_j(\pi B_g)] \, \tau(u_{\ell+1/2}) \,,
$$

$$(4.51c)$$

where u_∞ is the effective absorber amount from the Earth's surface to the top of atmosphere (p = 0, T = 0), and where [the atmosphere above $\ell = 1/2$ is assumed to be isothermal, with $T = T_{1/2} = 218$ K (Ghan *et al.*, 1982).]

b. *Cloudy sky*

Fractional cloud cover for longwave radiation is treated in the same manner as for solar radiation. From the detailed derivation provided in Appendix C, the downward flux at level $\ell+1/2$ for cloudy sky, where N cloud groups exist above level $\ell+1/2$, can be written as

$$
R^\downarrow_{\ell+1/2} = (1 - C_\ell) \pi B_{\ell+1/2} + C_\ell R''^\downarrow_{\ell+1/2} - \sum_{\ell'=0}^{\ell} [E^\downarrow_{\ell',\ell} S_{\ell',\ell} + G^\downarrow_{\ell',\ell} D''^\downarrow_{\ell',\ell}] \,,
$$

$$(4.52)$$

where

$$
E^\downarrow_{\ell',\ell} = \{1 - \max[C_{\ell'}, ..., C_{\ell_B[N(\ell')]}] \} \, P_{N(\ell')}
$$

$$(4.53)$$

and

$$
G^\downarrow_{\ell',\ell} = \max \{0, C_{\ell'-1} - \max[C_{\ell'}, ..., C_{\ell_B(n)+1}]\} \, P_{N(\ell')} \,.
$$

$$(4.54)$$

The upward flux at level $\ell+1/2$ for cloudy sky, where N cloud groups exist below level $\ell+1/2$, can be written as

$$R^{\uparrow}_{\ell+1/2} = (1 - C_{\ell+1})\,\pi B_{\ell+1/2} + C_{\ell+1}\,R''^{\uparrow}_{\ell+1/2} + \sum_{\ell'=\ell+1}^{L+1} [E^{\uparrow}_{\ell',\ell}\,S_{\ell',\ell} - G^{\uparrow}_{\ell',\ell}\,D''^{\uparrow}_{\ell',\ell}]\,,$$

(4.55)

where

$$E^{\uparrow}_{\ell',\ell} = \{1 - \max[C_{\ell_T[N(\ell')]}, \,...,\, C_{\ell'}]\}\,P_{N(\ell')}$$

(4.56)

and

$$G^{\uparrow}_{\ell',\ell} = \max\{0,\, C_{\ell'+1} - \max[C_{\ell_T(n)-1}\,,...,\, C_{\ell'}]\}\,P_{N(\ell')}\,.$$

(4.57)

In Eqs. (4.52) and (4.55) the downward and upward flux from the cloud, respectively, $R''^{\downarrow}_{\ell+1/2}$ and $R''^{\uparrow}_{\ell+1/2}$, are calculated as given in section 1.2.3 of Appendix C. The cloud overlap parameter P for the downward flux in Eqs. (4.53) and (4.54) differs from that for the upward flux in Eqs. (4.56) and (4.57), though for the sake of convenience the same expression is used.

4.2.2. Absorbers, spectral subdivisions and mean transmission functions

From Chou (1984), the IR spectrum is divided into the water vapor, CO_2, and O_3 bands, and the water vapor band is further subdivided into band-center and band-wing regions, as given in Table 4.3. The fraction $f_j(T)$ of these spectral bends are given in Appendix C and the total transmission function for each spectral interval, τ_j^T, is taken to be

$$\tau_j^T = \tau_j^{H_2O}\,\tau_j^{CO_2}\,\tau_j^{O_3}\,\tau_j^{H_2O\ cont.}\,,$$

(4.58)

where $\tau_j^{H_2O}$, $\tau_j^{CO_2}$, $\tau_j^{O_3}$, and $\tau_j^{H_2O\ cont.}$ are the transmission function of, respectively, water vapor, CO_2, O_3, and water vapor continuum.

Table 4.3. Spectral bands and absorbers.

Spectral band j	Wavenumber Interval (cm^{-1})	Absorber
1	0 - 340 1380 - 1900	H_2O band centers
2	340 - 540 800 - 980 1100 - 1380 1900 - 3000	H_2O band wings and H_2O continuum
3	540 - 800	H_2O 15 μm overlap, H_2O continuum and CO_2
4	980 - 1100	H_2O continuum and O_3

4.2.3. Transmission function for each gas

a. *Water vapor bands*

The transmission function of the centers and the wings of the water vapor bands for spectral bands 1 and 2 has been calculated using the LOWTRAN 6 code (Kneizys *et al.*, 1983), with a spectral interval of 5 cm^{-1}. The calculated transmission function is fitted to quadratic polynomials, as given in Appendix C.

b. *Overlap with carbon dioxide*

The transmission function for spectral band 3 due to the overlap of the

water vapor band with the carbon dioxide band has been defined by Chou (1984).

c. *Continuum*

The transmission function of the water vapor continuum in the spectral interval 2 has been calculated with the LOWTRAN 6 code and the fitted quadratic polynomials are presented in Appendix C. The transmission functions of the water vapor continuum for spectral intervals 3 and 4 have been calculated by Chou (1984).

d. *Carbon dioxide*

The transmission function for the spectral interval 3 due to CO_2 has been calculated by Chou and Peng (1983).

e. *Ozone*

The transmission function for the spectral interval 4 due to O_3, $\tau_4^{O_3}$, has been calculated with the LOWTRAN 6 code and fitted to the quadratic polynomials as given in Appendix C.

4.2.4. Cloud emissivity

Stephens (1978) parameterized the effective emissivity of a cloud for IR radiation in terms of the cloud water path, W (g m^{-2}), as

$$\varepsilon_\ell^{\uparrow,\downarrow} = 1 - \exp\left(-a_0^{\uparrow,\downarrow} W_\ell\right),$$

(4.59)

where $a_0^{\uparrow,\downarrow}$ defines a mass absorption coefficient for the total infrared flux. The obtained values of $a_0^{\uparrow}$ and $a_0^{\downarrow}$ for the liquid water clouds were, respectively, 0.130 m^{2}g^{-1} and 0.158 m^{2}g^{-1}, from the empirical fitting of eight different cloud types. For cirrus clouds, the $a_0^{\uparrow}$ and $a_0^{\downarrow}$ values were given as, respectively, 0.05 m^{2}g^{-1} and 0.06 m^{2}g^{-1} as given by Starr and Cox (1985). However, from Griffith *et al.* (1980) the values of $a_0^{\uparrow}$ and $a_0^{\downarrow}$ have been chosen as 0.096 m^{2}g^{-1} for the tropical region.

5. DEVELOPMENT OF THE CLOUD-RADIATION PARAMETERIZATION

The development of the cloud-radiation parameterization is initiated with the design and testing of a one-dimensional model for stratiform cloud parameterization with the object of understanding the role of parameterized evaporation and precipitation processes. The results of this study are described in section 5.1. Subsequently, the values of the parameters of the stratiform and cumuloform cloud parameterizations are determined by performing limited-duration sensitivity/tuning simulations with the OSU multilayer AGCM. The results of these simulations are described in section 5.2.

5.1. Tests of the Stratiform Cloud Parameterization Using a One-Dimensional Model

The one-dimensional model for the stratiform cloud parameterization is based on Eqs. (3.4) - (3.6). Stratiform clouds can be generated by large-scale moisture convergence and/or large-scale cooling such that the relative humidity of the environment exceeds the critical value U_{00}. When this occurs, the fractional cloud cover can be calculated prognostically from Eq. (3.23) or calculated diagnostically from Eq. (3.26). The first step is to determine whether or not there are any differences between the prognostic and diagnostic calculations of cloud cover. Then, the effects of including the evaporation and precipitation of cloud water, the latter for two values of the threshold value of cloud water, m_c are examined.

For these tests, the initial environmental conditions are temperature of 10°C, relative humidity of 70%, and pressure of 800 mb, with the latter a constant in time. To generate the cloud two different scenarios are used: (1) a convergence (or divergence) of moisture with no temperature advection, and (2) a cooling (or heating) with no moisture advection. In the

first case, the moisture convergence (divergence) rate is assumed to be 5% of the initial saturation mixing ratio per hour; and in the second case, the cooling (heating) is taken to be 0.5°C per hour is assumed. Thus, these tests are defined by:

$$A_q = C_q \times 0.05 \times q_s \, (10°C, 800 \, mb) \, / \, h \, ,$$

$$A_T = C_T \times 0.5°C \, /h \, ,$$

$$q_i = 0.7 \times q_s \, (10°C, 800 \, mb) \, ,$$

$$T_i = 10°C \, ,$$

$$U_{00} = 0.8$$

$$m_c = \begin{cases} 1 \times 10^{-4} \, g/g \, , & \text{for test P1,} \\ \\ 5 \times 10^{-4} \, g/g \, , & \text{for test P5,} \end{cases} \tag{5.1}$$

where

$$C_q, C_T = \begin{cases} 1, & \text{for convergence,} \\ 0, & \text{for no change,} \\ -1, & \text{for divergence,} \end{cases} \tag{5.2}$$

and q_i and T_i are the initial water vapor mixing ratio and temperature. A threshold value of 1×10^{-4} g/g (Rutledge and Schlesinger, 1985) is used for test P1, while the value of 5×10^{-4} g/g (Kessler, 1969) is used for test P5.

5.1.1. Comparison of the prognostic and diagnostic equations for fractional cloudiness

In Sundqvist's (1978, 1988) stratiform cloud parameterization, the fractional cloudiness can be calculated either diagnostically from Eq. (3.26) or prognostically from Eq. (3.23). Although the prognostic and diagnostic equations are self-consistent in the continuous form of the parameterization, they might give different results in the AGCM because

of its time discretization. In particular, in the diagnostic Eq. (3.26) the fractional cloudiness is dependent only upon the relative humidity U, which is calculated diagnostically from the prognostic values of the temperature and water vapor mixing ratio, which are found respectively, in Eqs. (3.4) and (3.5). However, in the prognostic Eq. (3.23) the fractional cloudiness is independent of U and is rather directly dependent upon the convergence of moisture and sensible heat. Therefore tests were performed with the discrete one-dimensional model to determine whether or not the fractional cloud covers provided by the diagnostic and prognostic equations were identical.

The growth of the fractional cloudiness in response to the large-scale convergence of moisture ($C_q = 1$, $C_T = 0$) is shown in Fig. 5.1 for simulations with three different time steps each using the leapfrog scheme. In all three cases, when the relative humidity U is less then U_{00}, all the moisture convergence is used to increase U; when U is larger than U_{00}, part of the moisture convergence is used to increase U and part is used for condensation. With a time step of 0.1 hour (Fig. 5.1(a)), the diagnostic fractional cloudiness reaches unity (i.e., overcast) after 14 hours, while the prognostic fractional cloudiness remains less than unity for the entire 24-hour integration. The difference between the prognostic and diagnostic values can be minimized by reducing the time step, as shown in Figs. 5.1(b) and (c).

This test indicates that the fractional cloud cover values provided by the prognostic and diagnostic equations are in agreement only for time steps less than about 0.1 hour. However, the time step for calculating the stratiform (and cumuloform) cloudiness and precipitation in the AGCM is one hour. With this time step the results from the diagnostic and prognostic equations would be different, with the size of the difference depending on the size of the moisture convergence (and/or the rate of cooling). However, despite the "time-truncation error" of the diagnostic equation compared to the prognostic equation with a sufficiently small time step, we have chosen to use the diagnostic equation in the AGCM for simplicity and computational economy. In any case, errors produced from the use of the less-exact diagnostic equation are likely smaller than errors of the Sundqvist parameterization itself, even in its continuous form.

Thus, the following tests are performed with the diagnostic equation.

5.1.2. Tests of the effects of evaporation and precipitation

The parameterization of stratiform clouds given by Eqs. (3.4) - (3.6) includes the evaporation of cloud water (E_c) as given by Eq. (3.39) and the autoconversion of cloud water into precipitation (P) as given by Eq. (3.40). The effects of these individual processes on the evolution of a stratiform cloud are examined and two different values of the threshold cloud water, m_c, are tested. Two sets of tests were performed, one with only large-scale moisture convergence and divergence, and a second with only large-scale cooling and heating. The tests in each set are summarized in Table 5.1. Since the results for each set of tests were basically the same, only the results for the set of tests with the moisture convergence and divergence are presented here.

Table 5.1. Tests of the stratiform cloud parameterization.

Test (panel)	Evaporation	Precipitation
1	No	No
2	Yes	No
3	No	P5
4	No	P1
5	Yes	P5
6	Yes	P1

The scenario of large-scale moisture convergence and divergence is that there is a constant convergence for the first 12 hours ($C_q = 1$), no convergence for the next 12 hours ($C_q = 0$), and a constant divergence of moisture after 24 hours ($C_q = -1$). For the entire length of each test there is no cooling or heating ($C_T = 0$). The evolutions of U and b for Tests 1 - 6 of Table 5.1 are presented in Fig. 5.2.
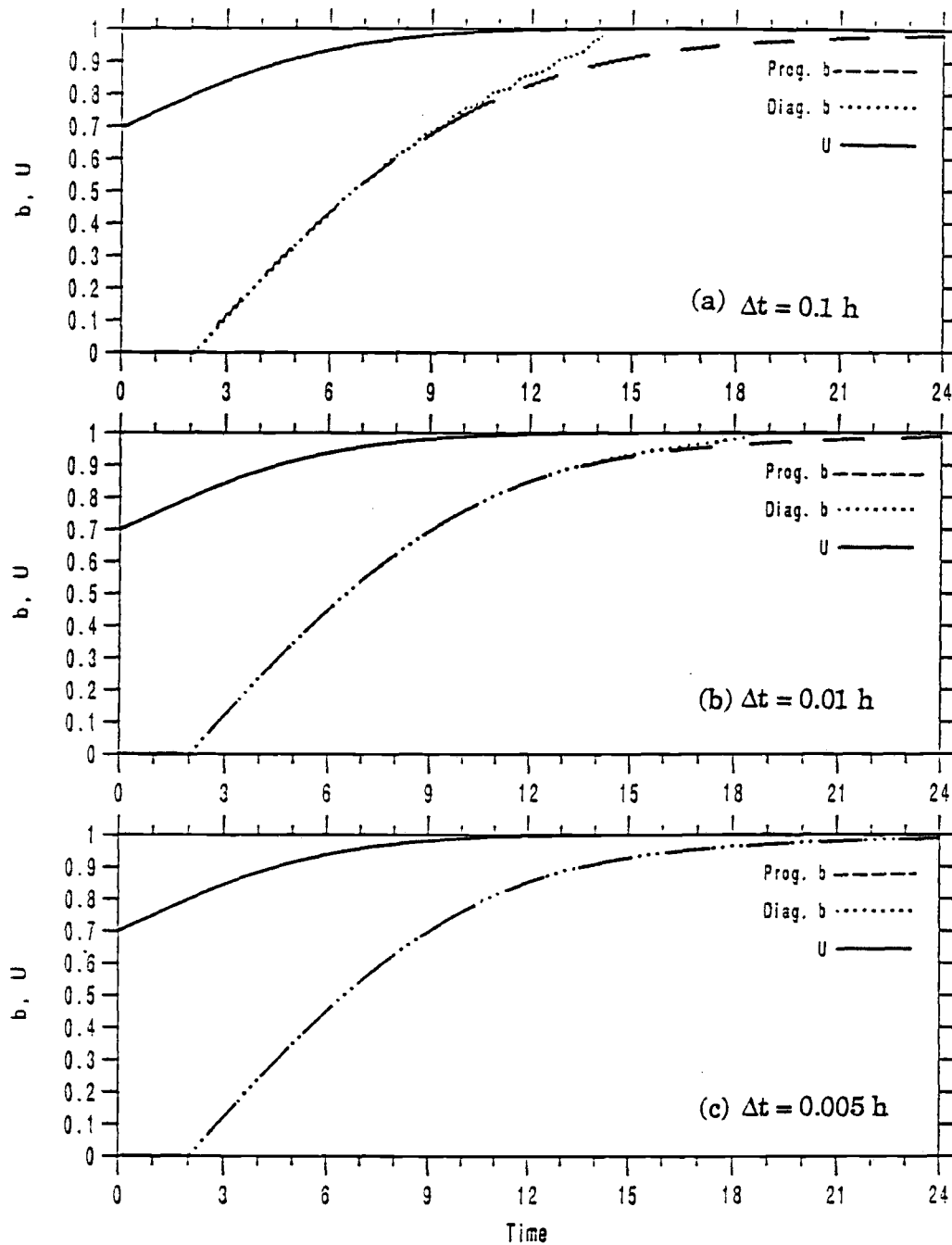
Fig. 5.1. Time evolution of the fractional cloud cover for the case of large-scale moisture convergence ($C_q = 1$, $C_T = 0$) as given by the diagnostic equation (3.26) and the prognostic equation (3.23), the latter for a time step of: (a) 0.1 hour, (b) 0.01 hour, and (c) 0.005 hour.
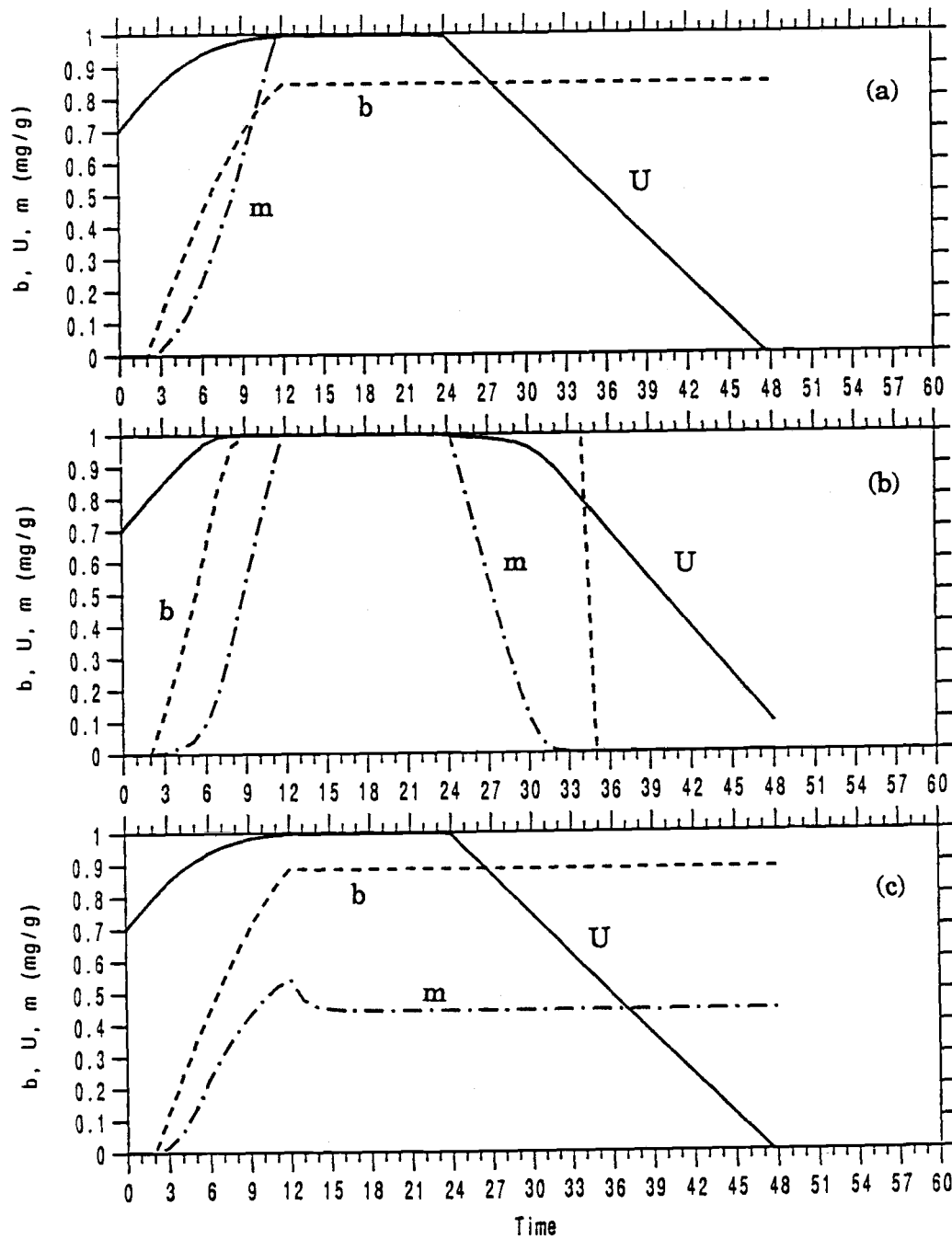
Fig. 5.2. Time evolution of the fractional cloud cover for the case of large-scale moisture convergence and divergence ($C_q = 1$ for 0-12 hours, $C_q = 0$ for 24 hours, $C_q = -1$ for > 24 hours; $C_T = 0$ for all time) for Tests 1-6 of Table 5.1. In each of these tests, $U_{00} = 0.8$.
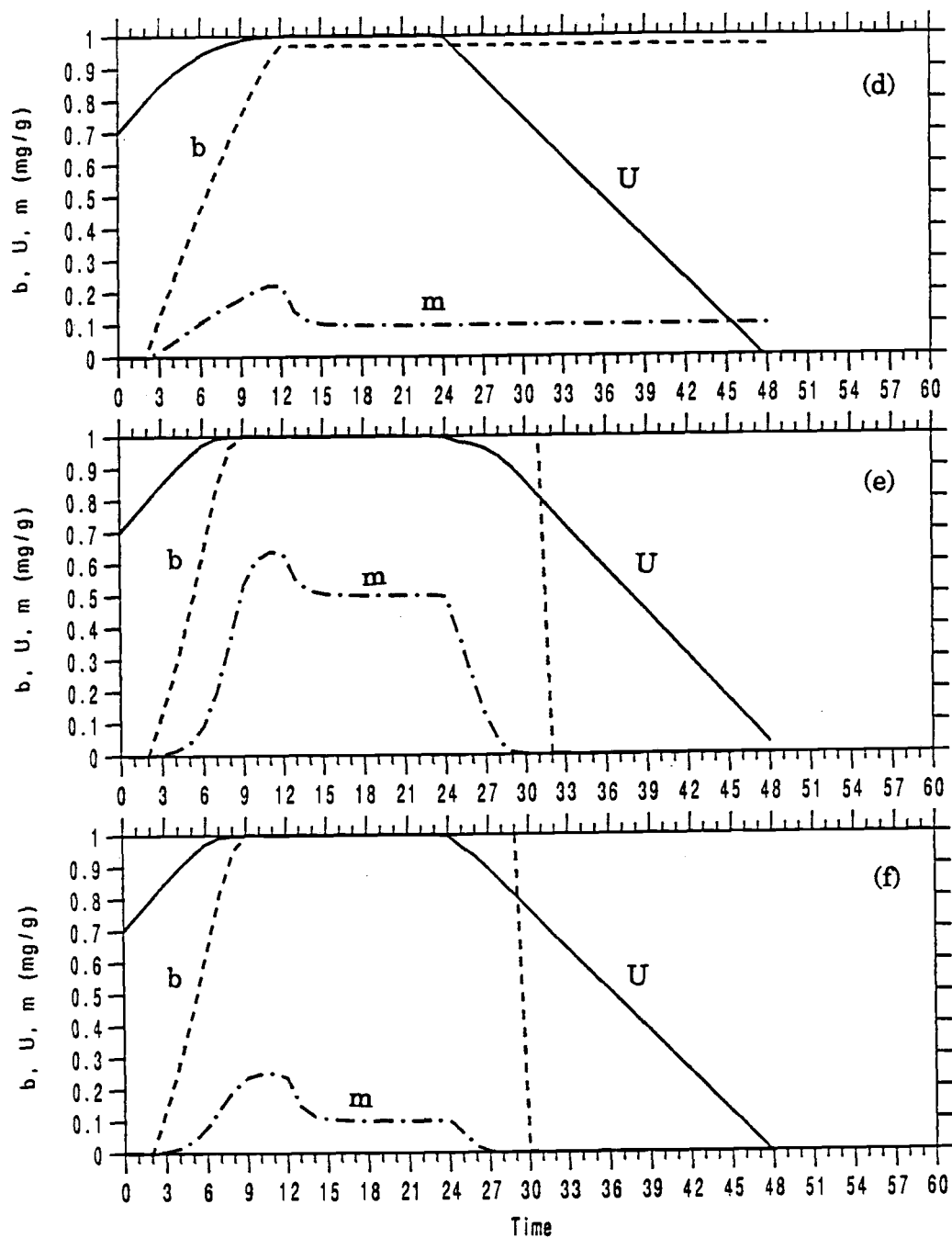
Fig. 5.2. Continued.

In Test 1 there is no evaporation or precipitation of cloud water. Figure 5.2(a) shows that U and b increase due to the moisture convergence during the first 12 hours. During this time, U reaches a maximum value at less than unity and b reaches 0.85, which is substantially less than unity due to the large dependence of b on U, as given by Eq. (3.26) for U > 0.9. During the following 12 hours, with the zero moisture convergence, there are no change in U, m, and b. After 24 hours, U decreases due to the moisture divergence, but since there is no evaporation or precipitation, the cloud water and cloud cover do not change as the environment dries.

In Test 2 there is evaporation of cloud water, but no precipitation. Figure 5.2(b) shows that now both U and b reach unity during the 12-hour moisture convergence period. This occurs because of enhanced moistening of the cloud-free environment by the evaporated cloud water. As in Test 1, there are no changes in U, m and b during the 12-hour period of zero moisture convergence. This occurs now because the environment is saturated, hence by Eq. (3.39) the evaporation is zero. After 24 hours, U decreases due to the moisture divergence, but the rate of decrease is less than that with no evaporation. In this test, cloud water now decreases with time due to evaporation, but the cloud cover remains at unity until the cloud water completely evaporates. At that time the cloudiness becomes zero.

In Tests 3 and 4, there is precipitation of cloud water, respectively, with $m_c = 1 \times 10^{-4}$ g/g and 5×10^{-4} g/g, but no evaporation. In comparison with Fig. 5.2(a), Figures 5.2(c) and 5.2(d) show that during the 12-hour period of moisture convergence, the fractional cloudiness is larger with precipitation than without precipitation and the cloud water is smaller. This figure also shows that the maximum cloud cover increases, and the minimum cloud water decreases, as the threshold value of cloud water m_c is decreased. Thus, the existence of precipitation, like the existence of evaporation, permits a more-rapid growth of cloud cover. This occurs because as the precipitation diminishes the cloud water a larger fraction of the moisture convergence is given to the environment for the expansion of cloud cover and a correspondingly smaller fraction is given to the cloud itself to increase the cloud water. During the 12-hour period of moisture convergence, the condensation rate is larger than the precipitation rate,

hence the cloud water increases. When moisture convergence becomes zero following hour 12, the condensation ceases but the precipitation continues until the cloud water decreases to the threshold value. Thereafter, the cloud water and cloud cover remain constant because of the absence of evaporation, even as the environment dries due to the moisture divergence.

In Tests 5 and 6 there is precipitation of cloud water (again, respectively with $m_c = 1 \times 10^{-4}$ g/g and 5×10^{-4} g/g), but there is evaporation. In comparison with Figs. 5.2(c) and 5.2(d), Figures 5.2(e) and 5.2(f) show that evaporation enhances the moistening of the environment, thereby increases the growth rates of U and b during the 12-hour period of moisture convergence. Again condensation decreases with the cessation of moisture convergence after hour 12, and the cloud water decreases to the threshold values. These threshold values are maintained until hour 24 because the saturation of the environment makes the evaporation zero. Thereafter, the cloud water decreases by evaporation as the moisture divergence dries the environment, with the cloud lifetime being larger for the cloud with the larger threshold value of cloud water.

The results of this study can be summarized as follows:

1) The values of fractional cloud cover given by the prognostic and diagnostic equations agree with each other only for time steps less than about 0.1 hour. Nevertheless, we have chosen to use the diagnostic equation for computational economy and because its errors are likely not larger than those of the parameterization itself.

2) Through its moistening of the environment, the evaporation of cloud water tends to enhance the growth of cloud cover.

3) Precipitation of cloud water tends to enhance the growth of cloud cover because the fraction of the moisture convergence given to the environment to expand the cloud cover increases as the cloud water decreases.

4) As the threshold value of cloud water m_c is decreased, the maximum cloud cover tends to increase and the minimum cloud water tends to decrease.

5.2. Difficulties of the Cloud-Radiation Parameterization Validation by Satellite Observations

Global satellite observations such as the ISCCP and NIMBUS-7/ERBE in which the earth's radiation budget can be measured accurately, are extremely useful for testing and validating new cloud-radiation parameterization. However, as noted by Hartmann *et al.* (1986) and Ramanathan (1987), the earth radiation budget from satellite observations pose several problems resulting from: the uncertainty of the fractional cloud cover algorithms from the satellite observation, the uncertainty in the instrument measurement, and the uncertainty in the radiative transfer models to compute the fluxes from the measured radiance, and poor diurnal sampling.

5.2.1. Cloud cover

a) *What is cloud?*

The fractional cloud cover is one of the most difficult problems in the observation and parameterization. Ground-based observations may pose problems in the accuracy and distribution of the data. Satellite observations can eliminate some of these problems, but fail to provide a clear distinction between "clear" and "cloud". For example, it may be difficult to observe the clouds over such cold and bright surfaces as ice and snow. Clouds are difficult to distinguish from surface ice or snow in visible imagery because they are bright, and in the infrared because they are cold. From a comparison with ground-based observation Henderson-Sellers *et al.* (1987) reported that in several cases the ISCCP data failed to

detect thin cirrus and small clouds identified by the ground observers and could be confused with the clouds over near-coastal locations. In contrast, Sassen *et al.* (1988) emphasized the effect of "subvisual" thin cirrus clouds, which are not visible to the unaided human eye, but which can be detected by the lidar. Thus, due to these satellite imagery uncertainties, the fractional cloud cover depends strongly upon the cloud-analysis algorithm.

b) *Retrieval of cloud from satellite images*

The threshold method is the most common technique for discriminating between cloud and clear. However, this method may produce large errors in fractional cloud cover estimations when individual imagery pixels are not completely covered by the clouds. Shenk and Solomonson (1972) demonstrated that these errors do not necessarily cancel from pixel to pixel, but tend to accumulate and produce large errors in the fractional cloud cover even for large regions containing many pixels. This is particularly true where the ratio of the areal cloud size to the pixel size (R) is small (R < 10), due to the effect of partially covered cloudy pixels. Note that the average cumuloform cloud size is about the same as the spatial resolution of the satellite sensor. The threshold method depends on the cloud radiative properties and clear backgrounds, the setting of the threshold, the size of the clouds, and the spatial resolution of the instruments (Coakley, 1987). Coakley and Bretherton (1982) demonstrated that the actual fractional cloud cover of each pixel is not 0 or 1, as assumed in the threshold method, but is between 0 and 1. Thus, the fractional cloud cover obtained by the threshold method can be different from the actual cloud cover. Coakley and Bretherton (1982), Arking and Childs (1985) and Coakley (1987) have sought to improve the threshold method by the release of a unit fractional cloud cover for each pixel or by selection of more proper threshold values. However, no technique has been developed for determination of fractional cloud cover of individual pixels for all cases. The cloud algorithm of ISCCP and NIMBUS-7 use threshold methods (Rossow *et al.*, 1985; Hwang *et al.*, 1988), and their fractional cloud covers are strongly dependent upon the

threshold values selected. One important difference between the two algorithms is that the clear window for the cloud/no-cloud pixel decisions is considerably wider in NIMBUS-7 observations than in the ISCCP observations. For the latter, there is approximately 6°C difference between the cloud/no-cloud threshold over the ocean and the expected clear atmosphere radiative temperature; the same difference, over land, is approximately 7 - 8°C.

Susskind *et al.* (1987) explained that their underestimation of tropical cloud cover (52%), retrieved by the GLAS physical inversion method (Susskind *et al.*, 1984) from the HIRS2/MSU sounding data, when compared to data provided by NIMBUS-7 THIR (80%), may have been caused by the overestimation of the THIR algorithm (Hwang *et al.*, 1988) in which the subpixel clouds are often treated as a full overcast.

c) *ISCCP data are not long enough for a cloud climatology*

ISCCP observations can somewhat overcome the poor diurnal sampling of the data by NIMBUS-7. ISCCP cloud data are achieved 8 times per day (Rossow *et al.*, 1985), while the NIMBUS-7 cloud data are taken only 2 times per day (Hwang *et al.*, 1988). However, at this time, the ISCCP data have not been provided for the lengths of time sufficient for the prediction of cloud climatology.

The only available ISCCP data for the month of July was taken during the El Niño/Southern Oscillation (ENSO) event of 1982/1983, which has been discussed in detail by Rasmusson and Wallace (1983) and Rasmusson and Hall (1983). Stowe *et al.* (1986), evaluating the NIMBUS-7 cloud cover data, reported that the July global minimum of the annual variation was enhanced with less than normal cloud cover in the northern hemisphere during the ENSO period (July 1983).

5.2.2. Cloud optical depth

Cloud optical depth, as is true of fractional cloud cover, is one of the most important cloud feedback parameters. However, cloud optical depth cannot be directly measured. It must be evaluated from the observed

radiance by a radiative transfer model. Thus, the value of the cloud optical depth depends strongly upon the radiative transfer model in use and upon the accuracy of the radiometers on the satellite.

The ISCCP cloud retrieval algorithm employs the threshold method to determine clear/cloud pixel (Rossow *et al.*, 1985). However, the actual cloud cover of a cloud pixel can be less than unity and in a clear pixel can be larger than zero. For total fractional cloud cover, the overestimations in the cloud pixels can be somewhat compensated by the underestimation in the clear pixels, even though the threshold method has a tendency to overestimate cloud fractional cover due to the resolution of present satellite radiometers (Shenk and Solomonson,1972; Coakley and Bretherton, 1982; Susskind *et al.*, 1987).

Coakley and Bretherton (1982) noted that if the actual fractional cloud cover in a cloud pixel is less than unity, the planetary albedo of the cloud pixel is not the same as the actual cloud albedo. The cloud pixel albedo (α_{pix}) can be written in terms of the fractional cloud cover (b_{pix}), clear sky albedo (α_{CLR}), and cloud albedo in a pixel (α_c) as

$$\alpha_{pix} = (1 - b_{pix}) \, \alpha_{CLR} + b_{pix} \, \alpha_c . \tag{5.3}$$

If b_{pix} is close to 1, then the first term on the right-hand-side of Eq. (5.3) is negligible in comparison to the second term. In this case, the cloud-pixel albedo is about the same as the actual cloud albedo. However, the error of cloud-pixel albedo with respect to the actual cloud albedo becomes larger in proportion to the increase in the difference of b_{pix} from 1. The dependence of the cloud-pixel albedos, and the error of the cloud-pixel albedos from actual cloud albedos, on fractional cloud cover for the cases $\alpha_{CLR} = 0.15$ and $\alpha_c = 0.5$ or 0.8 is shown in Fig. 5.3. When b_{pix} is 0.9, the cloud-pixel albedo is 0.46 (0.72) for the case $\alpha_c = 0.5$ (0.8). When b_{pix} is 0.8, the cloud-pixel albedo is 0.43 (0.67). In only one case, i.e., $b_{pix} = 1$, is the actual cloud albedo identical to the cloud-pixel albedo; otherwise, the cloud-pixel albedo is smaller than the actual cloud albedo. In Summary: The more significant the error, the larger the actual cloud albedo or the smaller the cloud pixel fractional cloud cover. Thus, cloud optical depth retrieved from

the cloud pixel albedo, based upon the assumption that $b_{pix} = 1$, can be significantly underestimated. When actual $b_{pix} = 0.8$, this assumption could lead to an approximate 15% underestimation of the cloud albedo, resulting in a significant underestimation of cloud optical depth. If b_{pix} is less than 0.8, the difference in the cloud optical depth may be so large that the cloud optical depth retrieved from the cloud-pixel albedo may not be characterized as the observed cloud optical depth.
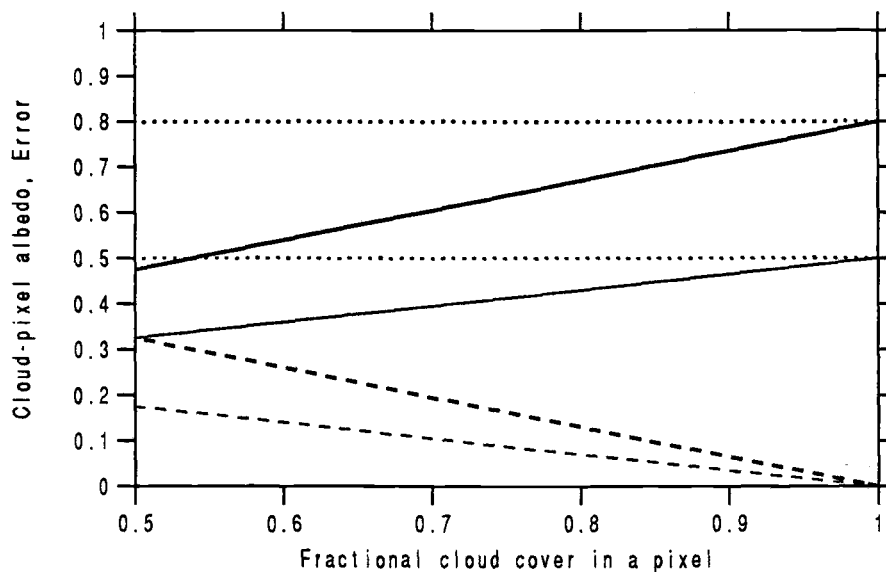
Fig. 5.3. Cloud-pixel albedos for the cases $\alpha_{CLR} = 0.15$ and $\alpha_c = 0.5\ (0.8)$ with various values of b_{pix}. Solid lines represent the cloud-pixel albedo and dashed lines represent the errors between cloud-pixel albedos and actual cloud albedos (thick line for $\alpha_c = 0.8$ and thin line for $\alpha_c = 0.5$).

5.2.3. NIMBUS-7 Earth Radiation Budget Experiment

The current wide-field-of-view (WFOV) measurements on NIMBUS-7 have provided the earth's radiation field data as the incoming solar radiation and earth-reflected and earth emitted radiation over a period of several years (Jacobowitz and Tighe, 1984; Kyle *et al.* 1985). However, the WFOV measurement does not correspond to a point measurement at the

top of the atmosphere. King and Curran (1980) reported that the effects of a nonuniform planetary albedo on the WFOV measurement is significant. Moreover, Jacobowitz *et al.*, (1984) showed that the planetary albedo observed by satellite depends upon the instruments. Arking and Vemury (1984) reported that the systematic differences between wide and narrow field of view measurements are due to a bias introduced in processing methods and the errors in calibration. The WFOV instruments underestimate and smooth the planetary albedos in comparison to the planetary albedos derived from the narrow-field-of-view (NFOV). Hucek *et al.* (1987) also reported that the WFOV archival method underestimates the tropical local maximum of the planetary albedo and overestimates the subtropical local minima when compared to NFOV data.

5.3. Development of the Cloud-Radiation Parameterization Using the Multilayer AGCM

Based upon information derived from the one-dimension model tests of stratiform cloud parameterization described in section 5.1, the next step was to develop and test cloud-radiation parameterization for the OSU multilayer AGCM. The objective of this development was to determine values for: (1) the stratiform-cloud parameters τ_s, a, U_{00}, and m_c, (the latter, separately for water and ice clouds); (2) the cumuloform-cloud parameters τ_c, α and C_0; and (3) the critical temperature for cirrus, T_i. When, the e-folding time for evaporation of cloud water, $\tau_c = \tau_s \equiv \tau$ is assumed, 8 parameters are provided, the values of which must be determined. It was not possible to choose n_i values for each parameter i and perform n_1 x n_2 x ... x n_8 simulations with the AGCM in order to obtain an optimum set of parameter values. Therefore, a "reasonable" set of values was determined by the selection of the "best" choice parameter from sensitivity simulations for a few of its values. The value of the parameter was then set equal to this "best" choice, and this selection procedure was repeated sequentially for the remaining parameters. The order of the parameters chosen in this way was C_0, U_{00}, τ, T_i, α, a, m_c for

water clouds and m_c for ice clouds. After completion of this selection procedure, it was evident that further improvements could be obtained by a refinement of the values for C_0, m_c for water clouds ($m_{c,w}$) and m_c for ice clouds ($m_{c,i}$), as well as for two cloud optical properties. Thus a second, final selection procedure was performed. The results of the initial and final selection procedures are presented in the two subsections which follow.

5.3.1. OSU multilayer atmospheric general circulation model

Although the OSU two-layer AGCM successfully simulates many features of the observed climate (e.g., Schlesinger and Gates, 1979, 1980, 1981), its coarse vertical resolution limits its usefulness as a tool for the development of physically-based cloud parameterization and their radiative interactions. Accordingly, a multilayer version of the AGCM was developed, with the object of extending the model's prognostic variables to include cloud water. The top of the model atmosphere is defined as the 200 mb surface (similar to the two-layer AGCM), and the troposphere below this surface is divided into seven layers.

The basic dynamic structure and physical processes of the multilayer model are identical to the OSU two-layer AGCM (Ghan et al., 1982). The principal changes in the model have been made to:

1) the boundary layer, for improvement of the simulated surface fluxes of heat, moisture, and momentum;

2) the subgrid-scale vertical transport of heat, moisture, and momentum in the free atmosphere, to be consistent with the model's increased vertical resolution;

3) the formulations of dry adiabatic adjustment, to be consistent with the model's increased vertical resolution;

4) the formulation of stratiform clouds and large-scale precipitation, based upon modification of the Sundqvist (1988) parameterization

with different parameterization of micro-cloud physics, allowing consideration of cloud water as additional prognostic variable and fractional cloud cover as a semi-prognostic variable;

5) the formulation of mid-level and penetrating convection, based upon modification of the Arakawa-Schubert (1974) parameterization, allowing consideration of convective cloud water as prognostic variable and determination of fractional cloud cover from the convective mass fluxes; and

6) the longwave and solar radiation parameterization, including cloud optical depth feedback and fractional cloud cover feedback.

Comprehensive documentation for these model changes is presented in Appendix A.

The OSU multilayer AGCM has been developed with computational efficiency in view, as well as the physically-based parameterization of clouds and their radiative interactions. Figure 5.4 illustrates the evolution of the OSU multilayer AGCM. Based upon physical processes identical to the OSU two-level AGCM the multilayer model (CONT) takes 190 sec of the CRAY-XMP CPU time for a one-day simulation. When the physically-based cloud-radiation parameterization considered in Chapters 3 and 4 were introduced, the model required 905 sec for a one-day simulation (MOD 1). However, through vectorizations introduced in MOD 2 - MOD 4 and MOD 6 and the application of a vectorized matrix solver from Geleyn (1988) in MOD 5, the multilayer model took only 235 sec for a one-day simulation. In Fig. 5.4 GAUSEL, COMTRX, RADCL, TRANS are the name of the subroutines used in the multilayer model.

5.3.2 Initial parameter selection

The schematic diagram for the initial parameter selection procedure is shown in Fig. 5.5. In this procedure, a 20-day control run for perpetual-July was performed and, for some of the parameters, a 20-day control run for perpetual-January was also performed. Test simulations were then

made for a few values of the first parameter to be selected, each test simulation for only 10 days starting from day 10 of the control. The values of cloud cover, cloud liquid water content, precipitation, and earth radiation budget components averaged over the last 5 days of the control and test simulations were then compared with the corresponding observations and a "best" value was chosen.

MLAM EVOLUTION
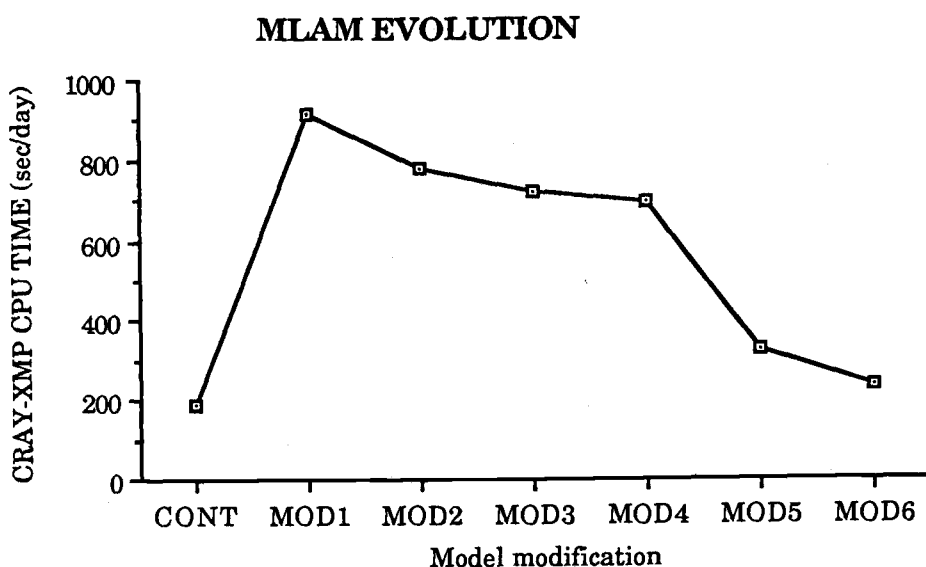
CONT : OSU multilayer AGCM with the same forcing calculation
      scheme except for the 7 layers.
MOD1 : New forcing calculation (cloud, precipitation, radiation).
MOD2 : Vectorize the matrix solve and remove GAUSEL.
MOD3 : Vectorize RADCL loop and remove COMTRX.
MOD4 : Put transmission functions in-line in TRANS.
MOD5 : Introduce the vectorized matrix solver from Geleyn (1988).
MOD6 : Replace the function calls with 1-line statement functions in
      TRANS.

Fig. 5.4. Evolution of the OSU multilayer AGCM in a sense of the
      computational efficiency.

Times, days
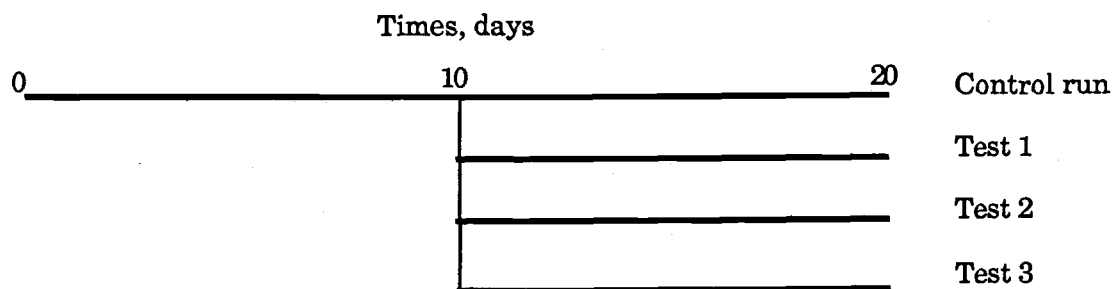
Fig. 5.5. Schematic diagram for the control and test simulations.

New perpetual-July and perpetual-January control simulations were made for 20 days with this "best" parameter value, each simulation starting at the initial times of the original control simulations. Next, perpetual-July and perpetual-January test simulations were made for a few values of the second parameter to be selected, again each simulation for only 10 days. The "best" value for this parameter was then chosen by comparing the values of cloud cover, cloud liquid water content, precipitation, and earth radiation budget components averaged over the last 5 days of the control and test simulations with the corresponding observations. New perpetual-July and perpetual-January control simulations were then made for 20 days with the "best" parameter values for the first and second parameters, again with each simulation starting at the initial times of the original control simulations. This procedure was then repeated in turn for each of the remaining 6 parameters.

To choose the "best" value for each of the parameters, both the relative and root-mean-square (rms) errors of the simulated global means, defined as follows with respect to the corresponding observed global means, were used:

$$\text{relative error} = \frac{S^g - O^g}{O^g} \, ,$$

(5.4)

$$\text{root–mean–square error} = \frac{\sum_{ij} \sqrt{(S_{i,j} - O_{i,j})^2} A_{i,j}}{\sum_{ij} A_{i,j}}, \tag{5.5}$$

where S^g and O^g are, respectively, the global means of the simulation and the observation; and $S_{i,j}$, $O_{i,j}$, and $A_{i,j}$ are, respectively, the simulation value, the observation value, and the area for a gridbox with longitudinal index i and latitudinal index j. Specifically, the relative and rms errors for the global-mean quantities shown in Table 5.2, were used.

Table 5.2. Quantities for which the relative and root-mean-squares errors of the global means were used to select the "best" value for C_0, U_{00}, τ, T_i, α, a, $m_{c,w}$ for water clouds, and $m_{c,i}$ for ice clouds.

Quantity	Symbol	Source of Observations
Relative Errors		
Fractional cloud cover	CLD	Rossow *et al.* (1985)
Precipitation	PREC	Jaeger (1976)
Cloud liquid water content	CLW	Njoku and Swanson (1983)
Outgoing longwave radiation	OLR	Kyle *et al.* (1985) [a]
Planetary albedo	ALB	Kyle *et al.* (1985) [a]
Absorbed solar radiation	ABS	Kyle *et al.* (1985) [a]
Absolute Errors		
Net radiation	NRAD	Kyle *et al.* (1985) [a]
Root-Mean-Square Errors		
Precipitation	RRN	Jaeger (1976)
Outgoing longwave radiation	ROLR	Kyle *et al.* (1985) [a]
Planetary albedo	RALB	Kyle *et al.* (1985) [a]
Absorbed solar radiation	RABS	Kyle *et al.* (1985) [a]
Net radiation	RNRD	Kyle *et al.* (1985) [a]

a. NIMBUS-7/NFOV (Narrow-Field-Of-View)

A schematic diagram of the relative and rms errors versus the values of a parameter in its antecedent-control and test simulations is shown in Fig. 5.6. The values for each of the 8 parameters tested in the initial selection procedure are shown in Table 5.3, wherein the "best" values are shown in bold faced-type. A brief description of each of these parameter tests is given below.

a. *Autoconversion rate for convective precipitation, C_0*

As indicated in Table 5.3, the autoconversion rate for cumuloform clouds, C_0, was the parameter whose value was chosen first. The perpetual-July control simulation used $C_0 = 0.002$, as suggested by Arakawa and Schubert (1974), while the test simulations used values equal to 2x, 3x and 4x the control value. Figure 5.7 shows that there is too much cloud liquid water in the model atmosphere with the control value of C_0 and that the cloud liquid water content is reduced by increasing C_0. Based on the results shown in Fig. 5.7, the 4x-value of C_0, or 0.008 m^{-1}, was selected the "best" value of the autoconversion rate for convective precipitation.

b. *Critical relative humidity for large-scale condensation, U_{00}*

The second parameter was the critical relative humidity for large-scale condensation, U_{00}. The perpetual-July control simulation used $U_{00} = 0.8$ as suggested by Sundqvist (1978). (Note that Sundqvist (1988) used $U_{00} = 0.75$ for land and $U_{00} = 0.85$ over oceans.) The test simulations used values of $U_{00} = 0.7$ and $U_{00} = 0$. The latter value was tested because it permits the generation of stratiform cloud whenever $Q > 0$, regardless of the relative humidity of the environment. Thus, it avoids the unphysical situation in which there is cloud water, but no cloud cover.

As shown in Fig. 5.8, the errors in the global-mean fractional cloud cover, precipitation, planetary albedo, and net radiation declined only slightly as the value of U_{00} was reduced. This result is in contrast to the larger sensitivity of the Sundqvist (1988) parameterization to the value of U_{00}. It appeared that the comparative insensitivity of our stratiform cloud
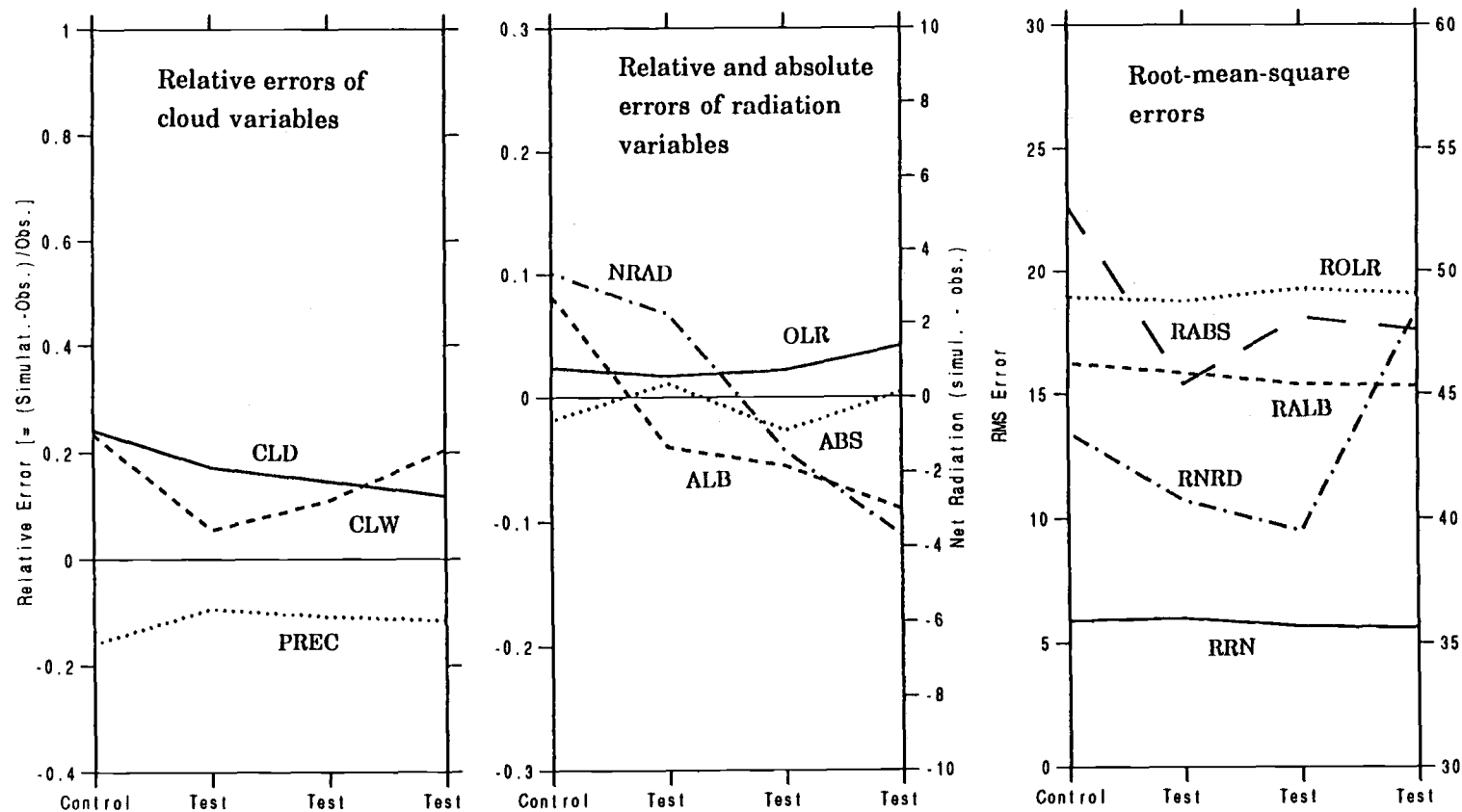
Fig. 5.6. Schematic representation of the relative and rms errors of global-mean cloud and radiation quantities versus the values of a parameter in its antecedent-control and test simulations.

Table 5.3. Initial selection of the parameters of the cloud parameterization.

Parameters	Equation	Initial value	Tested values			Reference for Initial value
Autoconversion rate of convective precipitation, C_0, m^{-1}	$P = C_0 \, M \, m \, \Delta z$	0.002	0.004	0.006	**0.008**	Arakawa and Schubert (1974)
Critical relative humidity value for condensation, U_{00}		0.8 for land	0.7	0.7	**0**	Sundqvist (1978)
		0.8 for ocean	0.8	0.7	**0**	
Characteristic time for the evapotation of cloud water, τ, min.	$E_c = -\dfrac{(U_s - U)}{\tau} \, m$	30	45	**50**	55	
Critical value of cirrus, T_i, °C		-40	-30	**-25**	-20	
Parameter for cumuloform fractional cloud cover, α, mb s^2/m	$b = \dfrac{\alpha M}{1 + \alpha M} \, U$	1	0.01	**10**	100	

Table 5.3. Initial selection of the parameters of the cloud parameterization (continued).

Parameters	Equation	Initial value	Tested values			Reference for Initial value
Autoconversion rate for stratiform precipitation, a, s^{-1}	$P = a\,(m - b\,m_c)$	$(3600)^{-1}$	$(5400)^{-1}$	$(1800)^{-1}$	$(1000)^{-1}$	Le Treut and Li (1987)
Threshold value for stratiform precipitation, m_c, g/g	$P = a\,(m - b\,m_{c,w})$	10^{-4} for $T \geq 0°C$	0.5×10^{-4}	2×10^{-4}	5×10^{-4}	Rutledge and Schlesinger (1985)
	$P = a\,(m - b\,m_{c,i})$	I_c for $T \leq T_i$ interpolated value $T_i < T < 0°C$	$0.9 \times I_c$	$0.8 \times I_c$	$0.7 \times I_c$	Heymsfield and Platt (1984)
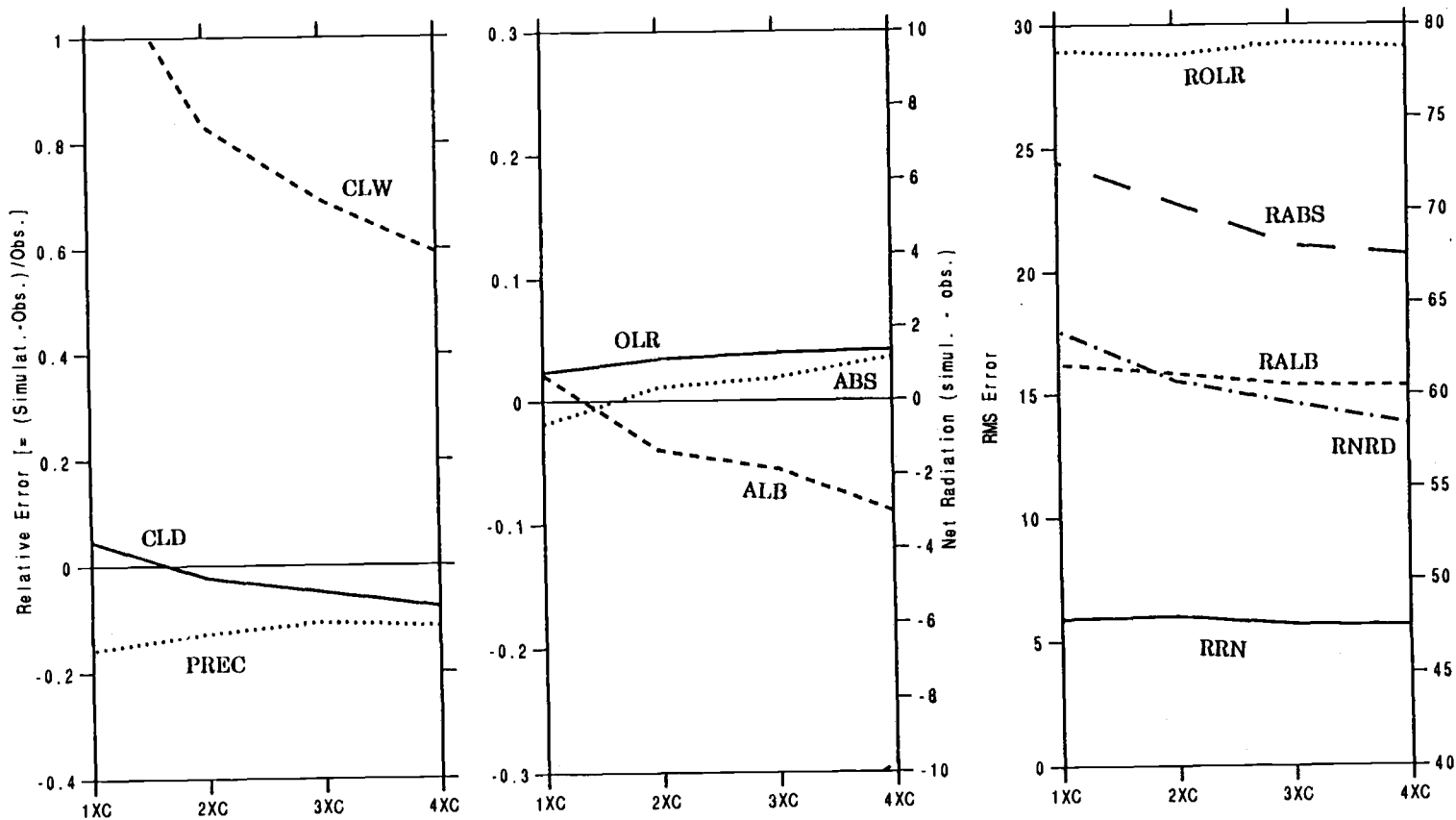
Fig. 5.7. The relative and rms errors of global-mean cloud and radiation quantities versus the values of C_0 in the antecedent-control and test simulations for perpetual July.
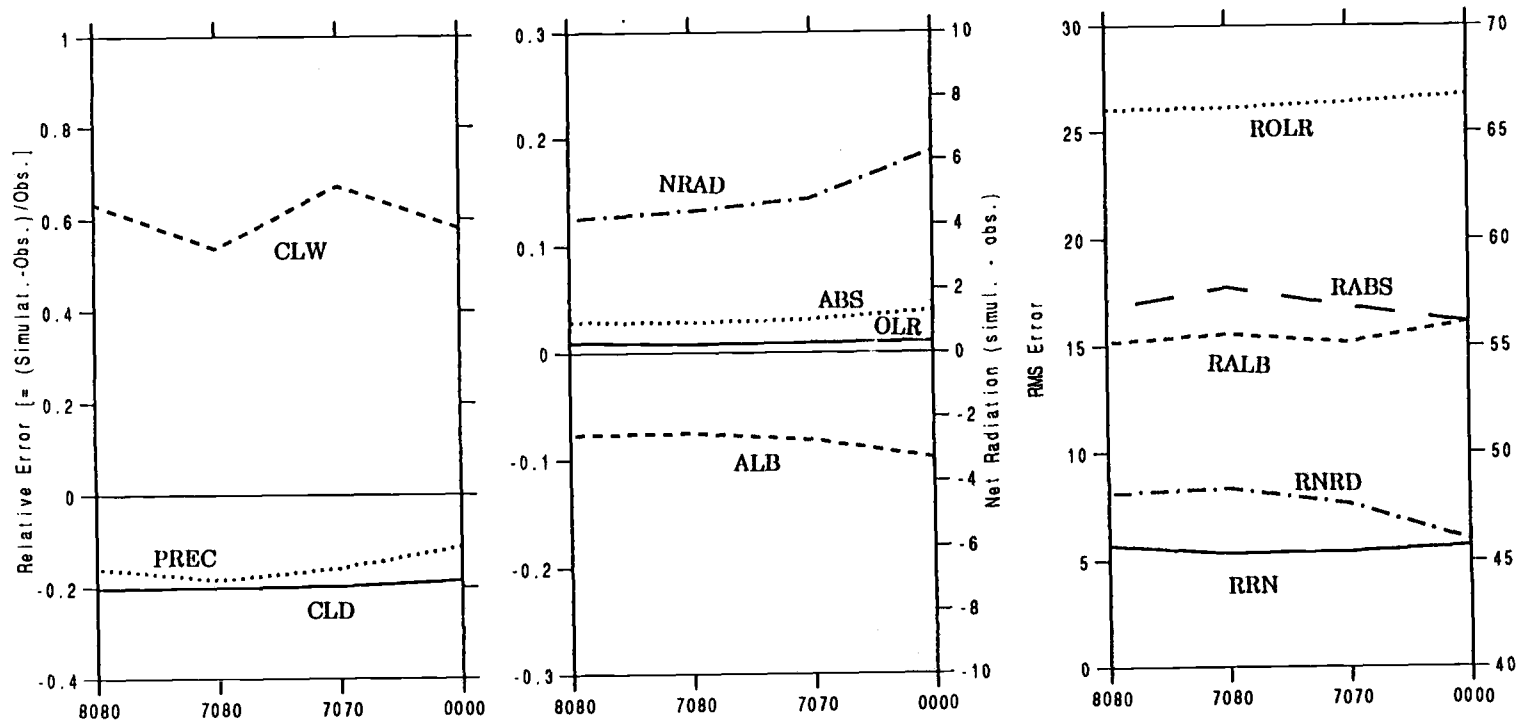
Fig. 5.8. The relative and rms errors of global-mean cloud and radiation quantities versus the values of U_{00} in the antecedent-control and test simulations for perpetual July. Dual values of U_{00} are shown on the abscissa, with the first value being U_{00} over land and the second value U_{00} over the ocean.

parameterization (hereafter referred to as the SO parameterization) as described in section 5.1, but with the moisture divergence after 24 hours taken as twice the value of the previous tests.

Figure 5.9 presents the results from the one-dimensional model for $U_{00} = 0$ and $U_{00} = 0.8$ for both the Sundqvist and SO parameterizations. This figure shows that the Sundqvist parameterization is sensitive to the choice of U_{00}, while the SO parameterization is not. This sensitivity of the Sundqvist parameterization occurs because a cloud can exist only so long as there is condensation. In the SO parameterization, however, the cloud can exist as long as it has cloud water.

Because the SO parameterization is insensitive to the choice of U_{00}, and because the choice of $U_{00} = 0$ avoids the physical inconsistency of having cloud water in the absence of cloud cover, $U_{00} = 0$ was chosen as the "best" value for the critical relative humidity for large-scale condensation.

c. *Characteristic time for the evaporation (sublimation) of cloud water (ice), τ*

The third parameter was the characteristic time for the evaporation (sublimation) of cloud water (ice), τ. As a prelude to the AGCM tests, tests were performed with the one-dimensional model described in section 5.1. The results of these tests for $\tau = 15$, 30, and 45 minutes are presented in Fig. 5.10. This figure shows that as τ is increased the stratiform cloud exists longer, this as a result of the reduced evaporation rate. Also, the maximum value of the cloud cover decreases as τ is increased, again as a result of the reduction of evaporation. However, this test shows that the stratiform cloud parameterization is relatively insensitive to the value of τ.

In the AGCM evaluations, the perpetual-July and perpetual-January control simulations used $\tau = 15$ minutes and the test simulations used $\tau = 30$, 45, 50 and 55 minutes. On the basis of the results presented in Figs. 5.11 and 5.12 the selected "best" value was $\tau = 50$ minutes.
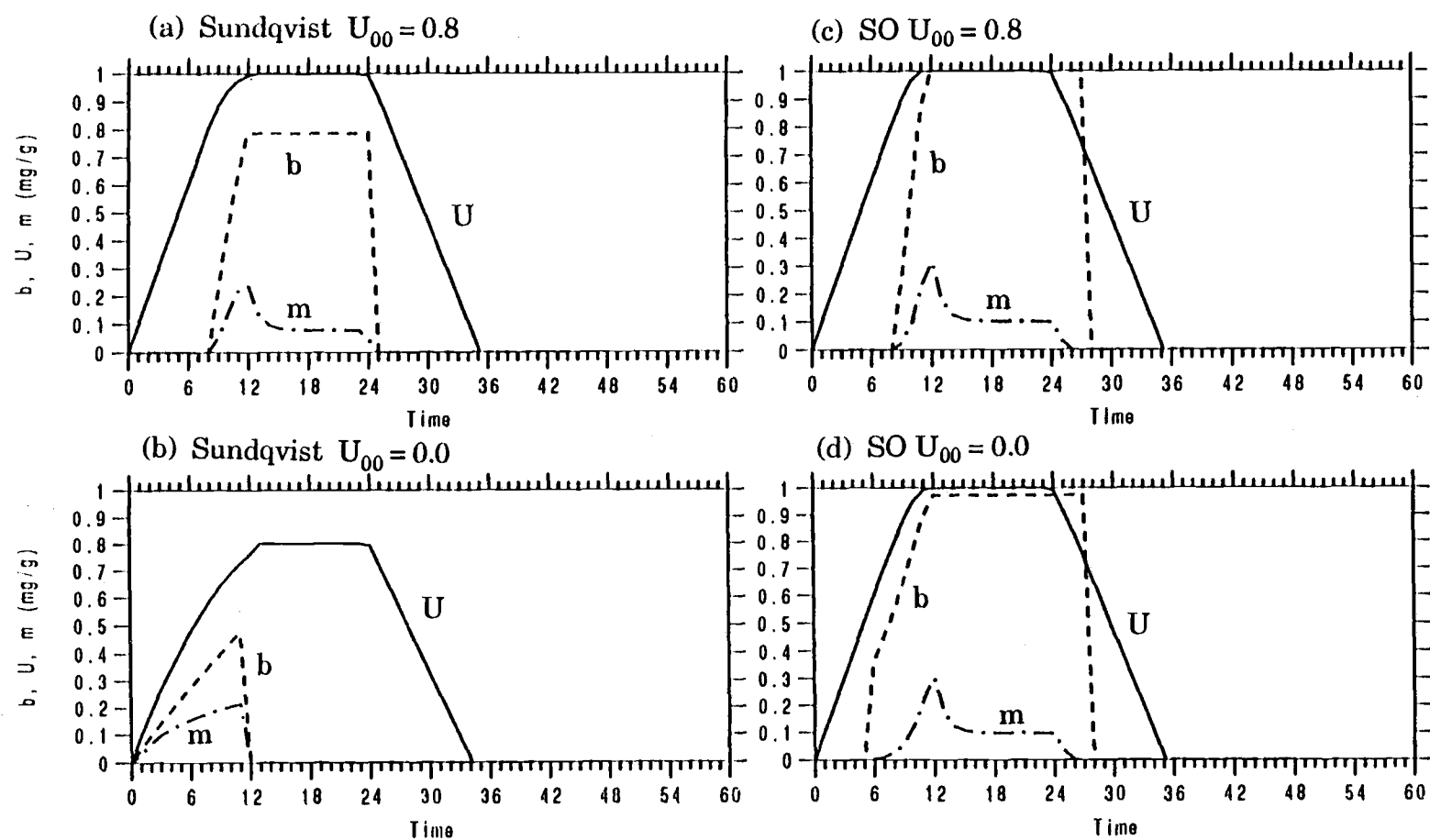
Fig. 5.9. Tests with the one-dimensional model of the sensitivity of the Sundqvist parameterization (panels a and b) and the SO parameterization (panels c and d) to U_{00} for $U_{00} = 0.8$ and $U_{00} = 0$.
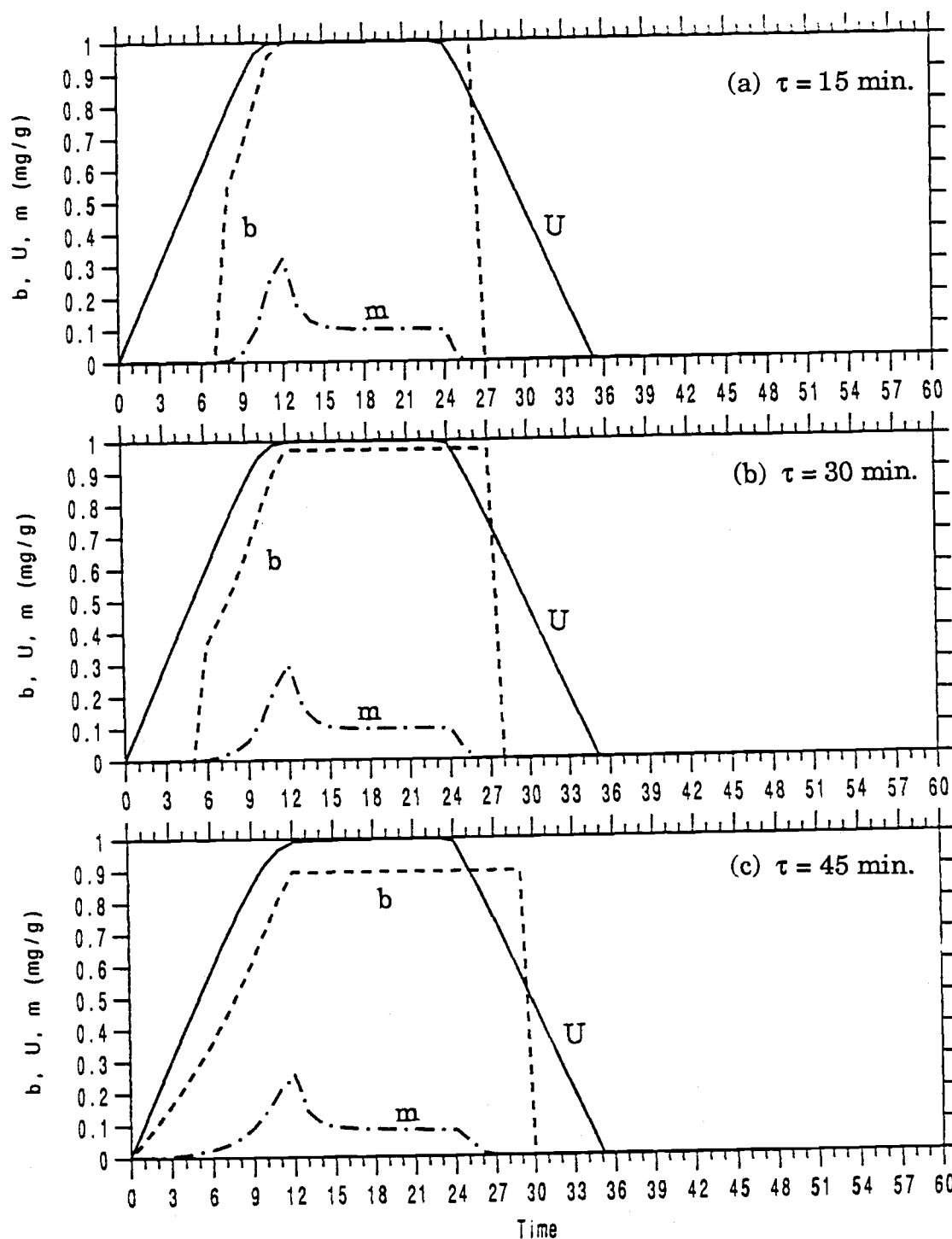
Fig. 5.10. Tests with the one-dimensional model of the sensitivity of the SO parameterization to τ for: (a) τ = 15, (b) τ = 30 and (c) τ = 45 minutes.
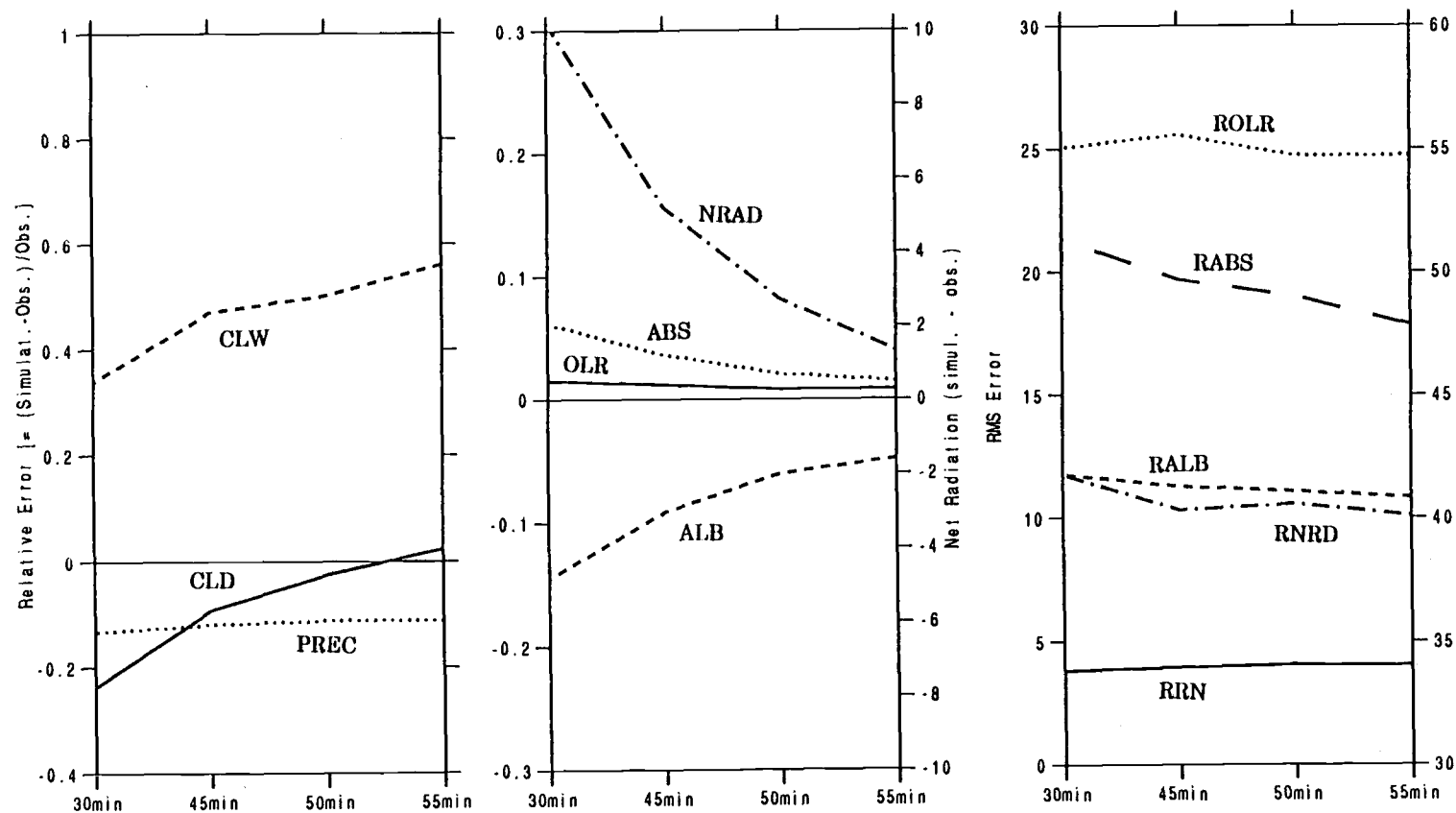
Fig. 5.11. The relative and rms errors of global-mean cloud and radiation quantities versus the values of τ in the antecedent-control and test simulations for perpetual July.
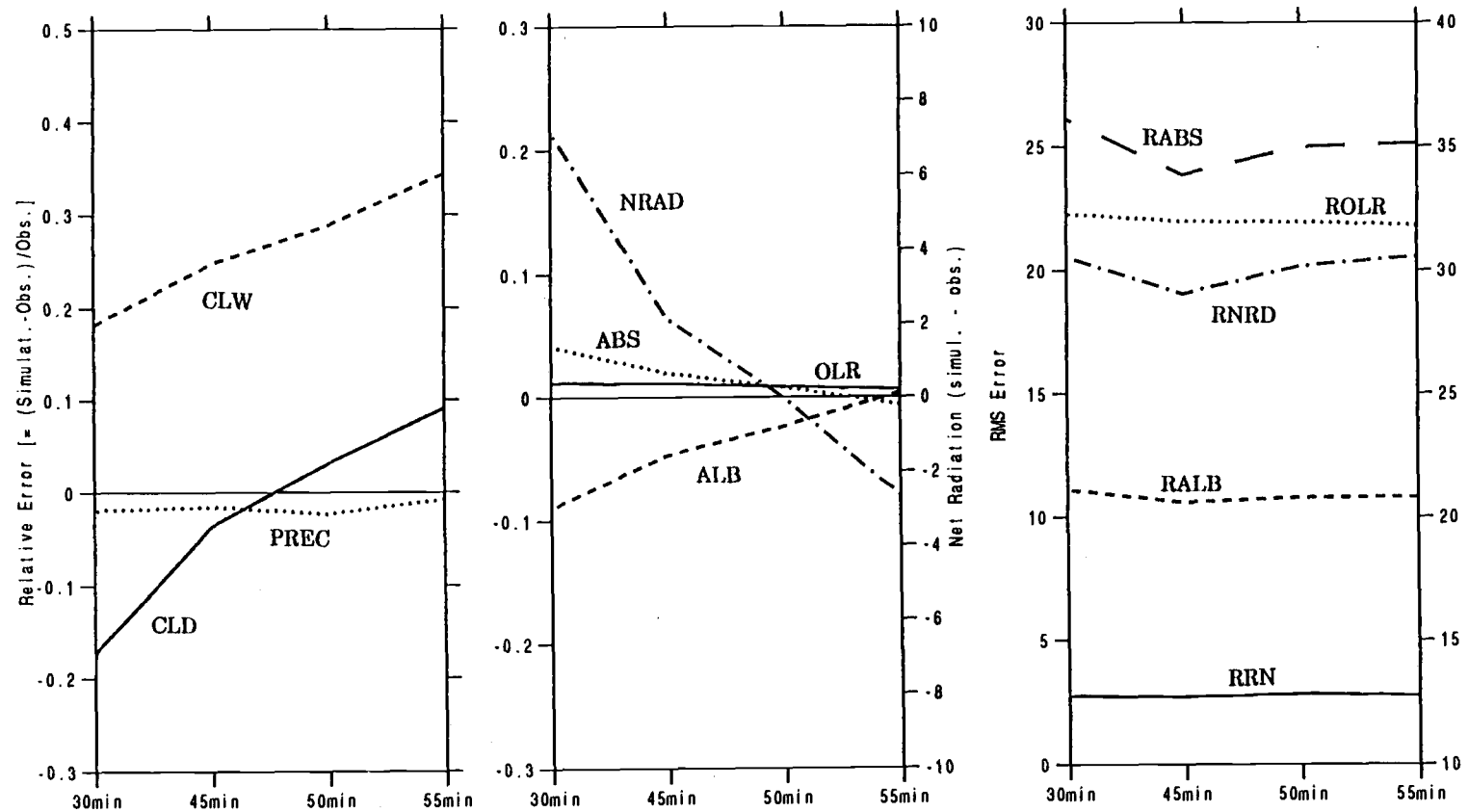
Fig. 5.12. As in Fig. 5.11, except for perpetual January.

d. *Critical temperature for cirrus, T_i*

The fourth parameter was the critical temperature for cirrus, T_i. The perpetual-July and perpetual-January control simulations used $T_i = -40^{\circ}C$ and the test simulations used values of $T_i = -20, -25,$ and $-30^{\circ}C$. Based on the results shown in Figs. 5.13 and 5.14 the "best" value of the critical temperature of cirrus clouds was $T_i = -25^{\circ}C$.

e. *Convective cloudiness parameter, α*

The fifth parameter was the parameter for the convective cloudiness, α. The perpetual-July control simulation used $\alpha = 1$ and the test simulations used values of $\alpha = 0.01, 10,$ and 100. The results of the AGCM simulations are presented in Fig. 5.15, which shows that the cloud and radiation budget terms are not sensitive to the value of α in the range of 0.01 to 100. This insensitivity is due to the restrictions in Eqs. (3.87) and (3.113) for, respectively, mid-level and penetrating convection, that the fractional cloud cover be not less than its antecedent value and that the cloud cover be less than the relative humidity of the environment. On the basis of Fig. 5.15, the selected "best" value was $\alpha = 10$.

f. *Autoconversion rate for stratiform clouds, a*

The sixth parameter was the parameter for the autoconversion rate for stratiform clouds, a. The perpetual-July control simulation used $a = (3600s)^{-1}$ and the test simulations used values of $a = (5400s)^{-1}, (1800s)^{-1},$ and $(1000s)^{-1}$. The results of the AGCM simulations for perpetual July are presented in Fig. 5.16, which shows that the cloud and radiation budget terms are not sensitive to the value of a when a is smaller than $(3600 s)^{-1}$. The selected "best" value was $a = (3600 s)^{-1}$.

g. *Precipitation threshold for stratiform water clouds, $m_{c,w}$*

The seventh parameter was the precipitation threshold for stratiform
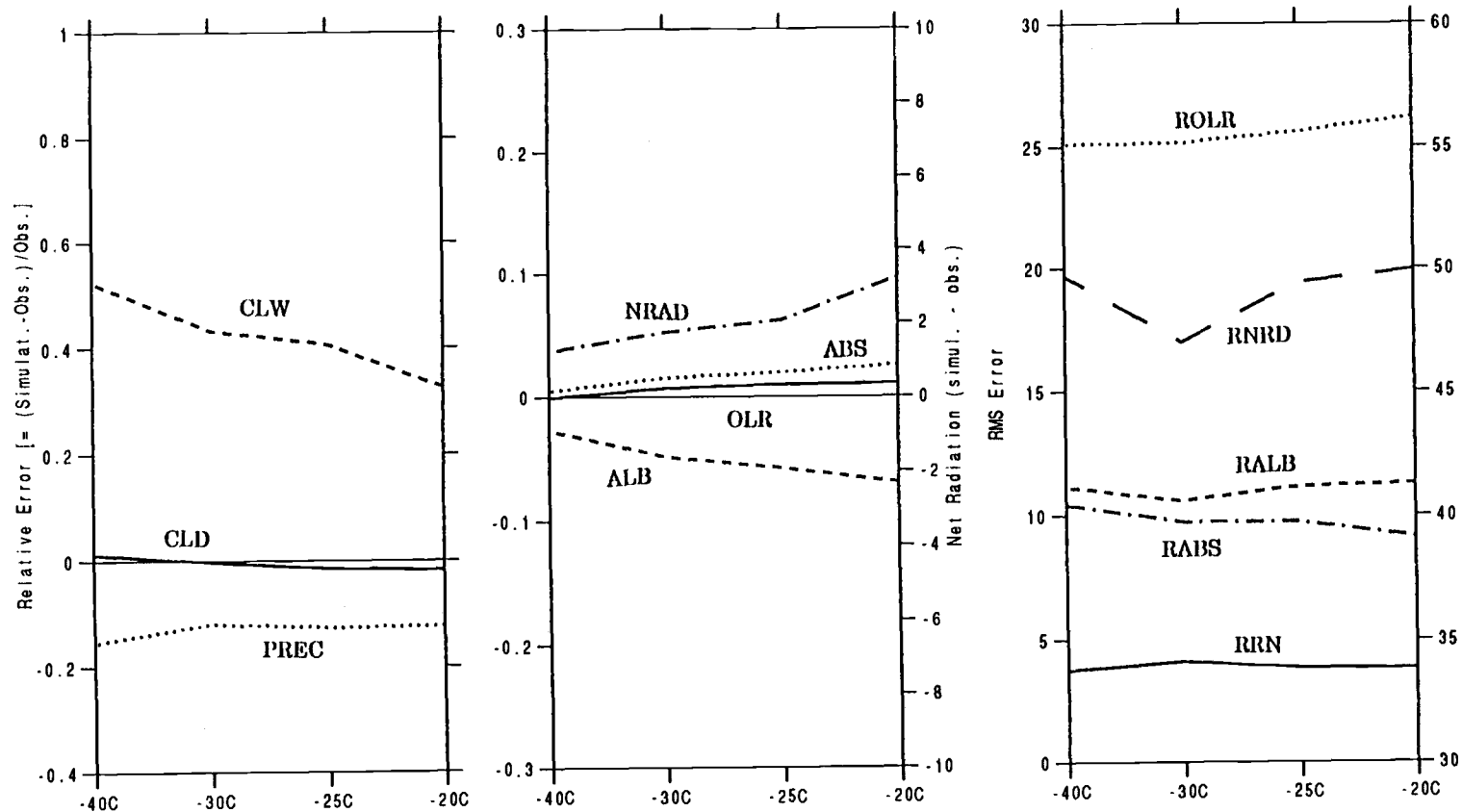
Fig. 5.13. The relative and rms errors of global-mean cloud and radiation quantities versus the values of T_i in the antecedent-control and test simulations for perpetual July.
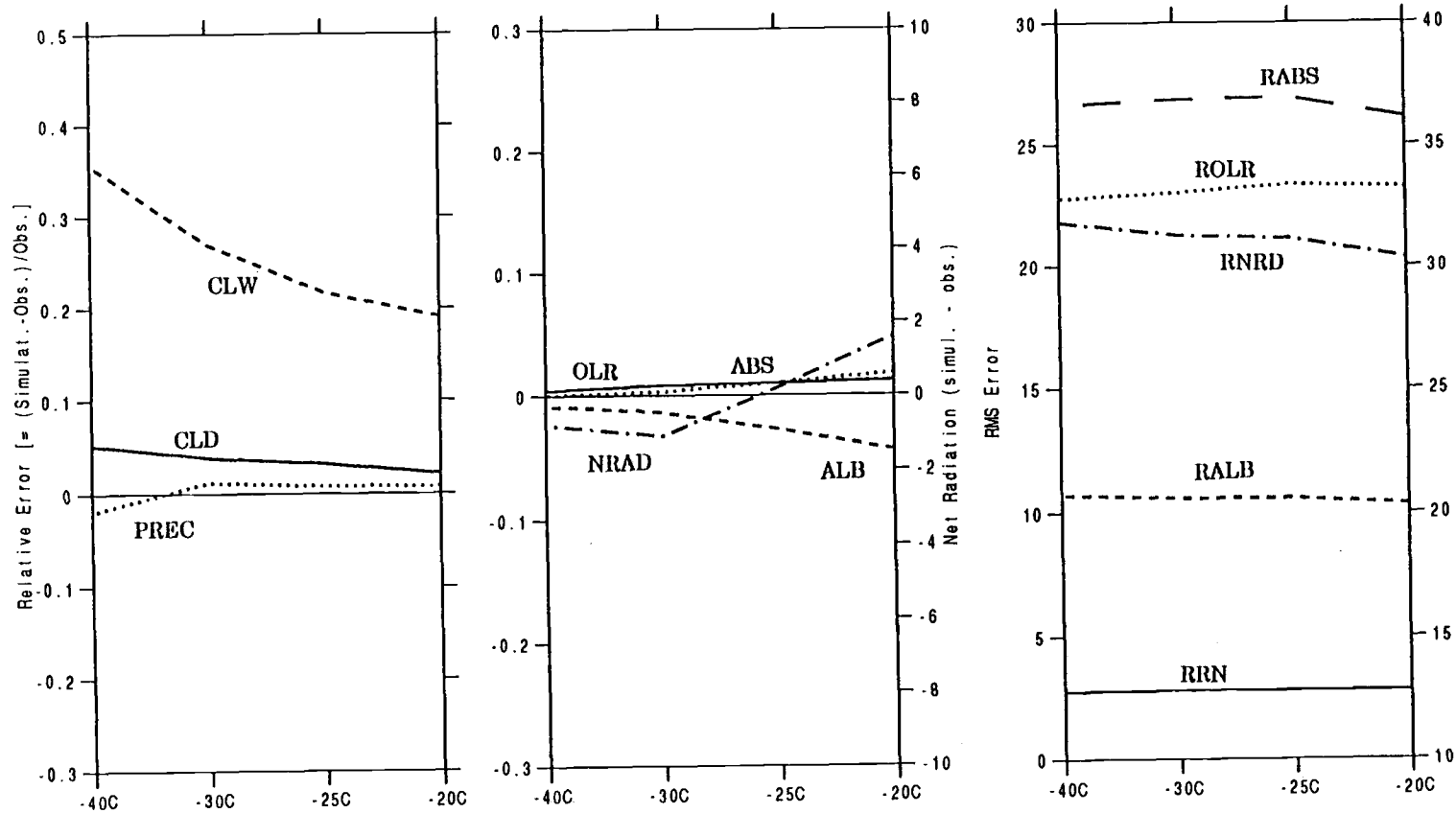
Fig. 5.14. As in Fig. 5.13, except for perpetual January.
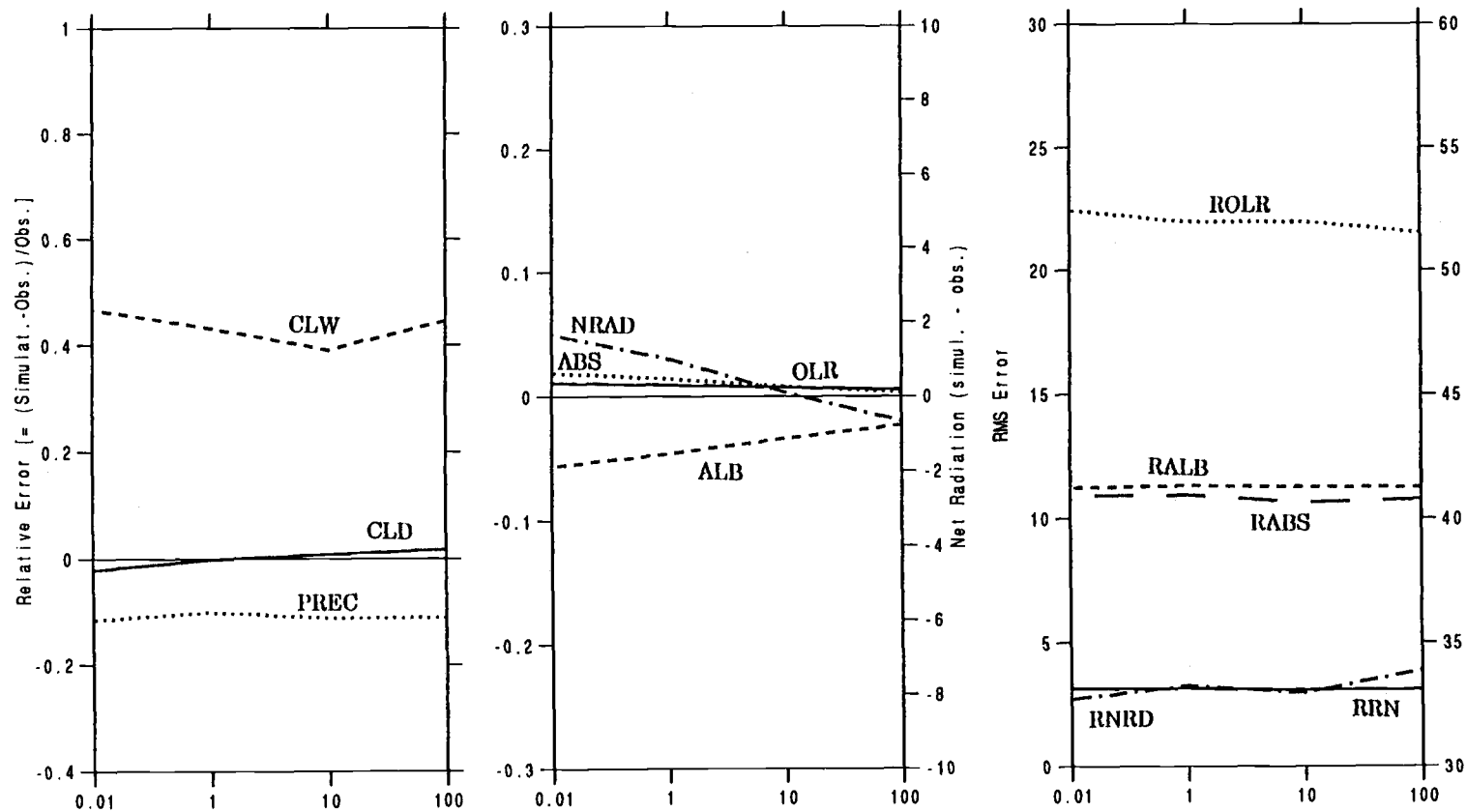
Fig. 5.15. The relative and rms errors of global-mean cloud and radiation quantities versus the values of α in the antecedent-control and test simulations for perpetual July.
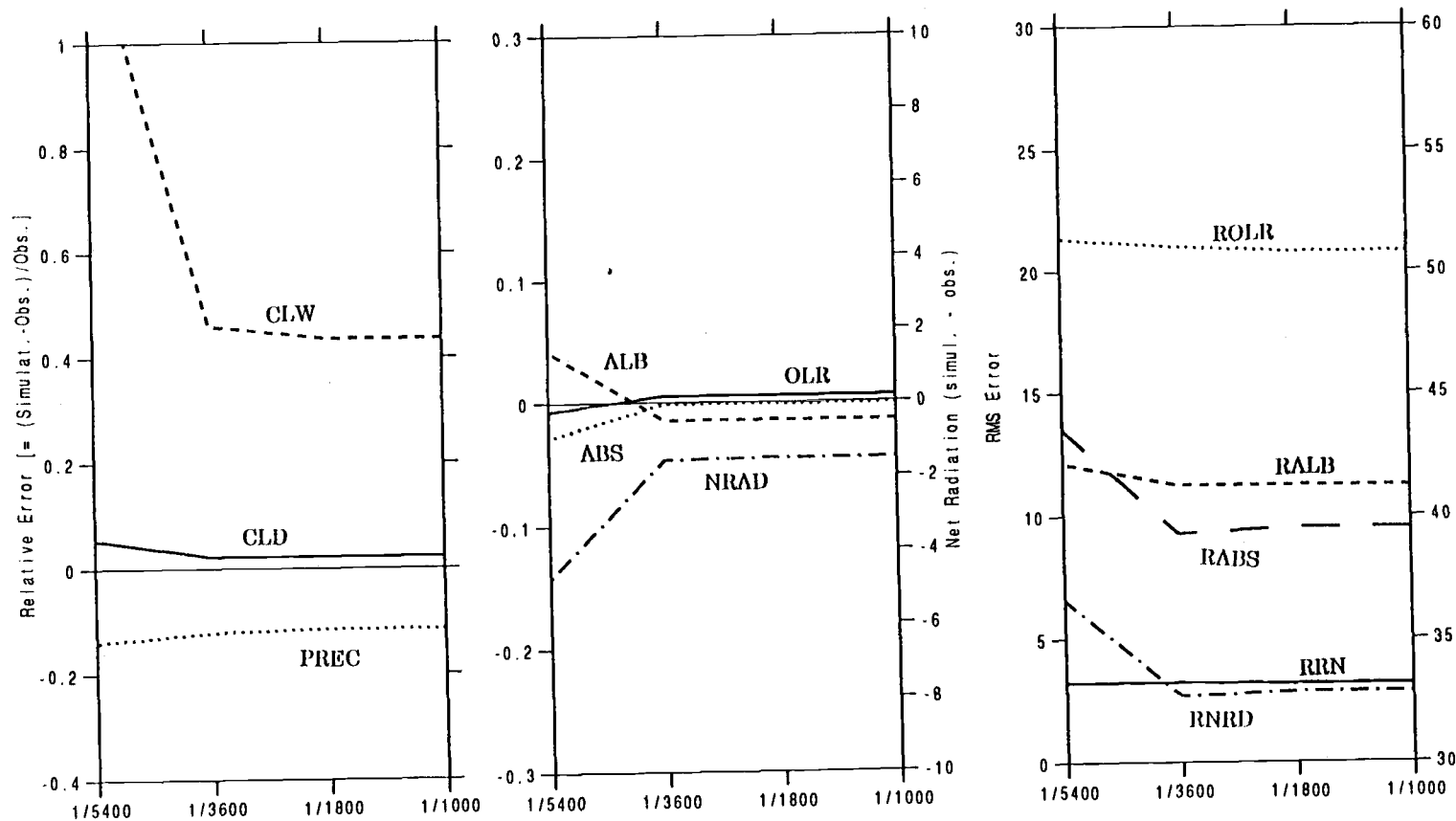
Fig. 5.16. The relative and rms errors of global-mean cloud and radiation quantities versus the values of a in the antecedent-control and test simulations for perpetual July.

water clouds, $m_{c,w}$. The perpetual-July control simulation used $m_{c,w} = 10^{-4}$ g/g, as suggested by Rutledge and Schlesinger (1985), and the test simulations used values of $m_{c,w}$ equal to 0.5x, 2x, and 5x the control-run value. Based on the results presented in Fig. 5.17 $m_{c,w} = 10^{-4}$ g/g was selected as the "best" value of the precipitation threshold for stratiform water clouds.

h. *Precipitation threshold for stratiform ice clouds, $m_{c,i}$*

The eighth and final parameter was the precipitation threshold for stratiform ice clouds, $m_{c,i}$. The perpetual-July and perpetual-January control simulation used 100% of the values $I_c(T_c)$, calculated from the data of Heymsfield and Platt (1984) as a function of temperature (see section 3.1.2), and the test simulations used 90%, 80%, and 70% of the control-run values. Based on the results presented in Figs. 5.18 and 5.19 the selected "best" value of the precipitation threshold for stratiform ice clouds, $m_{c,i}(T)$, was 70% of the control value.

5.3.3. Final parameter selection

Once the parameter values for C_0, U_{00}, τ, T_i, α, a, $m_{c,w}$ and $m_{c,i}$ were selected, the perpetual-July and perpetual-January control simulations were conducted for 20 day periods. The zonal-mean results of these simulations are presented in Figs. 5.20 and 5.21 for planetary albedo (ALB), outgoing longwave radiation (OLR) and net radiation at the top of the atmosphere (NRAD). The corresponding zonal means of the observations which we used in the initial parameter selection procedure, namely, the observations from the NFOV sensor on the NIMBUS-7 satellite (Kyle *et al.*, 1985), are also presented in Figs. 5.20 and 5.21. These figures show that the simulated ALB is in reasonable agreement with these observations. However a not-yet-published analysis by Kyle *et al.* (1989) shows that the NIMBUS-7/NFOV ALB values of Kyle *et al.* (1985) are about 3 - 4% larger than the ALB values based on the NOAA-9/ERBS WFOV and scanner data, and larger than the NIMBUS-7/WFOV data reanalyzed by Kyle *et al.* (1989)
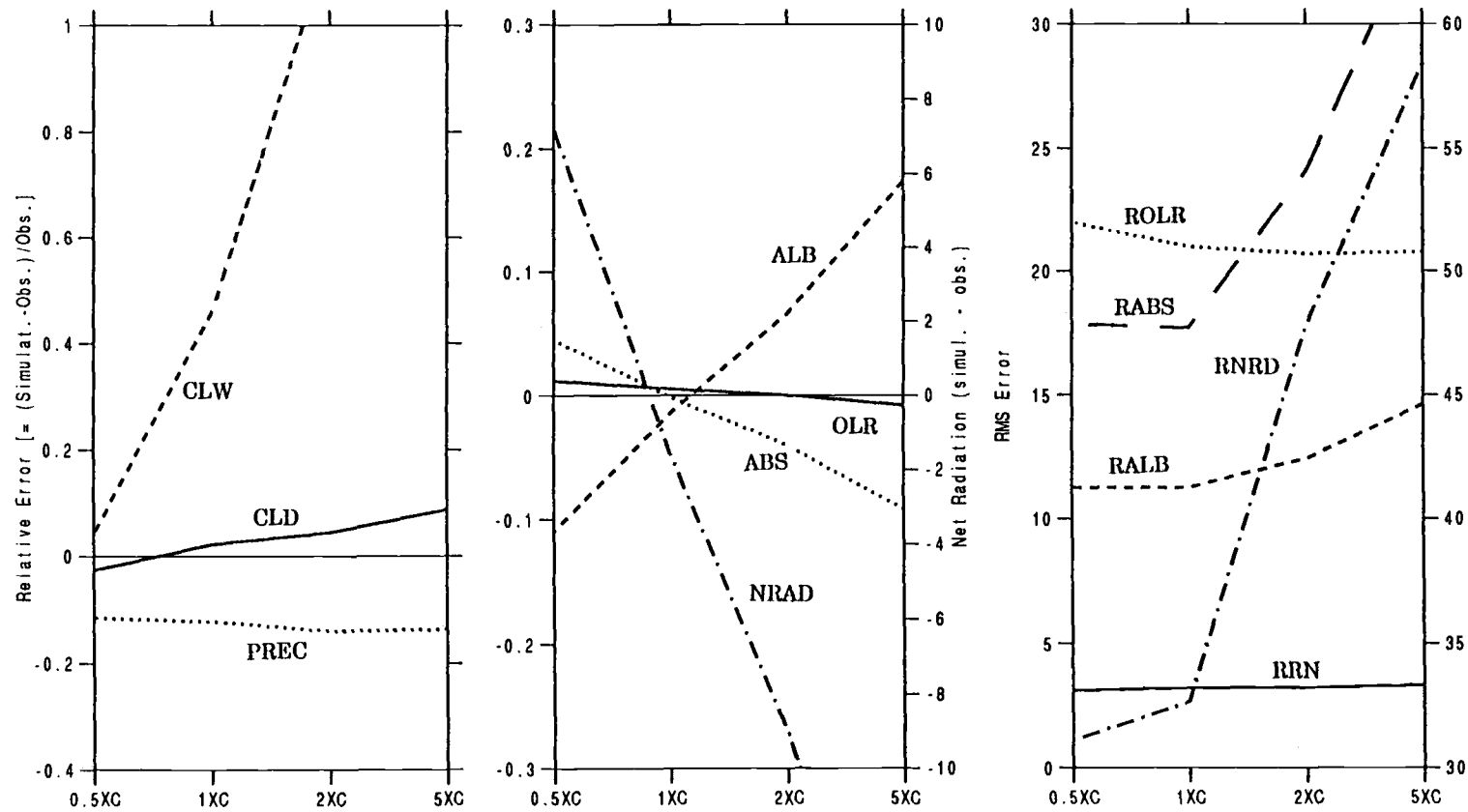
Fig. 5.17. The relative and rms errors of global-mean cloud and radiation quantities versus the values of $m_{c,w}$ in the antecedent-control and test simulations for perpetual July.
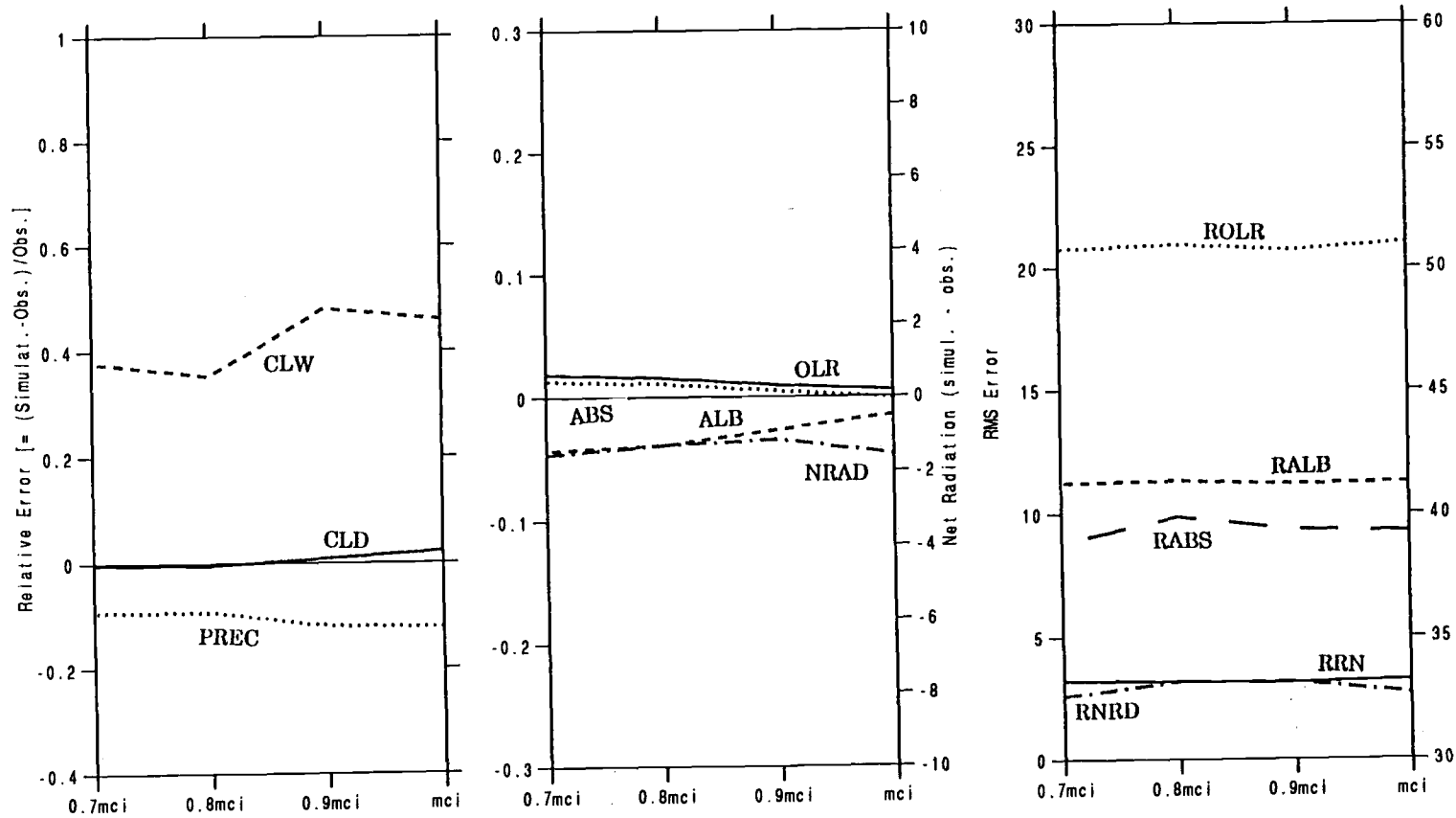
Fig. 5.18. The relative and rms errors of global-mean cloud and radiation quantities versus the values of $m_{c,i}$ in the antecedent-control and test simulations for perpetual July.
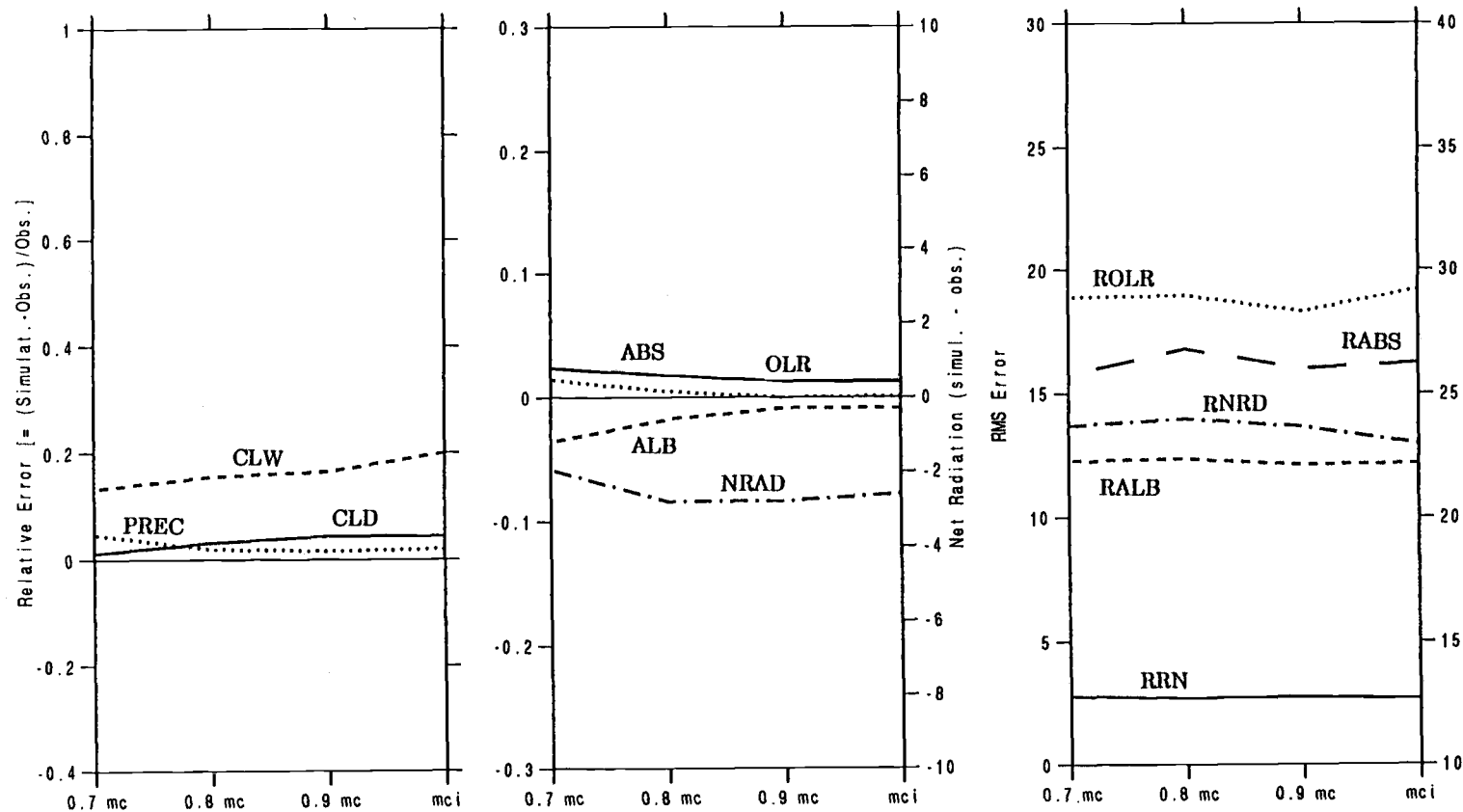
Fig. 5.19. As in Fig. 5.18, except for perpetual January.
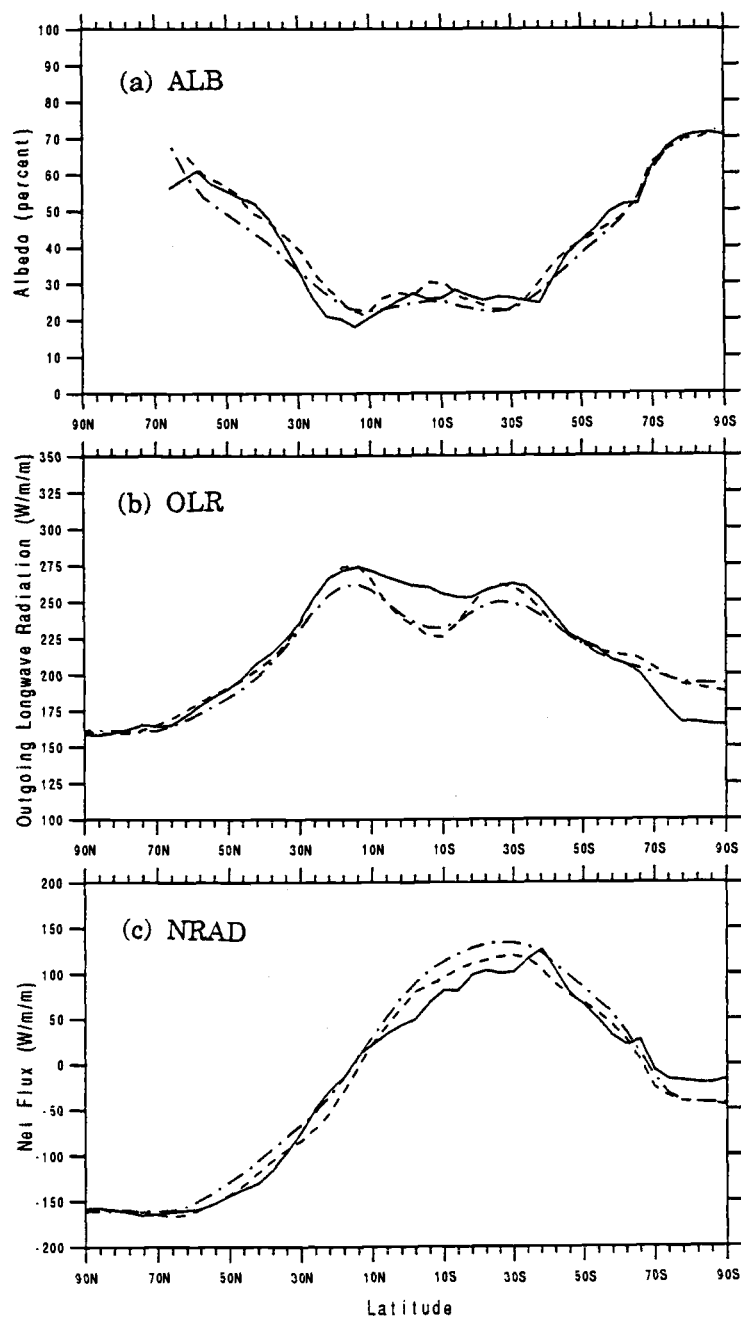
Fig. 5.20. Latitudinal distributions of the simulated (solid line) and observed (dashed line) zonal-mean ALB, OLR and NRAD for January. The observed data are from the NIMBUS-7 NFOV sensor (Kyle *et al.*, 1985). Observations from the NIMBUS-7 WFOV sensor (dashed-dotted line) are also presented from Kyle *et al.* (1985).
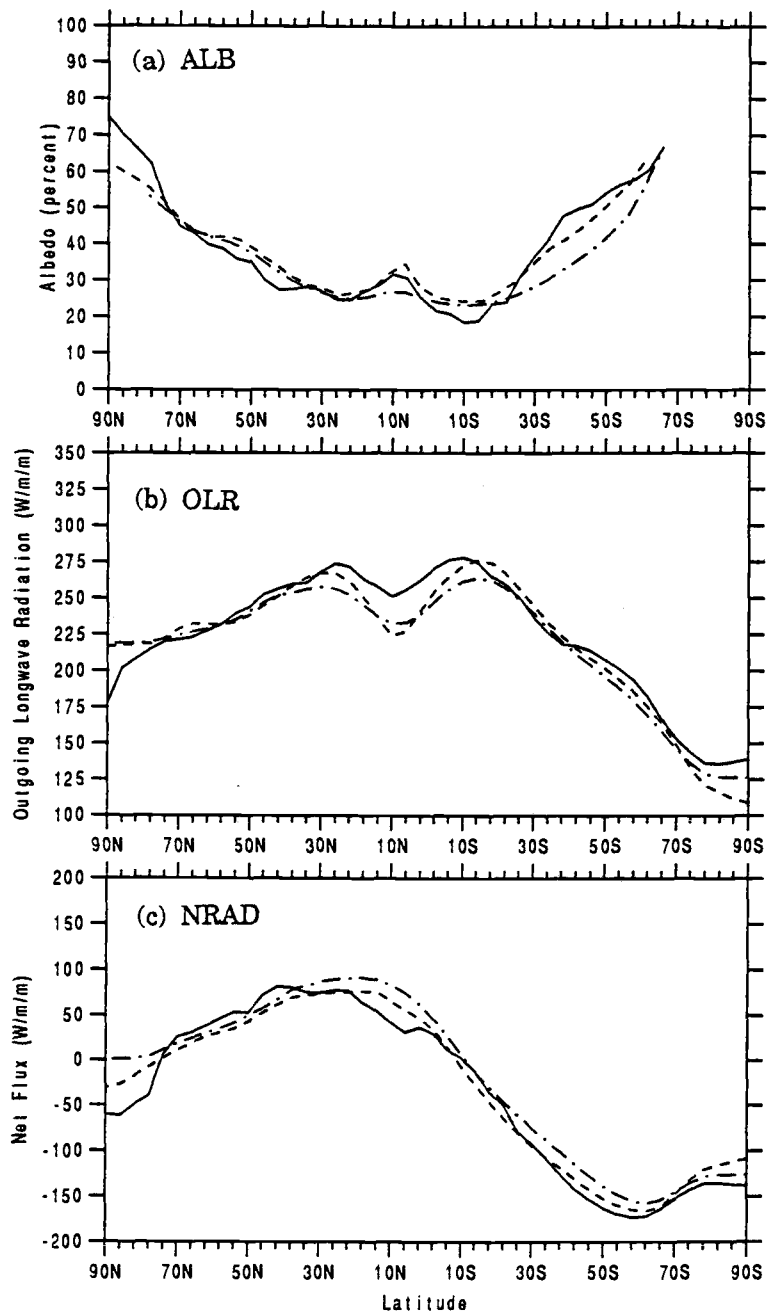
Fig. 5.21. As in Fig. 5.20, except for July.

(see Table 6.2). Consequently, the good agreement of our simulated ALB with the original NIMBUS-7/NFOV ALB values means that the simulated values are too large. Furthermore, Figs. 5.20 and 5.21 show that the tropical OLR minimum simulated by the model in January and July is not as deep as that observed by the NIMBUS-7/NFOV longwave radiation sensor. For these two reasons, it was determined that the cloud-radiation parameterization could be improved by performing a second, final set of parameter selection tests. Five parameters were chosen for these tests, two of which were already obtained in the initial selection procedure, and three of which were not. The parameters tested are listed in Table 5.4 in the order of testing, and the "best" values are shown in bold faced type. The procedure for obtaining these "best" values was similar to that used in the initial selection procedure. A brief description of each of the five parameter tests is given below.

a. *Mass absorption coefficient for the emissivity of ice clouds, $a_0^{\uparrow,\downarrow}$*

Because the emitting temperature of clouds is generally less than the emitting temperature of the surface, the excessive OLR simulated in the tropics can be reduced by increasing the emissivity of the clouds in the tropics. Because the highest clouds in the tropics are often sufficiently cold to be ice clouds, the emissivity of tropical ice clouds was considered. In the radiation parameterization the emissivity of ice clouds is given by

$$\varepsilon_\ell^{\uparrow,\downarrow} = 1 - \exp\left(-a_0^{\uparrow,\downarrow} W_\ell\right), \tag{5.6}$$

where $a_0^{\uparrow,\downarrow}$ is the mass absorption coefficient for the upward and downward longwave radiation and W is the ice-water path. In the initial formulation of the radiation parameterization, the mass absorption coefficients of Starr and Cox (1985) were adopted for all ice clouds, regardless of their latitude. These coefficients were 0.05 $g^{-1}m^2$ for the upward longwave radiation and 0.06 $g^{-1}m^2$ for the downward longwave radiation. However, Griffith *et al.* (1980) reported mass absorption coefficients for tropical ice clouds of 0.076 - 0.096 $g^{-1}m^2$, with 0.084 $g^{-1}m^2$ as the mean value. Because these values are

Table 5.4. Final selection of the parameters of the cloud parameterization.

Parameters	Equation	Initial value	Tested values			Reference for Initial value
Mass absorption coefficient ($a_0^{\uparrow,\downarrow}$) of cumuloform ice clouds	$\varepsilon^{\uparrow,\downarrow} =$ $1 - \exp(-a_0^{\uparrow,\downarrow} W)$	$a_0^{\uparrow} = 0.05$ $a_0^{\downarrow} = 0.06$	0.076	0.084	**0.096**	Starr and Cox (1985) Griffith *et al.* (1980)
Autoconversion rate of convective precipitation, C_0, m^{-1}	$P = C_0 M m \Delta z$	0.008	**0.002**	0.004	0.006	Table 5
Threshold value for stratiform precipitation, m_c, g/g	$P = a (m - b m_{c,w})$	10^{-4} for $T \geq 0°C$	**0.5×10^{-4}**	0.6×10^{-4}	0.8×10^{-4}	Table 5
	$P = a (m - b m_{c,i})$	$0.7 \times I_c$ for $T \leq T_i$ interpolated value $T_i < T < 0°C$	$0.6 \times I_c$	$0.5 \times I_c$	**$0.4 \times I_c$**	Table 5

Table 5.4. Final selection of the parameters of the cloud parameterization (continued).

Parameters	Equation	Initial value	Tested values			Reference for Initial value
Threshold value for stratiform precipitation for stratiform cloud formed from antecedent cumuloform clouds, $m_{c,i}$, g/g	$P = a\,(m - b\,m_{c,i})$	$0.7 \text{x} I_c$ for $T \le T_i$ interpolated value for $T_i < T < 0^{\circ}C$	$0.8 \text{x} I_c$	$1 \text{x} I_c$	**1.2xI$_c$**	Table 5
Multiple–scattering asymmetry factor for cumuloform clouds, g		0.60	**0.85**			Cess *et al.* (1985) Stephens (1984)

larger than those of Starr and Cox (1985), they would result in larger emissivity. Therefore, the effect of increasing the mass absorption coefficients for tropical ice clouds was tested, while retaining the Starr and Cox (1985) mass absorption coefficients for non-tropical ice clouds. To distinguish tropical ice clouds from non-tropical ice clouds, a latitudinal domain could have been prescribed for each. However, based on the latitude-altitude distribution of zonal-mean cloudiness simulated by the model (Fig. 5.22), it was determined that tropical ice clouds should be defined as cumuloform clouds when located above 500 mb, and non-tropical ice clouds should be defined as all other clouds.

For this parameter selection, the perpetual-July control simulation used $a_0^\uparrow = 0.05$ and $a_0^\downarrow = 0.06$ and the test simulations used values of $a_0^{\uparrow,\downarrow} = 0.076$, 0.084, and 0.096. The results of the AGCM simulations are presented in Fig. 5.23. Based on this figure, the "best" value of the mass absorption coefficient for tropical ice clouds was taken to be 0.096 $g^{-1}m^2$.

A new 20-day perpetual-July control simulation was then performed with this "best" value of $a_0^{\uparrow,\downarrow}$. As shown by comparing the upper panel of Fig. 5.24 (dotted line) with the middle panel of Fig. 5.21 (solid line), the increase in the mass absorption coefficient for "tropical" ice clouds has deepened the simulated OLR minimum, but not sufficiently to improve significantly the comparison with the observations.

b. *Autoconversion rate for convective precipitation, C_0*

Another way to increase the emissivity of tropical ice clouds of the model is by increasing their ice-water content. This can be accomplished by reducing the autoconversion rate for convective precipitation so that the clouds can hold more ice. Therefore, to improve the simulated tropical OLR test simulations with C_0 reduced to the values shown in Table 5.4 were performed. The results for $C_0 = 0.002$ are shown in Fig. 5.24 in terms of the zonal-mean OLR, fractional cloud cover, and cloud water content. This figure shows a significant reduction in the tropical OLR for $C_0 = 0.002$, and accordingly this was adopted as the "best" value. However, with this "best" value the simulated cloud water increased such that it is in worse
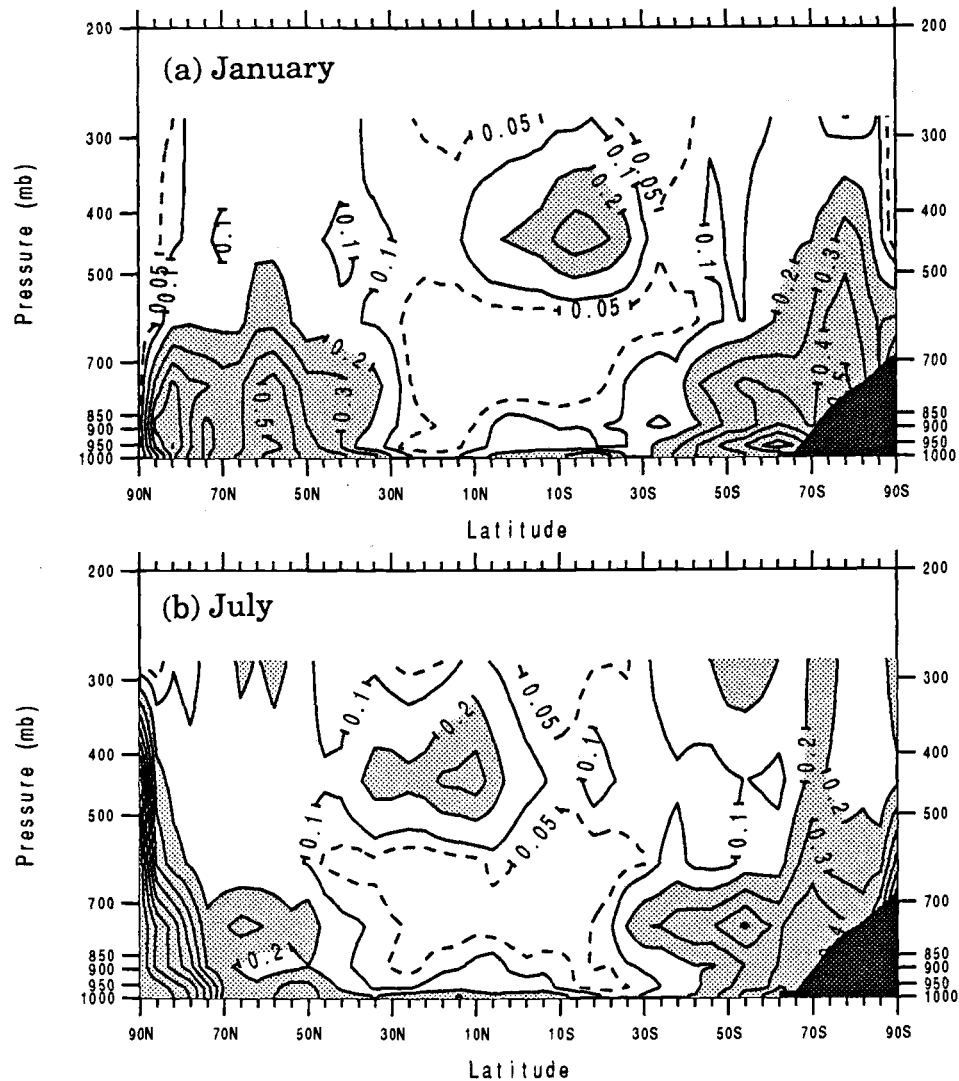
Fig. 5.22. Latitude-altitude distributions of the zonal-mean fractional cloud cover simulated for January and July. The contour interval is 0.1, with the 0.05 contour shown by the dashed line. Values larger than 0.2 are shown shaded.
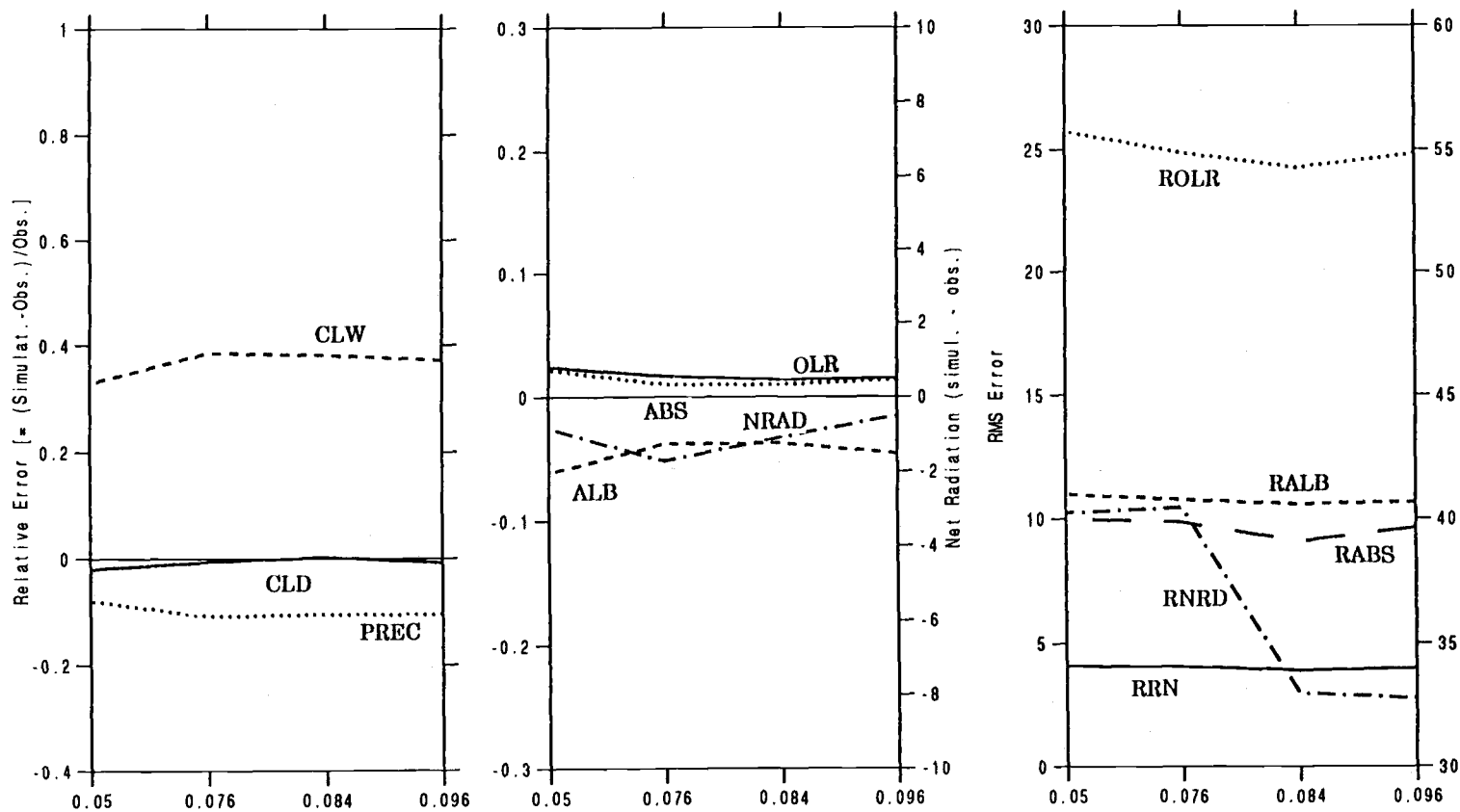
Fig. 5.23. The relative and rms errors of global-mean cloud and radiation quantities versus the values of $a_0^{\uparrow,\downarrow}$ in the antecedent-control and test simulations for perpetual July.
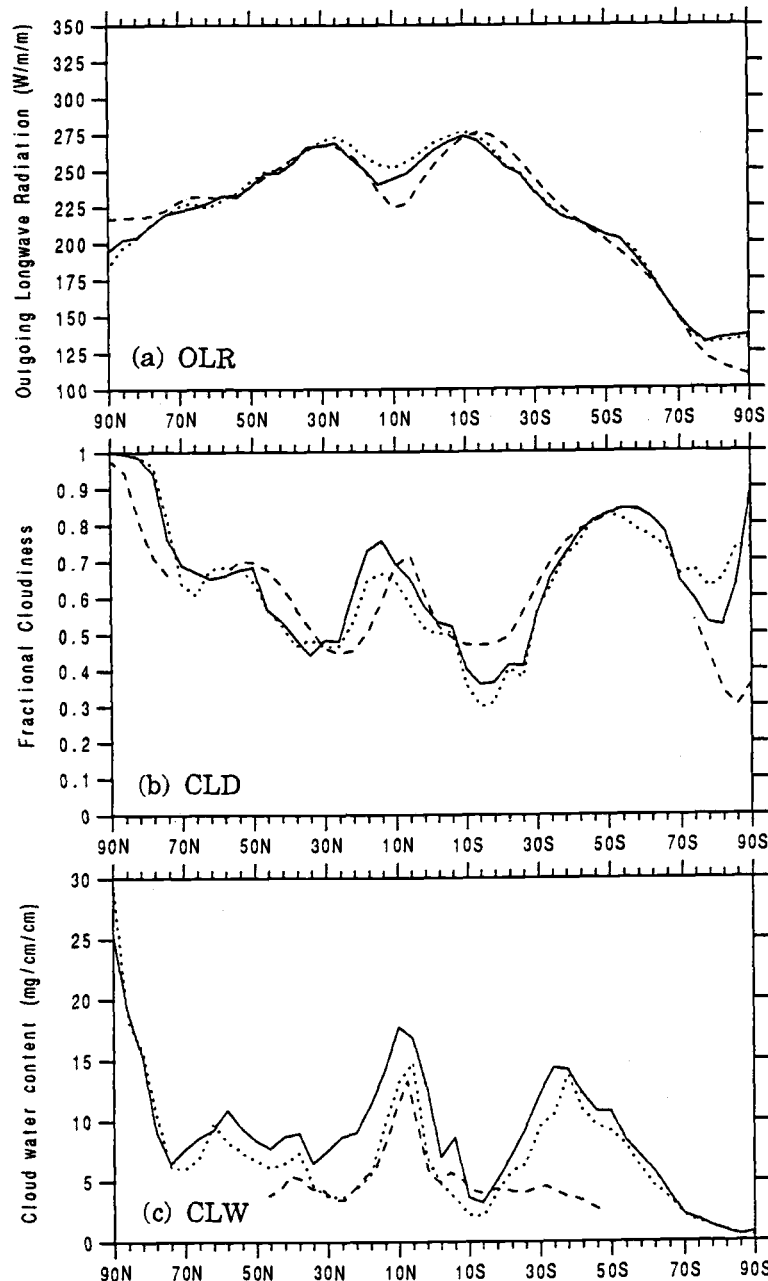
Fig. 5.24. Latitudinal distributions of the simulated (solid line) and observed (dashed line) OLR, cloud cover and cloud water for July. The simulated data were obtained with the "best" value for $C_0 = 0.002$. The dotted line represents the antecedent simulation with $C_0 = 0.008$. The observed data are from Kyle *et al.* 1985) for the OLR from NIMBUS-7 NFOV, Schlesinger *et al.* (1989) for the cloud cover, and Njoku and Swanson (1983) for the cloud water.

agreement with the observations than for $C_0 = 0.008$, particularly in the tropics. However, the increase in the tropical cloud water was an expected consequence of reducing C_0 and is the "trade-off" for obtaining the decrease in the tropical OLR minimum.

c. *Precipitation threshold for stratiform water clouds, $m_{c,w}$*

Decreasing the "best" value of C_0 from 0.008 to 0.002 also caused an increase in the cloud water in the mid-latitudes such that it too is in worse agreement with the observations than for $C_0 = 0.008$ (Fig. 5.24c). To reduce this excessive cloud water, the effects of decreasing the precipitation threshold for stratiform water clouds were tested using the values shown in Table 5.4. It was found that the cloud water was reduced in most latitudes for $m_{c,w} = 0.5 \times 10^{-4}$ g/g (Fig. 5.25c). Accordingly, this value was chosen as the "best" value for $m_{c,w}$.

d. *Precipitation threshold for stratiform ice clouds, $m_{c,i}$*

The new perpetual-July control with the revised "best" value of $m_{c,w}$ shows that the simulated cloudiness is still considerably larger than the observed cloudiness in high latitudes (Fig. 5.25b). To reduce this high-latitude cloudiness we tested the effects of reducing the precipitation threshold for ice clouds, $m_{c,i}$, using the values shown in Table 5.4. It was found that the largest decrease in high-latitude cloudiness was obtained for $m_{c,i} = 0.4 I_c$. However, a side effect of this change was an increase in the tropical OLR minimum. To remove this unwanted result, the precipitation threshold for those stratiform clouds formed from antecedent cumuloform clouds was selectively increased (Table 5.4). In particular, $m_{c,i} = 1.2 I_c$ was chosen for such stratiform clouds. Figure 5.26 shows that the effect on the high-latitude cloudiness of these changes in $m_{c,i}$ was minimal; however, there were small beneficial decreases in the tropical OLR minimum and in the mid-latitude cloud water.
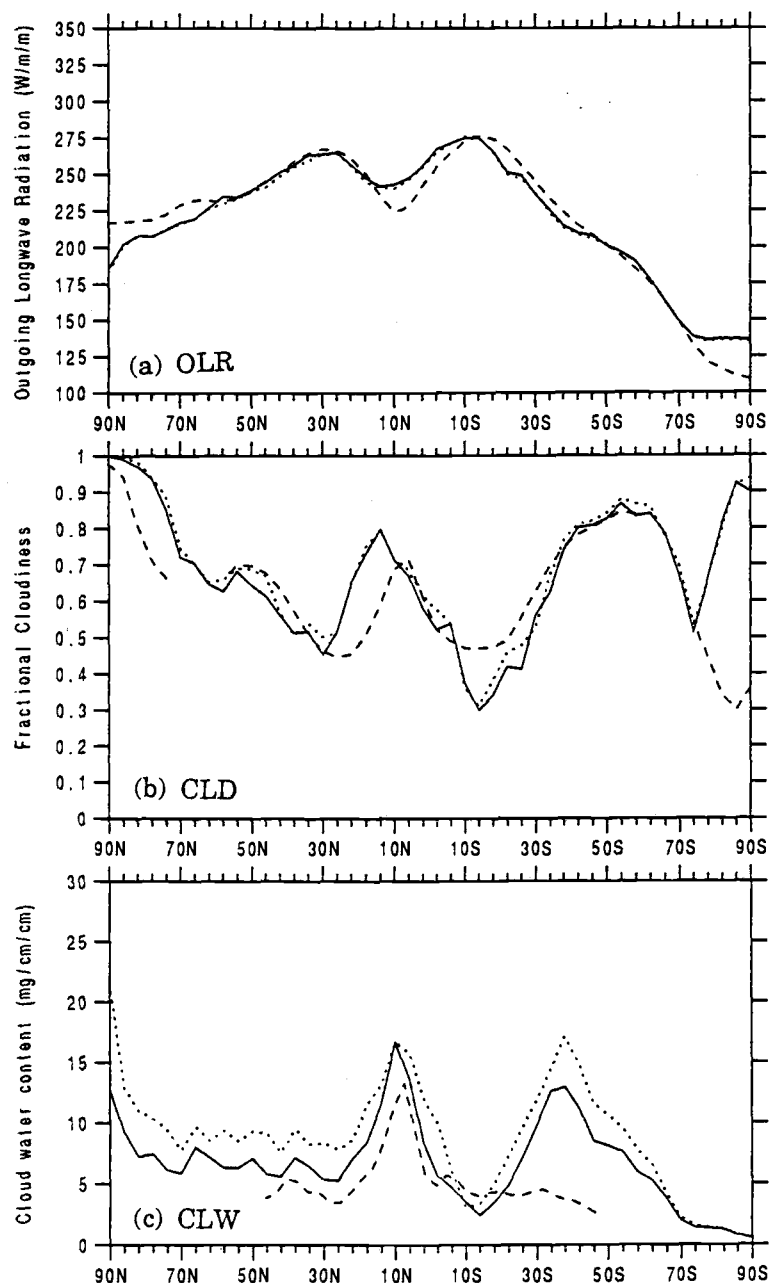
Fig. 5.25. As in Fig. 5.24, except the simulated data were obtained with the "best" value for $m_{c,w} = 0.5 \times 10^{-4}$ g/g. The dotted line represents the antecedent simulation with $m_{c,w} = 10^{-4}$ g/g.
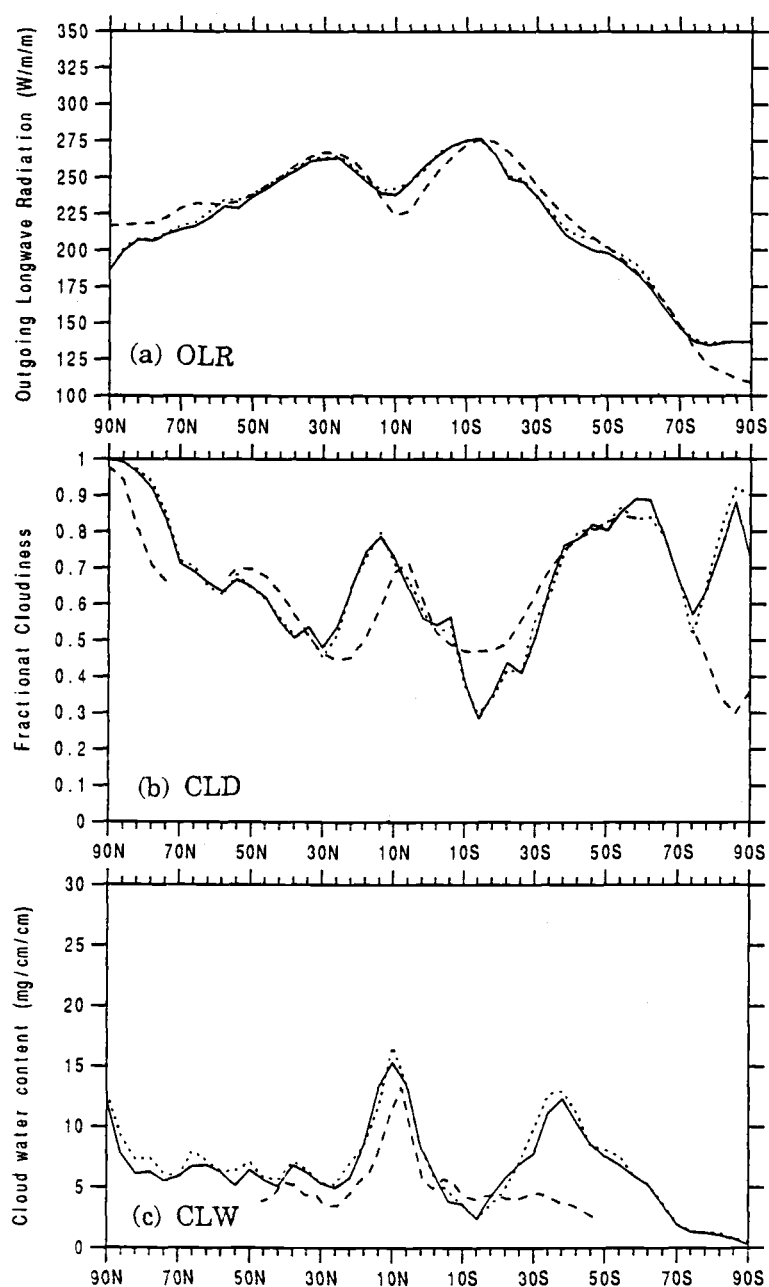
Fig. 5.26. As in Fig. 5.24, except the simulated data were obtained with the "best" value for $m_{c,i} = 0.4xI_c$ for stratiform clouds and $1.2xI_c$ for former cumuloform clouds   The dotted line represents the simulation of control run with the value for $m_{c,i} = 0.7xI_c$.

e. *Multiple-scattering asymmetry factor for cumuloform clouds*

When the final parameter selection process for the improvement of the OLR simulation, a parameter modification to bring the simulated ALB into better agreement with the most recent observations (Kyle *et al.*, 1989) described above was considered. In the radiation parameterization used in the initial parameter selection procedure, the multiple-scattering asymmetry factor was taken to be 0.6 for all clouds, this following Cess *et al.* (1985). However, Stephens (1984) reported that the asymmetry factor for cumuloform clouds is about 0.85. Accordingly, the asymmetry factor was increased from 0.6 to 0.85 for cumuloform clouds. The result of this revision was to decrease the simulated planetary albedo for both January and July by about 2% (Fig. 5.27) and thus bring it into better agreement with the values of Kyle *et al.* (1989).
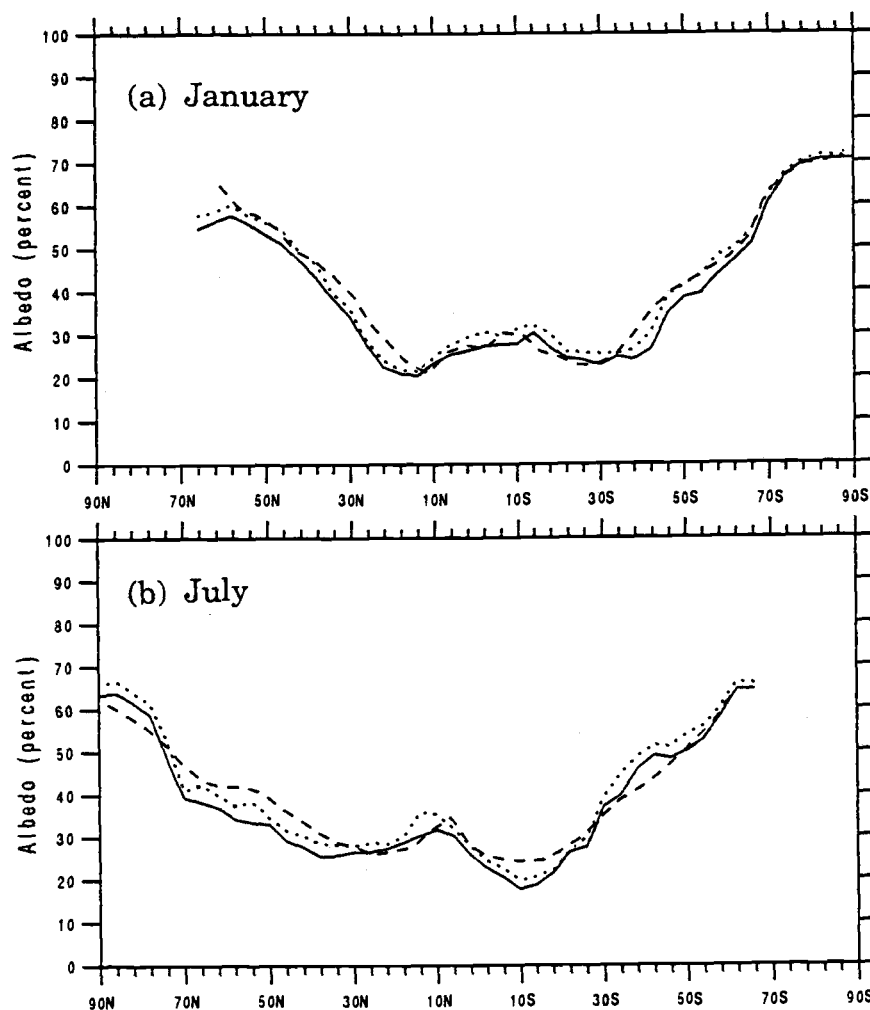
Fig. 5.27. Latitudinal distributions of the simulated (solid line) and observed (dashed line) ALB for January and July. The simulated data were obtained with the "best" value for asymmetry factor of 0.85. The dotted line represents the simulation of control run with the value for asymmetry factor of 0.6. The observed data are NIMBUS-7 NFOV from Kyle *et al.* (1985).

6. EVALUATION OF THE CLOUD-RADIATION PARAMETERIZATION

With the parameters selected by the final selection procedure described in Chapter 5, current simulations for January and July were compared with the corresponding observations to evaluate the performance of the cloud-radiation parameterization. In the following two subsections, results from the last perpetual-January and perpetual-July control simulations of the final selection procedure are presented for the characteristics of the clouds and precipitation, and for the components of the earth's radiation budget at the top of the atmosphere. Furthermore, compared to the performance of old cloud-radiation parameterization (Schlesinger and Oh, 1987) the improvement of new cloud-radiation parameterization is discussed in section 6.3.

6.1. Cloud Characteristics and Precipitation

The global-mean fractional cloud covers simulated for January and July by the AGCM with the new cloud-radiation parameterization are presented in Table 6.1, accompanied by corresponding values from an analysis of the ISCCP observations (Schlesinger *et al.*, 1989). Two values of the ISCCP data are presented, a VIS-IR value based on both visible and infrared observations, and an IR-only value based only on infrared observations. Both of these ISCCP values are not true global means due to the absence of satellite observations in the polar regions and over a sector centered at about 70°E longitude (see Fig. 6.2), the latter due to the absence of *INSAT* satellite data from the ISCCP archive (Schlesinger *et al.*, 1989). Also, the analysis of the ISCCP data by Schlesinger *et al.* (1989) set minimum bounds on the number of observations per month for a monthly mean to be calculated. This restriction further reduced the geographical coverage of the observations. This notwithstanding, it is of interest to compare the simulated global means with the ISCCP "global means."

Table 6.1 shows that the simulated global-mean cloud cover is larger than both of the observed values, particularly for January.

Table 6.1. Global means of the total cloudiness (%).

	January	July
AGCM	64.4	61.8
ISCCP/VIS-IR	60.2	59.9
ISCCP/IR-only	58.4	56.8

The zonal-mean fractional cloudiness simulated by the AGCM is presented in Fig. 6.1, together with the zonal-mean cloud-top pressure and cloud-top temperature. The corresponding ISCCP observations (Schlesinger et al., 1989) are also presented in Fig. 6.1. Again, the ISCCP values are not true zonal means due to the absence of the satellite observations in several geographical regions as previously discussed. Nevertheless, it is useful to compare the simulated zonal means with the "zonal means" from the observations.

Figure 6.1 shows that the fractional cloudiness simulated by the model is in reasonable agreement with the ISCCP observations, except in the subtropics of the winter hemisphere where the model underestimates the cloud cover, and over Antarctica where the model overestimates the cloud cover, particularly during January. However, the January ISCCP data for Antarctica do not agree with the ground-based cloud observations there (Warren el al., 1986), which give a value of about 50% . Thus, it is likely that the model's overestimation of the Antarctic cloud cover in January is not as large as Fig. 6.1a indicates. It is also therefore likely that the model's overestimate of the January global-mean cloud cover is not as large as Table 6.1 indicates.

To give some perspective to the results from the present model, the results from the UCLA/GLA AGCM (Harshvardhan et al., 1989) are
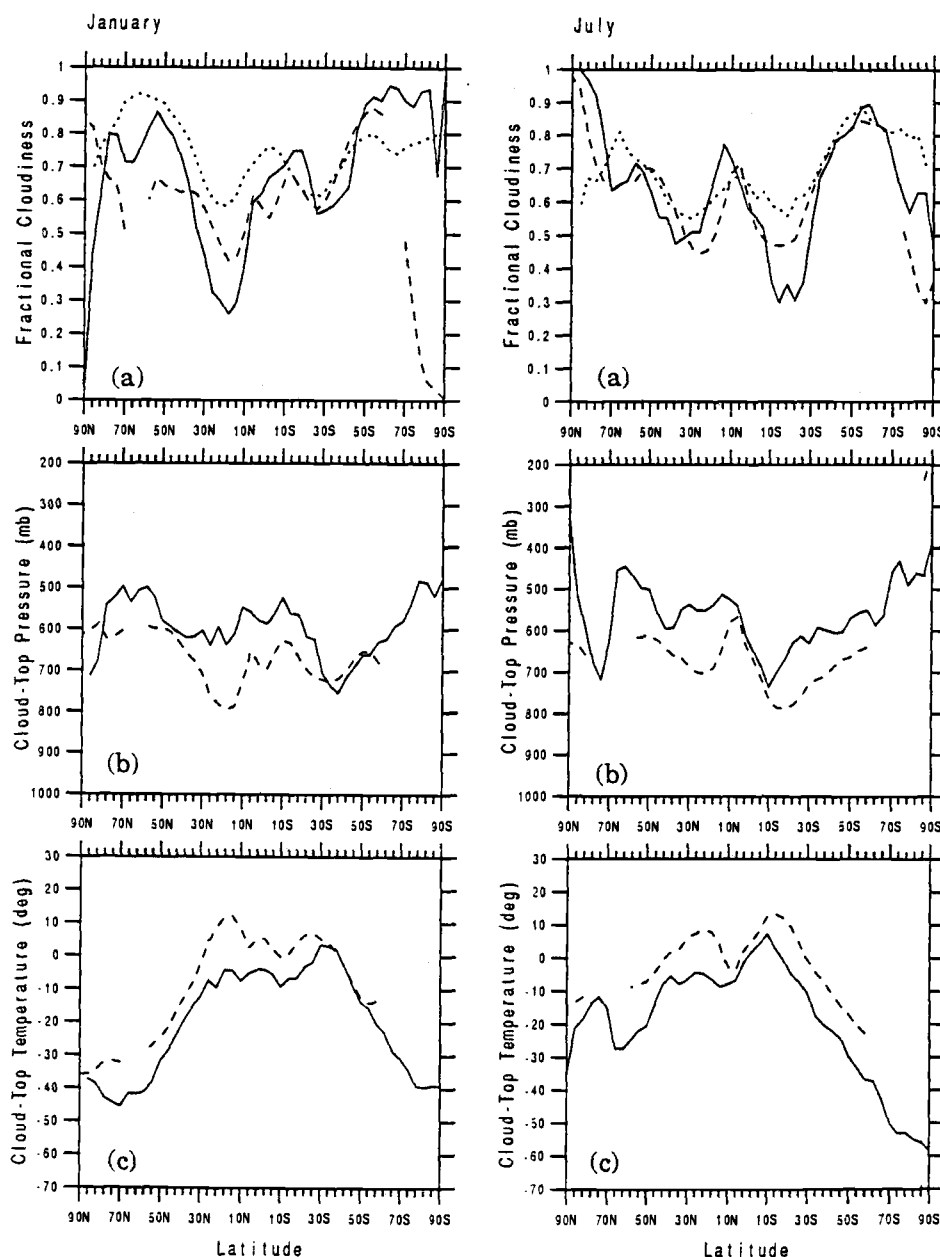
Fig. 6.1. Simulated and observed zonal-mean cloud characteristics for January and July: (a) fractional cloud cover, (b) cloud-top pressure, and (c) cloud-top temperature. The results simulated by the AGCM with the new cloud-radiation parameterization are shown by the solid line. The ISCCP observations from Schlesinger *et al.* (1989) are shown by the dashed line. The results simulated by the UCLA/GLA AGCM (Harshvardhan *et al.*, 1989) are shown by the dotted line.

presented in Fig. 6.1a. These results show that the UCLA/GLA AGCM overestimated the fractional cloudiness for January and July virtually everywhere.

Figure 6.1b shows that the cloud-top pressures simulated by the OSU multilayer AGCM with the new cloud-radiation parameterization are generally lower than the ISCCP cloud-top pressures for January and July, particularly in the subtropics. Correspondingly, Fig. 6.1c shows that the cloud-top temperatures simulated by the AGCM are colder than the ISCCP cloud-top temperatures, again particularly in the subtropics. These results, in conjunction with the underestimated subtropical cloud cover evident in Fig. 6.1a, indicate that the cloud parameterization has underestimated the stratocumulus clouds which occur at low elevations in the subtropics.

The geographical distributions of the fractional cloudiness simulated for January and July are presented, respectively, in Figs. 6.2 and 6.3, together with the observed ISCCP cloudiness (Schlesinger et al., 1989) and the difference between the simulated and observed fractional cloud cover. Figure 6.2 shows that the model has simulated reasonably well the observed cloudiness minima over the major desert areas and over the subtropical Pacific, the cloudiness maxima over the North Pacific and North Atlantic, and the band of maximum cloudiness centered near 60°S. The model, however, overestimates the January cloud cover where the observations display minima, namely, near 10°S in the Atlantic and Pacific oceans, over Central America, and over the Pacific Northwest region of North America. The model also fails to simulate the cloudiness maxima observed in the subtropics off the west coasts of North America and Africa, and underestimates the cloudiness over the maritime continent and over the western Pacific Ocean. Figure 6.3 shows that the model has also simulated reasonably well the observed July cloudiness minima over the major desert areas, at least in the southern hemisphere, the cloudiness maxima over the North Pacific and North Atlantic, and the band of maximum cloudiness centered near 60°S. However, the model also overestimates the July cloud cover where the observations display minima, namely, in the subtropics over the South Atlantic and the North and South Pacific oceans, over the southern part of South America, and over the
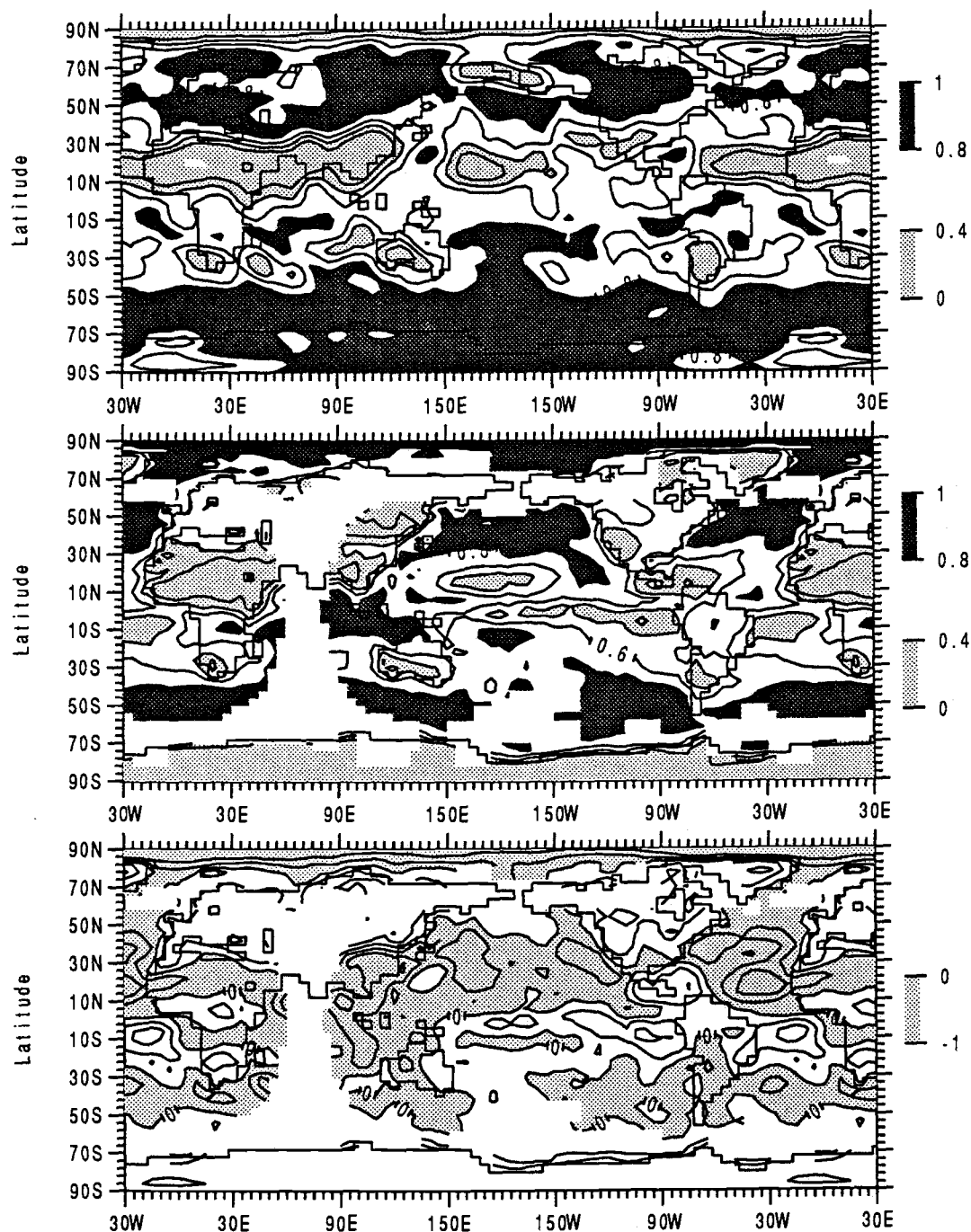
Fig. 6.2. Geographical distributions of the simulated (top panel), observed (middle panel), and simulated-minus-observed (bottom panel) fractional cloud cover for January. The distribution in each panel has been smoothed with a 9-point filter. The observed cloud cover is that from the analysis of the ISCCP data by Schlesinger *et al.* (1989). The contour interval is 0.2.
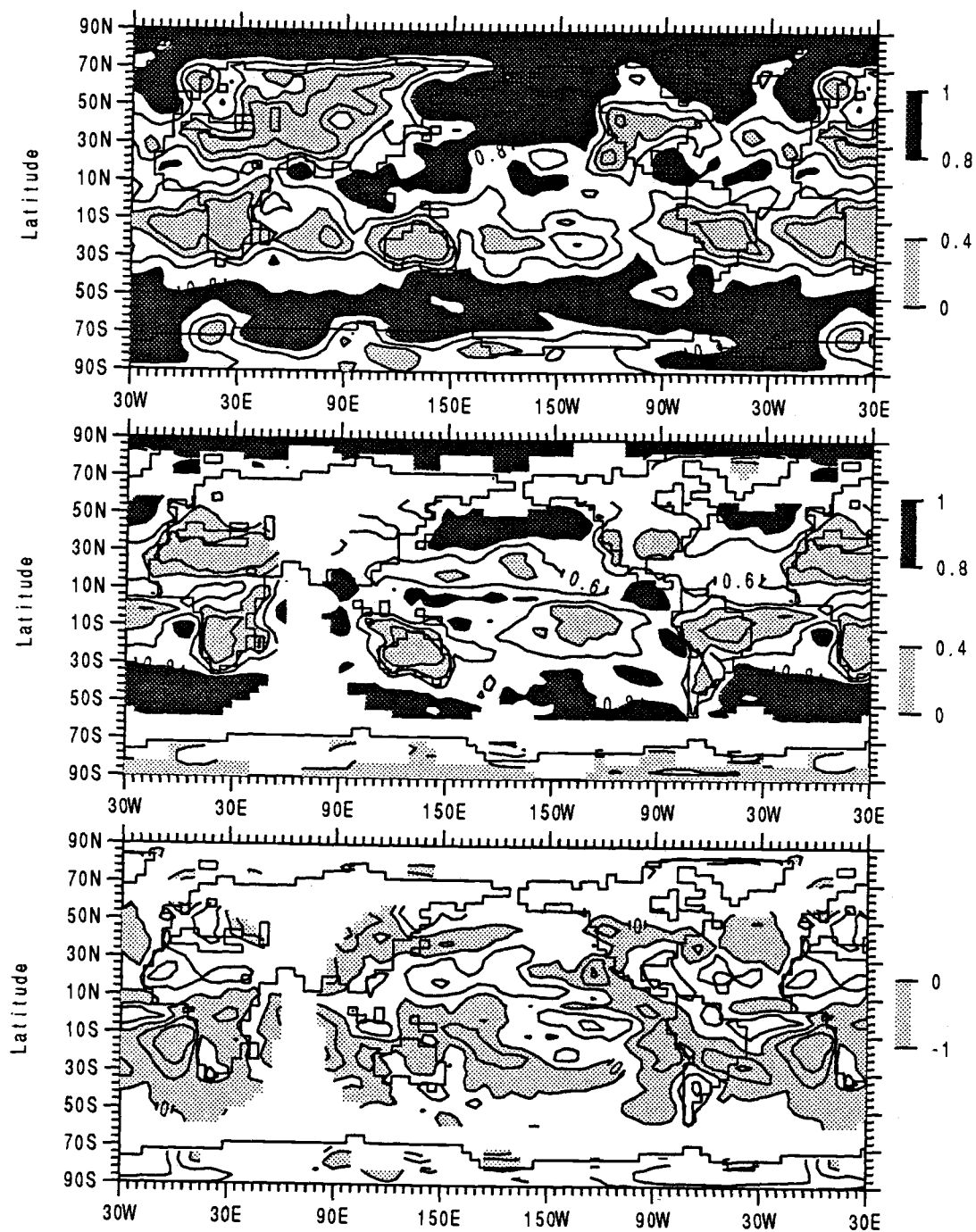
Fig. 6.3. As in Fig. 6.2, except for July.

southeast part of North America. The model also fails to simulate the July cloudiness maxima observed along the west coasts of the Americas and off the west coast of Africa, and underestimates the cloudiness to the east of New Guinea and Australia.

A comparison of Figs. 6.2 and 6.3 with Fig. 6.1 shows that the errors of the zonal-mean cloudiness in the subtropics are largely the result of the model's underestimation of the subtropical stratocumulus clouds off the west coasts of Africa and the Americas.

The latitude-altitude distributions of the zonal-mean fractional cloud cover and cloud water content simulated for January and July are presented in Fig. 6.4. Unfortunately, the corresponding observations for comparison with these simulated values are not available. Nevertheless, it is of interest to examine these results. Figure 6.4 shows that clouds are located at high altitudes in the tropical region and at low and middle altitudes in the middle and high latitudes. The tropical clouds represent the detrainment anvils associated with deep convection and may be, according to the cloud parameterization (section 3.2), be either cumuloform or stratiform clouds. This is also true for the clouds in the middle and high latitudes. Figure 6.4 shows that in general the cloud water maxima are associated with the cloudiness maxima. However, an interesting exception occurs in January centered at 34°N where a cloud water maximum occurs between 500 and 700 mb in the absence of a cloudiness maximum.

The zonal-mean vertically-integrated cloud liquid water content and zonal-mean cloud optical depth simulated for January and July are presented in Fig. 6.5, together with the corresponding observations based, respectively, on NIMBUS-7/SMMR data (Njoku and Swanson, 1983) and ISCCP data (Schlesinger *et al.*, 1989). These observations, again, are not true zonal means because the NIMBUS-7/SMMR data exists only over the ocean and the ISCCP data also do not exist everywhere. Nevertheless, it is indicated in Fig 6.5 that the cloud parameterization is capable of simulating the observed vertically-integrated cloud liquid water reasonably well for both January and July. However, the cloud parameterization overestimates the observed vertically-integrated cloud liquid water in the mid-latitudes of the winter hemisphere, particularly in July.
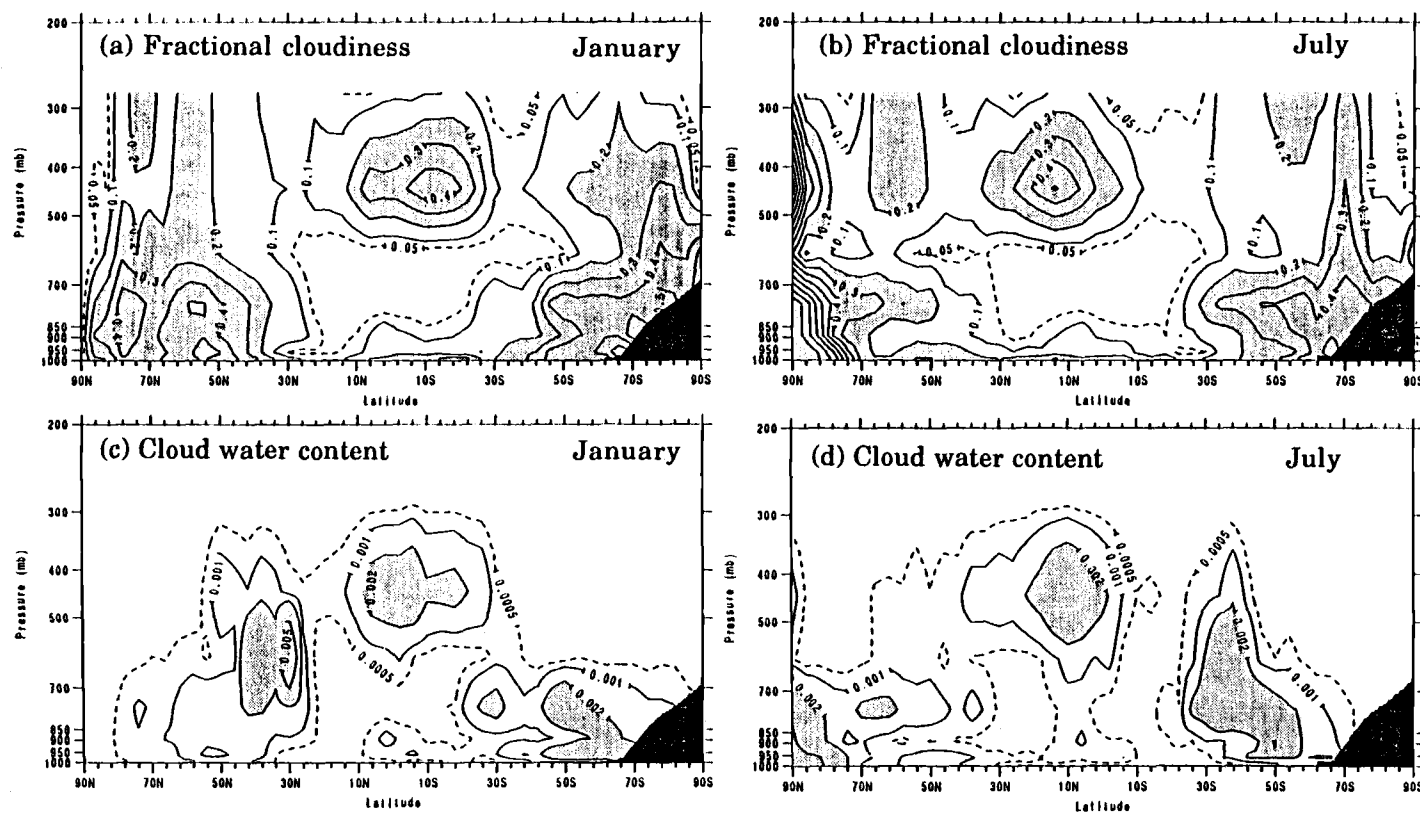
Fig. 6.4. Latitude-altitude distributions of the zonal-mean fractional cloud cover (upper panels) and cloud liquid water content (low panels) simulated for January and July. The contour interval for the fractional cloudiness is 0.1, with the 0.05 contour shown by the dashed line, and values larger than 0.2 are shown shaded. The contours for the cloud liquid water are 0.0005, 0.001, 0.002 and 0.005 g/m³, with values larger than 0.002 g/m³ shown shaded.
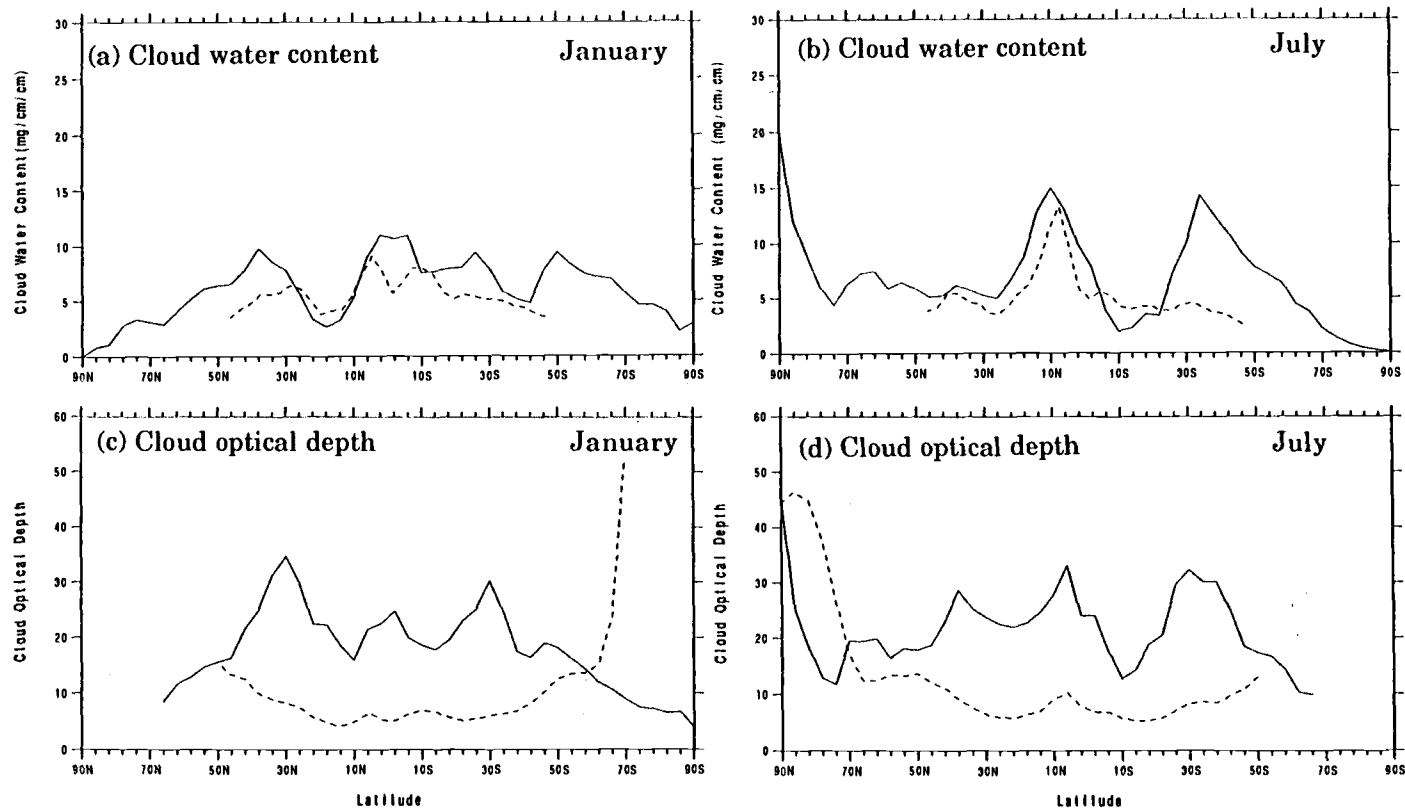
Fig. 6.5. Simulated (solid line) and observed (dashed line) zonal-mean cloud liquid water content (mg/cm^2) and cloud optical depth for January and July. The observed cloud liquid water contents are from NIMBUS-7/SMMR data (Njoku and Swanson, 1983) and the observed cloud optical depths are from ISCCP data (Schlesinger et al., 1989).

Despite the apparent success of the cloud parameterization in simulating the observed vertically-integrated cloud liquid water, Fig. 6.5 shows that the radiation parameterization is unsuccessful in the simulation of the observed cloud optical depth by a factor of about 3 - 4. However, there are several difficulties in obtaining "observed" cloud optical depth from the radiances measured by satellite sensors (see section 5.2.2). Consequently, to assess the likelihood that the discrepancies between the simulated and observed cloud optical depths are real, the simulated and observed components of the earth's radiation budget at the top of the atmosphere are compared below, following consideration of the most important component of the hydrological cycle simulated by the model.

The zonal-mean precipitation simulated by the AGCM is presented in Fig. 6.6, together with the observed zonal-mean precipitation from the global distribution of Jaeger (1976). The results show that the model reproduces the observed distribution reasonably well for both months, including the tropical maximum, the subtropical minima, and the mid-latitude maxima. Nevertheless, the model does not reproduce nature without error. In particular, the model somewhat overestimates the strength of the tropical maximum in both seasons, as well as the strength of the January mid-latitude maximum in the northern hemisphere, and underestimates the intensity of the mid-latitude maximum in the summer hemisphere, particularly in January. Also, the summer precipitation in the Arctic is overestimated by the model.

6.2. Earth Radiation Budget Components

The earth's radiation budget at the top of the atmosphere is comprised of the incident solar radiation, ISOL, the reflected solar radiation, RSOL, and the outgoing longwave radiation emitted by the earth to space, OLR. The net radiation at the top of the atmosphere, NRAD, can be expressed in terms of these components by

$$NRAD = ISOL - RSOL - OLR .$$

(6.1)
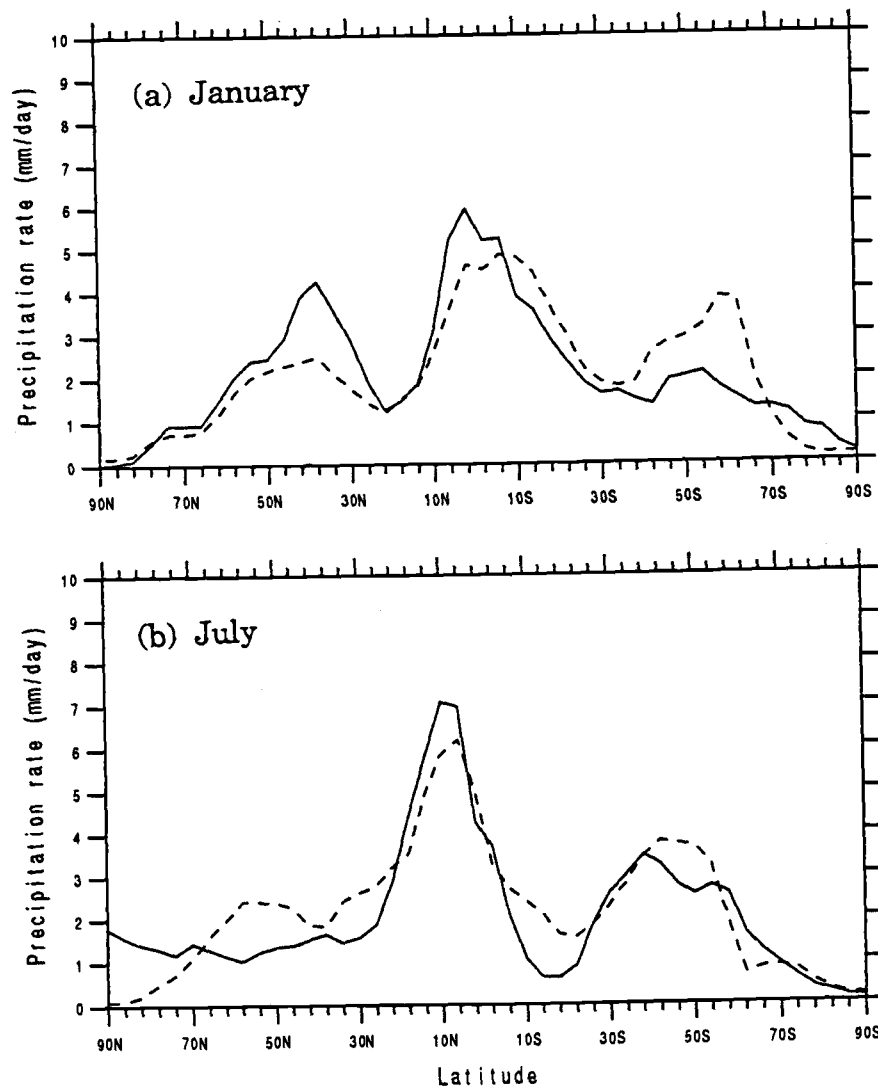
Fig. 6.6. Latitudinal distributions of the simulated (solid line) and observed (dashed line) zonal-mean precipitation rates for January and July. The observed data are from Jaeger (1976).

The reflected solar radiation can be expressed in terms of the incident solar radiation and the planetary albedo, ALB, by

$$RSOL = ALB \times ISOL . \qquad (6.2)$$

The net radiation can then be expressed as

$$NRAD = (1 - ALB) \, ISOL - OLR , \qquad (6.3)$$

or

$$NRAD = ABS - OLR , \qquad (6.4)$$

where

$$ABS = (1 - ALB) \, ISOL \qquad (6.5)$$

is the solar radiation absorbed by the earth. The net radiation therefore depends on ISOL, ALB (= RSOL/ISOL), and OLR. These three earth radiation budget "components" have been determined from satellite observations beginning in mid-1960s (e.g., Bandeen *et al.*, 1965; Vonder Harr and Suomi, 1969). As reviewed by Hartmann *et al.* (1986) and Ramanathan (1987), these "components" are uncertain as a result of instrument calibration difficulties, poor diurnal sampling, and the uncertainty in computing the radiative fluxes from the measured radiances. These uncertainties must be borne in mind when the simulated earth radiation budget components are compared with their observational counterparts.

The global-mean values of OLR, ALB, NRAD and ABS simulated for January and July by the AGCM with the new cloud-radiation parameterization are presented in Table 6.2, together with the corresponding observations from the WFOV and scanner instruments on the *NOAA-9* Earth Radiation Budget Satellite (ERBS), and the WFOV and NFOV instruments on the *NIMBUS-7* satellite. (The symbol SF in Table 6.2 indicates the type of filter which was applied to the WFOV data.) For OLR, the *NIMBUS-7* WFOV gives the largest values and the *NIMBUS-7* NFOV the smallest values, with a spread of 3.1 W/m² in January and 1.0 W/m² in July. For ALB, the *NIMBUS-7* NFOV gives the largest values

and the *NOAA-9*/ERBS the smallest values, with a spread of 3.74% in January and 3.33% in July. Because the effect of ALB on NRAD is larger here than that of OLR, the *NOAA-9*/ERBS gives the largest values for NRAD and the *NIMBUS-7* NFOV the smallest values, with a spread of 10.98 W/m^2 in January and 13.3 W/m^2 in July. Of the four satellite observations, those from the *NIMBUS-7* NFOV are consistently the most extreme, followed by the *NOAA-9*/ERBS WFOV observations. However, the observations from the *NOAA-9*/ERBS scanner and the *NOAA-9*/ERBS NFOV instruments are in good agreement with each other. Accordingly, the simulation results and the corresponding means for these two satellite observations are presented in Table 6.2 for purpose of comparison.

Table 6.2 shows that the simulated earth radiation budget components are in good agreement with the observations for both January and July. In particular, the AGCM underestimates the OLR by only 3.3 W/m^2 in January and 0.3 W/m^2 in July, and overestimates the ALB by only 1% in January and 0.5% in July. The model's negative OLR error (simulation minus observed) contributes to a negative error in NRAD, while the model's positive ALB error contributes to a positive error in NRAD (see Eq. (6.3)). As a result of these partially compensating errors, the model underestimates the NRAD by only 1.1 W/m^2 in January and 3.0 W/m^2 in July. These "errors" are in fact much smaller than the accuracy of the satellite observations. Table 6.2 shows that they are also smaller than the "errors" for OLR and NRAD given by the UCLA/GLA AGCM (Harshvardhan *et al.*, 1989).

Figures 6.7 and 6.8 present the zonal averages of the ALB, OLR and NRAD simulated by the model respectively for January and July, together with the corresponding observations from both the NIMBUS-7 NFOV and WFOV sensors. These figures show that the planetary albedo (ALB) simulated by the model is in good agreement with the observations for January, while for July the model underestimates the observed ALB in the northern hemisphere mid-latitudes and southern hemisphere tropics, and overestimates the WFOV ALB in the southern hemisphere mid-latitudes. For perspective, the ALB simulated by the UCLA/GLA AGCM is also presented in Figs. 6.2 and 6.3. It is seen that this model underestimates the January observed ALB in the middle latitudes of the northern

Table 6.2. The simulated and observed global-mean earth radiation budgets for January and July.

Data	OLR (W/m²)	ALB (%)	NRAD (W/m²)	ABS (W/m²)
January				
NOAA-9/ERBS (WFOV SF)[a]	231.38	29.86	15.88	
NOAA-9/ERBS (Scanner)[b]	231.87	30.86	11.86	
NIMBUS-7 (WFOV SF)[c]	233.2	30.5	12.96	
NIMBUS-7 (NFOV)[d]	230.1	33.6	4.9	235.0
0.5 (b + c)	232.5	30.7	12.4	
AGCM	229.36	31.72	11.34	240.70
UCLA/GLA AGCM[e]	222.	30.	25.	246.
July				
NOAA-9/ERBS (WFOV SF)[a]	237.86	28.13	-0.40	
NOAA-9/ERBS (Scanner)[b]	237.50	29.22	-3.64	
NIMBUS-7 (WFOV SF)[c]	237.9	29.2	-1.9	
NIMBUS-7 (NFOV)[d]	236.9	32.8	-13.7	223.2
0.5 (b + c)	237.7	29.2	-2.8	
AGCM	237.39	29.68	-5.75	231.64
UCLA/GLA AGCM[e]	233.	29.	2.	235.

a. Observations for January and July 1988; Kyle *et al.* (1989)
b. Observations for July 1985 and January 1986; Kyle *et al.* (1989)
c. Observations for July 1985 and January 1986; Kyle *et al.* (1989)
d. Observations for July 1979 and January 1980; Kyle *et al.* (1985)
e. Harshvardhan *et al.*, 1989
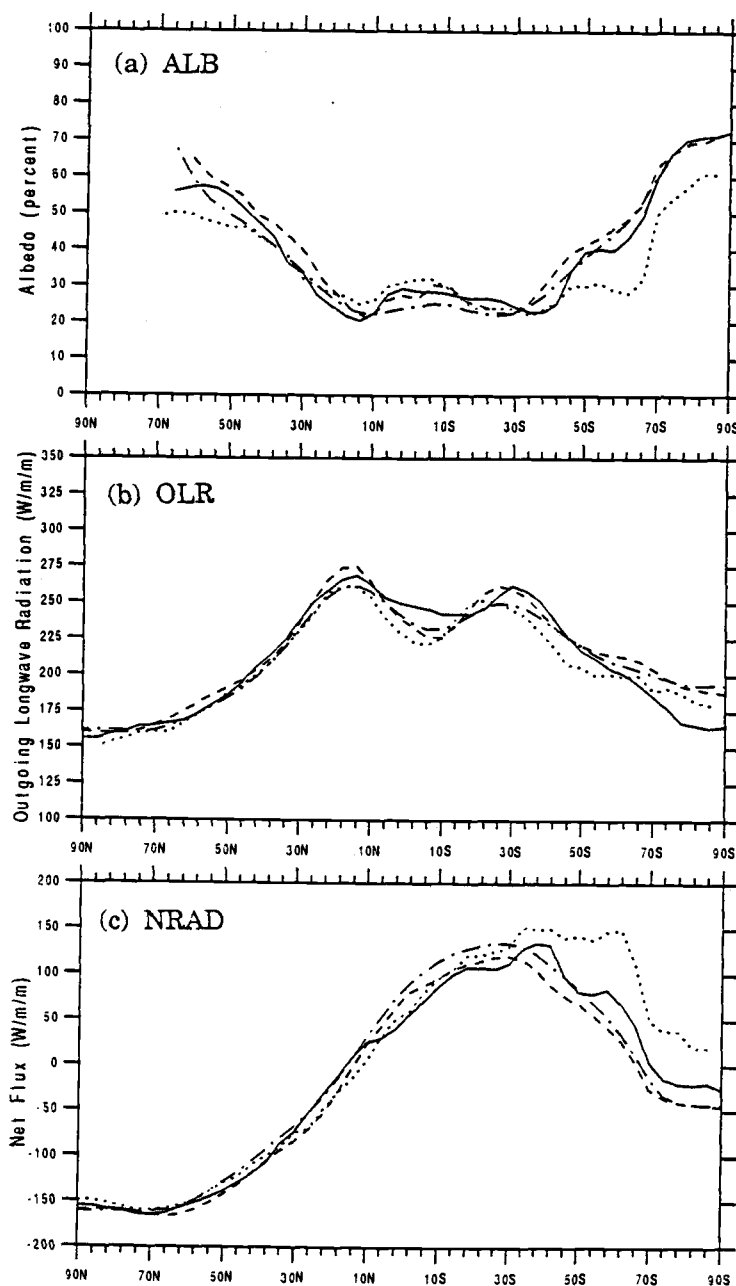
Fig. 6.7. Latitudinal distributions of the simulated (solid line) and observed (dashed line) zonal-mean ALB, OLR and NRAD for January. The observed data are from the NIMBUS-7 NFOV sensor (Kyle *et al.*, 1985). Observations from the NIMBUS-7 WFOV sensor (dashed-dotted line) are also presented from Kyle *et al.* (1985). The results simulated by the UCLA/GLA AGCM (Harshvardhan *et al.*, 1989) are shown by the dotted line.
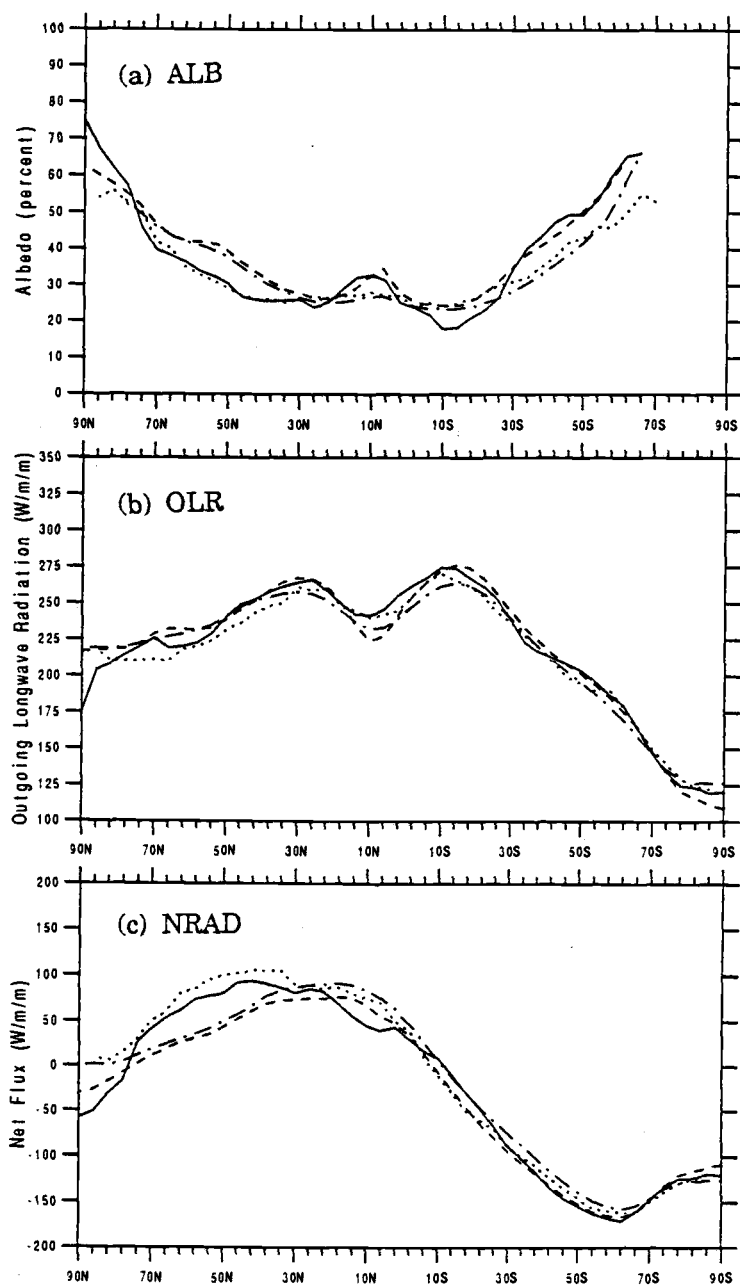
Fig. 6.8. As in Fig. 6.7, except for July.

hemisphere and in the middle and high latitudes of the southern hemisphere. For July, the UCLA/GLA model also underestimates the ALB from about 30°N to 70°N, as does our model, and is in better agreement with the WFOV observations in the middle latitudes of the southern hemisphere than the OSU multilayer AGCM.

The middle panels of Figs. 6.7 and 6.8 present the outgoing longwave radiation at the top of the atmosphere (OLR). These figures show that the OSU multilayer AGCM simulates the observed OLR reasonably well for both January and July. The model does underestimate the depth of the tropical OLR minimum for each month, this as expected based on the results of our final parameter selection procedure. The UCLA/GLA gives a better reproduction of this minimum than our model, at least for January. For this month, the OSU multilayer AGCM underestimates the OLR over Antarctica, while the UCLA/GLA model gives an underestimation in the middle latitudes of the southern hemisphere.

The lower panels of Figs. 6.7 and 6.8 present the net downward radiation at the top of the atmosphere (NRAD) which is related to the ALB and OLR data as given by Eq. (6.3). These figures show that our model is successful in reproducing the observed latitudinal distribution of the observed NRAD quite well except in the middle latitudes of the summer hemisphere where the simulated values exceed the observations, particularly in the Northern Hemisphere. However, the values of NRAD simulated by the UCLA/GLA AGCM for January and July are even larger than the observations in the summer hemisphere than the OSU multilayer AGCM.

The above comparison has shown that the AGCM with the new cloud-radiation parameterization is reasonably successful in simulating the observations of the earth's radiation budget at the top of the atmosphere. In section 6.1, however, a large discrepancy was evidenced between the simulated cloud optical depths and their observed counterparts, based on the ISCCP data. One possible explanation for this apparent contradiction is that the ISCCP cloud optical depths are not correct and are too small. Another possible explanation is that the differences between the simulated and observed cloud optical depths are real, but the earth radiation budget component are insensitive to these differences. However, if this is true, it

means that it is extremely difficult to obtain cloud optical depths from the observed earth radiation budget radiances, and therefore again suggests that the ISCCP cloud optical depths may be in error. Thus both of the above possibilities reduce to only one, and it therefore appears that cloud optical depth is not a quantity which can be used to evaluate the performance of a cloud-radiation parameterization.

6.3. Improvement of New Cloud-Radiation Parameterization

As discussed in Chapters 3 and 4, the principal merit of the developed cloud-radiation parameterization is that it offers cloud cover feedback and cloud optical depth feedback, which were not available from the earlier version of OSU multilayer AGCM (Schlesinger and Oh, 1987). The cloud generating scheme and the treatment of clouds in the radiation calculations of the earlier version of OSU multilayer AGCM can be characterized as follows: The model cloud overcasts the GCM gridbox completely whenever large-scale condensation or convection occurs, and disappearing momentarily in the absence of large-scale condensation or convection. Also, the model clouds are treated as blackbody in the longwave radiation calculations.

The developed cloud-radiation parameterization not only allows the feedbacks listed above, it also simulates successfully the clouds (CLD) and radiation budget terms (ALB, OLR, and NRAD), as discussed in sections 6.1 and 6.2 (Table 6.2). The improvement provided by the new cloud-radiation is clearly shown in Fig. 6.9, showing the zonal-averaged planetary albedo, fractional cloudiness, and the precipitation rate of the OSU multilayer AGCM for both January and July in comparison to those of the earlier version of the OSU multilayer AGCM.

The comparison in Fig. 6.9a indicates that the new cloud-radiation parameterization significantly improves the fractional cloudiness simulation in the tropics and the summer hemisphere, where the model with the old cloud-radiation parameterization obviously underestimated, for both January and July in comparison to the ISCCP data (Schlesinger *et al.*, 1989). In the winter hemisphere, both the old and new cloud-

radiation parameterizations accurately simulate the fractional cloudiness. As shown in Fig. 6.9b, the planetary albedo simulation for the new scheme becomes more realistic in all but the high latitudes, where the surface albedo is large due to the snow cover, for both January and July compared to the NIMBUS-7 NFOV (Kyle *et al.*, 1985). The simulated planetary albedo with the old cloud-radiation parameterization was considerably overestimated in the tropics and midlatitudes, though fractional cloudiness in those regions was significantly underestimated. The differences between old and new cloud-radiation parameterization are due to the prefixed values of the cloud optical properties, which may not be suitable, and a rudimentary cloud generating scheme in the earlier version. The simulated precipitation rates with the new scheme do not differ seriously from those of old scheme (Fig. 6.9c).

As noted above the new cloud-radiation parameterization not only offers cloud cover feedback and cloud optical depth feedback, it also significantly improves the fractional cloudiness and planetary albedo simulations in comparison to the earlier version of the OSU multilayer AGCM.
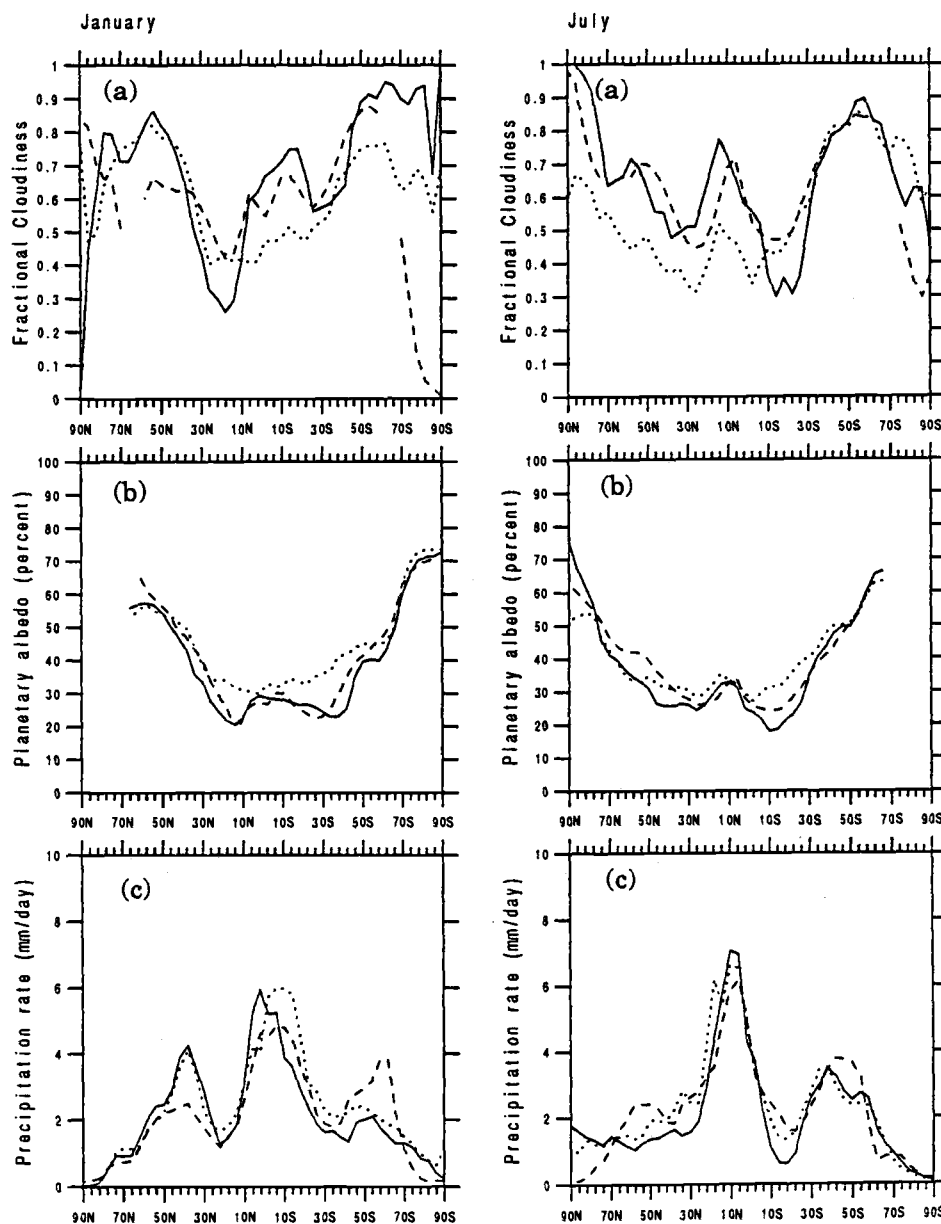
Fig. 6.9. Simulated and observed zonal-mean fractional cloud cover (a), planetary albedo (b), and precipitation rate (c) for January and July. Results simulated by the AGCM with the new cloud-radiation parameterization are shown by solid lines; observations from ISCCP (Schlesinger *et al.* 1989) (a), NIMBUS-7 NFOV (Kyle *et al.*, 1985) (b), and Jaeger (1976) (c) are shown by the dashed lines; results simulated with old cloud-radiation parameterization (Schlesinger and Oh, 1987) are shown by dotted lines.

7. SUMMARY AND CONCLUSION

In this study, a physically-based parameterization of clouds and their radiative interactions has been developed for a multilayer atmospheric general circulation model. In this cloud-radiation parameterization, cloud water is treated as a prognostic variable and the fractional cloud amount is predicted semi-prognostically. Moreover, stratiform and cumuloform clouds are allowed to coexist in a vertical atmospheric column, all clouds can exist either as liquid water clouds, ice clouds or mixed liquid water-ice clouds, and the radiative properties of clouds depend on their predicted cloud liquid water and ice amounts. The main purpose of developing this cloud-radiation parameterization is to enable the evaluation of cloud optical depth feedback, a feedback of potential importance for greenhouse-gas-induced climate change.

The parameterization of stratiform clouds is based on that of Sundqvist (1978, 1988) but differs in that: (1) the budget equations for water inside and outside a cloud have been made consistent; (2) cloud water evaporates regardless of whether or not there is condensation, with the evaporation rate depending on the difference between the cloud water mixing ratio and the saturation mixing ratio of the environment; (3) the fractional cloud cover remains at its antecedent value until the cloud water either evaporates completely or condensation occurs again; (4) the autoconversion of cloud water into precipitation is parameterized in a manner similar to that of Kessler (1969); and (5) the evaporation rate of rain is calculated following the formulation of Schlesinger et al. (1988).

The parameters which must be determined for the stratiform parameterization are: (1) the characteristic time for the evaporation of cloud water, τ_s; (2) the autoconversion rate of cloud water into precipitation, a; (3) the threshold relative humidity of the environment at which condensation can begin, U_{00}; and (4) the threshold cloud water above which precipitation can begin, m_c, this separately for liquid water

and ice clouds.

The parameterization of cumuloform clouds is based on the Arakawa-Schubert (1974) parameterization of penetrating convection. In this parameterization it is assumed that an ensemble of cumulus clouds exists, with each sub-ensemble member or cloud type identified by the layer in which it reaches neutral buoyancy and detrains. In the AS theory, a cloud type can be interpreted as a time average over a single cloud's life cycle in which the growing and dissipating stages are negligibly short and the cloud exists only in its mature stage. For the radiative effects of these cumuloform clouds, however, it is the mature and dissipating stages which are of greatest importance because only during these stages is the fractional cloudiness large. Therefore, in the proposed parameterization it is assumed that only the growing stage is negligibly short, and that the cloud is in its mature stage when its cloud-base mass flux is positive, and is in its dissipating stage thereafter when its cloud-base mass flux ceases. For the mature stage of a cloud, it is assumed that the entrainment layers do not store cloud water, as in the AS parameterization, but that the detrainment layer can store cloud water, unlike in the AS parameterization. The prognostic cloud water budget equation for the detrainment layer includes the flux of total water from the cloud layer below, the entrainment of water vapor from the environment, the detrainment of cloud water to the environment, the conversion of cloud water to precipitation, and the evaporation of cloud water into the environment. The fractional cloud cover during the mature stage is determined from an assumed diagnostic relation for the cloudiness in terms of the mass flux into the base of the detrainment layer. For the dissipating stage of a cloud, the cloud-base mass flux is zero and the cloud consists only of its detrainment shield. In the dissipating stage, it is assumed that there is no precipitation. Hence, the prognostic cloud water budget equation includes only the evaporation of cloud water into the environment. It is further assumed that the cloudiness remains at its maximum value of the mature stage during the dissipating stage.

The parameters which must be determined for the cumuloform parameterization are: (1) the characteristic time for the evaporation of cloud water, τ_c; (2) the parameter in the diagnostic equation for the

cloudiness in terms of the mass flux at the base of the detrainment layer, α; and (3) the conversion rate of cloud water into precipitation, C_o.

In the proposed parameterization, stratiform and cumuloform clouds can coexist within the same vertical atmospheric column, albeit not in the same layer. The identification of a cloud in a layer as either a stratiform or cumuloform cloud depends on the preceding cloud type, the large-scale condensation, and the convective mass flux in the layer. If there is convective mass flux, then the cloud type is taken to be cumuloform, regardless of whether the preceding cloud is stratiform or cumuloform. If there is large-scale condensation and no convection, the cloud is taken to be stratiform. If there is neither convection nor large-scale condensation, the cloud maintains its cloud type until it dissipates by evaporation.

When the temperature within a cloud is below 0°C, a three-phase mixture of water vapor, supercooled liquid water and ice can exist. It is assumed that the fraction of cloud water in the ice phase varies linearly from zero at 0°C to unity at a sub-zero temperature, T_i, which is another parameter which must be determined.

In the radiation parameterization, the solar spectrum is subdivided into three bands, two for Rayleigh scattering and ozone absorption, and one for water vapor absorption which is further subdivided into six intervals for the k-distribution method. The longwave spectrum is divided into four regions, one each for the CO_2 and O_3 bands, and one each for the line centers and line wings within the water vapor bands. The radiative properties of clouds are calculated from their prognostic cloud water content. The vertical distribution of clouds in the model is subdivided into individual cloud groups, with each group being defined as an ensemble of contiguous cloud layers, and the cloud groups being separated from each other by at least one layer of clear air. For both solar and longwave radiation, the contiguous cloud layers within each group are considered to overlap each other in the vertical to the maximum extent possible, while noncontiguous cloud groups are considered to randomly overlap each other in the vertical.

The values of the parameters of the stratiform and cumuloform cloud parameterizations were determined by performing limited-duration

sensitivity/tuning simulations with the OSU multilayer AGCM. First of all, however, a one-dimensional model of the stratiform cloud parameterization was developed and tested to understand the role of the parameterized evaporation and precipitation processes. The results of these tests showed that: (1) through its moistening of the environment, the evaporation of cloud water tends to enhance the growth of cloud cover; (2) precipitation of cloud water tends to enhance the growth of cloud cover because the fraction of the moisture convergence given to the environment to expand the cloud cover increases as the cloud water decreases, and (3) as the threshold value of cloud water m_c is decreased, the maximum cloud cover tends to increase and the minimum cloud water tends to decrease.

There are 8 parameters for the stratiform- and cumuloform-cloud parameterizations whose values must be determined, this after assuming that $\tau_c = \tau_s \equiv \tau$. It was not possible to choose n_i values for each parameter i and perform $n_1 \times n_2 \times ... \times n_8$ simulations with the AGCM to obtain the optimum set of parameter values. Therefore, a "reasonable" set of values was determined by the selection of the "best" choice for each parameter from sensitivity simulations for a few its values. The selection of the parameters was performed in two phases, an initial and a final selection phase.

In the initial parameter selection phase, 20-day perpetual-July and perpetual-January control simulations were performed with the AGCM. Test simulations were then made for a few values of the first parameter to be selected, each test simulation for only 10 days starting from day 10 of the control. The values of cloud cover, cloud liquid water content, precipitation and earth radiation budget components averaged over the last 5 days of the control and test simulations were then compared with the corresponding observations and a "best" value of the first parameter was chosen. Then new perpetual-July and perpetual-January control simulations were made for 20 days with this 'best" parameter value, each simulation starting at the initial times of the original control simulations. Next, perpetual-July and perpetual-January test simulations were made for a few values of the second parameter to be selected, again each simulation for only 10 days. The "best" value for this parameter was then chosen by comparing the values of cloud cover, cloud liquid water content,

precipitation and earth radiation budget components averaged over the last 5 days of the control and test simulations with the corresponding observations. New perpetual-July and perpetual-January control simulations were then made for 20 days with the "best" parameter values for the first and second parameters, again with each simulation starting at the initial times of the original control simulations. This procedure was then repeated in turn for each of the remaining 6 parameters.

The order of the parameters chosen in this way and their values are: C_0 = 0.008 m^{-1}; U_{00} = 0, τ = 50 minutes; T_i = -25°C, α = 10; a = (3600 s)$^{-1}$; $m_{c,w}$ = m_c = 10^{-4} g/g for stratiform water clouds; and $m_{c,i}$ = m_c = 0.7 $I_c(T_c)$ for stratiform ice clouds, where $I_c(T_c)$ are the values given by Heymsfield and Platt (1984) as a function of the cloud temperature T_c.

After completion of the selection process, an unpublished manuscript by Kyle *et al.* (1989) became available, indicating that the observed albedo values (ALB) which we used, namely the NIMBUS-7 NFOV data (Kyle *et al.*, 1985), are about 3 - 4% larger than the ALB values based on the NOAA-9/ERBS WFOV and scanner data, and are correspondingly larger than the NIMBUS-7/WFOV data reanalyzed by Kyle *et al.* (1989). Consequently, the good agreement of the simulated ALB with the original NIMBUS-7/NFOV ALB values means that the simulated values were too large. Furthermore, the tropical outgoing longwave radiation (OLR) minimum simulated by the model for January and July was not as deep as that observed by the NIMBUS-7/NFOV longwave radiation sensor. For these two reasons, a second and final set of parameter selection tests was performed for five parameters, two of which were already obtained in the initial selection procedure, and three of which were not. The order of the parameters chosen in the second selection process and their values are:

the mass absorption coefficient of cumuloform ice clouds, $a_0^{\uparrow,\downarrow}$ = 0.096; C_0 = 0.002 m^{-1}; $m_{c,w}$ = 0.5x10^{-4} g/g for stratiform water clouds; $m_{c,i}$ = 0.4 $I_c(T_c)$ for stratiform ice clouds; $m_{c,i}$ = 1.2 $I_c(T_c)$ for stratiform ice clouds formed from an antecedent cumuloform cloud; and the multiple scattering asymmetry factor for cumuloform clouds, g = 0.85.

The model does successfully simulate the cloud and radiation budget terms with the finally-selected cloud and radiation parameters as follows: The AGCM with the cloud-radiation parameterization simulates the

geographical distribution of cloudiness reasonably well for both January and July, including the cloudiness minima over the major desert areas and over the subtropical Pacific, the cloudiness maxima over the North Pacific and North Atlantic, and the band of maximum cloudiness centered near 60°S. However, the model overestimates the cloud cover where the ISCCP observations display minima, and fails to simulate the cloudiness maxima observed along the west coasts of the Americas and off the west coast of Africa. The latter errors are evident in the simulated zonal-mean cloud cover which is less than the observed cloud cover by about 10% in the subtropics of the winter hemisphere. Furthermore, the zonal-mean cloud-top pressures and cloud-top temperatures simulated by the model are generally lower and colder than the corresponding ISCCP observations, particularly in the subtropics. These results therefore indicate that the cloud parameterization underestimates the stratocumulus clouds which occur at low elevations in the subtropics.

The results also show that the AGCM with the cloud-radiation parameterization is capable of simulating reasonably well the observed latitudinal distributions of zonal-mean precipitation and vertically integrated cloud water for both January and July. However, the zonal-mean cloud optical depth simulated by the model is 3 - 4 times larger than that given by the ISCCP observations.

The global-mean values of the outgoing longwave radiation (OLR), planetary albedo (ALB), and net radiation at the top of the atmosphere (NRAD) simulated for January and July by the AGCM with the new cloud-radiation parameterization are in good agreement with the observations. In particular, the AGCM underestimates the OLR by only 3.1 W/m^2 in January and 0.3 W/m^2 in July, and overestimates the ALB by 1% in January and 0.5% in July. The model underestimates the NRAD by only 1.1 W/m^2 in January and 3.0 W/m^2 in July. These "errors" are in fact much smaller than the accuracy of the satellite observations.

The latitudinal distribution of the planetary albedo simulated by the model is in good agreement with the observations for January, while for July the model underestimates the observed ALB in the northern hemisphere mid-latitudes and southern hemisphere tropics by up to 10%. The model also simulates the latitudinal distribution of the observed zonal-

mean OLR reasonably well for both January and July. However, the model does underestimate the depth of the tropical OLR minimum for both January and July by about 10 W/m^2. Lastly, the model is successful in reproducing the observed latitudinal distribution of the observed zonal-mean NRAD except in the middle latitudes of the summer hemisphere where the simulated values exceed the observations by up to 50 W/m^2.

This successful simulation of cloud and radiation budget terms is primarily based on improvements provided by the new cloud-radiation parameterization. Compared to the old scheme simulation, the simulated fractional cloudiness and the planetary albedo simulated with the new cloud-radiation scheme are much closer to previously cited observations, particularly, for the tropics and midlatitudes in both January and July.

The climate obtained from the 20-day perpetual-January and perpetual-July simulations, in comparison with the observed climate, demonstrates that the AGCM with the new cloud-radiation parameterization is capable of successfully simulating many features of the observed cloud cover, vertically integrated cloud water, precipitation, the earth's radiation budget at the top of the atmosphere. The model is less successful in reproducing the cloud optical depths as given by the ISCCP observations. This apparent contradiction suggests that these optical depth observations may be in error and that the cloud optical depth is not a useful quantity to use in validating a cloud-radiation parameterization.

Comparison of the simulated and observed climates also shows that the cloud parameterization is deficient in its reproduction of the subtropical stratocumulus clouds. This is not surprising since the physics responsible for the generation, maintenance, and dissipation of these clouds is not specifically included in the current version of the cloud parameterization. To rectify this deficiency it will be necessary to include a model for stratocumulus clouds in the cloud-radiation parameterization.

BIBLIOGRAPHY

Ackerman, S. A., and S. K. Cox, 1982: The Saudi Arabian heat low: Aerosol distributions and thermodynamic structure. *J. Geophys. Res.*, **87**, 8991-9002.

Arakawa, A., 1975: Modelling clouds and cloud processes for use in climate models. In *The Physical Basis of Climate and Climate Modelling*, GARP Publications Series, No. 16, World Meteorological Organization and International Council of Scientific Unions, Geneva, 183-198.

Arakawa, A., and W. H. Schubert, 1974: Interaction of a cumulus cloud ensemble with the large scale environment, Part I. *J. Atmos. Sci.*, **31**, 674-701.

Arking, A., and J. D. Childs, 1985: Retrieval of the cloud cover parameters from multispectral satellite images. *J. Climate. Appl. Meteor.*, **24**, 322-333.

Arking, A., and S. Vemury, 1984: The NIMBUS 7 data set: A critical analysis . *J. Geophys. Res.*, **89**, 5,089-5,097.

Augustsson, T., and V. Ramanathan, 1977: A radiative-convective model study of the CO_2 climate problem. *J. Atmos. Sci.*, **34**, 448-451.

Bandeen, W. R., M. Halev, and J. Strange, 1965: A radiation climatology in the visible and infrared from the TIROS meteorological satellites, *NASA Tech. Note D-2534*, 30 pp.

Betts, A.K., and M.J. Miller, 1984: A new convective adjustment scheme. ECMWF Technical Report No. 43, 65pp.

Briegleb, B.P., P. Minnis, V. Ramanathan and E. Harrison, 1986: Comparison of regional clear-sky albedos infrared from satellite observation and model computations. *J. Climate Appl. Meteor.*, **25**, 214-216.

Cess, R. D., and G. L. Potter, 1987: Exploratory studies of cloud radiative forcing with a general circulation model. *Tellus*, **39A**, 460-473.

Cess, R.D., G.L. Potter, S.J. Ghan and W.L. Gates, 1985: The climatic effects of large injections of atmopsheric smoke and dust: A study of climate feedback mechanisms with one- and three-dimensional

climate model. *J. Geophys. Res.*, **90**, 12,937-12,950.

Charlock, T. P., 1981: Cloud optics as a possible stabilizing factor in climate change. *J. Atmos. Sci.*, **38**, 661-663.

Charlock, T. P., 1982: Cloud optical feedback and climate stability in a radiative-convective model. *Tellus*, **34**, 245-254.

Charlock, T. P., and V. Ramanathan, 1985: The albedo field and cloud radiative forcing produced by a general circulation model with internally generated cloud optics. *J. Atmos. Sci.*, **42**, 1408-1429.

Chou, M.-D., 1984: Broadband water vapor transmission functions for atmospheric IR flux computation. *J. Atmos. Sci.*, **41** 1775-1778.

Chou, M.-D., 1986: Atmospheric solar heating rate in the water vapor bands. *J. Climate Appl. Meteor.*, **25**, 1532-1542.

Chou, M.-D. and L. Peng, 1983: A parameterization of the absorption in 15μm CO_2 spectral region with application to climate sensitivity studies,*J. Atmos. Sci.*, **40**, 2183-2192.

Coakley, J. A., 1987: A dynamic threshold method for obtaining cloud cover from satellite imagery data. *J. Geophys. Res.*, **92**, 3985-3990.

Coakley, J. A., and F. P. Bretherton, 1982: Cloud cover from high-resolution scanner data: Detecting and allowing for partially filled fields of view. *J. Geophys. Res.*, **87**, 4917-4932.

Ellingson, R. G., and G. N. Serafino, 1984: Observations and calculations of aerosol heating over the Arabian Sea during MONEX. *J. Atmos. Sci.*, **41** 575-589.

Fouquart, Y., 1987: Radiative transfer in climate modeling (to be published).

Gates, W. L., Y.-J. Han and M. E. Schlesinger, 1985: The global climate simulated by a coupled atmosphere-ocean general circulation model: Preliminary results. In *Coupled Ocean-Atmosphere Models*, J.C.J. Nihoul, Ed., Elsevier, 131-151.

Geleyn, J.F., 1988: Personal communication.

Geleyn, J.F., and A. Hollingsworth, 1979: An economical analytical method for the computation of the interaction between scattering and line absorption of radiation. *Beitr. Phys. Atmos.*, **52**, 1-16.

Geleyn, J.-F., 1977: Parameterization of radiative transfer at ECMWF. Proceedings of the ECMWF 1977 seminar on the parameterization of

the physical processes in the free atmosphere, 273-345.

Ghan, S. J., 1986: Personal communication.

Ghan, S. J., J. W. Lingaas, M. E. Schlesinger, R. L. Mobley and W. L. Gates, 1982: A documentation of the OSU two-level atmospheric general circulation model. Report No. 35, Climatic Research Institute, Oregon State University, Corvallis, OR, 395 pp.

Griffith, K.T., S.K. Cox and R.C. Knollenberg, 1980: Infrared radiative properties of tropical cirrus clouds inferred from aircraft measurements. *J. Atmos. Sci.*, **37**, 1073-1083.

Han, Y.-J., W. L. Gates and M. E. Schlesinger, 1985: A critical evaluation of the air-sea-ice interaction simulated by the OSU coupled atmosphere-ocean GCM. In *Coupled Ocean-Atmosphere Models*, J.C.J. Nihoul, Ed., Elsevier, 167-182.

Hansen, J., D. Johnson, A. Lacis, S. Lebedeff, P. Lee, D. Rind and G. Russel, 1981: Climate impact of increasing atmospheric carbon dioxide. *Science*, **213**, 957-966.

Harshvardhan, D. A. Randall, T. G. Corsetti, and D. A. Dazlich, 1989: Earth radiation budget and cloudiness simulations with a general circulation model., submitted to *J. Atmos. Sci.*

Hartmann, D. L., V. Ramanathan, A. Berroir, and G. E. Hunt, 1986: Earth radiation budget data and climate research. *Rev. Geophys.*, **24**, 439-468.

Henderson-Seller, A., G. Seze, F. Drake, and M. Desbois, 1987: Surface-observed and satellite-retrieved cloudiness compared for the 1983 ISCCP special study area in Europe. *J. Geophys. Res.*, **92**, 4019-4033.

Heymsfield, A. J. , and C. M. R. Platt, 1984: A parameterization of the particle size spectrum of ice clouds in terms of the ambient temperature and ice water content. *J. Atmos. Sci.*, **41**, 846-855

Hucek, R. R., H. L. Kyle, and P. E. Ardanuy, 1987: NIMBUS-7 earth radiation budget wide field of view climate data set improvement 1. The earth albedo from deconvolution of shortwave measurements. *J. Geophys. Res.*, **92**, 4107-4123.

Hummel, J. R., 1982: Surface temperature sensitivities in a multiple cloud radiative-convective model with a constant and pressure dependent lapse rate. *Tellus*, **34**, 203-208.

Hummel, J. R., and R. A. Reck, 1981: Carbon dioxide and climate: The effects of water transport in radiative-convective models. *J. Geophys. Res.*, **86**, 12,035-12,038.

Hunt, B. G., 1981: An examination of some feedback mechanisms in the carbon dioxide climate problem. *Tellus*, **33**, 78-88.

Hunt, G. E., 1982: On the sensitivity of a general circulation model climatology to changes in cloud structure and radiative properties. *Tellus*, **34**, 29-38.

Hwang, P. H., L. L. Stowe, H. Y. M. Yeh, H. L. Kyle, and the NIMBUS-7 data processing team, 1988: The NIMBUS-7 global cloud climatology. *Bull Amer. Meteor. Soc.*, **69**, 743-752.

Jaeger, L., 1976: Monatskarten des Niederschlags fur die ganze Erde. Report No. 139, German Weather Service, Offenbach a. M., Germany, 38 pp.

Jacobowitz, J. H., and R. J. Tighe, 1984: The earth radiation budget derived from the NIMBUS-7 ERB experiment. *J. Geophys. Res.*, **89**, 4997-5010.

Jacobowitz, J. H., H. V. Soule, H. L. Kyle, F. B. House, and the Nimbus-7 ERB experiment team, 1984: The earth radiation budget experiment: An overview. *J. Geophys. Res.*, **89**, 5021 - 5038.

Kessler, E., III, 1969: On the distribution and continuity of water substance in atmospheric circulations. *Meteor. Monogr.*, **32**, 84 pp.

King M. D., and R. J. Curran, 1980: The effect of a nonuniform planetary albedo on the interpretation of earth radiation budget observations. *J. Atmos. Sci.*, **37**, 1262-1278.

King, M.D., and Harshvarthan, 1986: Comparative accuracy of selected multiple scattering approximations. *J. Atmos. Sci.*, **43**, 784-801.

Kneizys, F. X., E. P. Shettle, W. O. Gallery, J. H. Chetwynd, Jr.,L. W. Abreu, J. E. A. Selby, S. A. Clough and R. W. Fenn, 1983: *Atmospheric transmittance/Radiance: Computer code LOWTRAN6.* Optical Physics Div.,7670, Hanscom AFB, Bedford, MA, 200pp.

Kuo, H. L., 1965: On formation and intensification of tropical cyclones through latent heat release by cumulus convection. *J. Atmos. Sci.*, **22**, 40-63.

Kuo, H. L., 1974: Further studies of the parameterization of the influence of cumulus convection of large-scale flow. *J. Atmos. Sci.*, **31**, 1232-1240.

Kurihara, Y., 1973: A scheme of moist convective adjustment. *Mon. Wea. Rev.*, **101**, 547-553.

Kyle, H.L., P.E. Ardanuy and E.J. Hurley, 1985: The status of the Nimbus-7 Earth-Radiation-Budget data set. *Bull. Amer. Meteor. Soc.*, **66**, 1378-1388.

Kyle, H.L., A. Mecherikunnel, P.E. Ardanuy, L. Penn, B. Groveman, G.G. Campbell, and T.H. Vonder Harr, 1989: A comparison of two major earth radiation budget data sets. submitted to *J. Geophys. Res.*.

Labs, D., and H. Neckel, 1970: Transformation of the absolute solar radiation data into the "International Practical Temperature Scale of 1968." *Solar Physics*, **15**, 79-87.

Lacis, A.A., and J.E. Hansen, 1974: A parameterization for the absorption of solar radiation in the earth's atmosphere. *J. Atmos. Sci.*, **31**, 118-133.

LeTreut, H., and Z.-X. Li, 1987: Using Meteosat data to validate a prognostic cloud generation scheme. (unpublished).

Liou, K.-N., 1980: *An Introduction to Atmospheric Radiation*. Academic Press, New York, 392 pp.

Liou, K.-N., 1986: Influence of cirrus clouds on weather and climate processes: A global perspective. *Mon. Wea. Rev.*, **114**, 1167-1199.

Lord, S. J., 1978: Development and observational verification of a cumulus cloud parameterization. Ph.D. dissertation, Department of Atmospheric Sciences, University of California, Los Angeles, CA, 359 pp.

Luther, F. M., R. G. Ellingson, Y. Fouquart, S. Fells, N. Scott and W. J. Wiscomb, 1988: Intercomparison of radiation codes in climate models (ICRCCM): Longwave clear-sky results. *Bull. Amer. Meteor. Soc.*, **69**, 40-48.

Manabe, S., and R.F. Strickler, 1964: Thermal equlibrium of the atmosphere with a convective adjustment. *J. Atmos. Sci.*, **21**, 361-385.

Manabe, S., J.S. Smagorinsky, and R.F. Strickler, 1965: Simulated climatology of a general circulation model with a hydrogic cycle. *Mon. Wea. Rev.*, **93**, 769-798.

Manabe, S., and R. T. Wetherald, 1967: Thermal equlibrium of the atmosphere with a given distribution of a relative humidity. *J. Atmos.*

Sci., **24**, 241-259.

Manabe, S., and R. T. Wetherald, 1980: On the distribution of climate change resulting from an increase in CO_2 content of the atmosphere. *J. Atmos. Sci.*, **37**, 99-118.

Meleshko, V. P., and R. T. Wetherald, 1981: The effect of a geographical cloud distribution on climate: A numerical experiment with an atmospheric general circulation model. *J. Geophys. Res.*, **86**, 11,995-12,014.

Minnis, P., and E.F. Harrison, 1984: Diurnal variability of regional cloud and clear-sky radiative parameters derived from GOES data, III; November 1978 radiative parameters. *J. Clim. Appl. Meteorol.*, **23**, 1032 - 1051.

Neckel, H., and D. Labs, 1984: The solar radiation between 3,300 and 12,500 Å. *Solar Physics*, **90**, 205-258.

Njoku, E. G. and L. Swanson, 1983: Global measurements of sea surface temperature, wind speed and atmospheric water content from satellite microwave radiometry. *Mon. Wea. Rev.*, **111**, 1977-1987

Paltridge, G.W., and C.M.R. Platt, 1980: Aircraft measurements of solar and infrared radiation and the microphysics of cirrus clouds. *Vol. of Extended Abstracts, Int. Radiation Symp.*, Fort Collins, IAMAP, 419-421.

Payne, R.E., 1972: Albedo of the sea surface. *J. Atmos. Sci.*, **29**, 959-970.

Platt, C.M.R., and G.L. Stephens, 1980: The interpretation of remotely sensed high cloud emisttances. *J. Atmos. Sci.*, **37**, 2314-2322.

Ramanathan, V., 1987: The role of earth radiation budget studies in climate and general circulation research. *J. Geophys. Res.*, **92**, 4075-4095.

Ramanathan, V., R.D. Cess, E.F. Harrison, P. Minnis, B.R. Barkstrom, E. Ahmad, and D. Hartmann, 1989: Cloud-radiative forcing and climate: Results from the earth radiation budget experiment. *Science*, **243**, 57-63.

Randall, D. A., Harshvardhan, D. A. Dazlich, and T. G. Corsetti, 1988: Intraction among radiation, convection, and large-scale dynamics in a general circulation model. submitted to the *J. Atmos. Sci.*

Rasmusson, E. M., and S. M. Hall, 1983: The great equatorial Pacific

Ocean warming event of 1982-1983. *Weatherwise*, **36**, 166-175

Rasmusson, E. M., and J. M. Wallace, 1983: Meteorological aspects of the El Niño/Southern Oscillation. *Science*, **222**, 1195-1202.

Reck, R. A., 1979a: Comparison of fixed cloud-top temperature and fixed cloud-top altitude approximations in the Manabe-Wetherald radiative-convective atmospheric model. *Tellus*, **31**, 400-405.

Reck, R. A., 1979b: Carbon dioxide and climate: Comparison of one- and three- dimensional models. *Environment International*, **2**, 387-391.

Roads, J. O., G. K. Vallis and L. Remer, 1984: Cloud/climate sensitivity experiments. In *Climate Processes and Climate Sensitivity*, Maurice Ewing Series, 5, J.E. Hansen and T. Takahashi, Eds., American Geophysical Union, Washington, D.C., 130-163.

Roeckner, E., and U. Schlese, 1985: January simulation of clouds with a prognostic cloud cover scheme. Manuscript to be published in the proceedings of the ECMWF Workshop on the Representation of Clouds in Numerical Models.

Roeckner, E., U. Schlese, J. Biercamp and P. Loewe, 1987: Cloud optical depth feedbacks and climate modelling. *Nature* **329**, 138-140.

Rossow, W. B., F. Mosher, E. Kinsella, A. Arking, M. Desbois, E. Harrison, P. Minnis, E. Ruprecht, G. Seze, C. Simmer, and E. Smith, 1985: ISCCP cloud algorithm intercomparison., *J. Climate. Appl. Meteor.*, **24**, 877-903.

Rutledge, S. A., and P. V. Hobbs, 1983: The mesoscale and microscale structure and organization of clouds and precipitation in midlatitude cyclones. VIII. A model for the "seeder-feeder" process in warm-frontal rainbands. *J. Atmos. Sci.*, **40**, 1185-1206.

Rutledge, S. A., and M. E. Schlesinger, 1985: The treatment of clouds in general circulation models: Current status and more physically based parameterizations. Report No. 63, Climatic Research Institute, Oregon State University, Corvallis, 49 pp.

Sassen, K., M. K. Griffin, and G. G. Dodd, 1988: Optical scattering and microphysical properties of subvisual cirrus clouds, and climatic implications. Accepted for publication in J. Appl. Meteor..

Schlesinger, M. E., 1985: Feedback analysis of results from energy balance and radiative-convective models. In *Projecting the Climatic Effects of*

Increasing Carbon Dioxide, M.C. MacCracken and F.J. Luther, Eds., U.S. Department of Energy, pp. 280-318.

Schlesinger, M. E., 1988a: Quantitative analysis of feedbacks in climate model simulations of CO2-induced warming. In *Physically-Based Modelling and Simulation of Climate and Climatic Change*, M. E. Schlesinger (ed.), NATO Advanced Study Institute Series, Kluwer, Dordrecht, 653-736.

Schlesinger, M. E., 1988b: Negative or positive cloud optical depth feedback. *Nature*, **335**, 303-304.

Schlesinger, M. E., 1988c: How to make models for behaviour of clouds. *Nature*, **336**, 315-316.

Schlesinger, M. E., 1989: Quantitative Analysis of Feedbacks in Climate Model Simulations. In *Contribution of Geophysics to Climate Change Studies*, Proceedings of IUGG Symposium 15, Geophysical Monograph, A. Berger, R. Dickinson and J. Kidson (eds.), American Geophysical Union, Washington, D.C.

Schlesinger, M. E., and W. L. Gates, 1979: Numerical simulation of the January and July global climate with the OSU two-level atmospheric general circulation model. Report No. 9, Climatic Research Institute, Oregon State University, Corvallis, OR, 102 pp.

Schlesinger, M. E., and W. L. Gates, 1980: The January and July performance of the OSU two-level atmospheric general circulation model. *J. Atmos. Sci.*, **37**, 1914-1943.

Schlesinger, M. E., and W. L. Gates, 1981: Preliminary analysis of the mean annual cycle and interannual variability simulated by the OSU two-level atmospheric general circulation model. Report No. 23, Climatic Research Institute, Oregon State University, Corvallis, OR, 47 pp.

Schlesinger, M. E., and J. F. B. Mitchell, 1985: Model projections of equilibrium climate response to increased CO_2. In *Projecting the Climatic Effects of Increasing Carbon Dioxide*, M. C. MacCracken and F. M. Luther, DOE/ER-0237, U.S. Department of Energy, pp. 81-147.

Schlesinger, M. E., and J. F. B. Mitchell, 1987: Model projections of the equilibrium climate response to increased CO_2. *Rev. of Geophys.*, **25**,

760-798.

Schlesinger, M.E., and J.-H. Oh, 1987: Description of the multi-layer atmospheric general circulation model. Unpublished manuscript, Climatic Research Institute, Oregon State University, Corvallis, OR, 39 pp.

Schlesinger, M.E., J.-H. Oh, and Rosenfeld, 1988: A parameterization of the evaporation of rainfall. *Mon. Wea. Rev.*, **116**, 1887-1895.

Schneider, S. H., W. M. Washington and R. M. Chervin, 1978: Cloudiness as a climatic feedback mechanism: Effects on cloud amounts of prescribed global and regional surface temperature changes in the NCAR GCM. *J. Atmos. Sci.*, **35**, 2207-2221.

Schutz, C., and W. L. Gates, 1971: Global climate data for surface, 800 mb and 400 mb: January. R-915-ARPA, The Rand Corporation, Santa Monica, CA, 50 pp.

Shenk, E. W., and V. V. Solomonson, 1972: A simulation study exploring the effects of sensor spatial resolution on estimates of cloud cover from satellites. *J. Appl. Meteorol.*, **11**, 214-220.

Shukla, J., and Y. Sud, 1981: Effect of cloud-radiation feedback on the climate of a general circulation model. *J. Atmos. Sci.*, **38**, 2337-2353.

Slingo, A. (Editor), 1985: *Handbook of the Meteorological Office 11-layer atmospheric general circulation model.* Volumn 1: Model description. Available on request from the Dynamical Climatology Branch, Meteorological Office, Bracknell, Berkshire, U. K.

Slingo, J. M.,1980: A cloud parameterization scheme derived from GATE data for use wiht a numerical model. *Q. J. R. Meteorol. Soc.*, **106**, 747-770.

Slingo, J. M.,1987: The development and verification of a cloud prediction scheme for the ECMWF model. *Q. J. R. Meteorol. Soc.*, **113**, 899-927.

Smith, R. N. B., 1988: A scheme for predicting layer clouds and their water content in a general circulation model. DCTN 68, Dynamical Climatology , Meteorological Office, Bracknell, Berkshire, U. K.,30 pp

Somerville, R. C. J., and L. A. Remer, 1984: Cloud optical thickness feedbacks in the CO_2 climate problem. *J. Geophys. Res.*, **89**, 9668-9672.

Starr, D.O'C., and S.K. Cox, 1985: Cirrus clouds, Part II: Numerical experiments on the formation and maintenance of cirrus. *J. Atmos.*

Sci., **42**, 2682-2694.

Stephens, G. L., 1978: Radiation profiles in extended water clouds. II: Parameterization schemes. *J. Atmos. Sci.*, **35**, 2123-2132.

Stephens, G. L., 1984: The parameterization of radiation for numerical weather prediction and climate models. *Mon. Wea. Rev.*, **112**, 826-867.

Stephens, G. L., and P. J. Webster, 1981: Clouds and climate: Sensitivity of simple systems. *J. Atmos. Sci.*, **38**, 235-247.

Stowe, L. L., P. P. Pellegrino, P. H. Hwang, P. K. Bhartia, T. F. Eck, C. S. Long, C. G. Wellemeyer, and H-Y. M. Yeh: 1986: Spatial and temporal characteristics of global cloud cover as observed from the NIMBUS-7 satellite. in Preprint Volume Sixth conference on atmospheric radiation, May 13-16, 1986, Williamsburg, Va., the American Meteorological Society, Boston, Mass., 99-102.

Sundqvist, H., 1978: A parameterization scheme for non-convective condensation including prediction of cloud water content. *Quart. J. Roy. Met. Soc.*, **104**, 677-690.

Sundqvist, H., 1981: Prediction of stratiform clouds: Results from a 5-day forecast with a global model. *Tellus*, **33**, 242-253.

Sundqvist, H., 1988: Parameterization of condensation and associated clouds in models for weather prediction and general circulation simulation. In *Physically-based Modelling and Simulation of Climate and Climatic Change*, M.E. Schlesinger (ed.), Kluwer Academic Publishers, Dordrecht, The Netherlands, pp. 433-461.

Susskind, J., D. Reuter, and M. T. Chahine, 1987: Cloud fields retrieved from analysis of HIRS2/MSU sounding data. *J. Geophys. Res.*, **92**, 4035-4050.

Susskind, J., J. Rosenfield, D. Reuter, and M. T. Chahine, 1984: Remote sensing of the weather and climate parameters from HIRS2/MSU on TIROS-N. *J. Geophys. Res.*, **89**, 4677-4697.

Tiedke, M., 1984: Effect of penetrative cumulus convection on the large-scale flow in a general circulation model. *Beitr. Phys. Atmos.*, **57**, 216 - 239.

Tiedke, M., 1988: Parameterization of cumulus convection in large-scale models. In *Physically-based Modelling and Simulation of Climate and Climatic Change*, M.E. Schlesinger (ed.), Kluwer Academic

Publishers, Dordrecht, The Netherlands, pp. 375-431

U.S. Committee on Extension to the Standard Atmosphere, 1976: U.S. *standard atmosphere, 1976.* Washington D.C., 227pp.

Vonder Harr, T. H., and V. E. Suomi, 1969: Satellite observations of the earth's radiation budget. *Science*, **163**, 667-669.

Wang, W.-C., and P. H. Stone, 1980: Effect of ice-albedo on global sensitivity in a one-dimensional radiative-convective climate model. *J. Atmos. Sci.*, **37**, 545-552.

Wang, W.-C., W. B. Rossow, M.-S. Yao and M. Wolfson, 1981: Climate sensiivity of a one-dimensional radiative-convective model with cloud feedback. *J. Atmos. Sci.*, **38**, 1167-1178.

Warren, S. G., C. J. Hahn, J. London, R. M. Chervin and R. L Jenne, 1986: Global Distribution of Total Cloud Cover and Cloud Type Amounts Over Land. NCAR/TN-273 + STR. National Center for Atmospheric Research, Boulder, CO 29 pp + 199 Maps.

Welch, R.M., S.K. Cox and J.M. Davis, 1980: Solar Radiation and Clouds. *Meteor. Monogr.*, No. 39, Amer. Meteor. Soc., 93 pp.

Wetherald, R. T., and S. Manabe, 1980: Cloud cover and climate sensitivity. *J. Atmos. Sci.*, **37**, 1485-1510.

Wetherald, R. T., and S. Manabe, 1986: An investigation of cloud cover change in response to thermal forcing. *Climatic Change*, **8**, 5-23.

Appendices

Appendix A

DESIGN OF THE
OSU MULTI-LAYER ATMOSPHERIC GCM

TABLE OF CONTENTS

1. Introduction

Although the OSU two-layer atmospheric general circulation model (AGCM) successfully simulates many features of the observed climate (e.g., Schlesinger and Gates, 1979, 1980, 1981), its coarse vertical resolution limits its usefulness as a tool for the development of a physically-based parameterization of clouds and their radiative interactions. Accordingly, a multi-layer version of the AGCM has been developed. Based on the considerations of extending the model's prognostic variables to include both cloud liquid water and cloud ice, and of keeping the model within the memory capacity of the NCAR Cray 1A computers, it was decided to limit the vertical extent of the model to the troposphere. As shown in Fig. 1, the top of the model atmosphere is defined to be the 200 mb surface (as in the two-layer AGCM), and the troposphere below this surface is divided into seven layers. Figures 2 contrasts the vertical resolution of this 7-layer model with that of several other national (Fig. 2.a) and international (Fig. 2.b) models. It is seen that the vertical resolution of the 7-layer model is comparable to that of the other contemporary models.

The basic dynamical structure and physical processes of the multi-layer model are the same as those of the OSU two-layer AGCM (Ghan *et al.*, 1982). Therefore, only the differences between the multi-layer and two-layer models are documented below except the treatment of large-scale condensation and convection and radiation scheme in the model which is discussed in Chapter 3 and 4. In the following, the notation and vertical layering are given in Section 2. The basic differential equations and their vertically-differenced forms are presented in Sections 3 and 4, respectively. The the surface fluxes and the subgrid-scale vertical transport are described in Sections 5 and 6, respectively. Finally, the dry convective adjustment is discussed in Section 7.
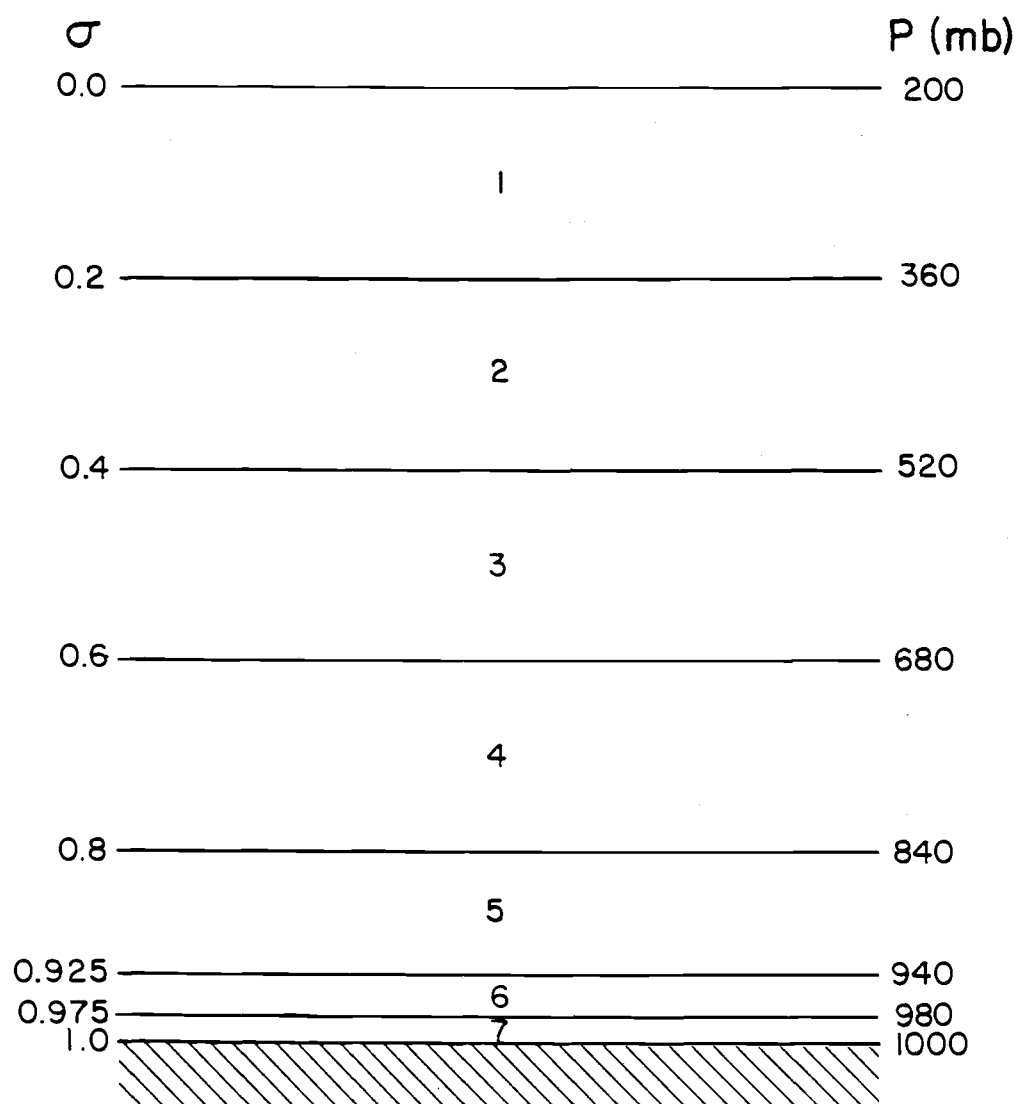
Fig. 1. Vertical structure of the multi-layer model. The values of pressure, except 200 mb, are nominal values.
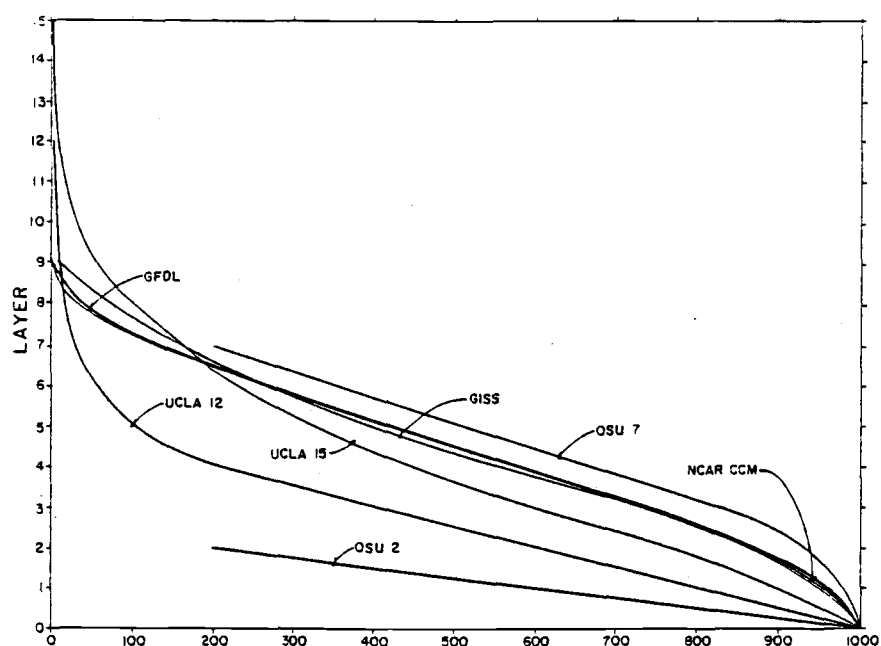
Fig. 2a. The vertical resolution of contemporary national atmospheric
general circulation models. GFDL, Geophysical Fluid Dynamics
Laboratory (Gordon *et al.*, 1982); GISS, Goddard Institute for Space
Studies (Hansen *et al.*, 1983); NCAR CCM, National Center for
Atmospheric Research Community Climate Model (Pitcher *et al.*,
1983); OSU 2, Oregon State University (Schlesinger and Gates,
1980); UCLA 12, University of California, Los Angeles (Arakawa
and Mintz, 1974); UCLA 15 (Mechoso *et al.*, 1982).
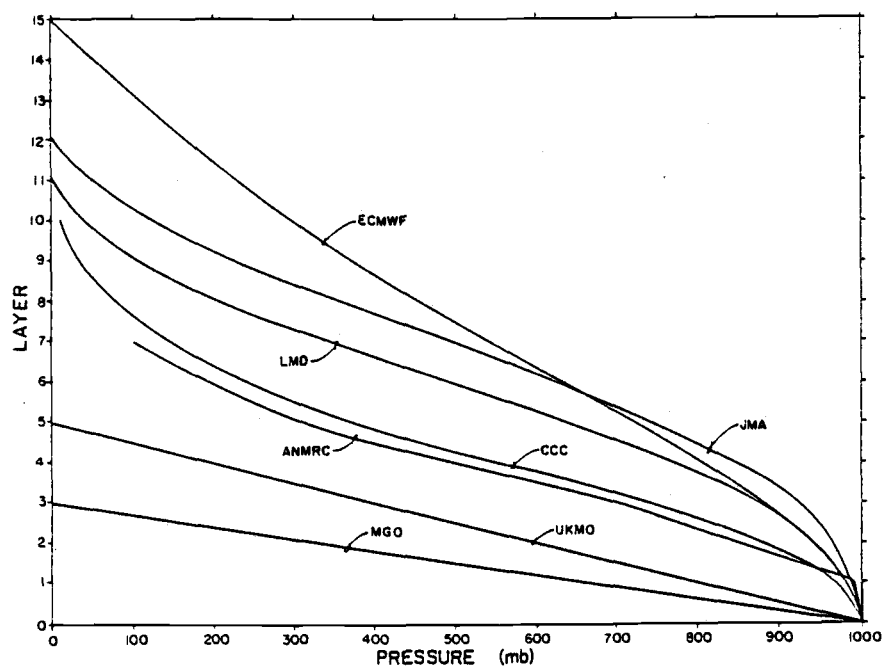
Fig. 2b. The vertical resolution of contemporary international atmospheric general circulation models. ANMRC, Australian Numerical Meteorology Research Centre (Bourke, *et al.*, 1977); CCC, Canadian Climate Centre (Boer *et al.*, 1984); ECMWF, European Centre for Medium Range Weather Forecasts (Louis, 1982); JMA, Japan Meteorological Agency (Kanamitsu *et al.*, 1983); LMD, Laboratoire de Meteorologie Dynamique (Sadourny *et al.*, undated); MGO, Main Geophysical Observatory (Meleshko *et al.*, 1979); UKMO, United Kingdom meteorological Office (Corby *et al.*, 1977).

2. Notation and Vertical Layering

The present model is constructed in the vertical using the σ-coordinate system,

$$\sigma = \frac{p - p_T}{\pi} ,$$

(1)

where p is the pressure, p_T the constant pressure at the top of the model atmosphere and $\pi = p_s - p_T$ is a measure of the variable surface pressure.

As shown in Fig. 3, the model's layers are indexed by integers $\ell = 1, 2,$ ..., L. The levels separating the layers are indexed by the half-integers $\ell = 1/2, 3/2, ..., L+1/2$. The basic variables of the model are carried at the integer levels, with certain additional variables and conditions carried at the half-integer levels.

The primary dependent (prognostic) variables are:

$\mathbf{V}$ = (u,v), horizontal velocity vector
T = temperature
$\pi = p_s - p_T$, surface pressure parameter
q = water vapor mixing ratio

The other dependent (diagnostic) variables are:

Φ = geopotential
α = specific volume
p = pressure
$\dot{\sigma}$ = $d\sigma/dt$, sigma "vertical" velocity

The forcing terms are:

> $\mathbf{F}$ = horizontal frictional force vector per unit mass
>
> $\dot{H}$ = diabatic heating rate per unit mass
>
> $\dot{Q}$ = rate of moisture addition per unit mass

The basic physical constants are:

> Ω = Earth's rotation rate
>
> f = $2\,\Omega \sin \phi$, Coriolis parameter
>
> a = radius of spherical Earth
>
> $\mathbf{k}$ = vertical unit vector
>
> c_p = specific heat at constant pressure for dry air
>
> R = specific gas constant for dry air
>
> g = acceleration of gravity

S_1 R_1

$\ell = 1/2$ ——— Model top, $p = p_T \equiv 200$ mb, $\dot{\sigma} \equiv 0$ ——— $\sigma_{1/2} = 0$

$\ell = 1$

$\ell = 1\,1/2$ ———

$\ell = 2$

$\vdots$

$\ell - 1$

$\ell - 1/2$ ——— $\hat{\sigma}_{\ell-1/2},\ \hat{P}_{\ell-1/2},\ \hat{\Theta}_{\ell-1/2}$

ℓ $\sigma_\ell,\ P_\ell,\ \Theta_\ell,\ \Phi_\ell$

$\ell + 1/2$ ——— $\hat{\sigma}_{\ell+1/2},\ \hat{P}_{\ell+1/2},\ \hat{\Theta}_{\ell+1/2}$

$\ell + 1$ $\dot{H},\ \dot{Q},\ F$

$\vdots$

$\ell = L - 1$

$\ell = L - 1/2$ ———

$\ell = L$ H_s E_s P τ_s S_{L+1} R_{L+1}

$\ell = L + 1/2$ ——— $\hat{\sigma}_{L+1/2} = 1,\ \hat{\Phi}_s$

Earth's surface, $p = p_s$, $\dot{\sigma} = 0$, $\Phi = \Phi_s$
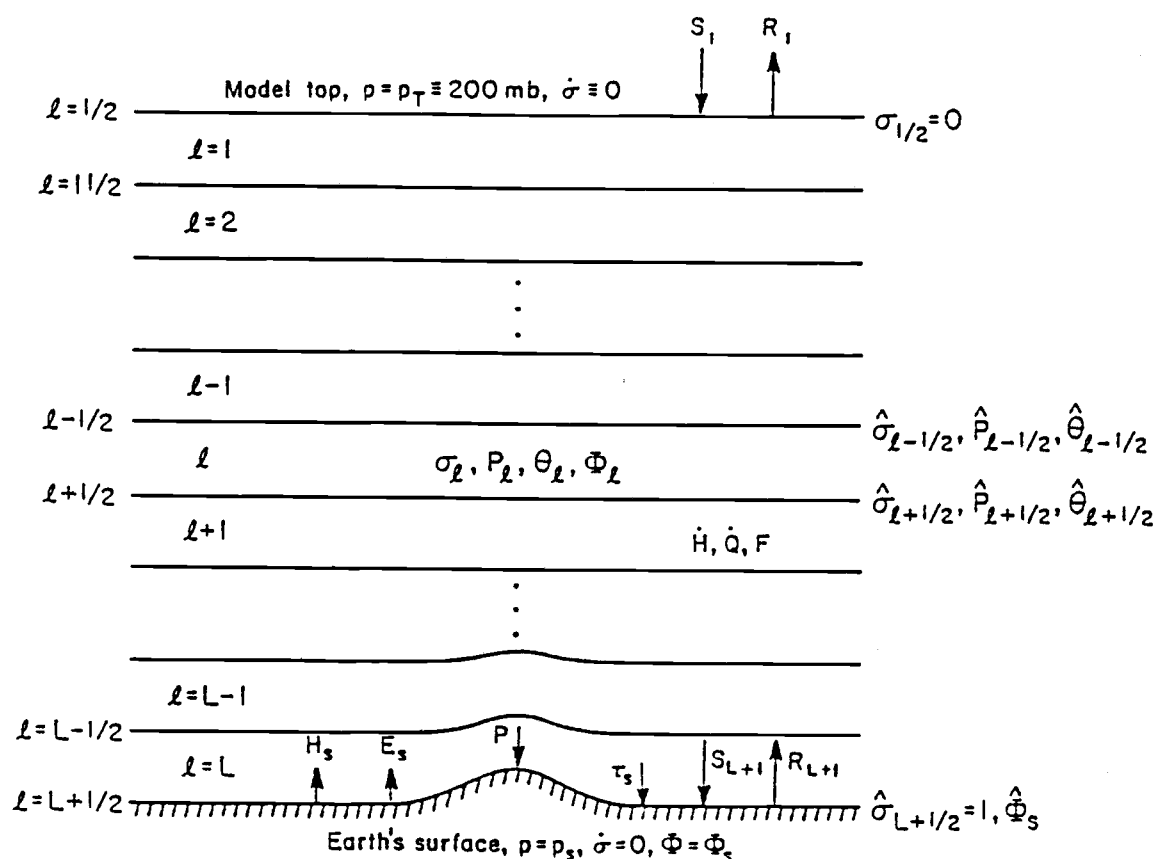
Fig. 3. Vertical indexing of an L-layer model. The model's layers are indexed by integers $\ell = 1, 2, ..., L$. The levels separating the layers are indexed by half-integers $\ell = 1/2, 3/2, ..., L+1/2$. See text for definition of symbols.

3. Differential Equations in σ -Coordinates

The horizontal momentum equation in vector form is

$$\frac{\partial}{\partial t} (\pi \mathbf{V}) + \nabla \cdot (\pi \mathbf{VV}) + \frac{\partial}{\partial \sigma} (\pi \mathbf{V} \dot{\sigma}) + f\mathbf{k} \times \pi \mathbf{V} + \pi \nabla \Phi + \pi \sigma \alpha \nabla \pi = \pi \mathbf{F} , \tag{2}$$

where

$$\nabla \cdot (\pi \mathbf{VV}) = (\pi \mathbf{V} \cdot \nabla) \mathbf{V} + \mathbf{V} \nabla \cdot (\pi \mathbf{V}) \tag{3}$$

is the divergence of the tensor $(\pi \mathbf{VV})$.

The thermodynamic energy equation can be written in the form

$$\frac{\partial}{\partial t} (\pi c_p T) + \nabla \cdot (\pi c_p T \mathbf{V}) + \left(\frac{p}{p_{00}}\right)^{\kappa} \frac{\partial}{\partial \sigma} (\pi c_p \dot{\sigma} \theta) + \pi \sigma \alpha \left(\frac{\partial \pi}{\partial t} + \mathbf{V} \cdot \pi\right) = \pi \dot{H} , \tag{4}$$

where θ, the potential temperature, is defined by

$$\theta = T \left(\frac{p_{00}}{p}\right)^{\kappa} \tag{5}$$

with $P_0 = 1000$ mb a reference pressure and $\kappa = R/c_p = 0.286$.

The mass continuity equation is

$$\frac{\partial \pi}{\partial t} + \nabla \cdot (\pi \mathbf{V}) + \frac{\partial}{\partial \sigma} (\pi \dot{\sigma}) = 0 . \tag{6}$$

and the moisture continuity equation is

$$\frac{\partial}{\partial t} (\pi q) + \nabla \cdot (q \mathbf{V}) + \frac{\partial}{\partial \sigma} (\pi q \dot{\sigma}) = \pi \dot{Q} . \tag{7}$$

Equations (2), (4), (6) and (7) are the four prognostic equations for the dependent variables $\mathbf{V}$, T, π and q. The formulation of the frictional force

(**F**), the heating rate (Ḣ) and the moisture addition rate (Q̇) are considered later. With the addition of the diagnostic equations of state

$$\alpha = \frac{RT}{p} \qquad (8)$$

and hydrostatic balance

$$\frac{\partial \Phi}{\partial \sigma} + \pi \alpha = 0 \qquad (9)$$

and appropriate boundary conditions, the dynamical system in σ-coordinates is complete.

4. Vertically-differenced Equations

The major simplifying feature of the σ-coordinate system lies in the treatment of the lower boundary condition of zero mass flux normal to the earth's surface. In the σ-coordinate system this becomes the condition $\dot{\sigma} = 0$ at $\dot{\sigma} = 1$. In addition, at the isobaric level $p = p_T$, the assumed free surface condition $dp/dt = 0$ becomes $\dot{\sigma} = 0$ at $\sigma = 0$.

The horizontal momentum equation, Eq. (2), is written for layer ℓ with corresponding subscripts as follows:

$$\frac{\partial}{\partial t} (\pi V_\ell) + \nabla \cdot (\pi V_\ell V_\ell) + \frac{\pi}{\Delta \sigma_\ell} (\dot{\sigma}_{\ell+1/2} V_{\ell+1/2} - \dot{\sigma}_{\ell-1/2} V_{\ell-1/2})$$

$$+ \pi f \mathbf{k} \times V_\ell + \pi \nabla \Phi_\ell + \pi \sigma_\ell \alpha_\ell \nabla \pi = \pi F_\ell , \qquad (10)$$

where

$$\Delta \sigma_\ell = \sigma_{\ell+1/2} - \sigma_{\ell-1/2} . \qquad (11)$$

To conserve kinetic energy, insofar as vertical advection is concerned, $V_{\ell+1/2}$ is taken as the arithmetic mean of V_ℓ and $V_{\ell+1}$.

The thermodynamic energy equation (4) for layer ℓ becomes

$$\frac{\partial}{\partial t}(\pi T_\ell) + \nabla \cdot (\pi T_\ell V_\ell) + \frac{\pi}{\Delta\sigma_\ell} P_\ell \left(\dot{\sigma}_{\ell+1/2}\, \theta_{\ell+1/2} - \dot{\sigma}_{\ell-1/2}\, \theta_{\ell-1/2}\right)$$

$$-\frac{\pi\,\alpha_\ell\,\delta_\ell}{c_p}\left(\frac{\partial\pi}{\partial t} + V_\ell \cdot \nabla\pi\right) = \frac{\pi\,\dot{H}_\ell}{c_p} \ . \tag{12}$$

To conserve the global integral of θ with respect to mass under adiabatic, frictionless conditions (Arakawa and Suarez, 1983), $\theta_{\ell+1/2}$ is taken as

$$\theta_{\ell+1/2} = \frac{(P_\ell - P_{\ell+1/2})\,\theta_{\ell+1} + (P_{\ell+1/2} - P_\ell)\,\theta_\ell}{P_{\ell+1} - P_\ell} \ , \tag{13}$$

where

$$\hat{P}_{\ell+1/2} = \left(\frac{\hat{p}_{\ell+1/2}}{p_{00}}\right)^\kappa , \tag{14}$$

and

$$P_\ell = \frac{1}{1+\kappa}\left(\frac{p_{\ell+1/2}\,P_{\ell+1/2} - p_{\ell-1/2}\,\hat{P}_{\ell-1/2}}{p_{\ell+1/2} - p_{\ell-1/2}}\right), \quad \ell = 1, ..., L \ , \tag{15}$$

with $p_{\ell\pm1/2}$ given by Eq. (1) and $\sigma_{\ell\pm1/2}$.

With the boundary conditions $\dot{\sigma} = 0$ at $\sigma = 0, 1$ the mass continuity Equation (6) yields a prognostic equation for the surface pressure

$$\frac{\partial \pi}{\partial t} = - \sum_{\ell=1}^{L} [\Delta\sigma_\ell \, \nabla \cdot (\pi \mathbf{V})]$$

(16)

and a diagnostic equation for the vertical velocity (Arakawa, 1972)

$$\dot{\sigma}_{\ell+1/2} = - \frac{\Delta\sigma_\ell}{\pi} \sum_{\ell=1}^{\ell} \left[\frac{\partial \pi}{\partial t} + \nabla \cdot (\pi \mathbf{V}) \right] .$$

(17)

From the hydrostatic equation (9) the geopotential at level ℓ can be written as (Arakawa and Suarez, 1983)

$$\Phi_L - \Phi_S = c_p \, (P_{L+1/2} - P_L) \, \theta_L \, ,$$

(18)

$$\Phi_\ell - \Phi_{\ell+1} = c_p \, [\theta_\ell \, (\hat{P}_{\ell+1/2} - P_\ell) + \theta_{\ell+1} \, (P_{\ell+1} - \hat{P}_{\ell+1/2})] \, , \quad \ell = 1, ..., L-1,$$

(19)

where Φ_S is the geopotential of the earth's surface.

The moisture continuity equation (7) for layer ℓ can be written as

$$\frac{\partial}{\partial t} \, (\pi q_\ell) + \nabla \cdot (\pi q_\ell \mathbf{V}_\ell) + \frac{\pi}{\Delta\sigma_\ell} \, (\dot{\sigma}_{\ell+1/2} \, \hat{q}_{\ell+1/2} - \dot{\sigma}_{\ell-1/2} \, \hat{q}_{\ell-1/2}) = \pi \, \dot{Q} \, .$$

(20)

The mixing ratio at the half-integer levels $\hat{q}_{\ell+1/2}$ is taken as the arithmetic mean

$$\hat{q}_{\ell+1/2} = \frac{1}{2} \, (q_\ell + q_{\ell+1}) \, .$$

(21)

This guarantees the conservation of the global integral of q^2 with respect to mass, but tends to generate negative mixing ratios by time truncation error where the mass flux is directed from low toward high mixing ratios, i.e. up

the water vapor gradient. To prevent the generation of negative mixing ratio, $\hat{q}_{\ell+1/2}$ is modified as

$$
\hat{q}_{\ell+1/2} = \begin{cases} \text{Min}\left[\hat{q}_{\ell+1/2},\ \dfrac{(1-\varepsilon)\,q_\ell}{-\dfrac{\Delta t}{\delta_\ell\sigma}\,\dot{\sigma}_{\ell+1/2}}\right], & \text{for } \dot{\sigma}_{\ell+1/2} \geq 0, \\[4ex] \text{Min}\left[\hat{q}_{\ell+1/2},\ \dfrac{(1-\varepsilon)\,q_{\ell+1}}{-\dfrac{\Delta t}{\delta_\ell\sigma}\,\dot{\sigma}_{\ell+1/2}}\right], & \text{for } \dot{\sigma}_{\ell+1/2} < 0. \end{cases}
$$

(22)

5. Surface Fluxes

The turbulent fluxes of momentum τ_s, sensible heat H_s, and moisture E_s at the earth's surface are parameterized by the bulk aerodynamic method as

$$\tau_s = \rho_s\, C_D\, |\mathbf{V}_s|\, \mathbf{V}_s,$$

(23)

$$H_s = \rho_s\, c_p\, C_H\, |\mathbf{V}_s|\, (T_g - T_L),$$

(24)

$$E_s = \rho_s\, C_E\, |\mathbf{V}_s|\, \beta\, (q^*_g - q_L),$$

(25)

where ρ_s is the surface air density, C_D the surface drag coefficient, C_H the heat transfer coefficient, C_E the moisture transfer coefficient, $|\mathbf{V}_s|$ the surface wind speed, $\mathbf{V}_s$ the surface wind vector, $q^*_g = q^*(T_g)$, and β the ratio of the actual evapotranspiration to the potential evapotranspiration.

The surface wind is given by

$$\mathbf{V}_s = 0.85\left[\mathbf{V}_L + \frac{\mathbf{V}_L - \mathbf{V}_{L-1}}{\sigma_L - \sigma_{L-1}}(1 - \sigma_L)\right].$$

(26)

The coefficients C_D, C_H and C_E are given by

$$C_D = C_{DN} F_D, \tag{27}$$

$$C_E = C_H = C_{DN} F_H, \tag{28}$$

where

$$C_{DN} = \begin{cases} 0.002\,(1 + 3\,z_s/5000), & \text{for nonwater surfaces}, \\ \\ \text{Min}\,[0.001\,(1 + 0.07\,|\mathbf{V}_s|\,), 0.0025\}, & \text{for over water surfaces}, \end{cases} \tag{29}$$

where z_s is the surface elevation (in meters). The coefficients F_D and F_H depended on the Richardson's number are defined as

$$F_D = \begin{cases} 1 - \dfrac{9.4\,Ri_B}{1 + 69.6\,C_{DN}\,(z_L/z_0)^{1/2}\,|\,Ri_B\,|^{1/2}}, & \text{for } Ri_B < 0, \\ \\ 1, & \text{for } Ri_B \ge 0, \end{cases} \tag{30}$$

and

$$0.74\,F_D = \begin{cases} 1 - \dfrac{9.4\,Ri_B}{1 + 49.8\,C_{DN}\,(z_L/z_0)^{1/2}\,|\,Ri_B\,|^{1/2}}, & \text{for } Ri_B < 0 \\ \\ 1, & \text{for } Ri_B \ge 0 \end{cases} \tag{31}$$

from Louis (1979) with

$$Ri_B = \frac{g \, z_L \, (T_L - T_g)}{0.5 \, (T_L + T_g) \, |V_s|^2} \, , \tag{32}$$

and z_0 the surface roughness defined as

$$z_0 = z_{0,st} + z_{0,top} \, . \tag{33}$$

The surface type roughness $z_{0,st}$ shown in Table 1 and the topographic roughness

$$z_{0,top} = 0.041 \Sigma^{0.71} \tag{34}$$

are based on Hansen *et. al.* (1983), where Σ is the standard deviation of the Gates and Nelson (1975) 1° x 1° surface heights within the model's 4° x 5° grid boxes.

To prevent excessively large surface fluxes the following constraints are imposed:

$$F_D \text{ and } F_H \leq 4 \, , \qquad \text{over nonwater surfaces} \, ,$$
$$C_D, \, C_E \text{ and } C_H \leq 0.005 \, , \quad \text{over water surfaces} \, . \tag{35}$$

Following Arakawa (1972) the coefficient β depends on the ground wetness w according to

$$\beta = \text{Min} \, (2w, 1) \tag{36}$$

with $\beta = 1$ for a snow-covered surface or when $q_L > q^*_g$ (dew deposit).

Table 1. Surface type roughness.

	Surface Type Description	$z_{0\,st}$(meters)
1	Woodland, grass, cultivation	0.32
2	Forest	1
3	Steppe and grassland	0.018
4	Steppe desert	0.01
5	Desert	0.005
6	Tundra, Mountains, Arctic flora	0.01
7	Water	$7.48 \times 10^{-7}\,V_s^{2.46}$
8	Land ice	4.3×10
9	Sea ice	4.3×10

6. Subgrid-scale Vertical Transport

The subgrid-scale vertical transport of momentum, sensible heat and moisture is parameterized as a diffusive process governed by

$$\frac{\partial Q}{\partial t} = -\frac{1}{\rho}\frac{\partial R}{\partial z} = \frac{g}{\pi}\frac{\partial F_Q}{\partial \sigma}\, , \tag{37}$$

where Q represents **V**, T or q and

$$F_Q = -\rho\,K\,\frac{\partial Q}{\partial t} = \frac{\rho^2\,g}{\pi}\,K\,\frac{\partial Q}{\partial \sigma} \tag{38}$$

and K is an eddy diffusivity. Substituting Eq. (38) into Eq. (37) and using centered differencing in space and backward differencing in time (for stability) with $F_Q = 0$ at $\sigma = 0$ and $F_Q = (F_Q)_s$ at $\sigma = 1$ gives

$$
\frac{Q_\ell^{(n+1)} - Q_\ell^n}{\Delta t} = \begin{cases}
\left(\dfrac{g}{\pi}\right)^2 \dfrac{1}{\delta_1 \sigma} \left[\rho_{3/2}^2 K_{3/2} \dfrac{Q_2^{(n+1)} - Q_1^{(n+1)}}{\sigma_2 - \sigma_1} \right], & \text{for } \ell = 1, \\[2ex]
\left(\dfrac{g}{\pi}\right)^2 \dfrac{1}{\delta_\ell \sigma} \left[\rho_{\ell+1/2}^2 K_{\ell+1/2} \dfrac{Q_{\ell+1}^{(n+1)} - Q_\ell^{(n+1)}}{\sigma_{\ell+1} - \sigma_\ell} \right. \\[2ex]
\qquad \left. -\rho_{\ell-1/2}^2 K_{\ell-1/2} \dfrac{Q_\ell^{(n+1)} - Q_{\ell-1}^{(n+1)}}{\sigma_\ell - \sigma_{\ell-1}} \right], \\[3ex]
\qquad\qquad\qquad\qquad\qquad \text{for } \ell = 2, \dots, L-1, \\[3ex]
\left(\dfrac{g}{\pi}\right) \dfrac{1}{\delta_L \sigma} \left[(F_Q)_s - \left(\dfrac{g}{\pi}\right) \rho_{L-1/2}^2 K_{L-1/2} \dfrac{Q_L^{(n+1)} - Q_{L-1}^{(n+1)}}{\sigma_L - \sigma_{L-1}} \right], \\[3ex]
\qquad\qquad\qquad\qquad\qquad \text{for } \ell = L,
\end{cases}
\tag{39}
$$

where from Eqs. (23) - (25)

$$
(F_Q)_s = \begin{cases}
-\rho_s C_D \left| \mathbf{V}_s^{(n)} \right| \mathbf{V}_s^{(n+1)}, & \text{for } Q = \mathbf{V}, \\[1ex]
\rho_s c_p C_H \left| \mathbf{V}_s^{(n)} \right| (T_g^{(n+1)} - T_L^{(n+1)}), & \text{for } Q = T, \\[1ex]
\rho_s C_E \left| \mathbf{V}_s^{(n)} \right| \beta \, (q_g^{*(n)} - q_L^{(n+1)}), & \text{for } Q = q.
\end{cases}
\tag{40}
$$

Equation (39) can be written as

$$
\begin{aligned}
A_1 Q_1^{(n+1)} + B_1 Q_2^{(n+1)} &= D_1, & &\text{for } \ell = 1, \\
A_\ell Q_{\ell-1}^{(n+1)} + B_\ell Q_\ell^{(n+1)} + C_\ell Q_{\ell+1}^{(n+1)} &= D_\ell, & &\text{for } \ell = 2, \dots, L-1, \\
A_L Q_{L-1}^{(n+1)} + B_L Q_L^{(n+1)} &= D_L, & &\text{for } \ell = L.
\end{aligned}
\tag{41}
$$

where the coefficients are

$$A_1 = 1 + \left(\frac{g}{\pi}\right)^2 \frac{\Delta t}{\delta_1 \sigma} \left[\frac{\rho_{3/2}^2 \, K_{3/2}}{\sigma_2 - \sigma_1}\right], \qquad \text{for } \ell = 1 \, ,$$

$$A_\ell = -\left(\frac{g}{\pi}\right)^2 \frac{\Delta t}{\delta_\ell \sigma} \left[\frac{\rho_{\ell-1/2}^2 \, K_{\ell-1/2}}{\sigma_\ell - \sigma_{\ell-1}}\right], \qquad \text{for } \ell = 2, ..., L-1 \, ,$$

$$-\left(\frac{g}{\pi}\right)^2 \frac{\Delta t}{\delta_L \sigma} \left[\frac{\rho_{L-1/2}^2 \, K_{L-1/2}}{\sigma_L - \sigma_{L-1}}\right], \qquad \text{for } Q = T \text{ and } q \, ,$$

$$A_L = \left\{ -\left(\frac{g}{\pi}\right)^2 \frac{\Delta t}{\delta_L \sigma} \left[\frac{\rho_{L-1/2}^2 \, K_{L-1/2}}{\sigma_L - \sigma_{L-1}}\right] - \rho_s \, C_D \, |V_s^{(n)}| \frac{1 - \sigma_L}{\sigma_L - \sigma_{L-1}} \frac{g}{\pi} \frac{\Delta t}{\delta_L \sigma} \, , \right.$$

$$\text{for } Q = V \, , \tag{42}$$

$$B_1 = 1 + \left(\frac{g}{\pi}\right)^2 \frac{\Delta t}{\delta_1 \sigma} \left[\frac{\rho_{3/2}^2 \, K_{3/2}}{\sigma_2 - \sigma_1}\right], \qquad \text{for } \ell = 1 \, ,$$

$$B_\ell = 1 + \left(\frac{g}{\pi}\right)^2 \frac{\Delta t}{\delta_\ell \sigma} \left[\frac{\rho_{\ell+1/2}^2 \, K_{\ell+1/2}}{\sigma_{\ell+1} - \sigma_\ell} + \frac{\rho_{\ell-1/2}^2 \, K_{\ell-1/2}}{\sigma_\ell - \sigma_{\ell-1}}\right], \quad \text{for } \ell = 2, ..., L-1 \, ,$$

$$B_L = 1 + \left(\frac{g}{\pi}\right)^2 \frac{\Delta t}{\delta_L \sigma} \left[\frac{\rho_{L-1/2}^2 \, K_{L-1/2}}{\sigma_L - \sigma_{L-1}}\right] + \frac{g}{\pi} \frac{\Delta t}{\delta_L \sigma} \mu \, , \qquad \text{for } \ell = L \, ,$$

$$\tag{43}$$

where

$$\mu = \begin{cases} \rho_s \, C_D \, |V_s^{(n)}| \left[1 + \dfrac{1 - \sigma_L}{\sigma_L - \sigma_{L-1}}\right], & \text{for } Q = V \, , \\[2ex] \rho_s \, c_p \, C_H \, |V_s^{(n)}| \, , & \text{for } Q = T \, , \\[2ex] \rho_s \, C_E \, |V_s^{(n)}| \, \beta \, , & \text{for } Q = q \, , \end{cases} \tag{44}$$

$$C_\ell = -\left(\frac{g}{\pi}\right)^2 \frac{\Delta t}{\delta_\ell \sigma} \left[\frac{\rho_{\ell+1/2}^2 \, K_{\ell+1/2}}{\sigma_{\ell+1} - \sigma_\ell}\right], \qquad \ell = 2, ..., L-1, \tag{45}$$

$$D_\ell = Q_\ell^{(n)} , \qquad \text{for } \ell = 1, ..., L-1,$$

$$D_L = Q_L^{(n)} + \frac{g}{\pi} \frac{\Delta t}{\delta_L \sigma} \upsilon ,$$

(46)

with

$$\upsilon = \begin{cases} 0 , & \text{for } Q = \mathbf{V} , \\ \rho_s \, c_p \, C_H \, |\mathbf{V}_s^{(n)}| T_g^{(n)} , & \text{for } Q = T , \\ \rho_s \, C_E \, |\mathbf{V}_s^{(n)}| \, \beta \, q_g^{*(n)} , & \text{for } Q = q . \end{cases}$$

(47)

Similar to the OSU two-level atmospheric GCM, the surface heat balance for a nonwater surface is given in the form

$$\Gamma \frac{T_g^{n+1} - T_g^n}{\Delta t} = F(T_g^{n+1})$$

$$\cong F(T_g^n) + \left(\frac{dF}{dT_g} \right)_{T_g^n} (T_g^{n+1} - T_g^n) ,$$

(48)

where

$$F(T_g) = S_{L+1/2} - R_{L+1/2} - \rho_s \, c_p \, C_H \, |\mathbf{V}_s| (T_g - T_L)$$

$$- L \, \rho_s \, C_E \, |\mathbf{V}_s| \, \beta \, (q_g^* - q_L) - \frac{K_{ice}}{D} (T_g - T_d) ,$$

(49)

$$\frac{dF}{dT_g} = -4 \, \sigma \, T_g^3 - \rho_s \, c_p \, C_H \, |\mathbf{V}_s| - L \, \rho_s \, C_E \, |\mathbf{V}_s| \, \beta \, \frac{q_g^*}{T_g} - \frac{K_{ice}}{D} ,$$

(50)

and

$$\Gamma = \left(\frac{2 \, k \, c}{\Omega} \right)^{1/2}$$

(51)

is the bulk thermal heat capacity over the e-folding depth of the diurnal temperature wave the skin depth $d = (2k/\Omega c)^{1/2}$, k is the thermal conductivity, Ω the frequency of diurnal forcing, c the specific volumetric heat capacity, D the sea ice thickness (prescribed as 3 m) and T_d the sea-surface temperature below the ice (prescribed as 271.5 K).

For a nonwater surface, the ground temperature, T_g, described in (48) is included in (39) through (40). Then the last equation in (41) is replaced by

$$A_L T_{L-1}^{n+1} + B_L T_L^{n+1} + C_L T_g^{n+1} = D_L^n ,$$

$$A_{L+1} T_L^{n+1} + B_{L+1} T_g^{n+1} = D_{L+1}^n , \qquad (52)$$

where

$$C_L = -\frac{g}{\pi} \frac{1}{\delta_L \sigma} \rho_s c_p C_H |V_s^{(n)}| ,$$

$$D_L = T_L^n ,$$

$$A_{L+1} = -\frac{\rho_s c_p C_H |V_s^{(n)}|}{\Gamma - \left(\dfrac{\partial F}{\partial T_g}\right)_{T_g^n} \Delta t} ,$$

$$B_{L+1} = 1 + \frac{\rho_s c_p C_H |V_s^{(n)}| + \dfrac{K_{ice}}{D}}{\Gamma - \left(\dfrac{\partial F}{\partial T_g}\right)_{T_g^n} \Delta t} ,$$

and

$$D_{L+1} = 1 + \frac{L \rho_s C_E |V_s^{(n)}| \beta (q_g^{*(n)} - q_L^{(n+1)}) - \dfrac{K_{ice}}{D} T_d}{\Gamma - \left(\dfrac{dF}{dT_g}\right)_{T_g^n} \Delta t} . \qquad (53)$$

The tridiagonal matrix equations (41) are solved using the method of Lindzen and Kuo (1969).

The eddy diffusivity for the free atmosphere is prescribed on the basis of the following considerations. For the purpose of the cloud parameterization

it is desirable to have a physically-based parameterization of cumulus convection in which there can be an explicit budget for cloud water. For this reason the Arakawa-Schubert-Lord (ASL) cumulus parameterization (Artakawa and Schubert, 1974; Lord, 1978) was selected. The ASL scheme requires that the free atmosphere not be conditionally unstable, and this requires a parameterization for middle-level convection (convection not based in the planetary boundary layer) and dry convection. The latter removes any dry instability. The resulting stability of the atmosphere makes it virtually useless to use a stability-dependent eddy diffusivity such as that proposed by Louis (1979) and used in the ECMWF model. Consequently, a stability-independent or "background" eddy diffusivity is determined from a "background" eddy viscosity μ_B (= K/ρ = 0.01 mb sec). For the boundary layer (ℓ =5, 6, 7) the eddy diffusivity is chosen as the larger value between a boundary layer "background" eddy viscosity (μ_B = 0.04 mb sec) and the value defined in terms of a mixing length ℓ and the magnitude of wind shear according to

$$K = \rho \, \frac{g}{\pi} \, \ell^2 \, \left| \frac{\partial V}{\partial \sigma} \right| .$$

(54)

Similar to the GFDL model (Gordon *et al.*, 1982), ℓ is taken to decrease linearly from 30 m at level σ_7 to zero at level $\sigma_{4+1/2}$

7. Dry Convective Adjustment

Following the subgrid-scale vertical diffusion of heat, momentum and water vapor, any residual dry adiabatic instability, $\theta_{\ell_1} < \theta_{\ell_2}$, $\ell_1 < \ell_2$ is removed by dry convective adjustment. This is necessary to prevent the removal of the absolute (dry) instability by the physical processes that remove conditional (moist) instability, namely the mid-level and penetrating convection described in the following two sections.

In the dry convective adjustment the dry static energy is conserved, that

is,

$$\sum_{\ell=\ell_1}^{\ell_2} (T_\ell + \Delta T_\ell)\, \delta_\ell \sigma \;=\; \sum_{\ell=\ell_1}^{\ell_2} T_\ell\, \delta_\ell \sigma \;,$$

or

$$\sum_{\ell=\ell_1}^{\ell_2} \Delta T_\ell\, \delta_\ell \sigma \;=\; 0 \;, \tag{55}$$

where ΔT_ℓ is the temperature change due to the adjustment, and the potential temperature is uniformly mixed to remove the gradient such that

$$\theta_\ell' \;=\; \bar{\theta} \;=\; \theta_\ell + \Delta T_\ell\, P_\ell \;,\; \ell_1 \le \ell \le \ell_2 \;, \tag{56}$$

where θ_ℓ' is the adjusted potential temperature and P_ℓ is defined by Eq. (15). Combining Eqs. (55) and (56) gives

$$\theta_\ell' \;=\; \frac{\displaystyle\sum_{\ell=\ell_1}^{\ell_2} T_\ell\, \delta_\ell \sigma}{\displaystyle\sum_{\ell=\ell_1}^{\ell_2} \frac{\delta_\ell \sigma}{P_\ell}} \;. \tag{57}$$

The adjusted temperature T_ℓ' is then given by (56) as

$$T_\ell' \;=\; \frac{\theta_\ell'}{P_\ell} \;,\; \ell_1 \le \ell \le \ell_2 \;. \tag{58}$$

Dry adiabatically unstable layers are adjusted as described above progressing from the bottom to the top of the model in a repetitive manner until there are no unstable layers remaining.

REFERENCES

Arakawa, A., 1972: Design of the UCLA general circulation model. Technical Report No. 7, Department of Meteorology, University of California, Los Angeles, CA, 116 pp.

Arakawa, A., and Y. Mintz, 1974: The UCLA atmospheric general circulation model. Department of Meteorology, UCLA, Los Angeles, CA, 90024.

Arakawa, A., and W. H. Schubert, 1974: Interaction of a cumulus cloud ensemble with the large scale environment, Part I. *J. Atmos. Sci.*, **31**, 674-701.

Arakawa, A., and M. J. Suarez, 1983: Vertical differencing of the primitive equations in sigma-coordinates. *Mon. Wea. Rev.*, **111**, 34-45.

Boer, G. J., N. A. McFarlane, R. Laprise, J. D. Henderson and J.-P. Blanchet, 1984: The Canadian Climate Centre spectral atmospheric general circulation model. *Atmosphere-Ocean*, **22**, 397-429.

Bourke, W., B. McAvaney, K. Puri and R. Thurling, 1977: Global modeling of atmospheric flow by spectral methods. In *Methods in Computational Physics*, **Vol. 17**, J. Chang, Ed., Academic Press, pp. 268-324.

Corby, G. A., A. Gilchrist and P. R. Rowntree, 1977: United Kingdom Meteorological Office five-level general circulation model. In *Methods in Computational Physics*, **Vol. 17**, J. Chang (ed.), Academic Press, New York, pp. 67-110.

Gates, W. L., and A. B. Nelson, 1975: A new (revised) tabulation of the Scripps topography on a 1 global grid. Part 1: Terrain heights. R-1276-1-ARPA, The Rand Corporation, Santa Monica, CA, 132 pp.

Ghan, S. J., J. W. Lingaas, M. E. Schlesinger, R. L. Mobley and W. L. Gates, 1982: A documentation of the OSU two-level atmospheric general circulation model. Report No. 35, Climatic Research Institute, Oregon State University, Corvallis, OR, 395 pp.

Gordon, C. T., and F. W. Stern, 1982: A description of the GFDL global spectral model. *Mon. Wea. Rev.*, **110**, 625-644.

Hansen, J., G. Russell, D. Rind, P. Stone, A. Lacis, S. Lebedeff, R. Ruedy

and L. Travis, 1983: Efficient three-dimensional global models for climate studies: Models I and II. *Mon. Wea. Rev.*, **111**, 609-662.

Kanamitsu, M., K. Tada, T. Kuda, N. Sato and S. Isa, 1983: Description of the JMA operational spectral model. *J. Meteor. Soc. of Japan*, 61, 812-827.

Lindzen, R. S., and H. L. Kuo, 1969: A reliable method for the numerical integration of a large class of ordinary and partial differential equations. *Mon. Wea. Rev.*, **97**, 732-734.

Lord, S. J., 1978: Development and observational verification of a cumulus cloud parameterization. Ph.D. dissertation, Department of Atmospheric Sciences, University of California, Los Angeles, CA, 359 pp.

Louis, J.-F., 1979: A parametric model of vertical eddy fluxes in the atmosphere. *Boundary Layer Meteor.*, **17**, 187-202.

Louis, J. F. (Ed.), 1982: ECMWF Forecast Model Documentation Manual, Volume 1, Theoretical Bases. European Centre for Medium Range Weather Forecasts, Reading, United Kingdom, 155 pp.

Mechoso, C. R., M. J. Suarez, K. Yamazaki, J. A. Spahr and A. Arakawa, 1982: A study of the sensitivity of numerical forecasts to an upper boundary in the lower stratosphere. *Mon. Wea. Rev.*, **110**, 1984-1993.

Meleshko, V. R., B. E. Shneerov, M. E. Shvets, L. R. Dmitrieva, G. V. Parshina, C. V. Bogachenko, V. A. Ponomarev, E. P. Yushina, L. H. Magazenkov and D. A. Sheinin, 1979: Simulation of January climate with a MGO general circulation model. In *Report of the JOC Study Conference on Climate Models: Performance, Intercomparison and Sensitivity Studies.* **Vol. 1**, GARP Publications Series No. 22, W. L. Gates, Ed., World Meteorological Organization, 371-408.

Pitcher, E. J., R. C. Malone, V. Ramanathan, M. L. Blackmon, K. Puri, and W. Bourke, 1983: January and July simulations with a spectral general circulation model. *J. Atmos. Sci.,* **40**, 580-604.

Sadourny, R, and K. Laval, undated: January and July performance of the LMD general circulation model. Laboratoire de Meteorologie Dynamique, Paris, 28 pp.

Schlesinger, M. E., and W. L. Gates, 1979: Numerical simulation of the January and July global climate with the OSU two-level atmospheric

general circulation model. Report No. 9, Climatic Research Institute, Oregon State University, Corvallis, OR, 102 pp.

Schlesinger, M. E., and W. L. Gates, 1980: The January and July performance of the OSU two-level atmospheric general circulation model. *J. Atmos. Sci.*, **37**, 1914-1943.

Schlesinger, M. E., and W. L. Gates, 1981: Preliminary analysis of the mean annual cycle and interannual variability simulated by the OSU two-level atmospheric general circulation model. Report No. 23, Climatic Research Institute, Oregon State University, Corvallis, OR, 47 pp.

Appendix B

SOLAR RADIATION PARAMETERIZATION FOR THE OSU MULTI-LAYER ATMOSPHERIC GCM

Table of Contents

List of Figures

1. Introduction

Solar radiation absorbed at the Earth's surface and in the atmosphere is the initial source of energy for the climate system. The major difficulty in computing the absorption of solar radiation is correctly incorporating the effects of multiple scattering. King and Harshvardhan (1986) concluded that the two-stream/delta-Eddington method is the most suitable for use in general circulation models in which it is most important to have accurate computations for moderately thick cloud layers and over a wide range of solar zenith angles. Here we describe the design of such a two-stream /delta-Eddington method for the OSU multi-layer atmospheric GCM.

2. Parameterization of the Solution of the Radiative Transfer Equation

The azimuthally-independent monochromatic radiative transfer equation is usually written in the form (Liou, 1980)

$$\mu \frac{dI(\delta,\mu)}{d\delta} = I(\delta,\mu) - \frac{\tilde{\omega}_0}{2} \int_{-1}^{1} P(\mu,\mu')\ I(\delta,\mu')\ d\mu' - \frac{S_\infty}{4\pi}\ P(\mu,\mu_0)\ \exp(-\delta/\mu_0)\ , \tag{1}$$

where $I(\delta,\mu)$ is the radiance in the direction $\mu = \cos \zeta$ (ζ = zenith angle) through the level defined by the optical depth

$$\delta = \int_{z}^{\infty} k\,\rho\,dz\ , \tag{2}$$

S_∞ is the solar flux associated with the collimated beam incident at direction μ_0 on the top of the atmosphere, P is the scattering phase function of the particle (air molecule or aerosol), and $\tilde{\omega}_0$ is its single scattering albedo, that is, the ratio of the scattering optical depth d_s to the total optical depth $\delta = \delta_s + \delta_a$, where δ_a is the absorption optical depth. Thus, $\tilde{\omega}_0 = 1$ for a nonabsorbing layer and $\tilde{\omega}_0 = 0$ when scattering is negligible. Also, $1 - \tilde{\omega}_0$

is the fraction of the incident radiation absorbed by the particle.

To determine the solar heating of the atmosphere and the surface in a GCM requires the upward and downward fluxes, F^+ and F^-, given by

$$F^{\pm}(\delta) = \int_0^1 \mu\, I(\delta, \pm\mu)\, d\mu \,.$$

(3)

To determine these fluxes from Eq. (1) requires the evaluation of the integrals with respect to both μ' and μ, plus integration with respect to δ and ultimately wavelength. Because of the need to determine the fluxes at thousands of grid points over the Earth's surface, and at many times during a day, the direct solution of Eqs. (1) and (3) is impractical for a GCM. Therefore, to economize on computer time, we use the two-stream approximation described below.

2.1. Two-stream approximation

In the two-stream approximation, originally developed by Schuster (1905), Eq. (1) is first integrated over the upward and downward hemispheres to obtain the following equations for the fluxes

$$\frac{dF^+(\delta)}{d\delta} = \alpha_1\, F^+(\delta) - \alpha_2\, F^-(\delta) - \alpha_3\, S(\delta)/\mu_0 \,,$$

(4a)

$$\frac{dF^-(\delta)}{d\delta} = \alpha_2\, F^+(\delta) - \alpha_1\, F^-(\delta) + \alpha_4\, S(\delta)/\mu_0 \,,$$

(4b)

$$\frac{dS(\delta)}{d\delta} = -\frac{S(\delta)}{\mu_0} \,,$$

(4c)

where the α_i coefficients contain hemispheric integrals of the form

$$\int_0^{\pm 1} P(\mu,\mu') \, I(\delta,\mu') \, d\mu' \ ,$$

and S is the downward parallel flux of solar radiation. These equations are then directly solved for the required fluxes.

There are many two-stream approximations as given by Eqs. (4) which differ in the approximation assumed for the phase function $P(\mu,\mu')$ (see, for example, Stephens, 1984). In the following section we describe one such approximation, the delta-Eddington approximation, and why it has been selected.

2.2. Delta-Eddington approximation

The solution of Eqs. (4) is relatively economical to obtain and is relatively accurate over the entire parameteric ranges of δ, $\tilde{\omega}_0$ and g, where the latter is the asymmetry factor defined as

$$g = \frac{1}{2} \int_{-1}^{+1} P(\mu,\mu') \, d\mu \ , \tag{5}$$

which varies from -1 for complete backscatter, to 0 for isotropic scatter, to +1 for complete forward scatter. However, difficulties such as negative albedos can occur for optically thin atmospheres using most of the approximations for the phase function. To avoid this, Joseph *et al.* (1976) introduced the following approximation for the phase function

$$P(\mu,\mu') \cong 2 \, f \, \delta_{\mu,\mu'} + (1-f)(1+3 \, g' \, \mu \, \mu') \ , \tag{6}$$

where $f = g^2$ is the fractional scattering into the forward peak and $\delta_{\mu,\mu'}$ is the Dirac delta function. This phase function simply redefines the optical depth, the single scattering albedo and the asymmetry factor of the two-stream equations to be

$$\delta \rightarrow \delta' = (1 - \tilde{\omega}_0 \ f) \, \delta \, ,$$

$$\tilde{\omega}_0 \rightarrow \tilde{\omega}_0' = (1 - f) \, \tilde{\omega}_0 \ / (1 - \tilde{\omega}_0 \ f) \, ,$$

$$g \rightarrow g' = g / (1 + g) \, . \tag{7}$$

The α_i coefficients resulting in Eqs. (4) from this delta-Eddington method are

$$\alpha_1 = \frac{1}{4} \, [7 - \tilde{\omega}_0' \, (4 + 3 \ g')] \, ,$$

$$\alpha_2 = -\frac{1}{4} \, [1 - \tilde{\omega}_0' \, (4 - 3 \ g')] \, ,$$

$$\alpha_3 = \frac{1}{4} \, (2 - 3 \ g' \ \mu_0) \, \tilde{\omega}_0'^2 \, ,$$

$$\alpha_4 = \tilde{\omega}_0' - \alpha_3 \, . \tag{8}$$

To determine these α_i coefficients it is necessary to know μ_0, δ, $\tilde{\omega}_0$ and g. The calculation of μ_0 is described in the following section and the expressions for δ, $\tilde{\omega}_0$ and g are presented in section 3.

2.3. Vertical discretization

At the top of the atmosphere the solar flux S_∞ is given by

$$S_\infty = \bar{S}_\infty \left(\frac{\bar{r}_E}{r_E} \right)^2 \, , \tag{9}$$

where $\bar{S}_\infty$ is the solar constant at one astronomical unit $\bar{r}_E$, and r_E is the Earth-sun distance. The extraterrestrial solar flux incident on a horizontal surface is $S_\infty \cos \zeta$, where ζ is the solar zenith angle,

$$\mu_0 = \cos \zeta_0 = \sin \phi \sin d + \cos \phi \cos d \cos h \, , \tag{10}$$

ϕ is the latitude, d is the solar declination, and h is the hour angle of the sun. In the GCM the hour angle at each grid point is updated every simulated hour, and the solar declination and Earth-sun distance are updated once each simulated day.

In the atmosphere, solar radiation is absorbed by water vapor, ozone, carbon dioxide and clouds, and is scattered by air molecules (Rayleigh scattering) and clouds. However, the heating by ozone absorption below 200 mb is negligible compared with the heating by water vapor absorption (Manabe and Strickler, 1964), and the amount of Rayleigh scattering is negligible above 200 mb due to its exponential decrease with decreasing pressure. Consequently, we can assume that there is only ozone absorption in the stratosphere (above 200 mb), as shown schematically in Fig. 1, and that there is no ozone absorption in the troposphere (below 200 mb) where there is Rayleigh scattering and scattering by clouds, and absorption by water vapor, carbon dioxide and clouds. Therefore, the two-stream/ delta-Eddington approximation for multiple scattering with absorption is applied only to the troposphere as described below.

The troposphere is divided into the L layers of the GCM as shown in Fig. 1. Within each layer we assume that the α coefficients in Eq. (8) are constant. Each layer ℓ is then characterized by its optical depth $\Delta\delta_\ell$ and its values for $\alpha_{1\ell}, \alpha_{2\ell}, \alpha_{3\ell}$ and $\alpha_{4\ell}$. Following Geleyn and Hollingsworth (1979) Equations (4) can then be integrated analytically across each layer and the results expressed as

$$\begin{bmatrix} S_b \\ F_b^- \\ F_t^+ \end{bmatrix}_\ell = \begin{bmatrix} a_1 & 0 & 0 \\ a_2 & a_4 & a_5 \\ a_3 & a_5 & a_4 \end{bmatrix}_\ell \cdot \begin{bmatrix} S_t \\ F_t^- \\ F_b^+ \end{bmatrix}_\ell . \tag{11}$$

Here (S_b, F_b^-, F_t^+) and (S_t, F_t^-, F_b^+) are the outgoing and incoming fluxes to the layer, with subscripts t and b denoting the top and bottom of the layer (Fig. 2), and a_1 is the transmission for the parallel beam, a_2 is the diffuse transmission for the parallel beam, a_3 is the diffuse reflection for the parallel beam, a_4 is the transmission for diffuse radiation, and a_5 is the reflection for diffuse radiation. In Eq. (11) the coefficients a_4 and a_5 appear
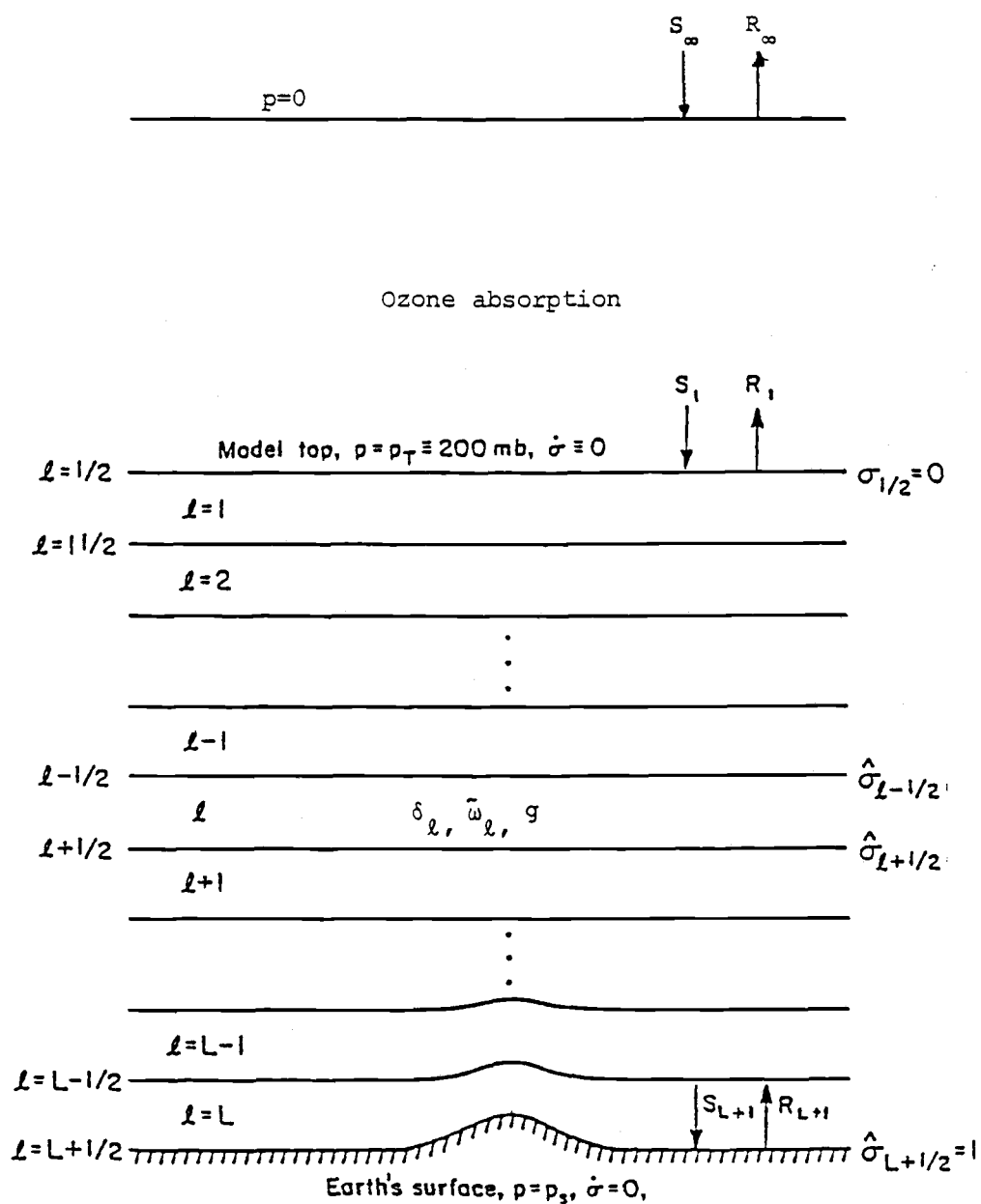
Fig. 1. Vertical indexing of a L-layer model. The model's layers are indexed by integers $\ell = 1, 2, ..., L$. The levels separating the layers are indexed by half-integers $\ell = 1/2, 3/2, ..., L+1/2$. See text for definition of symbols.

in the expressions for both F_b^- and F_t^+ because we do not distinguish between the layer optical properties for the upward and downward diffuse fluxes. The coefficients $a_{i\ell}$ $(i = 1,5)$ are analytical functions of $\Delta\delta_\ell$, $\alpha_{1\ell}$, $\alpha_{2\ell}$, $\alpha_{3\ell}$, $\alpha_{4\ell}$ and μ_0 which are given in the Appendix.
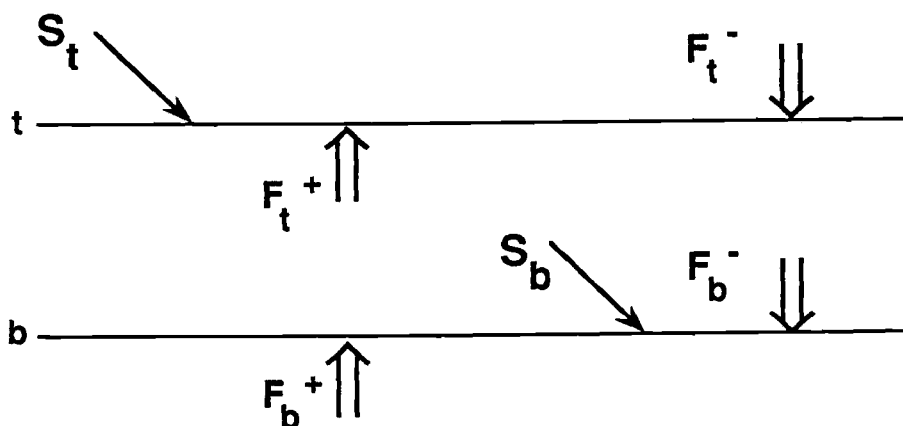
Fig. 2. Schematic representation of layer ℓ showing the distinction between incoming and outgoing fluxes. A parallel flux is denoted by ($\downarrow$) and a diffuse flux by ($\Downarrow$).

Having computed the a_i coefficients for all the L layers we have 3L linear equations for 3L+3 unknown fluxes. This linear system is completed by three boundary conditions, namely, $(S_t)_1$,

$$(F_t^-)_1 = F^-(0) = 0 \tag{12}$$

at the top of the atmosphere, and

$$(F_b^+)_L = F^+(\delta_s) = \alpha_s(\mu_0)\,S(\delta_s) + \tilde{\alpha}_s\,F^-(\delta_s) \tag{13}$$

at the bottom of the atmosphere, where $\alpha_s(\mu_0)$ and $\tilde{\alpha}_s$ are the surface albedos for the parallel and diffuse fluxes, respectively.

The linear system of 3L+3 equations for the 3L+3 unknowns can then be written in matrix form as

$$\mathbf{A}\vec{F} = \vec{S}, \tag{14}$$

where $\mathbf{A}$ is a band-structured matrix with all diagonal elements equal to one and the other nonzero elements equal to $-a_{i\ell}$, $-\alpha_s(\mu_0)$ or $-\tilde{\alpha}_s$, $\vec{F}$ is the vector of the fluxes which consists of the subvectors (S, F^-, F^+) appropriate to each layer; and S is the source vector with only one nonzero element equal to $\mu_0 S_\infty$.

Fractional cloud cover is treated by assuming maximum overlap (Geleyn and Hollingsworth, 1979) for vertically contiguous cloud layers and random overlap (Manabe and Strickler, 1964) for vertically noncontiguous cloud layers (see Fig. 3). Considering a partially covered layer we assume that it is characterized by two sets of $(\alpha_1, \alpha_2, \alpha_3, \alpha_4)_\ell$, one for the cloud part (superscript c) and one for the cloud-free part (superscript f). Then Eq. (11) can be replaced by

$$\begin{bmatrix} S_b^f \\ F_b^\downarrow \\ F_t^\uparrow \end{bmatrix}_\ell = \begin{bmatrix} a_1^f & 0 & 0 \\ a_2^f & a_4^f & a_5^f \\ a_3^f & a_5^f & a_4^f \end{bmatrix}_\ell \cdot \begin{bmatrix} b_1 S_t^f + (1-b_3) S_t^c \\ b_1 F_t^{\downarrow f} + (1-b_3) F_t^{\downarrow c} \\ b_2 F_b^{\uparrow f} + (1-b_4) F_b^{\uparrow c} \end{bmatrix}_\ell \tag{15}$$

and

$$\begin{bmatrix} S_b^c \\ F_b^{\downarrow c} \\ F_t^{\uparrow c} \end{bmatrix}_\ell = \begin{bmatrix} a_1^c & 0 & 0 \\ a_2^c & a_4^c & a_5^c \\ a_3^c & a_5^c & a_4^c \end{bmatrix}_\ell \cdot \begin{bmatrix} (1-b_1) S_t^f + b_3 S_t^c \\ (1-b_1) F_t^{\downarrow f} + b_3 F_t^{\downarrow c} \\ (1-b_2) F_b^{\uparrow f} + b_4 F_b^{\uparrow c} \end{bmatrix}_\ell, \tag{16}$$

where the coefficients b_i are defined for the maximum overlapping as

$$b_{1\ell} = \frac{1 - \max(C_\ell, C_{\ell-1})}{1 - C_{\ell-1}}, \qquad b_{2\ell} = \frac{1 - \max(C_\ell, C_{\ell+1})}{1 - C_{\ell+1}}$$

$$b_{3\ell} = \frac{\min(C_\ell, C_{\ell-1})}{C_{\ell-1}}, \qquad b_{4\ell} = \frac{\min(C_\ell, C_{\ell+1})}{C_{\ell+1}} \tag{17}$$

and C_ℓ is the partial cloudiness in layer ℓ. In Eqs. (15) and (16), for convenience, the fluxes for the cloudy part of a layer have been weighted by C for that layer, and the fluxes for the clear part of a layer by 1 - C. When $C_{\ell\pm1}$ = 0 or 1, Eq. (17) is indeterminate; in this case the coefficients $b_{1\ell}, b_{2\ell}, b_{3\ell},$ and $b_{4\ell}$ are set equal to one to represent the random overlapping.
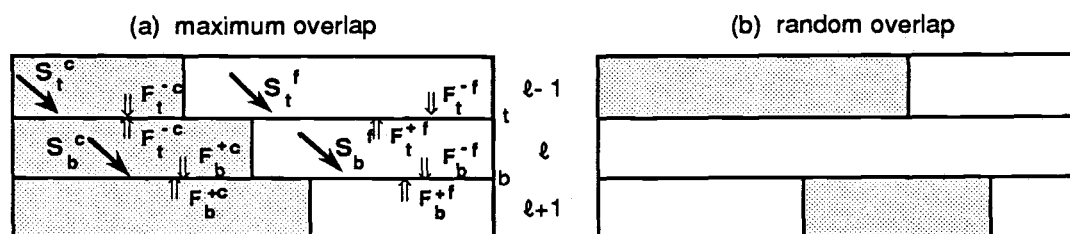
Fig. 3. Schematic representation of cloud geometry assuming: (a) maximum overlap and (b) random overlap.

2.4. Spectral discretization

The spectral solar irradiance is taken from Labs and Neckel (1970) for spectral intervals 0 - 0.33 μm and 1.2 - 4 μm, and from Neckel and Labs (1984) for 0.33 - 1.2 μm. The solar constant S_∞ integrated over this spectrum from 0 to 4 μm is 1362.3 W m⁻².

The major absorbers in the atmosphere are ozone in the stratosphere and water vapor in the troposphere. Ozone absorbs solar radiation effectively in the ultraviolet ($\lambda \leq 0.35$ μm) and visible (0.5 μm $\leq \lambda \leq 0.7$ μm), while water vapor absorbs in the near-infrared range (0.7 μm $\leq \lambda \leq 4$ μm). Thus in the model the spectrum is subdivided into three frequency bands as shown in Table 1, two for wavelengths less than 0.69 μm and one for wavelengths greater than 0.69 μm. The latter region is further subdivided into six intervals according to the water vapor absorption coefficient as described in subsection 3.1.2(a).

Table 1. The subdivision of the solar spectrum used in the model.

Index i	Wavelength interval, $\lambda_i - \lambda_{i+1}$ (mm)	Fraction of incident flux
1	0.00 - 0.44	0.128
2	0.44 - 0.69	0.331
3	0.69 - 4.	0.541

3. Parameterization of the Layer Optical Properties

As noted in section 2.2, to determine the α_i and a_i coefficients for a layer it is necessary to determine δ, $\tilde{\omega}_0$ and g for the layer. The calculation of these quantities is described below, first for the stratosphere and then for the troposphere.

3.1. Clear part of an atmospheric layer

3.1.1. Rayleigh scattering

The scattering optical thickness for the clear part of an atmospheric layer is calculated by assuming that the atmosphere within the layer is homogeneous. This gives

$$\delta = \delta_{\ell,i} = \delta_{R,i}\,\delta\sigma_\ell, \quad i = 1, 2,$$

(18)

where $\delta\sigma_\ell$ is the σ-thickness of layer ℓ and $\delta_{R,i}$ is the spectrally- averaged Rayleigh scattering optical depth given by

$$\delta_{R,i} = \frac{\int_{\lambda_i}^{\lambda_{i+1}} \delta_\lambda \, S_{\infty,\lambda} \, d\lambda}{\int_{\lambda_i}^{\lambda_{i+1}} S_{\infty,\lambda} \, d\lambda} \, ,$$

$$(19)$$

where

$$\delta_\lambda = r \, \lambda^{-4} \tag{20}$$

and λ is the wavelength of the radiation in μm and $r = 8.8 \times 10^{-3} \, \mu m^4$ which is given by Ghan (1986) to fit the data in Coakley *et al.* (1983). The values of $\delta_{R,i}$ are shown in Table 2.

Table 2. Spectrally-averaged Rayleigh scattering optical depth $\delta_{R,i}$ versus wavelength interval i.

Index i	Wavelength interval, $\lambda_i - \lambda_{i+1}$ (μm)	$\delta_{R,i}$
1	0.00 - 0.44	1.384
2	0.44 - 0.69	0.102

The single scattering albedo for Rayleigh scattering is

$$\tilde{\omega} = \tilde{\omega}_{\ell,i} = 1, \quad i = 1, 2 \, , \tag{21}$$

and

$$g = 0 \, , \tag{22}$$

because Rayleigh scattering is isotropic.

3.1.2. Absorption

a) Water vapor absorption

The solar flux at pressure level p integrated over the spectral interval where water vapor absorbs is

$$F(p) = \mu \int_{\lambda_3}^{\lambda_4} S_{\infty,\lambda}\, \tau_\lambda\, d\lambda \,, \tag{23}$$

where $S_{\infty,\lambda}$ is the solar flux at the top of the atmosphere,

$$\tau_\lambda(p) = \exp\left\{ -\frac{1}{\mu\,g} \int_0^p k_\lambda\,[p',T(p')]\, q(p')\, dp' \right\}, \tag{24}$$

k_λ is the absorption coefficient, q is the water vapor mixing ratio, g is the acceleration of gravity and $\mu = \cos\zeta$.

Chou (1986) introduced the absorption coefficient in the form

$$k_\lambda(p,T) = k_\lambda(p_r,T_r)\, f(p,T) \,, \tag{25}$$

where subscript r denotes reference values,

$$f(p,T) = (p/p_r)^m\, R(T/T_r) \tag{26}$$

with m a constant less than unity and R a function. Chou and Arking (1981) adopted $P_r = 300$ mb, $T_r = 240$ K, m = 0.8 and $R(T/T_r) = 1$.

Using Eq. (23) and $R(T/T_r) = 1$, Equation (24) becomes

$$\tau_\lambda(p) = \exp[\,-k_\lambda(p_r,T_r)\, w(p)/\mu\,] \,, \tag{27}$$

where w is the scaled water vapor amount given by

$$w(p) = \frac{1}{g} \int_0^p f(p',T')\, q'(p')\, dp' \,. \tag{28}$$

The transmitted solar flux at pressure level p is then given by

$$F(u) = \mu \int_{\lambda_3}^{\lambda_4} S_{\infty,\lambda} \exp[-k_\lambda(p_r,T_r) u] \, d\lambda , \tag{29}$$

where $u = w(p)/\mu$. The total transmittance and absorptance can then be defined by

$$\tau(u) = \frac{F(u)}{\mu S_\infty} \tag{30}$$

and

$$A(u) = 1 - \tau(u) . \tag{31}$$

We have calculated A(u) from Eqs. (29) - (31) using the values of $S_{\infty,\lambda}$ from Labs and Neckel (1970) and Neckel and Labs (1984) from which $S_\infty = 1362.3 \text{ Wm}^{-2}$, together with the values of $k_\lambda(p_r,T_r)$ computed by Chou (1986) with a resolution of 0.025 cm^{-1}. Following Lacis and Hansen (1974), the resulting water vapor absorptance A(u) can be expressed in terms of a probability distribution p(k), where p(k) dk is the fraction of the incident flux that is associated with an absorption coefficient between k and k + dk. Then, A(u) can be rewritten as

$$A(u) = \int p_k \, e^{-ku} \, dk$$

$$= \sum_n p(k_n) \, e^{-k_n u} \, \Delta k_n . \tag{32}$$

We have calculated the values of the discrete probability distribution $p(k_n)$ and the absorption coefficients k_n by the exponential-sum fitting method of Wiscomb and Evans (1977). Table 3 gives the values of k_n and $p(k_n) \, \Delta k_n$ for n = 6 which fits the line-by-line transmittivity given by Eq. (30) within 0.04% for $10^{-2} < u < 10$ cm.

Table 3. Discrete probability distribution of water vapor absorption coefficients.

n	k_n(cm)	$p(k_n)\,\Delta k_n$
1	1.E-10	0.6806
2	0.0174	0.2026
3	0.3006	0.0510
4	1.3725	0.0262
5	5.0388	0.0188
6	32.0000	0.0208

Figure 4 shows the results of the exponential-sum fitting given in Table 3 compared to the line-by-line transmittivity given by Chou (1986). This exponent-sum fitting is based not only on the updated solar spectrum and the line-by-line calculated transmittivity, but also has only 6 terms so that it is more economical than other similar fitting (e.g., Lacis and Hansen, 1974; Somerville *et al.*, 1974).

The optical properties of each layer are specified by the absorption optical depth of the layer

$$\delta = \delta_{\ell,n} = k_n\, w_\ell , \tag{33}$$

where

$$w_\ell = u^*_{H_2O,\ell} \sec \zeta \tag{34}$$

is the effective water vapor amount in layer ℓ, with

$$u^*_{H_2O,\ell} = \frac{1}{g} \int_{P_{\ell-1/2}}^{P_{\ell+1/2}} q_\ell \left(\frac{p}{p_r}\right)^m dp , \tag{35}$$

and by the single scattering albedo
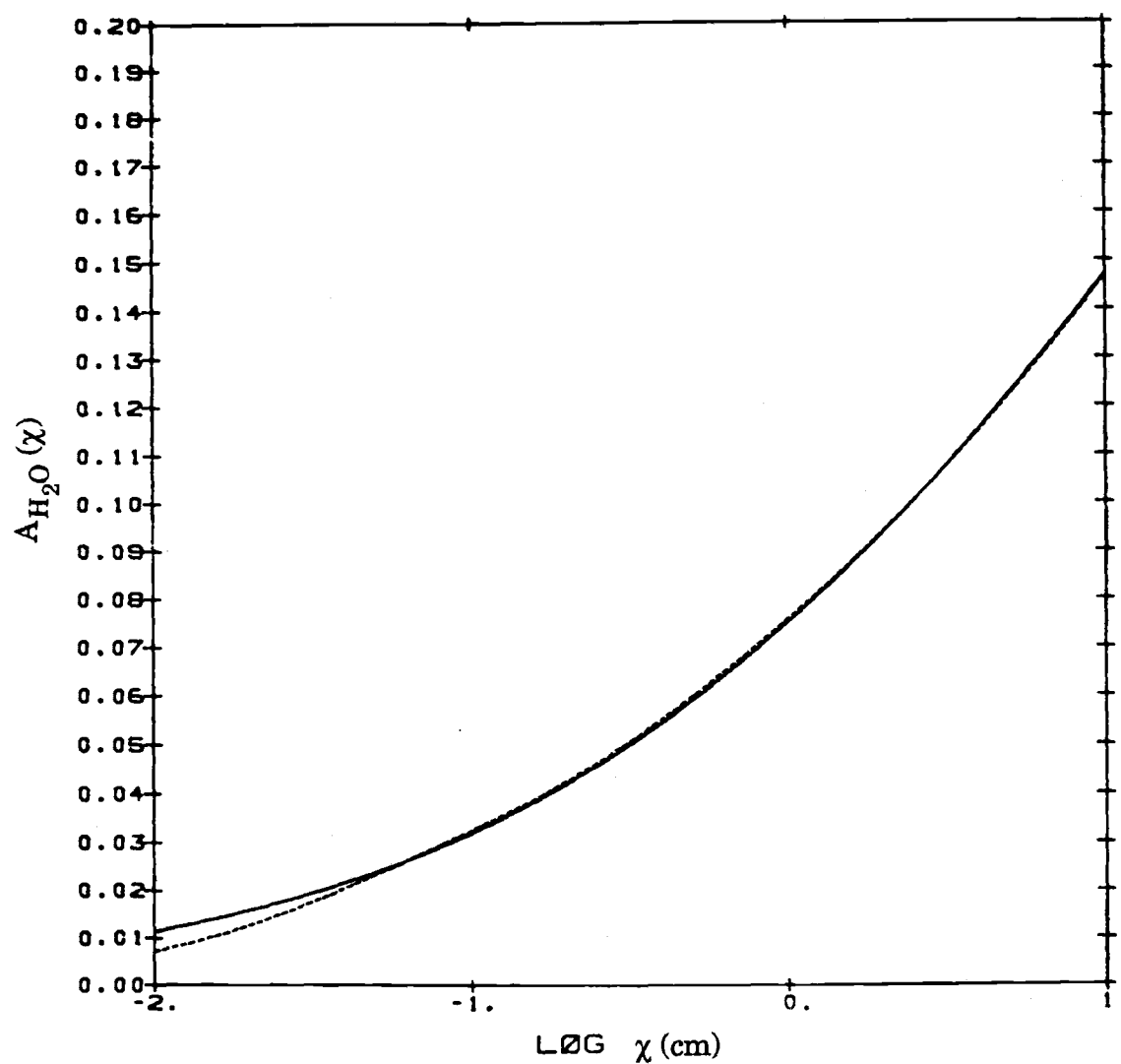
Fig. 4. Absorptivity function for water vapor. The solid line is from Chou
(1986) and the dotted line is the result of the exponential-sum fitting.

$$\bar{\omega}_{\ell,n} = 0 \; . \tag{36}$$

In Eq. (35) m and p_r are chosen to be 0.8 and 300 mb as in Chou (1986). Vertical interpolation of q_ℓ is assumed the same form as in the longwave radiation (for detail see Appendix C).

b) Ozone absorption

Although the model's top is formally at 200 mb (at least for now), we include the stratosphere in the radiative transfer parameterization. In the stratosphere we neglect scattering and only include absorption of the downward direct solar radiation by ozone. Thus, we replace Eq. (12)

$$(S_t)_1 \equiv (F_t^-)_1 = \mu_0 \, S_\infty \, T_{O_3} \, (M\Omega_1) \; , \tag{37}$$

where

$$M = \frac{35}{\sqrt{1224 \, \mu_0^2 + 1}} \tag{38}$$

is the magnification factor (Rodgers, 1967) and Ω_1 is the total ozone from the top of the atmosphere to the 200 mb surface.

An absorptivity function for ozone has been calculated based on Schlesinger (1976) from

$$1 - T_{O_3,i} \, (\chi) = A_{O_3,i} \, (\chi) = \frac{\int_{\lambda_i}^{\lambda_{i+1}} S_{\infty,\lambda} \, [1 - \exp(-k_\lambda \, n_s \, \chi)] \, d\lambda}{\int_{\lambda_i}^{\lambda_{i+1}} S_{\infty,\lambda} \, d\lambda} \; , \quad i = 1, 2 \; , \tag{39}$$

where χ is the ozone amount, k_λ is the ozone absorption cross section from Ackerman (1971), n_s is the Loschmidt number, and $S_{\infty,\lambda}$ is the

monochromatic extraterrestrial solar flux from Labs and Neckel (1970) and Neckel and Labs (1984). The calculated absorptivity function is presented in Table 4 and is shown in Fig. 5 in comparison with the ozone absorptivities of Schlesinger (1976) and Lacis and Hansen (1974). The calculated ozone absorptivity (solid line) is less than that of Schlesinger (1976) but is almost the same as that of Lacis and Hansen (1974). Consequently, for computational economy, the analytical expression given by Lacis and Hansen (1974) for the ozone absorptivity

$$
A_{O_3}(\chi) = \begin{cases} \dfrac{1.082\,\chi}{(1+138.6\,\chi)^{0.805}} + \dfrac{0.0658\,\chi}{1+(103.6\,\chi)^3}, & \text{for } 0 < \lambda \leq 0.44\ \mu m \\[3mm] \dfrac{0.02118\,\chi}{1+0.042\,\chi+0.000323\,\chi^2}, & \text{for } 0.44 < \lambda \leq 0.69\ \mu m \end{cases}
$$

(40)

is used rather than the values in Table 4.

The scattering in the stratosphere is ignored due to the negligible amount of Rayleigh scattering and cloud there. Thus,

$$\tilde{\omega}_0 = 0 \tag{41}$$

and δ can be calculated as

$$\delta = -\ln(1 - A_{O_3}). \tag{42}$$

c) Carbon Dioxide absorption

The absorption by CO_2 is included in both the stratosphere, wherein ozone is the principal absorber, and the troposphere, wherein the water vapor and clouds are the major absorbers of solar radiation. The transmittivity of CO_2 has been calculated based on the Fouquart (1987) parameterization by means of Pade Approximation. The transmittivity of CO_2 is given in the form:

Table 4. Ozone absorptivity function, $A_{O_3,i}(\chi)$, for the spectral intervals shown in Table. 1.E-5 means 10^{-5}.

χ (cm-NTP)	$A_{O_3,i}(\chi)$ i = 1	i = 2	χ (cm-NTP)	$A_{O_3,i}(\chi)$ i = 1	i = 2
1E-5	1.006E-4	6.352E-7	1E-1	1.987E-1	6.335E-3
2	2.011	1.275E-6	2	1.283	1.261E-2
3	3.013	1.906	3	1.403	1.883
4	4.014	2.541	4	1.493	2.500
5	5.012	3.183	5	1.565	3.111
6	6.009	3.821	6	1.625	3.716
7	7.004	4.449	7	1.676	4.316
8	7.997	5.092	8	1.722	4.911
9	8.988	5.727	9	1.763	5.500
1E-4	9.978	6.365	1E-0	1.800	6.084
2	1.977E-3	1.273E-5	2	2.053	1.165E-1
3	2.938	1.909	3	2.208	1.673
4	3.882	2.546	4	2.321	2.140
5	4.808	3.182	5	2.408	2.568
6	5.718	3.818	6	2.481	2.960
7	6.611E-2	4.454	7	2.542	3.322
8	7.487	5.091	8	2.595	3.655
9	8.349	5.727	9	2.642	3.961
1E-3	9.195	6.363	1E+1	2.684	4.244
2	1.688E-2	1.273E-4	2	2.965	6.163
3	2.337	1.909	3	3.140	7.153
4	2.890	2.545			
5	3.365	3.181			
6	3.778	3.817			
7	4.140	4.453			
8	4.461	5.089			
9	4.747	5.725			
1E-2	5.005	6.361			
2	6.705	1.272E-3			
3	7.711	1.907			
4	8.442	2.541			
5	9.019	3.175			
6	9.499	3.808			
7	9.908	4.441			
8	1.027E-1	5.073			
9	1.059	5.704			
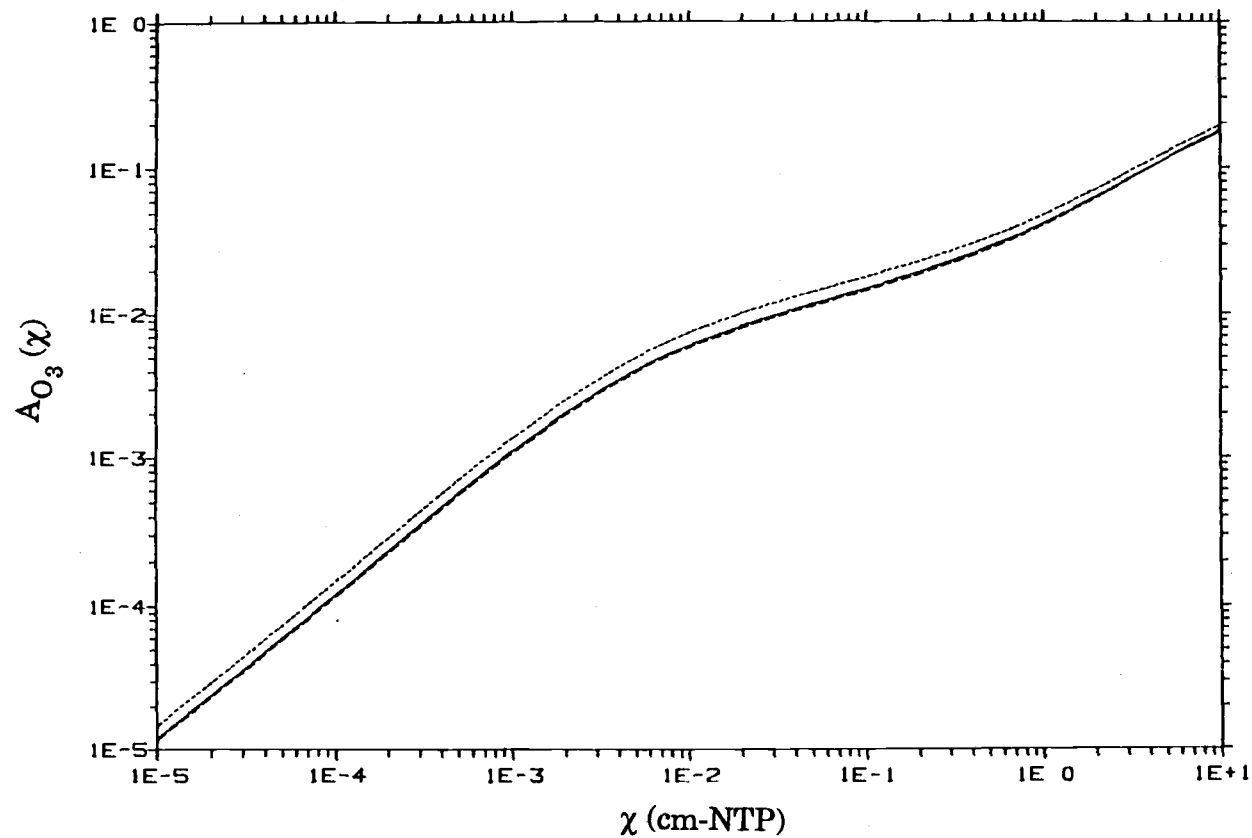
Fig. 5. Ozone absorptivity $A_{O_3}(\chi)$ of Table 4 (solid line) compared with that of Schlesinger (1976) (dotted line) and Lacis and Hansen (1974) (dashed line).

$$T_{CO_2}(u) = 0.93 + 0.07 \, \frac{\sum\limits_i a_i u^i}{\sum\limits_j b_j u^j} \, ,$$

(43)

where the coefficients a_i and b_j are given in Table 5.

Table 5. Parameterization of CO_2 absorption by mean of Pade Approximation (from Fouquart, 1987).

i,j	a_i	b_j
1	6.074E+6	6.074E+6
2	2.379E+8	2.379E+8
3	1.978E+8	2.070E+8
4	7.973E+6	9.314E+6
5	1.221E+4	1.966E+4
6	0	1

3.2. Cloudy part of an atmospheric layer

3.2.1. Liquid water cloud

The optical depth for a cloud layer comprised only of liquid water is calculated following Stephens (1978) as

$$\log_{10}(\delta_\ell^{wc}) = \begin{cases} 0.2633 + 1.07095 \ln[\log_{10}(LWP_\ell)], \\ \qquad \text{for } \tilde{\omega}_0 = 1, \ \lambda \leq 0.69 \ \mu m, \\ \\ 0.3492 + 1.6518 \ln[\log_{10}(LWP_\ell)], \\ \qquad \text{for } \tilde{\omega}_0 < 1, \ \lambda > 0.69 \ \mu m, \end{cases}$$

(44)

where LWP_ℓ is the liquid water path defined as

$$
\begin{aligned}
LWP_\ell &= \frac{1}{g} \int_{p_{\ell-1/2}}^{p_{\ell+1/2}} q_{c,\ell} \, dp \\
&= q_{c,\ell} \frac{p_{\ell+1/2} - p_{\ell-1/2}}{g} \\
&= q_{c,\ell} \frac{\pi}{g} (\sigma_{\ell+1/2} - \sigma_{\ell-1/2}) \,,
\end{aligned}
\tag{45}
$$

and $q_{c,\ell}$ is the mixing ratio of cloud liquid water in ℓ-th layer.

The optical properties of cloud for wavelengths less than 0.69 μm are chosen as

$$
\delta_{\ell,i} = \delta_\ell^{wc} \,,
\tag{46}
$$

$$
\tilde{\omega}_{\ell,i} = \tilde{\omega}_{\ell,i}^{wc} = 1 \,,
\tag{47}
$$

$$
g_i^{wc} = 0.84 \,, \quad i = 1,2 \,,
\tag{48}
$$

where i is the index for the wavelength interval in Table 1 and the asymmetry factor g has been chosen based on Cess *et al.* (1985). The optical properties of clouds for wavelengths greater than 0.69 μm are

$$
\delta_{\ell,n} = \delta_\ell^{wc} + k_n w_\ell \,,
\tag{49}
$$

$$
\tilde{\omega}_{\ell,n} = \text{the value from Stephens (1978)},
\tag{50}
$$

$$
g_{\ell,n}^{wc} = \begin{cases} 0.76 \ \text{ for stratiform clouds} \,, \\[2mm] 0.85 \ \text{ for cumuloform clouds, } n = 1,...,6 \,, \end{cases}
\tag{51}
$$

where n is the index for $p(k_n)$ given in Table 3 and δ_ℓ^{wc} is the optical depth due to cloud liquid water in ℓ-th layer and k_n is given in Table 3. The

values of asymmetry factor g are chosen following Cess *et al.* (1985) for the stratiform clouds and Stephens (1984) for the cumuloform clouds.

3.2.2. Pure ice cloud (cirrus)

Relatively little is known of the radiative properties of cirrus clouds in spite of their potentially significant impact on the thermal structure of the atmosphere (e.g., Manabe and Strickler, 1964; Cox, 1971; and Starr, 1976). Only a few observational studies of the microphysical properties of cirrus have been made (e.g., Heymsfield, 1975a, b, c, 1977; Ryan *et al.*, 1972; Griffith and Cox, 1977; Platt and Dilley, 1979; Paltridge and Platt, 1980). These studies have shown that cirrus clouds contain predominantly nonspherical hexagonal ice columns. This nonsphericity of the ice crystals creates a great deal of difficulty to understand and parameterize the radiative properties of cirrus clouds.

Starr and Cox (1985) parameterized the radiative properties of cirrus clouds based on an empirical study (Reynolds and Vonder Haar, 1977), theoretical studies (Welch *et al.*, 1980; Starr, 1982) and observational studies (Platt *et al.*, 1980; Paltridge and Platt, 1980). We follow the parameterization of the radiative properties of Starr and Cox (1985). The radiative properties of a cirrus cloud are diagnosed as functions of the ice water path

$$
\begin{aligned}
\text{IWP}_\ell &= \frac{1}{g} \int_{p_{\ell-1/2}}^{p_{\ell+1/2}} q_{i,\ell} \, dp \\
&= q_{i,\ell} \frac{p_{\ell+1/2} - p_{\ell-1/2}}{g} \\
&= q_{i,\ell} \frac{\pi}{g}(\sigma_{\ell+1/2} - \sigma_{\ell-1/2}) ,
\end{aligned}
\tag{52}
$$

where $q_{i,\ell}$ is the mixing ratio of cloud ice in ℓ-th layer.

Griffith *et al.* (1980) reported the effective infrared flux emittance ε_ℓ of cirrus cloud as

$$\varepsilon_\ell = 1 - \exp\left(-\beta\, IWP_\ell\right), \tag{53}$$

where β is the effective infrared mass absorption coefficient. Following Paltridge and Platt (1980), we choose $\beta = 0.056\ m^2\,g^{-1}$ based on observed flux profiles in cirrostratus clouds. Starr and Cox (1985) introduced an empirical relationship between the visible albedo a and effective infrared emittance as

$$\alpha_\ell\,(\zeta = 60^\circ) = 0.557\ \varepsilon_\ell + 0.105\ \varepsilon_\ell^{\,2} \tag{54}$$

based on the results of Platt and Stephens (1980) and the theoretical results of Welch *et al.* (1980). Also the absorptance a_ℓ is introduced as

$$a_\ell\,(\zeta = 35^\circ) = 0.283\ \alpha_\ell\,(\zeta = 35^\circ). \tag{55}$$

The dependence of α and a on the solar zenith angle are not well known for cirrus. Starr and Cox (1985) assumed that the dependence of α on ζ is similar to the dependence in Stephens (1978) for liquid water cloud, that is,

$$\alpha_\ell\,(\zeta) = (0.161 + 0.0117\,\zeta + 0.386 \times 10^{-4}\,\zeta^2)\,\alpha_\ell\,(60^\circ)$$
$$+ (0.914 - 0.0152\,\zeta)\,[\alpha_\ell\,(60^\circ)]^2, \tag{56}$$

where $\alpha_\ell\,(60^\circ)$ is given from Eq. (54), and

$$a_\ell\,(\zeta) = 1.01\,a_\ell(35^\circ) + 0.716\,[\,a_\ell(35^\circ)]^2$$
$$+ \{-0.246 \times 10^{-2}\,a_\ell(35^\circ) + 0.765 \times 10^{-2}\,[a_\ell(35^\circ)]^2\}\,\zeta$$
$$- 0.493 \times 10^{-3}\,[\,a_\ell(35^\circ)]^2\,\zeta^2, \tag{57}$$

and $a_\ell(35^\circ)$ is given by Eq. (55). Thus, the optical depth is

$$\delta_\ell^{ic} = -\ln\,[\,1 - \alpha_\ell(\zeta) - a_\ell\,(\zeta)\,], \tag{58}$$

and the single-scattering albedo can be obtained from Stephens (1978). Then the optical properties of a cirrus layer are

$$\delta_{\ell,n} = \delta_\ell^{ic} + k_n \, w_\ell \, , \tag{59}$$

$$\tilde{\omega}_\ell = \begin{cases} 1, & \text{for } \lambda \leq 0.69 \, \mu m, \\ \text{the value from Stephens (1978), for } \lambda > 0.69 \, \mu m, \end{cases} \tag{60}$$

$$g_\ell = g_\ell^{ic} = 0.82 \, , \tag{61}$$

the latter from Cess *et al.* (1985).

3.2.3. Mixed-phase cloud

Many clouds consist not only of liquid water but also of ice. To treat these mixed phase clouds we simply assume a linear combination of the radiative properties of liquid-water cloud and pure-ice cloud based on the ratio of water path of each phase to the total water path. Thus,

$$\delta_{\ell,n} = \delta_\ell^{wc} + \delta_\ell^{ic} + k_n \, w_\ell \, , \tag{62}$$

$$\tilde{\omega}_{\ell,n} = \gamma_\ell \, \tilde{\omega}_{\ell,n}^{wc} + (1 - \gamma_\ell) \, \tilde{\omega}_{\ell,n}^{ic} \, , \tag{63}$$

$$g_\ell = \begin{cases} 0.84 \ \text{for } \lambda < 0.69 \, \mu m \, , \\ \gamma_\ell \, g_\ell^{wc} + (1 - \gamma_\ell) \, g_\ell^{ic} \ \text{for } \lambda \geq 0.69 \, \mu m \, , \end{cases} \tag{64}$$

where

$$\gamma_\ell = \frac{LWP_\ell}{LWP_\ell + IWP_\ell} \tag{65}$$

with g^{wc} given by Eq. (51) and g^{ic} by Eq. (61).

3.3. Surface

The surface type index was established to account for the different surface albedos of various surfaces. However, since snow mass is a prognostic variable in the model, the combined effects of snow mass and surface type must be considered. Following Manabe and Holloway (1975), the surface albedo α_s of any nonwater surface type varies with the snow mass S from its snow-free value α_{sb} to its snow-covered value α_{sc} at some critical snow mass,

$$\alpha_s = \begin{cases} \alpha_{sb} + s^{1/2}(\alpha_{sc} - \alpha_{sb}), & \text{for } s < s_c = 1 \text{ g cm}^{-2} \\ \\ \alpha_{sc}, & \text{for } s \geq s_c . \end{cases} \tag{66}$$

Surface albedos for each of the nine surface types are shown in Table 6. The values for surface types 1-6 and 8 and 9, both with and without snow cover, are the same as those in Table 2.2 of Ghan *et al.* (1982).

The surface albedo (α_s) for water is taken as 0.07 for the diffuse solar flux. For the direct solar flux the albedo for water is obtained from the fit by Briegleb *et al.* (1986) of Payne's (1972) tabulated values,

$$\alpha_s(\zeta) = \frac{0.026}{[(\cos \zeta)^{1.7} + 0.065]} + 0.15(\cos \zeta - 0.1)(\cos \zeta - 0.5)(\cos \zeta - 1.0) . \tag{67}$$

4. Intercomparison with Other Models

New solar radiation scheme is compared with both current scheme (Ghan *et al.*, 1982) and other models reported in the Intercomparison of Radiation Codes in Climate Models (ICRCCM) (Luther and Fouquart, 1985) for various sky conditions.

Figure 6 shows the relative net flux absorbed by atmosphere for H_2O only with surface albedo $\alpha_s = 0.2$. The net absorbed fluxes with the new

Table 6. The surface albedo assigned to the model's surface types with and without snow cover.

Surface Type	Description	Surface Albedo, α_s	
		Bare Surface, α_{sb}	Snow-covered Surface, α_{sc}
1	Woodland, grass cultivation	.12	.50
2	Forest	.10	.41
3	Steppe and grassland	.1	.58
4	Steppe desert	.20	.53
5	Desert	.25	.55
6	Tundra, mountains Arctic flora	.19	.70
7	Water	Diffuse flux: Direct flux:	.07 Briegleb *et al.* (1986)
8	Land ice	.45	.80
9	Sea ice	.45	.80
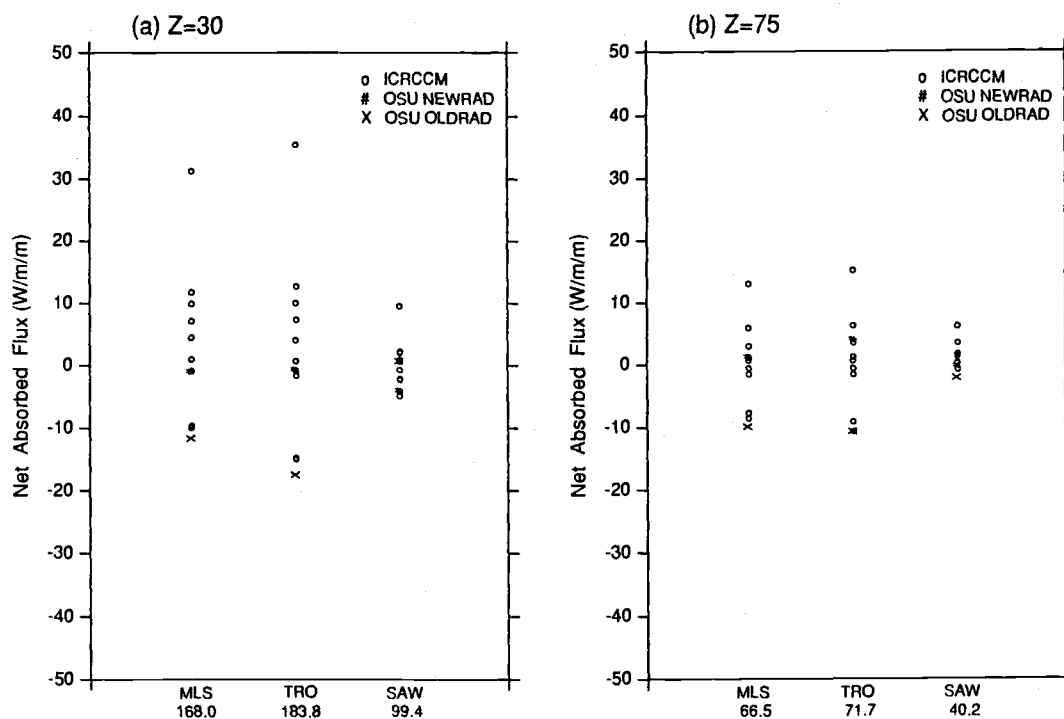
Fig. 6. The relative net flux absorbed by the ICRCCM models shown by 0 (Luther and Fouquart, 1985) for the H_2O absorption-only case. MLS, TRO and SAW represent the midlatitude summer, tropical and subarctic winter cases of McClatchey *et al.* (1973). Within the box represents the median value, and the horizontal lines outside the rectangle are the extreme values. The number under the box is the median value which has been subtracted from all the values. Z denotes the zenith angle and A the surface albedo. The results for the present parameterization are shown by # and those for its predecessor (Ghan *et al.*, 1982) by X.

solar scheme are located near the median values for all sky conditions, while the current solar radiation scheme significantly underestimates the atmospheric absorption of solar radiation for all sky conditions except the subarctic winter. This feature is shown more clearly in Figs. 7 and 8 which represent the net absorbed flux by atmosphere for the cases which include the absorption of H_2O, O_2 and CO_2. With O_3 absorption (Figs. 9 and 10) the reported net absorbed fluxes are quite scattered and the new solar radiation scheme is belong to 50 - 75% region while the current scheme is located 25 - 50% region except the subarctic winter case with $\zeta = 30^0$. When scattering is considered the reported net absorbed fluxes are more scattered as seen in Figs. 11 and 12. Here the extreme values are cutoff at 50 or -50 Wm^{-2} when these values exceed the cutoff values. With scattering the net absorbed flux simulated by new scheme is locted about 75% for $\zeta = 30^0$ and outside of rectangle for $\zeta = 75^0$ while current scheme compensates the deficit of absorption with scattering so that the net absorbed flux is within rectangle except the subarctic winter case.
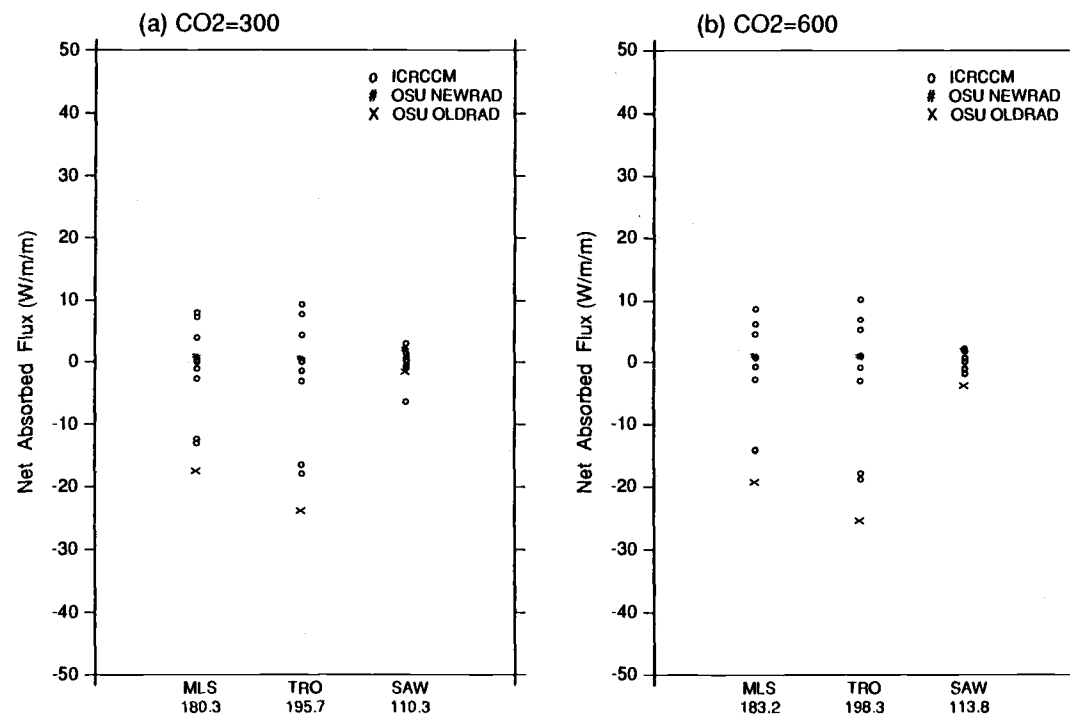
Fig. 7. As in Fig. 6, except including H_2O, O_2 and CO_2 absorption (a) 300 ppm and (b) 600 ppm for $Z = 30°$.
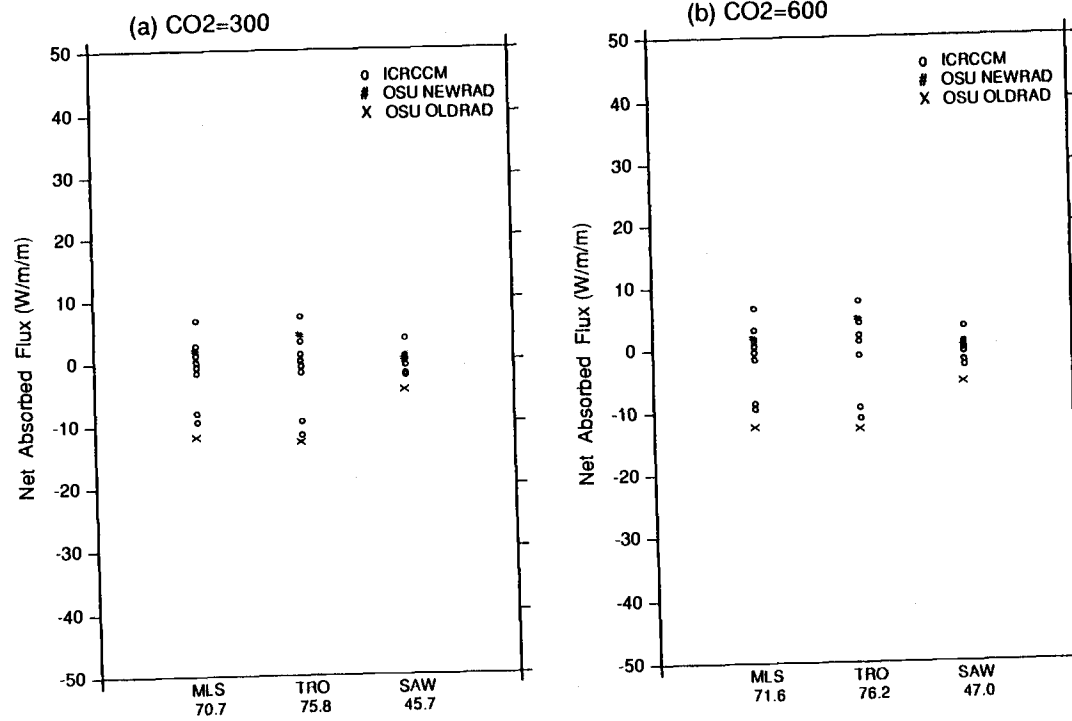
Fig. 8. As in Fig. 7, except for Z = 75° .
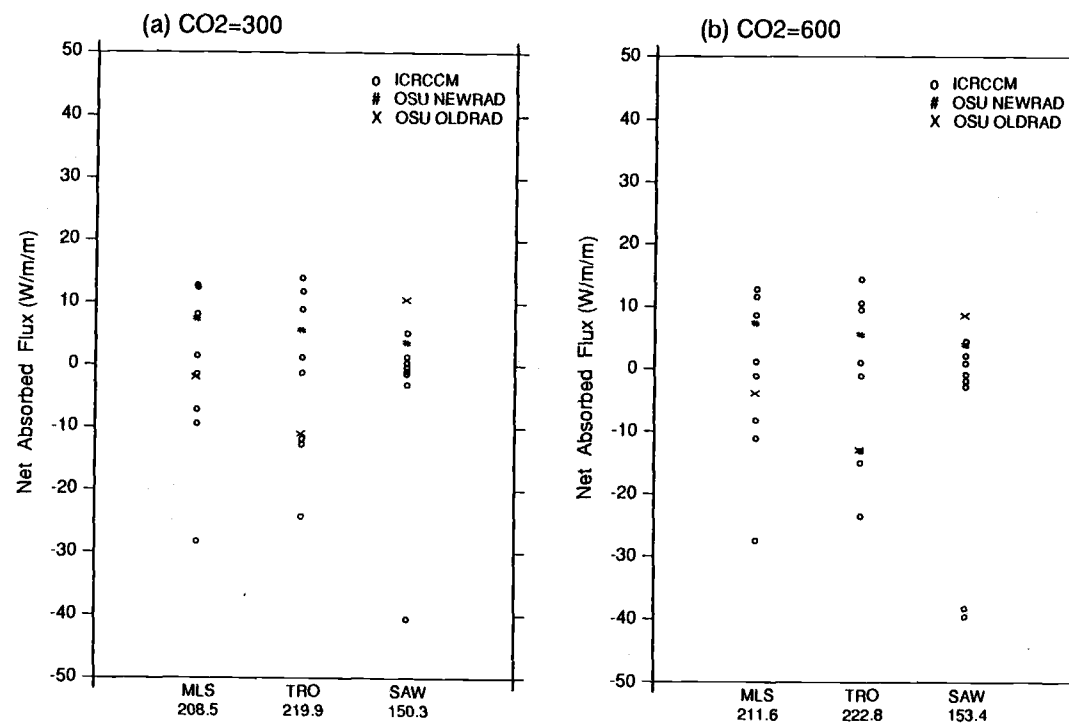
Fig. 9. As in Fig. 7, except also including O_3 absorption.
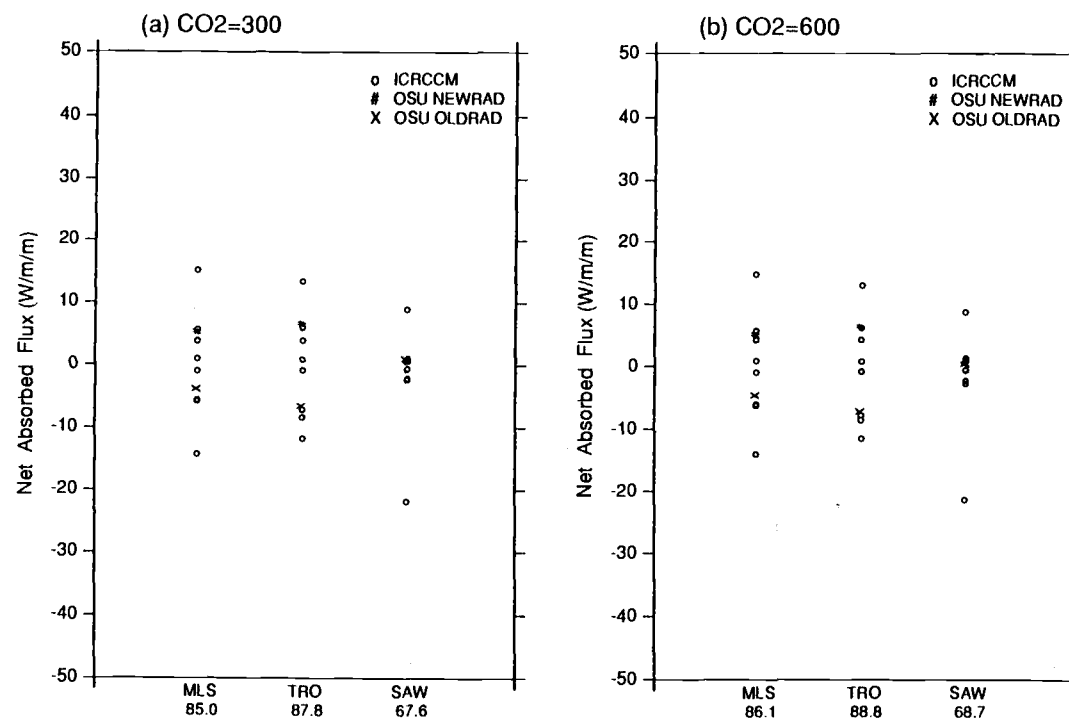
Fig. 10. As in Fig. 8, except also including O_3 absorption.
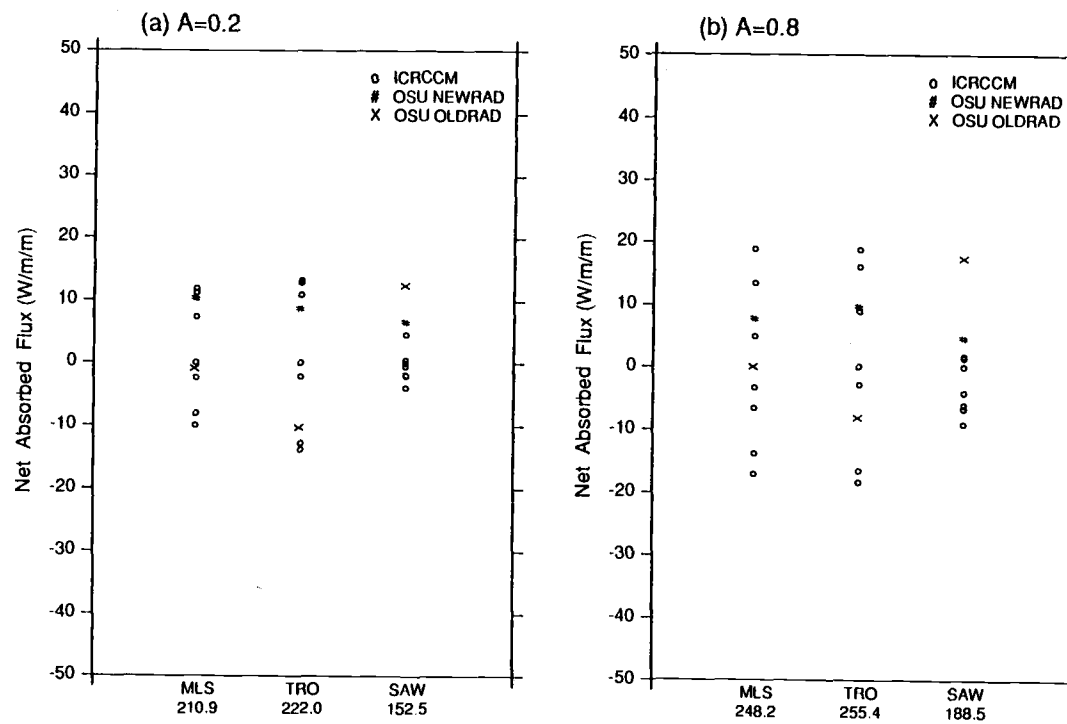
Fig. 11. As in Fig. 7, except including all gases and scattering.
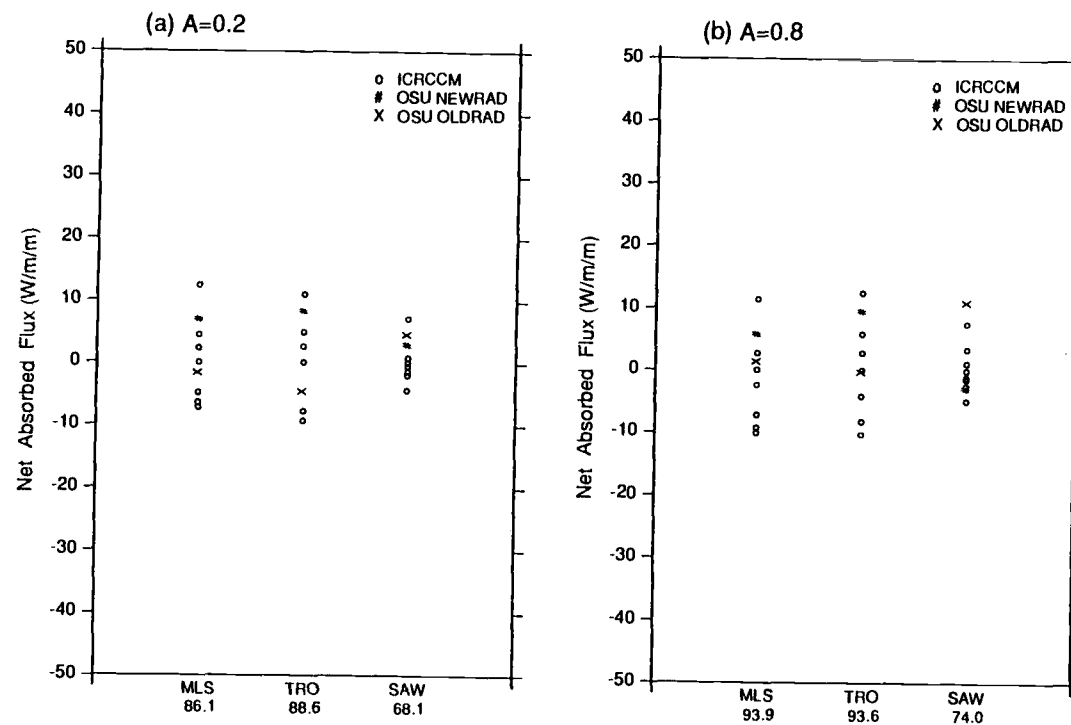
Fig. 12. As in Fig. 8, except including all gases and scattering.

APPENDIX

Analytic Expressions for the a_i Coefficients

The analytic expressions for the a_i coefficients in Eqs. (11) are derived below following Geleyn (1977) and Geleyn and Hollingsworth (1979).

From the equation for parallel radiation, Eq. (4c), we find

$$S(\delta) = a_1 S(0), \tag{A.1}$$

where

$$a_1 = \exp\left[-\frac{\Delta\delta}{\mu_0}\right]. \tag{A.2}$$

1. Solution for $S = 0$

If $S(0) = 0$, Eqs. (4a) and (4b) become

$$\frac{dF^+(\delta)}{d\delta} = \alpha_1 F^+(\delta) - \alpha_2 F^-(\delta), \tag{A.3a}$$

$$\frac{dF^-(\delta)}{d\delta} = \alpha_2 F^+(\delta) - \alpha_1 F^-(\delta). \tag{A.3b}$$

a) General case, $\alpha_1 \neq \alpha_2$

We combine both Eqs. (A.3a) and (A.3b) as

$$\frac{d}{d\delta}[F^+(\delta) - \beta F^-(\delta)] = F^+(\delta)(\alpha_1 - \beta \alpha_2) - F^-(\delta)(\alpha_2 - \beta \alpha_1). \tag{A.4}$$

Homogeneous solutions are obtained when

$$\beta = \frac{\alpha_2 - \beta\,\alpha_1}{\alpha_1 - \beta\,\alpha_2}\,, \tag{A.5}$$

or

$$\beta^2\,\alpha_2 - \beta\,\alpha_1 + \alpha_2 = 0\,. \tag{A.6}$$

The solutions of Eq. (A.6) are

$$\beta_1 = \frac{\alpha_1 - \varepsilon}{\alpha_2}\,,$$

$$\beta_2 = \frac{\alpha_1 + \varepsilon}{\alpha_2} = \frac{1}{\beta_1}\,,$$

$$\varepsilon = \sqrt{\alpha_1^2 - \alpha_2^2}\,. \tag{A.7}$$

Substituting Eq. (A.7) into Eq. (A.4) we obtain

$$\frac{d}{d\delta}\,(F^+ - \beta_1 F^-) = \varepsilon\,(F^+ - \beta_1 F^-) \tag{A.8}$$

with the solution

$$F^+(\delta) - \beta_1 F^-(\delta) = C_1 e^{\varepsilon\,\delta}\,, \tag{A.9}$$

and

$$\frac{d}{d\delta}\,(F^+ - \beta_2 F^-) = -\varepsilon\,(F^+ - \beta_2 F^-) \tag{A.10}$$

with the solution

$$F^+(\delta) - \beta_2 F^-(\delta) = C_2 e^{-\varepsilon\,\delta}\,. \tag{A.11}$$

From Eqs. (A.9) and (A.11)

$$F^+(\delta) = \frac{C_1 \beta_2 e^{\varepsilon\delta} - C_2 \beta_1 e^{-\varepsilon\delta}}{\beta_2 - \beta_1} ,$$

$$F^-(\delta) = \frac{C_1 e^{\varepsilon\delta} - C_2 e^{-\varepsilon\delta}}{\beta_2 - \beta_1} .$$

(A.12)

Using the boundary conditions at the bottom and top of a layer of optical thickness $\Delta\delta$,

$$C_1 \beta_2 e^{\varepsilon\Delta\delta} - C_2 \beta_1 e^{-\varepsilon\Delta\delta} = (\beta_2 - \beta_1) F^+(\Delta\delta) ,$$

$$C_1 \qquad - C_2 \qquad = (\beta_2 - \beta_1) F^-(0) ,$$

(A.13)

solving for C_1 and C_2, and substituting into Eqs. (A.12) gives

$$F^+(0) = \frac{(\beta_2 - \beta_1) F^+(\Delta\delta) + (e^{\varepsilon\Delta\delta} - e^{-\varepsilon\Delta\delta}) F^-(0)}{\beta_2 e^{\varepsilon\Delta\delta} - \beta_1 e^{-\varepsilon\Delta\delta}} = a_4 F^+(\Delta\delta) + a_5 F^-(0)$$

$$F^-(\Delta\delta) = \frac{(e^{\varepsilon\Delta\delta} - e^{-\varepsilon\Delta\delta}) F^+(\Delta\delta) + (\beta_2 - \beta_1) F^-(0)}{\beta_2 e^{\varepsilon\Delta\delta} - \beta_1 e^{-\varepsilon\Delta\delta}} = a_5 F^+(\Delta\delta) + a_4 F^-(0) ,$$

(A.14)

where

$$a_4 = \frac{\left(\frac{1}{\rho} - \rho\right)}{\left(\frac{1}{\tau\rho} - \tau\rho\right)} = \frac{\tau(1-\rho^2)}{1-\tau^2\rho^2} ,$$

(A.15)

$$a_5 = \frac{\left(\frac{1}{\tau} - \tau\right)}{\left(\frac{1}{\tau\rho} - \tau\rho\right)} = \frac{\rho(1-\tau^2)}{1-\tau^2\rho^2} ,$$

(A.16)

and

$$\tau = e^{-\varepsilon\Delta\delta} \text{ and } \rho = \beta_1 .$$

(A.17)

b) Case without absorption, $\alpha_1 = \alpha_2 = \alpha$

In this case we allow the Rayleigh scattering only so that $\omega_0 = 1$ and $g = 0$. Then Eqs. (A.3a) and (A.3b) become

$$\frac{dF^+(\delta)}{d\delta} = \alpha \, [F^+(\delta) - F^-(\delta)] = \frac{dF^-(\delta)}{d\delta} , \tag{A.18}$$

hence

$$F^+(\delta) = F^-(\delta) + C . \tag{A.19}$$

The solutions of Eq. (A.18) are then

$$F^+(\delta) = \alpha \, \delta \, C + D$$

$$F^-(\delta) = (\alpha \, \delta - 1) \, C + D . \tag{A.20}$$

The integration constants C and D can be obtained from the boundary conditions $F^+(\Delta\delta)$ and $F^-(0)$ and substituted into Eq. (A.20) to give

$$F^+(0) = \frac{F^+(\Delta\delta) + \alpha \, \Delta\delta \, F^-(0)}{1 + \alpha \, \Delta\delta} = a_4 \, F^+(\Delta\delta) + a_5 \, F^-(0) , \tag{A.21}$$

$$F^-(\Delta\delta) = \frac{\alpha \, \Delta\delta \, F^+(\Delta\delta) + F^-(0)}{1 + \alpha \, \Delta\delta} = a_5 \, F^+(\Delta\delta) + a_4 \, F^-(0) , \tag{A.22}$$

where

$$a_4 = \frac{1}{1 + \alpha \, \Delta\delta} , \tag{A.23}$$

$$a_5 = \frac{\alpha \, \Delta\delta}{1 + \alpha \, \Delta\delta} . \tag{A.24}$$

2. Solution for $S \neq 0$

For the particular solutions obtained above let's try to derive the expression valid for any S where $S(\delta) = \mu_0 I_0(\delta)$. Let

$$F_1 = F^+ - \gamma_1 S ,$$ (A.25)

$$F_2 = F^- - \gamma_2 S .$$ (A.26)

Then from Eqs. (4) and the definition $S(\delta) = \mu_0 I_0(\delta)$ we obtain

$$\frac{dF_1}{d\delta} = \alpha_1 F_1 - \alpha_2 F_2 + I_0(\delta) [\gamma_1 + \alpha_1 \gamma_1 \mu_0 - \alpha_2 \gamma_2 \mu_0 - \alpha_3] ,$$

$$\frac{dF_2}{d\delta} = \alpha_2 F_1 - \alpha_1 F_2 + I_0(\delta) [\gamma_2 + \alpha_2 \gamma_1 \mu_0 - \alpha_1 \gamma_2 \mu_0 + \alpha_4] .$$ (A.27)

We seek γ_1 and γ_2 so that

$$\gamma_1 (1 + \alpha_1 \mu_0) - \gamma_2 \alpha_2 \mu_0 = \alpha_3 ,$$

$$\gamma_1 \alpha_2 \mu_0 + \gamma_2 (1 - \alpha_1 \mu_0) = -\alpha_4 .$$ (A.28)

The discriminant of the system is

$$1 - \alpha_1^2 \mu_0^2 + \alpha_2^2 \mu_0^2 = 1 - \varepsilon^2 \mu_0^2 ,$$ (A.29)

where ε is given by Eq. (A.7).

a) General case ($\varepsilon\,\mu_0 \neq 1$)

$$\gamma_1 = \frac{\alpha_3 - \mu_0\,(\alpha_1\,\alpha_3 + \alpha_2\,\alpha_4)}{1 - \varepsilon^2\,\mu_0^2} \, ,$$

$$\gamma_2 = \frac{-\,\alpha_4 - \mu_0\,(\alpha_1\,\alpha_4 + \alpha_2\,\alpha_3)}{1 - \varepsilon^2\,\mu_0^2} \, ,$$

(A.30)

and

$$a_2 = -\,a_5\,\gamma_2 - a_4\,\gamma_1\,a_1 + \gamma_1 \, ,$$

$$a_3 = -\,a_4\,\gamma_2 - a_5\,\gamma_1\,a_1 + a_1\,\gamma_2 \, .$$

(A.31)

b) Resonance case ($\varepsilon\,\mu_0 = 1$)

We no longer have a solution with γ_1 and γ_2 constants. We therefore seek a solution with

$$\gamma_1 = \gamma_1^0 + \gamma_1'\,\frac{\delta}{\mu_0} \, ,$$

$$\gamma_2 = \gamma_2^0 + \gamma_2'\,\frac{\delta}{\mu_0} \, .$$

(A.32)

With the use of (A.25), (A.26), and (A.27), the equations are now

$$\left(\gamma_1^0 + \gamma_1'\,\frac{\delta}{\mu_0}\right)(1 + \alpha_1\,\mu_0) - \left(\gamma_2^0 + \gamma_2'\,\frac{\delta}{\mu_0}\right)\alpha_2\,\mu_0 = \alpha_3 + \gamma_1' \, ,$$

$$\left(\gamma_1^0 + \gamma_1'\,\frac{\delta}{\mu_0}\right)\alpha_2\,\mu_0 + \left(\gamma_2^0 + \gamma_2'\,\frac{\delta}{\mu_0}\right)(1 - \alpha_1\,\mu_0) = -\,\alpha_4 + \gamma_2' \, .$$

(A.33)

From (A.33) we may write

$$\frac{\dot{\gamma_1}}{\dot{\gamma_2}} = \frac{\alpha_2 \,\mu_0}{1 + \alpha_1 \,\mu_0} = \frac{1 - \alpha_1 \,\mu_0}{-\alpha_2 \,\mu_0} = \frac{-\alpha_4 + \dot{\gamma_2}}{\alpha_3 + \dot{\gamma_1}} \,.$$

(A.34)

Then we obtain

$$\gamma_1{}' = \frac{-\alpha_3 + \mu_0 \,(\alpha_1 \alpha_3 + \alpha_2 \,\alpha_4)}{2} \,,$$

$$\gamma_2{}' = \frac{\alpha_4 + \mu_0 \,(\alpha_1 \alpha_4 + \alpha_2 \,\alpha_3)}{2} \,.$$

(A.35)

The choice of one of the two γ^0 is then arbitrary. Among the infinity of solutions the most symmetrical one is

$$\gamma_1^0 = \mu_0 \,\frac{\alpha_1 \,\alpha_3 + \alpha_2 \,\alpha_4}{2} \,,$$

$$\gamma_2^0 = \mu_0 \,\frac{\alpha_1 \,\alpha_4 + \alpha_2 \,\alpha_3}{2} \,.$$

(A.36)

Then we get results

$$a_2 = -a_5 \,\gamma_2^0 - a_4 \left(\gamma_1^0 + \dot{\gamma_1} \,\frac{\delta}{\mu_0} \right) a_1 + \gamma_1^0 \,,$$

$$a_3 = -a_4 \,\gamma_2^0 - a_5 \left(\gamma_1^0 + \dot{\gamma_1} \,\frac{\delta}{\mu_0} \right) a_1 + \left(\gamma_2^0 + \dot{\gamma_2} \,\frac{\delta}{\mu_0} \right) a_1 \,.$$

(A.37)

REFERENCES

Ackerman, M., 1971: Ultraviolet solar radiation related to mesospheric processes. *In Mesospheric Models and Related Experiments*. G. Fiocco (Ed.), Reidel, Dordrecht, Holland, pp. 148-150.

Briegleb, B.P., P. Minnis, V. Ramanathan and E. Harrison, 1986: Comparison of regional clear-sky albedos infrared from satellite observation and model computations. *J. Climate Appl. Meteor.*, **25**, 214-216.

Cess, R.D., G.L. Potter, S.J. Ghan and W.L. Gates, 1985: The climatic effects of large injections of atmopsheric smoke and dust: A study of climate feedback mechanisms with one- and three-dimensional climate model. *J. Geophys. Res.*, **90**, 12,937-12,950.

Chou, M.-D., 1986: Atmospheric solar heating rate in the water vapor bands. *J. Climate Appl. Meteor.*, **25**, 1532-1542.

Chou, M.-D., and A. Arking, 1981: An efficient method for computing the absorption of solar radiation by water vapor. *J. Atmos. Sci.*, **38**, 798-807.

Coakley, J.A., Jr., R.D. Cess and F.B. Yurevich, 1983: The effect of tropospheric aerosols on the Earth's radiation budget: A parameterization for climate models. *J. Atmos. Sci.*, **40**, 116-138.

Cox, S.K., 1971: Cirrus clouds and the climate. *J. Atmos. Sci.*, **28**, 1513-1515.

Fouquart, Y., 1987: Radiative transfer in climate modeling (to be published).

Geleyn, J.F., 1977: Parameterization of radiative transfer at ECMWF. Proceedings of the ECMWF 1977 seminar on the parameterization of the physical processes in the free atmosphere, 273-345.

Geleyn, J.F., and A. Hollingsworth, 1979: An economical analytical method for the computation of the interaction between scattering and line absorption of radiation. *Beitr. Phys. Atmos.*, **52**, 1-16.

Ghan, S., 1986: personal communication.

Ghan, S., J.W. Lingaas, M.E. Schlesinger, R.L. Mobley and W.L. Gates, 1982: *A documentation of the OSU two-level atmospheric general*

circulation model. Report No. 35, Climatic Research Institute, Oregon State University, Corvallis, OR, 395 pp.

Griffith, K.T., and Cox, S.K., 1977: *Infrared radiative properties of broadband cirrus inferred from broadband measurements.* Atmos. Sci. Paper No. 269, Atmospheric Sciences, Colorado State University.

Griffith, K.T., S.K. Cox and R.C. Knollenberg, 1980: Infrared radiative properties of tropical cirrus clouds inferred from aircraft measurements. *J. Atmos. Sci.*, **37**, 1073-1083.

Heymsfield, A.J., 1975a: Cirrus uncinus generating cells and the evolution of cirricorm clouds. Part I: Aircraft observations of the growth of the ice phase. *J. Atmos. Sci.*, **32**, 799-808.

Heymsfield, A.J. 1975b: Cirrus uncinus generating cells and the evolution of cirriform clouds. Part II: The structure and circulations of the cirrus uncinus generating head. *J. Atmos. Sci.*, **32**, 809-819.

Heymsfield, A.J. 1975c: Cirrus uncinus generating cells and the evolution of cirriform clouds. Part III: Numerical computations of the growth of the ice phase. *J. Atmos. Sci.*, **32**, 820-830.

Heymsfield, A.J. 1977: Precipitation development in stratiform ice clouds: A microphysical and dynamical study. *J. Atmos. Sci.*, **34**, 367-381.

Joseph, J.H., W.J. Wiscombe and J.A. Weinman, 1976: The delta-Eddington approximation for radiative flux transfer. *J. Atmos. Sci.*, **33**, 2452-2459.

King, M.D., and Harshvarthan, 1986: Comparative accuracy of selected multiple scattering approximations. *J. Atmos. Sci.*, **43**, 784-801.

Lacis, A.A., and J.E. Hansen, 1974: A parameterization for the absorption of solar radiation in the earth's atmosphere. *J. Atmos. Sci.*, **31**, 118-133.

Labs, D., and H. Neckel, 1970: Transformation of the absolute solar radiation data into the "International Practical Temperature Scale of 1968." *Solar Physics*, **15**, 79-87.

Liou, K.-N., 1980: *An Introduction to Atmospheric Radiation.* Academic Press, New York, 392 pp.

Luther, M. F., and Y. Fouquart, 1985: unpublished manuscript.

Manabe, S., and J.L. Holloway, Jr., 1975: The seasonal variation of the hydrologic cycle as simulated by a global model of the atmosphere. *J.*

Geophys. Res., **80**, 1617-1649.

Manabe, S., and R.F. Strickler, 1964: Thermal equlibrium of the atmosphere with a convective adjustment. *J. Atmos. Sci.*, **21**, 361-385.

McClatchey, R. A., R. W. Fenn, J. E. A. Selby, J. S. Garing, and F. E. Volz, 1973: *Optical properties of the atmosphere.* AFCRL-70-0527, Air Force Cambridge Research Laboratories, Bedford, MA, pp85.

Neckel, H., and D. Labs, 1984: The solar radiation between 3,300 and 12,500 Å . *Solar Physics*, **90**, 205-258.

Paltridge, G.W., and C.M.R. Platt, 1980: Aircraft measurements of solar and infrared radiation and the microphysics of cirrus clouds. Vol. of Extended Abstracts, Int. Radiation Symp., Fort Collins, IAMAP, 419-421.

Payne, R.E., 1972: Albedo of the sea surface. *J. Atmos. Sci.*, **29**, 959-970.

Platt, C.M.R., and A.C. Dilley, 1979: Remote sounding of high clouds: I. Infrared emissivity of cirrostratus. *J. Appl. Met.*, **18**, 1144-1150.

Platt, C.M.R., D.W. Reynolds and N.C. Abshire, 1980: Satellite and lidar observations of the albedo, emittance and optical depth of cirrus compared to model calculations. *Mon. Wea. Rev.*, **108**, 195-204.

Platt, C.M.R., and G.L. Stephens, 1980: The interpretation of remotely sensed high cloud emisttances. *J. Atmos. Sci.*, **37**, 2314-2322.

Reynolds, D.W., and T.H. Vonder Haar, 1977: A bispectral method for cloud parameter determination. *Mon. Wea. Rev.*, **105**, 446-457.

Rodgers, C.D., 1967: *The radiative heat budget of the troposphere and lower stratosphere.* Report No. A2, Planetary Circulations Project, Department of Meteorology, M.I.T., 99 pp.

Ryan, R.T., M. Blau, Jr., P.C. Von Thuna, M.L. Cohen and G.D. Roberts, 1972: Cloud microstructure as determined by an optical cloud particle spectrometer. *J. Appl. Met.*, **11**, 149-156.

Schlesinger, M.E., 1976: *A numerical simulation of the general circulation of atmospheric ozone.* Ph.D. Dissertation, Department of Meteorology, University of California, Los Angeles, CA, 376 pp.

Schuster, A., 1905: Radiation through a foggy atmosphere, *Astrophys. J.*, **21**, 1-22.

Sommerville, R.C.J., P.H. Stone, M. Halem, J.E. Hansen, J.S. Hogan, L.M.

Druyan, G. Russel, A.A. Lacis, W.J. Quirk and J. Tenenbaum, 1974: The GISS model of the global atmosphere. *J. Atmos. Sci.*, **31**, 84-117.

Starr, D.O'C., 1976: *The sensitivity of tropical radiative budgets to cloud distribution and the radiative properties of clouds.* Atmos. Sci. Paper 254, Colo. State University, Fort Collins, 117 pp. [NTIS PB 263-227.]

Starr, D.O'C., 1982: *Numerical Experiments on the Formation and Maintenance of Cirriform Clouds.* Ph.D. dissertation, Colo. State University, Fort Collins, 352 pp.

Starr, D.O'C., and S.K. Cox, 1985: Cirrus clouds, Part II: Numerical experiments on the formation and maintenance of cirrus. *J. Atmos. Sci.*, **42**, 2682-2694.

Stephens, G.L., 1978: Radiation profiles in extended water clouds. Part II: Parameterization schemes. *J. Atmos. Sci.*, **35**, 2123-2132.

Stephens, G.L., 1984: The parameterization of radiation for numerical weather prediction and climate models. *Mon. Wea. Rev.*, **112**, 826-867.

Welch, R.M., S.K. Cox and J.M. Davis, 1980: Solar Radiation and Clouds. *Meteor. Monogr.*, No. **39**, Amer. Meteor. Soc., 93 pp.

Wiscomb, W.J., and J.W. Evans, 1977: Exponential-sum fitting of radiative transmission functions. *J. Comp. Phys.*, **24**, 416-444.

Appendix C

LONGWAVE RADIATION PARAMETERIZATION

Table of Contents

List of Figures

List of Figures/continued

In this paper a longwave radiation parameterization for the multi-layer model is described and its results are compared with the results of the radiative transfer models that participated in the Intercomparison of Radiation Codes used in Climate Models (ICRCCM, Luther *et al.*, 1988).

1. Basic equations

1.1. Clear sky

Based upon the assumptions that the atmosphere is plane parallel, that radiation is isotropic, and the scattering by air molecules and aerosols is negligible, the frequency-integrated downward and upward fluxes of longwave radiation at a level z can be expressed by (Liou, 1980)

$$R_z^\downarrow = \int_0^\infty \pi B_\nu(T_z)\, d\nu + \int_{T_z}^0 dT \int_0^\infty \frac{d}{dT}[\pi B_\nu(T)]\, \tau_\nu(\Delta u)\, d\nu \tag{1}$$

and

$$R_z^\uparrow = \int_0^\infty \pi B_\nu(T_z)\, d\nu + \int_{T_z}^{T_g} dT \int_0^\infty \frac{d}{dT}[\pi B_\nu(T)]\, \tau_\nu(\Delta u)\, d\nu, \tag{2}$$

where ν is the frequency, $\pi B_\nu(T)$ is the blackbody flux emitted at temperature T, T_z is the temperature at level z, T_g is the temperature of the Earth's surface, τ_ν is the monochromatic transmission function, and $\Delta u = |u - u_z|$ where u and u_z are, respectively, the absorber amount at the level of temperature T and z. The second term on the right-hand-side of Eq. (1) can be written as follows

$$\int_{T_z}^0 dT \int_0^\infty \frac{d}{dT}[\pi B_\nu(T)]\, \tau_\nu(\Delta u)\, d\nu$$

$$= \int_{T_z}^0 dT \sum_{j=1}^J \frac{d}{dT} \int_{\nu_{L,j}}^{\nu_{U,j}} \pi B_\nu(T)\, \tau_\nu(\Delta u)\, d\nu$$

$$= \int_{T_z}^0 dT \sum_{j=1}^J \frac{d}{dT}\left[\tau_j(\Delta u) \int_{\nu_{L,j}}^{\nu_{U,j}} \pi B_\nu(T)\, d\nu \right]. \tag{3}$$

In Eq. (3), the infrared spectrum has been subdivided into $j = 1,...,J$ spectral intervals, each bounded by $v_{L,j}$ and $v_{U,j}$, with $v_{L,1} = 0$, $v_{U,J} = \infty$, and where

$$\tau_j(\Delta u) \equiv \frac{\displaystyle\int_{v_{L,j}}^{v_{U,j}} \pi B_v(T) \, \tau_v(\Delta u) \, dv}{\displaystyle\int_{v_{L,j}}^{v_{U,j}} \pi B_v(T) \, dv} \tag{4}$$

is the mean transmission function for interval j. By introducing

$$f_j(T) \equiv \frac{\displaystyle\int_{v_{L,j}}^{v_{U,j}} \pi B_v(T) \, dv}{\pi B(T)} \, , \tag{5}$$

the fraction of blackbody radiation for interval j, where

$$\pi B(T) = \int_{v_{L,1}}^{v_{U,J}} \pi B_v(T) \, dv = \sigma T^4 \tag{6}$$

and σ is the Stefan-Boltzmann constant, Eq. (3) can be written as

$$\int_{T_z}^{0} dT \int_{0}^{\infty} \frac{d}{dT} [\pi B(T)] \, \tau_j(\Delta u) \, dv$$

$$= \sum_{j=1}^{J} \int_{T_z}^{0} \left\{ f_j(T) \, \tau_j(\Delta u) \left[\frac{d(\pi B)}{dT} \right] + \pi B(T) \, \frac{d}{dT} [f_j(T) \, \tau_j(\Delta u)] \right\} \, dT \, . \tag{7}$$

Because $\pi B(T)$ has a strong dependence on T as shown by Eq. (6), while $f_j(T)$ and $\tau_j(\Delta u)$ have only a weak dependence (see section 2), we neglect the second term on the right-hand side of Eq. (7) to obtain

$$\int_{T_z}^{0} dT \int_{0}^{\infty} \frac{d}{dT} [\pi B(T)] \, \tau_j(\Delta u) \, dv \cong \sum_{j=1}^{J} \int_{\pi B_z}^{0} f_j(\pi B) \, \tau_j(\Delta u) \, d(\pi B) \, , \tag{8}$$

where

$$\pi B_z = \pi B(T_z) \, . \tag{9}$$

The substitution of Eq. (8) into Eq. (1) then gives

$$R_z^\downarrow = \pi B_z + \sum_{j=1}^{J} \int_{\pi B_z}^{0} f_j(\pi B) \, \tau_j(\Delta u) \, d(\pi B) \, . \tag{10}$$

Similarly, Eq. (2) can be written as

$$R_z^\uparrow = \pi B_z + \sum_{j=1}^{J} \int_{\pi B_z}^{\pi B_g} f_j(\pi B) \, \tau_j(\Delta u) \, d(\pi B) \, , \tag{11}$$

where

$$\pi B_g = \pi B(T_g) = \sigma T_g^4 \, . \tag{12}$$

From Eq. (10) the vertically-discrete form of the downward flux at the bottom of layer ℓ (see Fig. 1 in solar radiation parameterization) can be written as

$$
\begin{aligned}
R_{\ell+1/2}^\downarrow &= \pi B_{\ell+1/2} + \sum_{j=1}^{J} \sum_{\ell'=0}^{\ell} \int_{\pi B_{\ell+1/2}}^{\pi B_{\ell-1/2}} f_j(\pi B) \, \tau_j(|u - u_{\ell+1/2}|) \, d(\pi B) \\
&= \pi B_{\ell+1/2} - \sum_{j=1}^{J} \sum_{\ell'=0}^{\ell} C_{\ell',\ell}^{j} \\
&= \pi B_{\ell+1/2} - \sum_{\ell'=0}^{\ell} S_{\ell',\ell} \, ,
\end{aligned}
\tag{13}
$$

where

$$C_{\ell',\ell}^{j} \equiv \int_{\pi B_{\ell+1/2}}^{\pi B_{\ell-1/2}} f_j(\pi B) \, \tau_j(|u - u_{\ell+1/2}|) \, d(\pi B) \tag{14}$$

represents the contribution to the flux at level $\ell+1/2$ from layer ℓ', including a nonzero contribution from $C^j_{0,\ell}$ when the model atmosphere is restricted to the troposphere with $\ell = 1/2$ corresponding to the tropopause, and

$$S_{\ell',\ell} = \sum_{j=1}^{J} C^j_{\ell',\ell} .$$

(15)

Similarly, the upward flux at level $\ell+1/2$ can be written as

$$R^{\uparrow}_{\ell+1/2} = \pi B_{\ell+1/2} + \sum_{\ell'=\ell+1}^{L+1} S_{\ell',\ell} .$$

(16)

We calculate $C^j_{\ell',\ell}$ by the trapezoidal rule to obtain

$$C^j_{0,\ell} = \begin{cases} 0, & \ell = 1/2 \text{ is the top of the atmosphere,} \\[2mm] \frac{1}{2} f_j (\pi B_{1/2}) [\tau_j(|u_\infty - u_{\ell+1/2}|) + \tau_j(|u_{1/2} - u_{\ell+1/2}|)] \pi B_{1/2}, \\[2mm] & \ell = 1/2 \text{ is the tropopause,} \end{cases}$$

(17a)

$$\begin{aligned} C^j_{\ell',\ell} = \frac{1}{2} [\, & f_j(\pi B_{\ell'+1/2}) \, \tau_j(|u_{\ell'+1/2} - u_{\ell+1/2}|) \\ & + f_j(\pi B_{\ell'-1/2}) \, \tau_j(|u_{\ell'-1/2} - u_{\ell+1/2}|)] \, (\pi B_{\ell'+1/2} - \pi B_{\ell'-1/2}) , \\ & \hspace{6cm} 1 \le \ell \le L , \end{aligned}$$

(17b)

and

$$C^j_{L+1,\ell} = (\pi B_g - \pi B_{L+1/2}) \frac{1}{2} [f_j(\pi B_{L+1/2}) + f_j(\pi B_g)] \, \tau(u_{\ell+1/2}) ,$$

(17c)

where u_∞ is the effective absorber amount from the Earth's surface to the top of atmosphere ($p = 0$, $T = 0$), and where the atmosphere above $\ell = 1/2$ is assumed to be isothermal with $T = T_{1/2} = 218$ K (Ghan *et al.*, 1982).

1.2. Cloudy sky

The fractional cloud cover for longwave radiation is treated in the same manner as for solar radiation. The vertical distribution of clouds is subdivided into individual cloud groups, with each group being comprised of an ensemble of contiguous cloud layers, and the cloud groups being separated from each other by at least one layer of clear air. The contiguous cloud layers within each group are considered to overlap each other vertically to the maximum extent possible, while the noncontiguous cloud groups are considered to overlap each other randomly in the vertical.

To derive the radiative transfer equations for this case of joint random-maximum overlap, we begin in subsection 1.2.1 with the simpler case of pure random overlap. In this case a cloud group is taken to consist of only a single layer, with the cloud groups (layers) being randomly overlapped. Subsequently, in subsection 1.2.2 we will return to the definition of a cloud group as a ensemble of maximum-overlapped contiguous cloud layers and determine how the detailed structure of these cloud groups modifies the radiative transfer for the simpler case of pure random overlap. However, if one does not wish to incur the increased complexity of the joint random-maximum overlap case, the results of subsection 1.2.1 for the pure random overlap case can be used directly together with the results of section 1.2.3.

1.2.1. Random overlap

As for the clear atmosphere we determine here both the downward and upward longwave fluxes $R^{\downarrow}_{\ell+1/2}$ and $R^{\uparrow}_{\ell+1/2}$ at an arbitrary half-integer level $\ell+1/2$.

a. *Downward flux*

For the downward flux we consider that there are $N(\ell)$ clouds above level $\ell+1/2$ as shown in Fig. 1a, with the clouds being counted downward from the top of the atmosphere toward level $\ell+1/2$, and with the cloudiness of the

(a) for downward flux
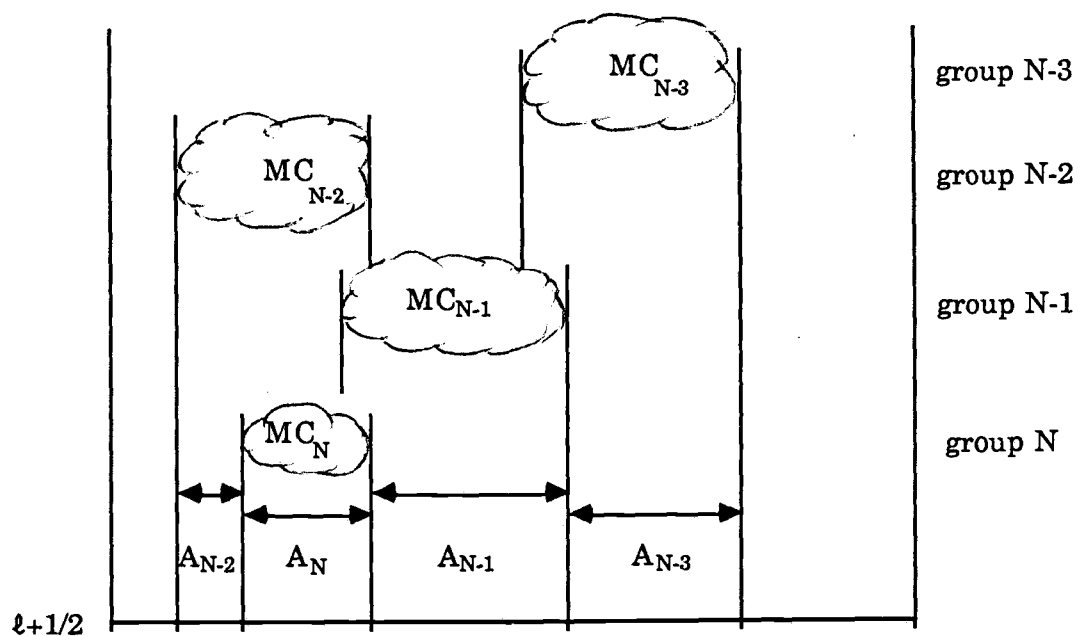
(b) for upward flux
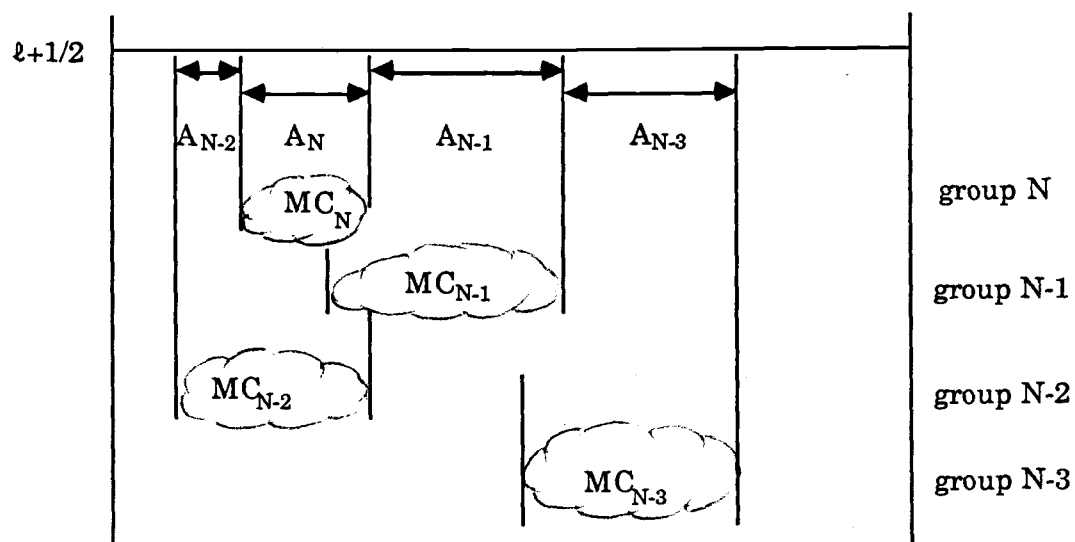
Fig. 1. Fractional area subtended by each cloud group at level $\ell+1/2$ (a) for downward flux and (b) for upward flux.

n-th cloud being characterized by MC_n. Then

$$R^{\downarrow}_{\ell+1/2} = \sum_{n=0}^{N(\ell)} A_n \, (R^{\downarrow}_{\ell+1/2})_n \,,$$

$$(18)$$

where A_0 is the fractional area at level $\ell+1/2$ subtended by the clear atmosphere above, A_n is the fractional area at level $\ell+1/2$ subtended by cloud $n \neq 0$, and $(R^{\downarrow}_{\ell+1/2})_n$ is the contribution to the downward flux from the n-th cloud.

The value of A_0 is given by the product of all the clear areas,

$$A_0 = \prod_{i=0}^{N(\ell)-1} (1 - MC_{N(\ell)-i}) \,,$$

$$(19)$$

while the value of A_n is given by the product of MC_n with the product of the clear areas $(1 - MC_i)$ for each cloud i between cloud n and level $\ell+1/2$,

$$A_n = MC_n \prod_{i=0}^{N(\ell)-(n+1)} (1 - MC_{N(\ell)-i}) \,, \quad 1 \le n \le N(\ell) \,.$$

$$(20)$$

In Eqs. (19) and (20) the product is unity if its upper limit is negative. From these definitions it can be shown that

$$\sum_{n=0}^{N(\ell)} A_n = 1 \,.$$

$$(21)$$

From a consideration of the derivation of Eq. (13), $(R^{\downarrow}_{\ell+1/2})_n$ can be written as

$$
(R^{\downarrow}_{\ell+1/2})_n =
\begin{cases}
\pi B_{\ell+1/2} - \displaystyle\sum_{\ell'=0}^{\ell} S_{\ell',\ell} \,, & \text{if } n = 0 \\[4ex]
\pi B_{\ell+1/2} - S''_{\ell_B(n)+1,\ell} - \displaystyle\sum_{\ell'=\ell_B(n)+2}^{\ell} S_{\ell',\ell} \,, & \\[2ex]
\qquad \text{if } 0 < n < N(\ell) \text{ or } n = N(\ell) \text{ and } \ell_B(N) \neq \ell & \\[2ex]
R''^{\downarrow}_{\ell+1/2} \,, & \text{if } n = N(\ell) \text{ and } \ell_B(N) = \ell \,,
\end{cases}
\tag{22}
$$

where the summation is zero if the upper limit is less than the lower limit, $S_{\ell',\ell}$ is given by Eqs. (15) and (17), $S''_{\ell_B(n)+1,\ell}$ is the the contribution from the layer just below the n-th cloud layer, the latter being located in layer $\ell_B(n)$[1] $\leq \ell$, and $R''^{\downarrow}_{\ell+1/2}$ is the downward flux at the bottom of the cloud in layer ℓ which is defined in section 1.2.3. The quantity $S''_{\ell_B(n)+1,\ell}$ is given by Eqs. (15) and (17b) with $\ell' = \ell_B(n)+1$, but with $\pi B_{\ell'-1/2}$ replaced with the downward flux at the bottom of the cloud in layer $\ell'-1$, $R''^{\downarrow}_{\ell'-1/2}$, this to allow for the fact that this cloud may not be a blackbody. Thus,

$$
S''_{\ell',\ell} = S_{\ell',\ell} + D''^{\downarrow}_{\ell',\ell} \,,
\tag{23}
$$

where

$$
D''^{\downarrow}_{\ell',\ell} = \sum_{j=1}^{J} \frac{1}{2} \left[f_j(\pi B_{\ell'+1/2})\, \tau_j(|u_{\ell'+1/2} - u_{\ell+1/2}|) \right.
$$
$$
\left. + f_j(\pi B_{\ell'-1/2})\, \tau_j(|u_{\ell'-1/2} - u_{\ell+1/2}|) \right] (\pi B_{\ell'-1/2} - R''^{\downarrow}_{\ell'-1/2})
\tag{24}
$$

for $\ell' = \ell_B(n)+1$ is a measure of the nonblackness of the n-th cloud.

---

[1] $\ell_B(n)$ denotes the layer in which the n-th cloud has its base. Similarly, $\ell_T(n)$ denotes the layer in which the n-th cloud has its top. For the case of random cloud overlap, $\ell_B(n) = \ell_T(n)$. For the the case of joint random-maximum cloud overlap, $\ell_B(n)$ and $\ell_T(n)$ need not be equal.

Substituting Eqs. (22) and (23) into Eq. (18) and using Eq. (21) gives

$$
R^{\downarrow}_{\ell+1/2} = \begin{cases}
\pi B_{\ell+1/2} - A_0 \sum_{\ell'=0}^{\ell} S_{\ell',\ell} - \sum_{n=1}^{N(\ell)} A_n \left(\sum_{\ell'=\ell_B(n)+1}^{\ell} S_{\ell',\ell} \right) \\[2ex]
\quad - \sum_{n=1}^{N(\ell)-1} A_n D''^{\downarrow}_{\ell_B(n)+1,\ell} - A_{N(\ell)} D''^{\downarrow}_{\ell_B[N(\ell)]+1,\ell} \,, \quad \text{if } \ell_B[N(\ell)] < \ell, \\[4ex]
(1 - A_{N(\ell)}) \pi B_{\ell+1/2} + A_{N(\ell)} R''^{\downarrow}_{\ell+1/2} - A_0 \sum_{\ell'=0}^{\ell} S_{\ell',\ell} \\[2ex]
\quad - \sum_{n=1}^{N(\ell)-1} A_n \left(\sum_{\ell'=\ell_B(n)+1}^{\ell} S_{\ell',\ell} \right) - \sum_{n=1}^{N(\ell)-1} A_n D''^{\downarrow}_{\ell_B(n)+1,\ell} \,, \\[2ex]
\hspace{6cm} \text{if } \ell_B[N(\ell)] = \ell.
\end{cases}
$$

(25)

Defining C_ℓ as the fractional cloudiness in layer ℓ,

$$
C_\ell = \begin{cases}
0 , & \text{if } \ell_B[N(\ell)] < \ell, \\[2ex]
A_{N(\ell)} = MC_{N(\ell)} , & \text{if } \ell_B[N(\ell)] = \ell .
\end{cases}
$$

(26)

Equation (25) can then be written as

$$
R^{\downarrow}_{\ell+1/2} = (1 - C_\ell) \pi B_{\ell+1/2} + C_\ell R''^{\downarrow}_{\ell+1/2} - \sum_{n=0}^{N(\ell)} A_n \left(\sum_{\ell'=0}^{\ell} F^{\downarrow}_{\ell',n} S_{\ell',\ell} \right)
$$
$$
\quad - \sum_{n=1}^{N(\ell)-1} A_n D''^{\downarrow}_{\ell_B(n)+1,\ell} - \delta_{C_\ell,0} A_{N(\ell)} D''^{\downarrow}_{\ell_B[N(\ell)]+1,\ell} \,,
$$

(27)

where

$$F^{\downarrow}_{\ell',n} = \begin{cases} 1 \, , & \text{if } n = 0 \\ 0 \, , & n > 0 \text{ and } \ell' \leq \ell_B(n) \\ 1 \, , & n > 0 \text{ and } \ell' > \ell_B(n) \end{cases} \tag{28}$$

and $\delta_{C_\ell,0}$ is the Dirac-delta function. The order of the summations in the third term of Eq. (27) can be reversed so that the resulting equation has the same form as Eq. (13) for the clear atmosphere:

$$R^{\downarrow}_{\ell+1/2} = (1 - C_\ell) \pi B_{\ell+1/2} + C_\ell R''^{\downarrow}_{\ell+1/2} - \sum_{\ell'=0}^{\ell} \left[\sum_{n=0}^{N(\ell)} A_n F^{\downarrow}_{\ell',n} \right] S_{\ell',\ell}$$

$$- \left[\sum_{n=1}^{N(\ell)-1} A_n D''^{\downarrow}_{\ell_B(n)+1,\ell} + \delta_{C_\ell,0} A_{N(\ell)} D''^{\downarrow}_{\ell_B[N(\ell)]+1,\ell} \right]$$

or

$$R^{\downarrow}_{\ell+1/2} = (1 - C_\ell) \pi B_{\ell+1/2} + C_\ell R''^{\downarrow}_{\ell+1/2} - \sum_{\ell'=0}^{\ell} [E^{\downarrow}_{\ell',\ell} S_{\ell',\ell} + G^{\downarrow}_{\ell',\ell} D''^{\downarrow}_{\ell',\ell}] \, , \tag{29}$$

where

$$E^{\downarrow}_{\ell',\ell} = \sum_{n=0}^{N(\ell)} A_n F^{\downarrow}_{\ell',n}$$

$$= A_0 + \sum_{n=1}^{N(\ell'-1)} A_n \, , \tag{30}$$

with $N(\ell')$ being the number of clouds above level $\ell'+1/2$, and

$$G^{\downarrow}_{\ell',\ell} = \begin{cases} A_n, & \text{if } \ell' = \ell_B(n) + 1, \\ \\ 0, & \text{if } \ell' \neq \ell_B(n) + 1. \end{cases} \tag{31}$$

From Eqs. (19) and (20), Eqs. (30) and (31) can then be rewritten as

$$E^{\downarrow}_{\ell',\ell} = \prod_{i=0}^{N(\ell)-1} (1 - MC_{N(\ell)-i}) + \sum_{n=1}^{N(\ell'-1)} \left\{ MC_n \prod_{i=0}^{N(\ell)-(n+1)} (1 - MC_{N(\ell)-i}) \right\}$$

$$= \prod_{i=0}^{N(\ell)-[N(\ell'-1)+1]} (1 - MC_{N(\ell)-i}) \tag{32}$$

and

$$G^{\downarrow}_{\ell',\ell} = \begin{cases} MC_{N(\ell'-1)} \prod_{i=0}^{N(\ell)-[N(\ell'-1)+1]} (1 - MC_{N(\ell)-i}) & \text{if } \ell'-1 = \ell_B[N(\ell')] \\ \\ 0, & \text{if } \ell'-1 \neq \ell_B[N(\ell')] \end{cases}$$

or

$$G^{\downarrow}_{\ell',\ell} = C_{\ell'-1} \prod_{i=0}^{N(\ell)-[N(\ell'-1)+1]} (1 - MC_{N(\ell)-i}). \tag{33}$$

b. *Upward flux*

For the upward flux we consider that there are $N(\ell)$ clouds below level $\ell+1/2$ as shown in Fig. 1b, with the clouds being counted upward from the Earth's surface toward level $\ell+1/2$, and with the cloudiness of the n-th cloud being characterized by MC_n.[2] Then,

$$R^{\uparrow}_{\ell+1/2} = \sum_{n=0}^{N(\ell)} A_n \, (R^{\uparrow}_{\ell+1/2})_n \,,$$

$$(34)$$

where A_o is the fractional area at level $\ell+1/2$ subtended by the clear atmosphere below, A_n is the fractional area at level $\ell+1/2$ subtended by cloud $n \neq 0$, and $(R^{\uparrow}_{\ell+1/2})_n$ is the contribution to the upward flux from the n-th cloud.

The values of A_o and A_n are given by Eqs. (19) and (20). From a consideration of the derivation of Eq. (16), $(R^{\uparrow}_{\ell+1/2})_n$ can be written as

$$(R^{\uparrow}_{\ell+1/2})_n = \begin{cases} \pi B_{\ell+1/2} + \displaystyle\sum_{\ell'=\ell+1}^{L+1} S_{\ell',\ell} & \text{if } n=0 \\[2em] \pi B_{\ell+1/2} + S''_{\ell_T(n)-1,\ell} + \displaystyle\sum_{\ell'=\ell+1}^{\ell_T(n)-2} S_{\ell',\ell} & \text{if } 0 < n < N(\ell) \text{ or} \\[1em] & \qquad n=N(\ell) \text{ and } \ell_T(N) \neq \ell+1 \\[1em] R''^{\uparrow}_{\ell+1/2} \,, & \text{if } n=N(\ell) \text{ and } \ell_T(N) = \ell+1 \end{cases}$$

$$(35)$$

where the summation is zero if the upper limit is less than the lower limit,

[2]To simplify the equations we use the same symbols for quantities such as $N(\ell)$ whose identification in terms of either the upward or downward flux is evident from the equations in which it appears.

$S_{\ell',\ell}$ is given by Eqs. (15) and (17), $S''_{\ell_T(n)-1,\ell}$ is the the contribution from the layer just above the n-th cloud layer, the latter being located in layer $\ell_T(n)^1$ > $\ell+1$, and $R''^{\uparrow}_{\ell+1/2}$ is the upward flux at the top of the cloud in layer ℓ which is defined in section 1.2.3.

$S''_{\ell_T(n)-1,\ell}$ is given by Eqs. (15) and (17b) with $\ell' = \ell_T(n)-1$, but with $\pi B_{\ell'+1/2}$ replaced with the upward flux at the top of a cloud in layer $\ell'+1$, $R''^{\uparrow}_{\ell'+1/2}$. This allows for the fact that this cloud may not be a blackbody. Thus,

$$S''_{\ell',\ell} = S_{\ell',\ell} - D''^{\uparrow}_{\ell',\ell} , \tag{36}$$

where

$$D''^{\uparrow}_{\ell',\ell} = \sum_{j=1}^{J} \frac{1}{2} [f_j(\pi B_{\ell'+1/2}) \tau_j(|u_{\ell'+1/2} - u_{\ell+1/2}|)$$

$$+ f_j(\pi B_{\ell'-1/2}) \tau_j(|u_{\ell'-1/2} - u_{\ell+1/2}|)] (\pi B_{\ell'+1/2} - R''^{\uparrow}_{\ell'+1/2}) \tag{37}$$

for $\ell' = \ell_T(n)-1$ is a measure of the nonblackness of the n-th cloud.

Substituting Eqs. (35) and (36) into Eq. (34) and using Eq. (21) gives

$$R^{\uparrow}_{\ell+1/2} = \begin{cases} \pi B_{\ell+1/2} + A_0 \sum_{\ell'=\ell+1}^{L+1} S_{\ell',\ell} + \sum_{n=1}^{N(\ell)} A_n \left(\sum_{\ell'=\ell+1}^{\ell_T(n)-1} S_{\ell',\ell} \right) \\ \quad - \sum_{n=1}^{N(\ell)-1} A_n D''^{\uparrow}_{\ell_T(n)-1,\ell} - A_{N(\ell)} D''^{\uparrow}_{\ell_T[N(\ell)]-1,\ell} \\ \qquad\qquad\qquad \text{if } \ell_T[N(\ell)] > \ell+1 \\ [1- A_{N(\ell)}] \pi B_{\ell+1/2} + A_{N(\ell)} R''^{\uparrow}_{\ell+1/2} + A_0 \sum_{\ell'=\ell+1}^{L+1} S_{\ell',\ell} \\ \quad + \sum_{n=1}^{N(\ell)-1} A_n \left(\sum_{\ell'=\ell+1}^{\ell_T(n)-1} S_{\ell',\ell} \right) - \sum_{n=1}^{N(\ell)-1} A_n D''^{\uparrow}_{\ell_T(n)-1,\ell} , \\ \qquad\qquad\qquad \text{if } \ell_T[N(\ell)] = \ell+1. \end{cases} \tag{38}$$

Defining $C_{\ell+1}$ as the fractional cloudiness in layer $\ell+1$,

$$C_{\ell+1} = \begin{cases} 0 & \text{if } \ell_T[N(\ell)] > \ell+1 \\ \\ A_{N(\ell)} = MC_{N(\ell)} . & \text{if } \ell_T[N\ell)] = \ell+1 \end{cases} \tag{39}$$

Equation (38) can then be rewritten as

$$R^{\uparrow}_{\ell+1/2} = (1- C_{\ell+1})\, \pi B_{\ell+1/2} + C_{\ell+1} R''^{\uparrow}_{\ell+1/2} + \sum_{n=0}^{N(\ell)} A_n \left(\sum_{\ell'=\ell+1}^{L+1} F^{\uparrow}_{\ell',n}\, S_{\ell',\ell} \right)$$

$$- \sum_{n=1}^{N(\ell)-1} A_n\, D''^{\uparrow}_{\ell_T(n)-1,\ell} - \delta_{C_{\ell+1},0}\, A_{N(\ell)}\, D''^{\uparrow}_{\ell_T[N(\ell)]-1,\ell} , \tag{40}$$

where

$$F^{\uparrow}_{\ell',n} = \begin{cases} 1 , & \text{for } n=0 , \\ 0 , & \text{for } n>0 \text{ and } \ell' \geq \ell_T(n) , \\ 1 , & \text{for } n>0 \text{ and } \ell' < \ell_T(n) . \end{cases} \tag{41}$$

Equation (40) can be written in the form of Eq. (16) for clear atmosphere as

$$R^{\uparrow}_{\ell+1/2} = (1- C_{\ell+1})\, \pi B_{\ell+1/2} + C_{\ell+1} R''^{\uparrow}_{\ell+1/2} + \sum_{\ell'=\ell+1}^{L+1} \left[\sum_{n=0}^{N(\ell)} A_n F^{\uparrow}_{\ell',n} \right] S_{\ell',\ell}$$

$$- \left[\sum_{n=1}^{N(\ell)-1} A_n\, D''^{\uparrow}_{\ell_T(n)-1,\ell} - \delta_{C_{\ell+1},0}\, A_{N(\ell)}\, D''^{\uparrow}_{\ell_T[N(\ell)]-1,\ell} \right]$$

or

$$R^{\uparrow}_{\ell+1/2} = (1- C_{\ell+1})\, \pi B_{\ell+1/2} + C_{\ell+1} R''^{\uparrow}_{\ell+1/2} + \sum_{\ell'=\ell+1}^{L+1} [E^{\uparrow}_{\ell',\ell}\, S_{\ell',\ell} - G^{\uparrow}_{\ell',\ell}\, D''^{\uparrow}_{\ell',\ell}] , \tag{42}$$

where

$$E_{\ell',\ell}^{\uparrow} = \sum_{n=0}^{N(\ell)} A_n \, F_{\ell',n}^{\uparrow}$$

$$= A_0 + \sum_{n=1}^{N(\ell')} A_n \, , \tag{43}$$

and

$$G_{\ell',\ell}^{\uparrow} = \begin{cases} A_n \, , & \text{for } \ell' = \ell_T(n) - 1 \, , \\ \\ 0 \, , & \text{for } \ell' \neq \ell_T(n) - 1 \, . \end{cases} \tag{44}$$

From Eqs. (19) and (20), Eqs. (43) and (44) can then be rewritten as

$$E_{\ell',\ell}^{\uparrow} = \prod_{i=0}^{N(\ell)-1} (1 - MC_{N(\ell)-i}) + \sum_{n=1}^{N(\ell')} \left\{ MC_n \prod_{i=0}^{N(\ell)-(n+1)} (1 - MC_{N(\ell)-i}) \right\}$$

$$= \prod_{i=0}^{N(\ell)-[N(\ell')+1]} (1 - MC_{N(\ell)-i}) \tag{45}$$

and

$$G_{\ell',\ell}^{\uparrow} = \begin{cases} MC_{N(\ell')} \prod_{i=0}^{N(\ell)-[N(\ell')+1]} (1 - MC_{N(\ell)-i}) \, , & \text{for } \ell'+1 = \ell_T[N(\ell')] \, , \\ \\ 0 \, , & \text{for } \ell'+1 \neq \ell_T[N(\ell')] \, , \end{cases}$$

or

$$G_{\ell',\ell}^{\uparrow} = C_{\ell'+1} \prod_{i=0}^{N(\ell)-[N(\ell')+1]} (1 - MC_{N(\ell)-i}) \, . \tag{46}$$

1.2.2. Joint random and maximum overlap

a. *Downward flux*

Now, consider there are $m(n)$ cloud layers with a maximum overlap in the cloud group n as shown in Fig. 2. Then, the fractional area at level $\ell+1/2$ subtended by cloud group n is subdivided into the fractional sub-area subtended by individual cloud layer in the cloud group n as

$$A_n = \sum_{k=1}^{m(n)} A_{n,k} \, , \tag{47}$$

where the fractional sub-area of the cloud group n is defined as

$$A_{n,k} = \max\{\, 0, C_{\ell_T(n)+k-1} - \max[C_{\ell_T(n)+k}, ..., C_{\ell_B(n)+1}]\} \, P_n \, , \quad 1 \le k \le m(n) \, , \tag{48}$$

and

$$P_n = \begin{cases} \{1 - \max[C_{\ell_T[N(\ell)]}, ..., C_\ell]\} \displaystyle\prod_{i=1}^{N(\ell)-(n+1)} (1 - MC_{N(\ell)-i}) \, , & \text{for } n < N(\ell), \\[2em] 1 \, , & \text{for } n = N(\ell) \, . \end{cases} \tag{49}$$

Note that P_n is the same form as the product term in Eq. (19). If there is any layer of which the fractional cloudiness is less than the fractional cloudiness of any below layer in the same cloud group, the fractional sub-area at level $\ell+1/2$ subtended by this cloud is zero as the layer $\ell_T(n)+m(n)-1$ in Fig. 2a. Then, the downward flux at level $\ell+1/2$ can be written by Eq. (18) as

$$R^\downarrow_{\ell+1/2} = \sum_{n=0}^{N(\ell)} \sum_{k=1}^{m(n)} A_{n,k} \, (R^\downarrow_{\ell+1/2})_{n,k} \, . \tag{50}$$
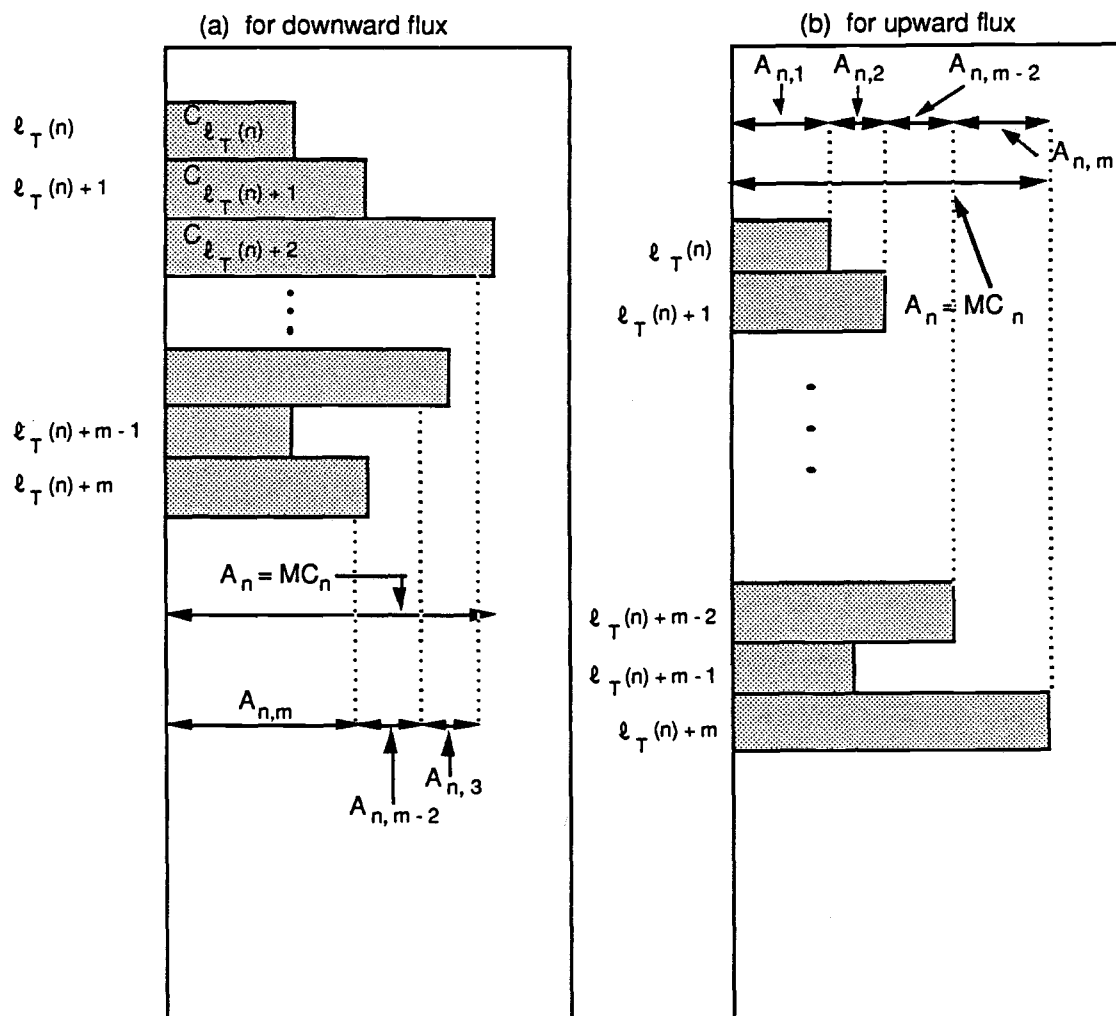
Fig. 2. Fractional area at level $\ell+1/2$ subtended by each cloud in group n in which m clouds are overlapped (a) for downward flux and (b) for upward flux.

With similar procedure in the previous section, the downward flux at level $\ell+1/2$ can be written by Eq. (25) as

$$R^{\downarrow}_{\ell+1/2} = \left[\sum_{n=0}^{N(\ell)}\sum_{k=1}^{m(n)} A_{n,k} - C_{\ell}\right]\pi B_{\ell+1/2} + C_{\ell} R''^{\downarrow}_{\ell+1/2} - A_0 \sum_{\ell'=0}^{\ell} S_{\ell',\ell}$$
$$- \sum_{n=1}^{N(\ell)}\sum_{k=1}^{m(n)} A_{n,k}\left(\sum_{\ell'=\ell_T(n)+k}^{\ell} S_{\ell',\ell}\right) - \sum_{n=1}^{N(\ell)-1}\sum_{k=1}^{m(n)} A_{n,k} D''^{\downarrow}_{\ell_T(n)+k,\ell}$$
$$- \sum_{k=1}^{m[N(\ell)]-1} A_{N(\ell),k} D''^{\downarrow}_{\ell_T[N(\ell)]+k,\ell} - \delta_{C_{\ell},0} D''^{\downarrow}_{\ell_B[N(\ell)]+1,\ell},$$

or

$$R^{\downarrow}_{\ell+1/2} = (1-C_{\ell})\pi B_{\ell+1/2} + C_{\ell} R''^{\downarrow}_{\ell+1/2} - \sum_{\ell'=0}^{\ell}\left\{\sum_{n=0}^{N(\ell)}\left[\sum_{k=1}^{m(n)} A_{n,k} F^{\downarrow}_{\ell',n,k}\right]\right\} S_{\ell',\ell}$$
$$- \sum_{n=1}^{N(\ell)-1}\sum_{k=1}^{m(n)} A_{n,k} D''^{\downarrow}_{\ell_T(n)+k,\ell} - \sum_{k=1}^{m[N(\ell)]-1} A_{N(\ell),k} D''^{\downarrow}_{\ell_T[N(\ell)]+k,\ell}$$
$$- \delta_{C_{\ell},0} D''^{\downarrow}_{\ell_B[N(\ell)]+1,\ell}, \tag{51}$$

where

$$\sum_{n=0}^{N(\ell)}\sum_{k=1}^{m(n)} A_{n,k} = 1, \tag{52}$$

and

$$F^{\downarrow}_{\ell',n,k} = \begin{cases} 1, & \text{for } n=0, \\ 0, & \text{for } n>0 \text{ and } \ell' < [\ell_T(n)+k], \\ 1, & \text{for } n>0 \text{ and } \ell' \geq [\ell_T(n)+k]. \end{cases} \tag{53}$$

Similar to Eq. (29), Equation (51) can then be rewritten as

$$R^{\downarrow}_{\ell+1/2} = (1 - C_\ell)\, \pi B_{\ell+1/2} + C_\ell\, R"^{\downarrow}_{\ell+1/2} - \sum_{\ell'=0}^{\ell} [E^{\downarrow}_{\ell',\ell}\, S_{\ell',\ell} + G^{\downarrow}_{\ell',\ell}\, D"^{\downarrow}_{\ell',\ell}]\,,$$

(54)

where

$$E^{\downarrow}_{\ell',\ell} = \sum_{n=0}^{N(\ell)} \left[\sum_{k=1}^{m(n)} A_{n,k}\, F^{\downarrow}_{\ell',n,k} \right]$$

$$= A_0 + \sum_{n=1}^{N(\ell')} \left[\sum_{k=1}^{\ell'-\ell_T(n)} A_{n,k} \right]\,,$$

(55)

and

$$G^{\downarrow}_{\ell',\ell} = \begin{cases} A_{n,k}\,, & \text{for } \ell' = \ell_T(n) + k\,, \\[2mm] 0\,, & \text{for } \ell' \neq \ell_T(n) + k\,. \end{cases}$$

(56)

From Eqs. (19), (47), (48) and (49) Equations (55) and (56) can be written as

$$E^{\downarrow}_{\ell',\ell} = \prod_{i=0}^{N(\ell)-1} (1 - MC_{N(\ell)-i})$$

$$+ \sum_{n=1}^{N(\ell')} \left[\sum_{k=1}^{\ell'-\ell_T(n)} \max\{0,\, C_{\ell_T(n)+k-1} - \max[C_{\ell_T(n)+k}, ..., C_{\ell_B(n)}]\}\, P_n \right]$$

$$= \{1 - \max[C_{\ell'}, ..., C_{\ell_B[N(\ell')]}]\}\, P_{N(\ell')}\,,$$

(57)

and

$$G^{\downarrow}_{\ell',\ell} = \max\{0,\, C_{\ell'-1} - \max[C_{\ell'}, ..., C_{\ell_B(n)+1}]\}\, P_{N(\ell')}\,.$$

(58)

b. *Upward flux*

As shown in Fig. 2b, the fractional area at level $\ell+1/2$ subtended by cloud group n can be expressed as in Eq. (47) with a different form of the fractional sub-area of the cloud group n, such that

$$A_{n,k} = \max\{0, C_{\ell_T(n)+k-1} - \max[C_{\ell_T(n)-1}, ..., C_{\ell_T(n)+k-2}]\} P_n, \quad 1 \le k \le m(n),$$

(59)

with

$$P_n = \begin{cases} \{1 - \max[C_\ell, ..., C_{\ell_B[N(\ell)]}]\} \displaystyle\prod_{i=1}^{N(\ell)-(n+1)} (1 - MC_{N(\ell)-i}), & \text{for } n < N(\ell), \\[4ex] 1, & \text{for } n = N(\ell). \end{cases}$$

(60)

If the fractional cloudiness of any layer is less than the fractional cloudiness of layer above it within the same cloud group, the fractional sub-area at level $\ell+1/2$ subtended by this cloud is zero, as in the layer $\ell_T(n)+m(n)-1$ in Fig. 2b. Then, the upward flux at level $\ell+1/2$ can be written from Eq. (34) as

$$R^{\uparrow}_{\ell+1/2} = \sum_{n=0}^{N(\ell)} \sum_{k=1}^{m(n)} A_{n,k} (R^{\uparrow}_{\ell+1/2})_{n,k}.$$

(61)

With a procedure similar to that used in the previous section, the upward flux at level $\ell+1/2$ can be written by Eq. (38) as

$$R^\uparrow_{\ell+1/2} = \left[\sum_{n=0}^{N(\ell)} \sum_{k=1}^{m(n)} A_{n,k} - C_{\ell+1} \right] \pi B_{\ell+1/2} + C_{\ell+1} R''^\uparrow_{\ell+1/2} - A_0 \sum_{\ell'=\ell+1}^{L+1} S_{\ell',\ell}$$

$$- \sum_{n=1}^{N(\ell)} \sum_{k=1}^{m(n)} A_{n,k} \left(\sum_{\ell'=\ell+1}^{\ell_T(n)+k-1} S_{\ell',\ell} \right) - \sum_{n=1}^{N(\ell)-1} \sum_{k=1}^{m(n)} A_{n,k} D''^\uparrow_{\ell_T(n)+k-1,\ell}$$

$$- \sum_{k=1}^{m[N(\ell)]-1} A_{N(\ell),k} D''^\uparrow_{\ell_T[N(\ell)]+k-1,\ell} - \delta_{C_{\ell+1},0} D''^\uparrow_{\ell_T[N(\ell)]-1,\ell} \,,$$

or

$$R^\uparrow_{\ell+1/2} = (1 - C_{\ell+1}) \pi B_{\ell+1/2} + C_{\ell+1} R''^\uparrow_{\ell+1/2} - \sum_{\ell'=\ell+1}^{L+1} \left\{ \sum_{n=0}^{N(\ell)} \left[\sum_{k=1}^{m(n)} A_{n,k} F^\uparrow_{\ell',n,k} \right] \right\} S_{\ell',\ell}$$

$$- \sum_{n=1}^{N(\ell)-1} \sum_{k=1}^{m(n)} A_{n,k} D''^\uparrow_{\ell_T(n)+k-1,\ell} - \sum_{k=1}^{m[N(\ell)]-1} A_{N(\ell),k} D''^\uparrow_{\ell_T[N(\ell)]+k-1,\ell}$$

$$- \delta_{C_{\ell+1},0} D''^\uparrow_{\ell_T[N(\ell)]-1,\ell} \,,$$

$$(62)$$

where

$$\sum_{n=0}^{N(\ell)} \sum_{k=1}^{m(n)} A_{n,k} = 1,$$

$$(63)$$

and

$$F^\uparrow_{\ell',n,k} = \begin{cases} 1, & \text{for } n = 0 \,, \\ 0, & \text{for } n > 0 \text{ and } \ell' \geq [\ell_T(n) + k] \,, \\ 1, & \text{for } n > 0 \text{ and } \ell' < [\ell_T(n) + k] \,. \end{cases}$$

$$(64)$$

Similar to Eq. (42), Equation (62) can then be rewritten as

$$R^{\uparrow}_{\ell+1/2} = (1 - C_{\ell+1})\,\pi B_{\ell+1/2} + C_{\ell+1}\,R''^{\uparrow}_{\ell+1/2} + \sum_{\ell'=\ell+1}^{L+1} [E^{\uparrow}_{\ell',\ell}\,S_{\ell',\ell} - G^{\uparrow}_{\ell',\ell}\,D''^{\uparrow}_{\ell',\ell}]\,,$$

(65)

where

$$E^{\uparrow}_{\ell',\ell} = \sum_{n=0}^{N(\ell)} \left[\sum_{k=1}^{m(n)} A_{n,k}\,F^{\uparrow}_{\ell',n,k} \right]$$

$$= A_0 + \sum_{n=1}^{N(\ell')} \left[\sum_{k=1}^{\ell'-\ell_T(n)} A_{n,k} \right],$$

(66)

and

$$G^{\uparrow}_{\ell',\ell} = \begin{cases} A_{n,k}\,, & \text{for } \ell' = \ell_T(n) + k - 1\,, \\[2em] 0\,, & \text{for } \ell' \neq \ell_T(n) + k - 1. \end{cases}$$

(67)

From Eqs. (19), (47), (59) and (60) Equations (66) and (67) can be written as

$$E^{\uparrow}_{\ell',\ell} = \prod_{i=0}^{N(\ell)-1} (1 - MC_{N(\ell)-i})$$

$$+ \sum_{n=1}^{N(\ell')} \left[\sum_{k=1}^{\ell'-\ell_T(n)} \max\{0,\, C_{\ell_T(n)+k-1} - \max[C_{\ell_T(n)-1},\, ...,\, C_{\ell_T(n)+k-2}]\}\,P_n \right]$$

$$= \{1 - \max[C_{\ell_T[N(\ell')]},\, ...,\, C_{\ell'}]\}\,P_{N(\ell')}\,,$$

(68)

and

$$G^{\uparrow}_{\ell',\ell} = \max\{0,\, C_{\ell'+1} - \max[C_{\ell_T(n)-1},\, ...,\, C_{\ell'}]\}\,P_{N(\ell')}\,.$$

(69)

1.2.3. Fluxes from the clouds

a. *Downward flux*

Consider a cloud in layer ℓ. The downward flux at level $\ell+1/2$ can be written as a sum of the clear part flux, $R'^{\downarrow}_{\ell+1/2}$, and the cloud part flux, $R''^{\downarrow}_{\ell+1/2}$, such that

$$R^{\downarrow}_{\ell+1/2} = (1 - C_{\ell})\, R'^{\downarrow}_{\ell+1/2} + C_{\ell}\, R''^{\downarrow}_{\ell+1/2}\,. \tag{70}$$

If the clouds are blackbodies, then the flux from clouds can be written as

$$R''^{\downarrow}_{\ell+1/2} = \pi B_{\ell+1/2}\,. \tag{71}$$

However, the clouds are not necessary to be blackbodies always. Assuming that the clouds are grey bodies, the downward flux at the bottom of cloud, $R''^{\downarrow}_{\ell+1/2}$, can be written as

$$R''^{\downarrow}_{\ell+1/2} = \varepsilon^{\downarrow}_{\ell}\, \pi B_{\ell+1/2} + (1 - \varepsilon^{\downarrow}_{\ell})\, R^{\downarrow}_{t}\,, \tag{72}$$

where $\varepsilon^{\downarrow}_{\ell}$ is the downward effective emissivity (Stephens, 1978) of the cloud in layer ℓ and the downward flux at the top of cloud layer ℓ, $R^{\downarrow}_{t}$, depends upon the structure of the adjacent cloud layers, shown in Fig. 3 as

$$R^{\downarrow}_{t} = \begin{cases} \dfrac{C_{\ell-1}}{C_{\ell}}\, R''^{\downarrow}_{\ell-1/2} + \dfrac{C_{\ell} - C_{\ell-1}}{C_{\ell}}\, R'^{\downarrow}_{\ell-1/2}\,, & \text{for } C_{\ell} > C_{\ell-1}\,, \\[4mm] R''^{\downarrow}_{\ell-1/2}\,, & \text{for } C_{\ell} \le C_{\ell-1}\,. \end{cases} \tag{73}$$

The clear downward flux at the top of cloud layer ℓ, $R'^{\downarrow}_{\ell-1/2}$, can be obtained as follows:

(a) for downward flux

$C_\ell > C_{\ell-1}$

$C_\ell \leq C_{\ell-1}$

$$R_t^\downarrow = \frac{C_{\ell-1}}{C_\ell} R_{\ell-\frac{1}{2}}^{''\downarrow} + \frac{C_\ell - C_{\ell-1}}{C_\ell} R_{\ell-\frac{1}{2}}^{'\downarrow}$$

$$R_t^\downarrow = R_{\ell-\frac{1}{2}}^{''\downarrow}$$

(b) for upward flux

$C_{\ell+1} > C_{\ell+2}$

$C_{\ell+1} \leq C_{\ell+2}$

$$R_b^\uparrow = \frac{C_{\ell+2}}{C_{\ell+1}} R_{\ell+\frac{3}{2}}^{''\uparrow} + \frac{C_{\ell+1} - C_{\ell+2}}{C_{\ell+1}} R_{\ell+\frac{3}{2}}^{'\uparrow}$$

$$R_b^\uparrow = R_{\ell+\frac{3}{2}}^{''\uparrow}$$
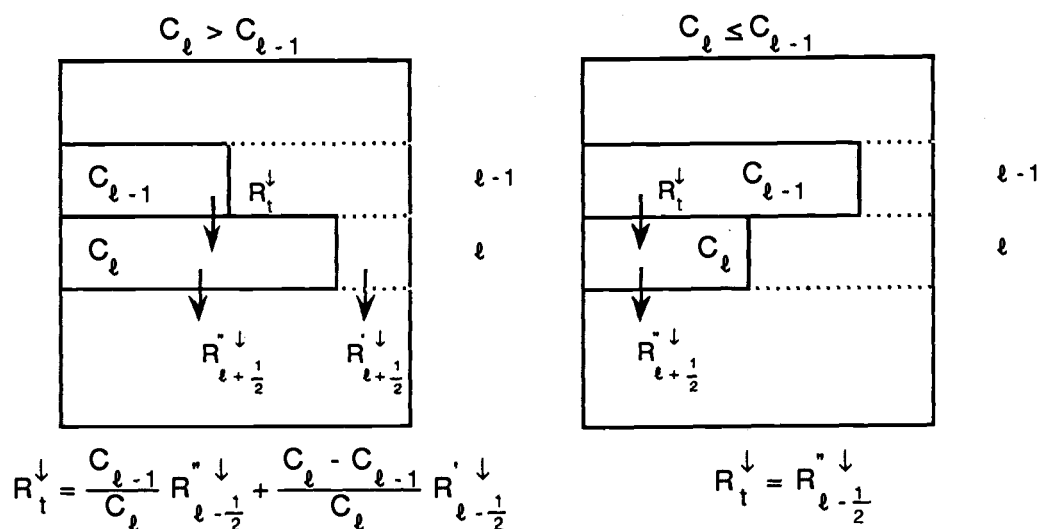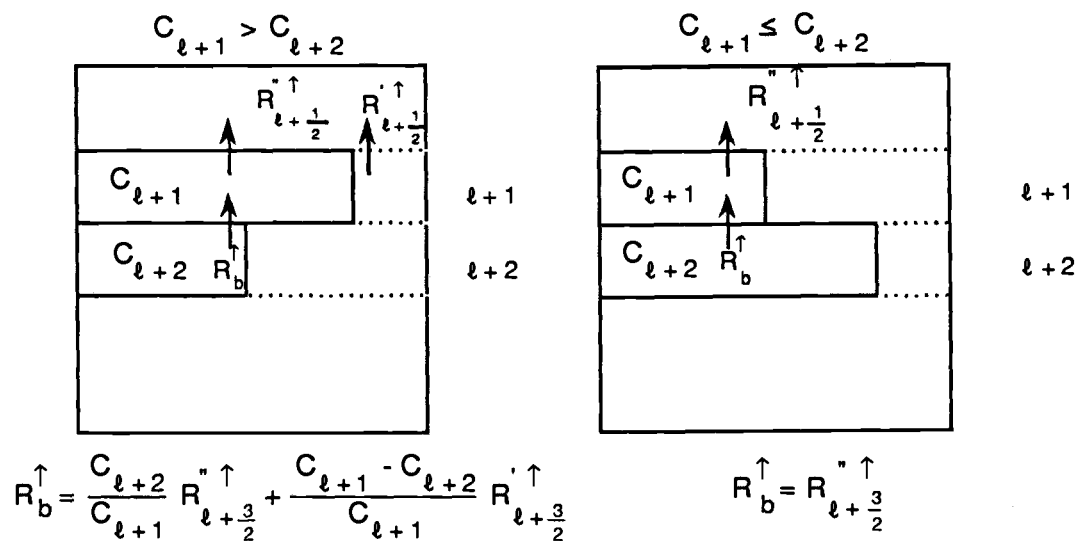
Fig. 3. Schematic representation of cloud geometry for the infrared radiation (a) for downward flux and (b) for upward flux.

From Eq. (70) the clear flux at level $\ell+1/2$ can be written as

$$R'^{\downarrow}_{\ell+1/2} = \frac{1}{(1-C_\ell)} (R^{\downarrow}_{\ell+1/2} - C_\ell R''^{\downarrow}_{\ell+1/2}) .$$

(74)

Similarly, the clear flux at level $\ell-1/2$ can be written as

$$R'^{\downarrow}_{\ell-1/2} = \frac{1}{(1-C_{\ell-1})} (R^{\downarrow}_{\ell-1/2} - C_{\ell-1} R''^{\downarrow}_{\ell-1/2}) .$$

(75)

Then, the downward flux at the bottom of cloud layer ℓ, $R''^{\downarrow}_{\ell+1/2}$, can be obtained by solving Eq. (72) from the top, where $R''^{\downarrow}_{1/2} = 0$ and with, in sequence, Eqs. (73) and (75).

b. *Upward flux*

When there is a cloud in layer $\ell+1$, the upward flux at level $\ell+1/2$ can be written as a sum of the clear part flux, $R'^{\uparrow}_{\ell+1/2}$, and the cloud part flux, $R''^{\uparrow}_{\ell+1/2}$, such that

$$R^{\uparrow}_{\ell+1/2} = (1 - C_{\ell+1}) R'^{\uparrow}_{\ell+1/2} + C_{\ell+1} R''^{\uparrow}_{\ell+1/2} .$$

(76)

Similar to the downward flux, the upward flux at the top of cloud layer $R''^{\uparrow}_{\ell+1/2}$ can be written as

$$R''^{\uparrow}_{\ell+1/2} = \varepsilon^{\uparrow}_{\ell+1} \pi B_{\ell+1/2} + (1 - \varepsilon^{\uparrow}_{\ell+1}) R^{\uparrow}_b ,$$

(77)

where $\varepsilon^{\uparrow}_{\ell+1}$ is the upward effective emissivity of cloud in layer $\ell+1$ and $R^{\uparrow}_b$, the upward flux at the bottom of cloud layer $\ell+1$, depends upon the structure of the adjacent cloud layers shown in Fig. 3 as

$$R_b^{\uparrow} = \begin{cases} \dfrac{C_{\ell+2}}{C_{\ell+1}}\, R''^{\uparrow}_{\ell+3/2} + \dfrac{C_{\ell+1}-C_{\ell+2}}{C_{\ell+1}}\, R'^{\uparrow}_{\ell+3/2}\,, & \text{for } C_{\ell+1} > C_{\ell+2}\,, \\[3em] R''^{\uparrow}_{\ell+3/2}\,, & \text{for } C_{\ell+1} \le C_{\ell+2}\,, \end{cases} \quad (78)$$

where the clear downward flux at the bottom of cloud layer $\ell+1$, $R''^{\uparrow}_{\ell+3/2}$, can be obtained as follows:

From Eq. (76) the clear flux at level $\ell+3/2$ can be written as

$$R'^{\uparrow}_{\ell+3/2} = \frac{1}{(1-C_{\ell+1})}\,(R^{\uparrow}_{\ell+3/2} + C_{\ell+1}\, R''^{\uparrow}_{\ell+3/2})\,. \tag{79}$$

Similarly, the clear flux at level $[\ell+2]+1/2$ can be written as

$$R'^{\uparrow}_{[\ell+2]+1/2} = \frac{1}{(1-C_{\ell+2})}\,(R^{\uparrow}_{[\ell+2]+1/2} + C_{\ell+2}\, R''^{\uparrow}_{[\ell+2]+1/2})\,. \tag{80}$$

Then, the upward flux at the top of the cloud, $R''^{\uparrow}_{\ell+1/2}$, can be obtained by solving Eq. (77) from the bottom layer where $R''^{\uparrow}_{L+1/2} = 0$, in sequence, with Eqs. (78) and (80).

2. Absorbers, Spectral Subdivision and Mean Transmission Function

From Chou (1984), we divide the IR spectrum as shown in Fig. 4, into water vapor, CO_2, and O_3 bands, and further subdivide the water vapor band into band-center and band-wing regions. The spectral bands, $j = 1$ through $j = 4$, are shown in Fig. 4 and are defined in Table 1.

The fraction $f_j(T)$, defined in Eq. (5) has been calculated using a spectral resolution of 1 cm^{-1} for 5 K temperature intervals from 180 K to 320 K. The results and their fit are presented in Fig. 5 by

$$f_j = a_j + b_j\,x + c_j\,x^2 \tag{81}$$

with the coefficients given in Table 2 and

$$x = T - 250\ \text{K}. \tag{82}$$

The maximum error of this fitted function is 4.5% at T = 180 K.

Band index j

	2	1	2	4	2	3	2	1

H_2O Band centers

H_2O Band wings

H_2O 15 µm overlap

H_2O continuum

CO_2

O_3

| 3000 | | 1380 | | 980 | | 540 | 0 |
| 1900 | | 1100 | | 800 | | 340 | |
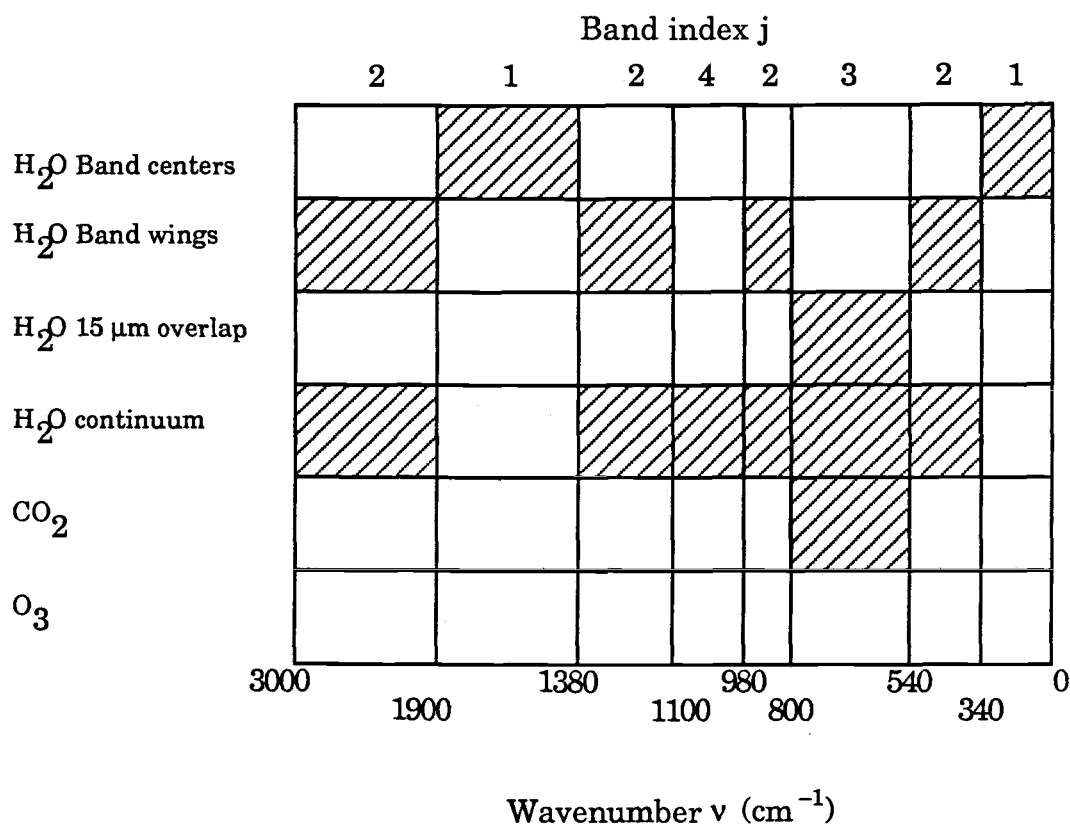
Wavenumber ν (cm^{-1})

Fig. 4. Absorbers taken into account in the longwave radiation parameterization and their spectral subdivisions.

Table 1. Spectral bands and absorbers.

Spectral band j	Wavenumber Interval (cm^{-1})	Absorber
1	0 - 340 1380 - 1900	H_2O band centers
2	340 - 540 800 - 980 1100 - 1380 1900 - 3000	H_2O band wings and H_2O continuum
3	540 - 800	H_2O 15 µm overlap, H_2O continuum and CO_2
4	980 - 1100	H_2O continuum and O_3

Table 2. Coefficients of $f_j = a_j + b_j x + c_j x^2$ with x = T - 250 K.

	Coefficients of $f_j = a_j + b_j x + c_j x^2$		
j	a_j	b_j	c_j
1	2.087×10^{-1}	-9.1680×10^{-4}	1.1602×10^{-5}
2	4.5136×10^{-1}	4.5766×10^{-4}	-2.3100×10^{-6}
3	2.824×10^{-1}	2.5117×10^{-5}	-7.8014×10^{-6}
4	5.7533×10^{-2}	4.3402×10^{-4}	-1.4908×10^{-6}
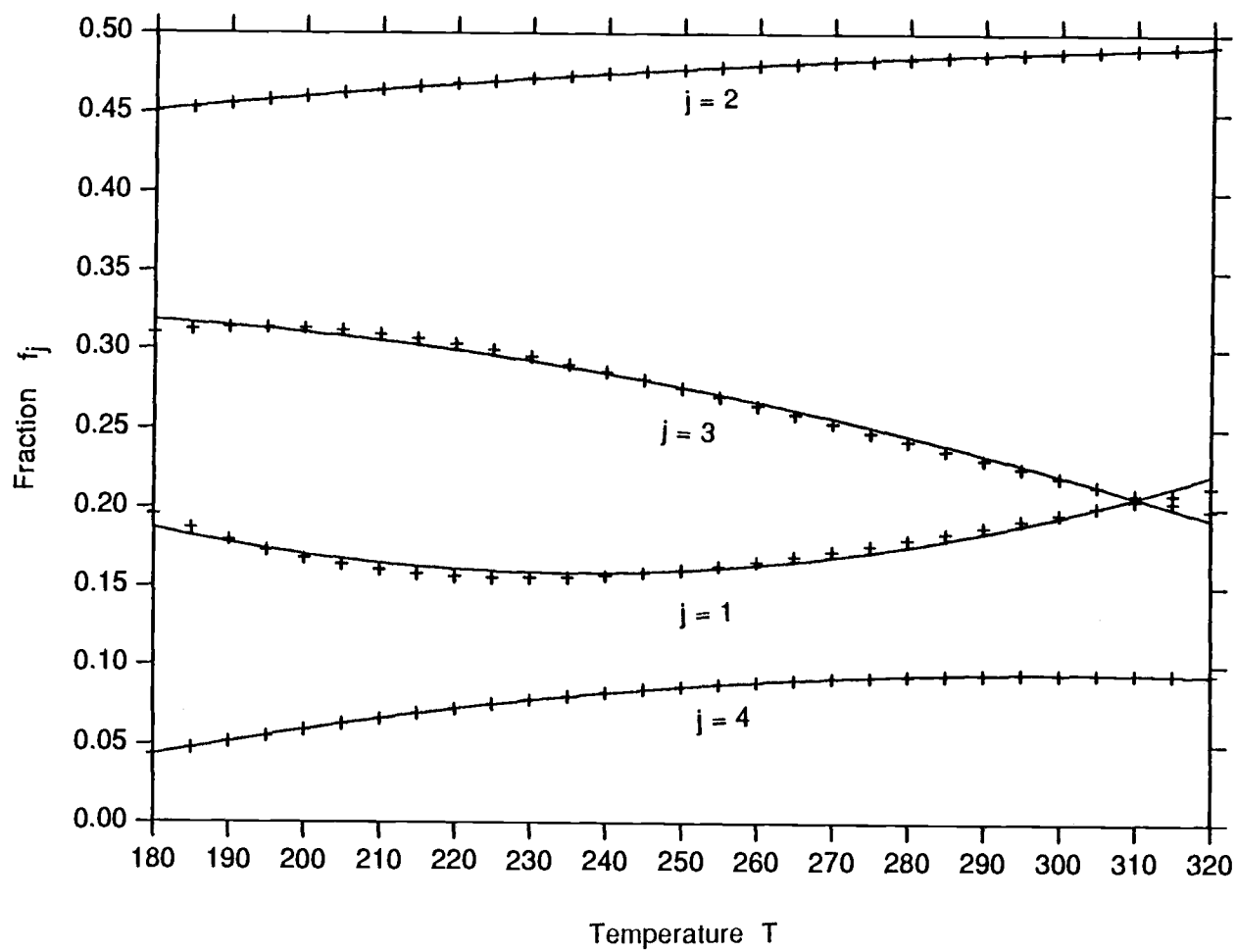
Fig. 5. Fraction f_j versus temperature T. The values calculated from Eq. (5) are shown by the crosses and the fit of Eq. (81) by the solid lines.

From Eqs. (4) and (5) the mean transmission function, $\tau_j(\Delta u)$, is defined as

$$\tau_j(\Delta u) = \frac{\int_{v_{L,j}}^{v_{U,j}} \pi B_v(T)\, \tau_v(\Delta u)\, dv}{f_j\, \pi B(T)} \, .$$

(83)

And the total transmission function for each spectral interval τ_j^T is assumed to be

$$\tau_j^T = \tau_j^{H_2O}\, \tau_j^{CO_2}\, \tau_j^{O_3}\, \tau_j^{H_2O\ cont.} \, ,$$

(84)

where $\tau_j^{H_2O}$, $\tau_j^{CO_2}$, $\tau_j^{O_3}$, and $\tau_j^{H_2O\ cont.}$ are the transmission function of, respectively, water vapor, CO_2, O_3, and water vapor continuum.

3. Transmission Function for Each Gas

3.1. Water vapor bands

3.1.1. Line centers

The transmission function for spectral band 1 of the centers of the water vapor bands is calculated using the LOWTRAN 6 code (Kneizys *et al.*, 1983) with a spectral interval of 5 cm^{-1} for the range of water vapor amounts from 10^{-8} to 10 g cm^{-2}. The calculated transmission function is presented in Table 3, with the coefficients of the sequence of fitted quadratic polynomials, as

$$\tau_1^{H_2O} = a_i + b_i\, x + c_i\, x^2 \, , \qquad x_{i-1} \le x < x_i \, ,$$

(85)

where

$$x = \log(u_{H_2O}) \, .$$

(86)

Table 3. Transmission function for spectral band 1 due to the centers of the water vapor bands together with the coefficients of their fitted quadratic polynomials $\tau_1^{H_2O}(x) = a_i + b_i x + c_i x^2$.

i	x	$\tau_1^{H_2O}$	a_i	b_i	c_i
1	-8.0	8.67088E-01			
2	-7.9	8.67078E-01	8.58894E-01	-1.95414E-03	-1.16229E-04
3	-7.8	8.67065E-01			
4	-7.7	8.67050E-01	8.56911E-01	-2.46411E-03	-1.49015E-04
5	-7.6	8.67031E-01			
6	-7.5	8.67009E-01	8.52069E-01	-3.73543E-03	-2.32459E-04
7	-7.4	8.66981E-01			
8	-7.3	8.66949E-01	8.46068E-01	-5.36219E-03	-3.42717E-04
9	-7.2	8.66910E-01			
10	-7.1	8.66863E-01	8.37938E-01	-7.62881E-03	-5.00680E-04
11	-7.0	8.66806E-01			
12	-6.9	8.66731E-01	8.31641E-01	-9.36272E-03	-6.19889E-04
13	-6.8	8.66644E-01			
14	-6.7	8.66545E-01	8.07208E-01	-1.66038E-02	-1.15635E-03
15	-6.6	8.66422E-01			
16	-6.5	8.66263E-01	7.92384E-01	-2.09937E-02	-1.48118E-03
17	-6.4	8.66075E-01			
18	-6.3	8.65850E-01	7.53609E-01	-3.31364E-02	-2.43180E-03
19	-6.2	8.65576E-01			
20	-6.1	8.65255E-01	7.04829E-01	-4.90237E-02	-3.72530E-03
21	-6.0	8.64861E-01			
22	-5.9	8.64377E-01	7.03753E-01	-4.92389E-02	-3.73126E-03
23	-5.8	8.63819E-01			
24	-5.7	8.63141E-01	5.76704E-01	-9.29741E-02	-7.49508E-03
25	-5.6	8.62313E-01			
26	-5.5	8.61357E-01	6.23011E-01	-7.65116E-02	-6.03200E-03
27	-5.4	8.60281E-01			
28	-5.3	8.58998E-01	4.95444E-01	-1.23326E-01	-1.03265E-02
29	-5.2	8.57508E-01			
30	-5.1	8.55787E-01	3.69114E-01	-1.72138E-01	-1.50416E-02
31	-5.0	8.53765E-01			
32	-4.9	8.51437E-01	3.24970E-01	-1.89921E-01	-1.68324E-02
33	-4.8	8.48772E-01			
34	-4.7	8.45621E-01	2.29697E-01	-2.28505E-01	-2.07356E-02
35	-4.6	8.42054E-01			
36	-4.5	8.38097E-01	1.26127E-01	-2.74275E-01	-2.57910E-02
37	-4.4	8.33623E-01			
38	-4.3	8.28535E-01	5.31058E-02	-3.06842E-01	-2.94209E-02
39	-4.2	8.22859E-01			
40	-4.1	8.16505E-01	-1.85320E-01	-4.20857E-01	-4.30510E-02
41	-4.0	8.09291E-01			
42	-3.9	8.01311E-01	-2.32444E-01	-4.45700E-01	-4.63166E-02
43	-3.8	7.92405E-01			
44	-3.7	7.82454E-01	-3.86111E-01	-5.26453E-01	-5.69256E-02
45	-3.6	7.71364E-01			
46	-3.5	7.59133E-01	-5.88526E-01	-6.40486E-01	-7.29831E-02
47	-3.4	7.45443E-01			
48	-3.3	7.30102E-01	-5.83706E-01	-6.35635E-01	-7.19732E-02
49	-3.2	7.13321E-01			
50	-3.1	6.94805E-01	-8.16094E-01	-7.80171E-01	-9.44467E-02
51	-3.0	6.74400E-01			
52	-2.9	6.52003E-01	-7.97736E-01	-7.66649E-01	-9.19791E-02

Table 3. Continued.

i	x	$\tau_1^{H_2O}$	a_i	b_i	c_i
53	-2.8	6.27766E-01			
54	-2.7	6.01710E-01	-6.84527E-01	-6.84503E-01	-7.70809E-02
55	-2.6	5.74113E-01			
56	-2.5	5.44845E-01	-8.41379E-01	-8.06230E-01	-1.00696E-01
57	-2.4	5.13563E-01			
58	-2.3	4.80895E-01	-4.91348E-01	-5.14740E-01	-4.00114E-02
59	-2.2	4.47426E-01			
60	-2.1	4.12932E-01	-4.42326E-01	-4.66762E-01	-2.83316E-02
61	-2.0	3.77872E-01			
62	-1.9	3.42544E-01	-2.96058E-01	-3.19788E-01	8.58850E-03
63	-1.8	3.07387E-01			
64	-1.7	2.73213E-01	-1.20999E-01	-1.28141E-01	6.10286E-02
65	-1.6	2.40259E-01			
66	-1.5	2.08697E-01	-8.72734E-02	-8.63951E-02	7.39456E-02
67	-1.4	1.78613E-01			
68	-1.3	1.51047E-01	-7.95385E-03	2.00867E-02	1.09535E-01
69	-1.2	1.25672E-01			
70	-1.1	1.02898E-01	3.04480E-02	8.25230E-02	1.34897E-01
71	-1.0	8.28221E-02			
72	-0.9	6.53696E-02	2.85281E-02	7.92969E-02	1.33591E-01
73	-0.8	5.05887E-02			
74	-0.7	3.81051E-02	1.65846E-02	5.15874E-02	1.17616E-01
75	-0.6	2.79738E-02			
76	-0.5	2.00993E-02	8.70824E-03	2.38535E-02	9.32713E-02
77	-0.4	1.40903E-02			
78	-0.3	9.58887E-03	3.67627E-03	-7.29856E-04	6.32628E-02
79	-0.2	6.35275E-03			
80	-0.1	4.09364E-03	2.49848E-03	-1.26319E-02	3.31974E-02
81	0.0	2.49848E-03			
82	0.1	1.56614E-03	2.49848E-03	-1.07800E-02	1.45662E-02
83	0.2	9.25134E-04			
84	0.3	5.13258E-04	2.30350E-03	-8.74054E-03	9.24359E-03
85	0.4	2.86256E-04			
86	0.5	1.36537E-04	1.67349E-03	-5.04479E-03	3.94176E-03
87	0.6	6.56515E-05			
88	0.7	2.92192E-05	6.51869E-04	-1.50220E-03	8.75292E-04
89	0.8	1.02925E-05			
90	0.9	0.00000E+00	4.63160E-04	-9.77781E-04	5.14621E-04
91	1.0	0.00000E+00			

Figure 6 compares the actual and fitted transmission functions. The error of the fitted transmission function is less than 3.2×10^{-4} % for the values of transmission function greater than 0.01. For values outside this range ($x < -8$) the transmission function is linearly interpolated to be 1 at $x = -20$.

3.1.2. Line wings

The transmission function for spectral band 2 of the wings of the water vapor bands is calculated in a manner similar to that for the centers of the water vapor bands. The resulting transmission functions and the coefficients for the fitted quadratic polynomials are presented in Table 4 for the range of water vapor amounts from 10^{-4} to 10^5 g cm^{-2}. Figure 7 provides a comparison of the actual and fitted transmission functions. The maximum error is less than 2.1×10^{-3} % for values of the transmission function greater than 0.01. Similar to the line centers, the transmission function is linearly interpolated to be 1 at $x = -20$ for range $x < -4$.

3.1.3. Overlap with carbon dioxide

The transmission function for spectral band 3 for the overlap of the water vapor band and the carbon dioxide band has been defined by Chou (1984) as

$$\tau_3^{H_2O}(W) = \exp\left[-\frac{6.7\,W}{1 + 16\,W^{0.6}}\right],$$

$$(87)$$

where W is the absorber amount given by

$$W = \int \frac{p}{p_r}\, r\, (T - T_r)\, q_{H_2O}\, \frac{d\,p}{g}$$

$$(88)$$

with p the pressure, q_{H_2O} the water vapor mixing ratio, g the acceleration of gravity, $p_r = 550$ mb, $T_r = 256$ K, and $r = 0.016$.
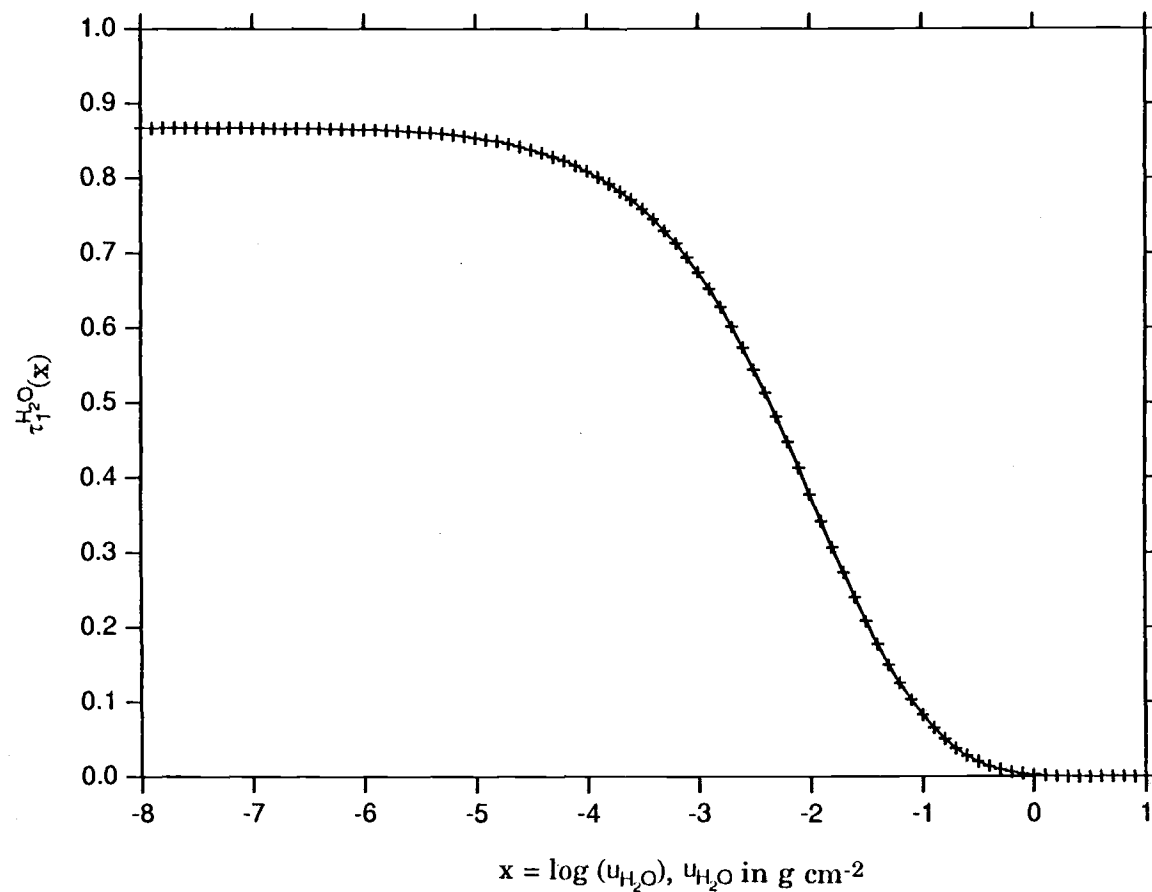
Fig. 6. Comparison of the actual (crosses) and fitted (solid line) values of the transmission function $\tau_1^{H_2O}$ due to the centers of the water vapor bands.

Table 4. Transmission function for spectral band 2 due to the wings of the water vapor bands together with the coefficients of their fitted quadratic polynomials $\tau_2^{H_2O} (x) = a_i + b_i x + c_i x^2$.

i	x	$\tau_2^{H_2O}$	a_i	b_i	c_i
1	-4.0	9.91107E-01			
2	-3.9	9.89641E-01	7.19992E-01	-1.22257E-01	-1.36195E-02
3	-3.8	9.87902E-01			
4	-3.7	9.85807E-01	7.81077E-01	-8.88090E-02	-9.04772E-03
5	-3.6	9.83531E-01			
6	-3.5	9.80895E-01	6.30279E-01	-1.71940E-01	-2.05040E-02
7	-3.4	9.77849E-01			
8	-3.3	9.74396E-01	6.84207E-01	-1.39777E-01	-1.57092E-02
9	-3.2	9.70630E-01			
10	-3.1	9.66279E-01	5.63414E-01	-2.13707E-01	-2.70163E-02
11	-3.0	9.61388E-01			
12	-2.9	9.56078E-01	5.18198E-01	-2.45620E-01	-3.26299E-02
13	-2.8	9.50115E-01			
14	-2.7	9.43396E-01	4.88529E-01	-2.66131E-01	-3.61712E-02
15	-2.6	9.35954E-01			
16	-2.5	9.27768E-01	3.96945E-01	-3.37785E-01	-5.01822E-02
17	-2.4	9.18579E-01			
18	-2.3	9.08394E-01	3.65408E-01	-3.64716E-01	-5.59283E-02
19	-2.2	8.97090E-01			
20	-2.1	8.84600E-01	3.39332E-01	-3.88286E-01	-6.12542E-02
21	-2.0	8.70886E-01			
22	-1.9	8.55813E-01	2.73423E-01	-4.54524E-01	-7.78962E-02
23	-1.8	8.39182E-01			
24	-1.7	8.21152E-01	3.57428E-01	-3.60120E-01	-5.13770E-02
25	-1.6	8.02095E-01			
26	-1.5	7.81547E-01	3.17663E-01	-4.06549E-01	-6.48622E-02
27	-1.4	7.59702E-01			
28	-1.3	7.36720E-01	3.66831E-01	-3.35330E-01	-3.90769E-02
29	-1.2	7.12956E-01			
30	-1.1	6.88560E-01	3.90092E-01	-2.96427E-01	-2.28106E-02
31	-1.0	6.63708E-01			
32	-0.9	6.38233E-01	3.91684E-01	-2.91219E-01	-1.91957E-02
33	-0.8	6.12374E-01			
34	-0.7	5.87079E-01	4.20262E-01	-2.25499E-01	1.83016E-02
35	-0.6	5.62150E-01			
36	-0.5	5.37700E-01	4.30182E-01	-1.90483E-01	4.91052E-02
37	-0.4	5.14232E-01			
38	-0.3	4.92004E-01	4.32152E-01	-1.82420E-01	5.69524E-02
39	-0.2	4.70914E-01			
40	-0.1	4.51215E-01	4.33162E-01	-1.72292E-01	8.23386E-02
41	0.0	4.33162E-01			
42	0.1	4.16839E-01	4.33162E-01	-1.69707E-01	6.48027E-02
43	0.2	4.01813E-01			
44	0.3	3.87932E-01	4.33038E-01	-1.67672E-01	5.77272E-02
45	0.4	3.75206E-01			
46	0.5	3.63324E-01	4.28365E-01	-1.44163E-01	2.81588E-02
47	0.6	3.52005E-01			
48	0.7	3.41090E-01	4.19260E-01	-1.14610E-01	4.19804E-03
49	0.8	3.30258E-01			
50	0.9	3.19352E-01	4.05150E-01	-7.98856E-02	-1.71617E-02
51	1.0	3.08103E-01			
52	1.1	2.96543E-01	3.97077E-01	-6.47733E-02	-2.42011E-02

Table 4. Continued.

| i	x	$\tau_2^{H_2O}$	a_i	b_i	c_i
53	1.2	2.84500E-01			
54	1.3	2.72064E-01	3.74930E-01	-3.01259E-02	-3.76941E-02
55	1.4	2.58874E-01			
56	1.5	2.45105E-01	3.86298E-01	-4.74573E-02	-3.11144E-02
57	1.6	2.30714E-01			
58	1.7	2.15823E-01	4.53617E-01	-1.30288E-01	-5.64140E-03
59	1.8	2.00820E-01			
60	1.9	1.85454E-01	4.67290E-01	-1.42719E-01	-2.95562E-03
61	2.0	1.70030E-01			
62	2.1	1.54308E-01	5.56278E-01	-2.27324E-01	1.70998E-02
63	2.2	1.38929E-01			
64	2.3	1.24041E-01	5.88878E-01	-2.57748E-01	2.41936E-02
65	2.4	1.09637E-01			
66	2.5	9.57579E-02	5.41472E-01	-2.19423E-01	1.64550E-02
67	2.6	8.22076E-02			
68	2.7	6.97264E-02	6.92607E-01	-3.40654E-01	4.07250E-02
69	2.8	5.80598E-02			
70	2.9	4.74661E-02	8.27978E-01	-4.38176E-01	5.82875E-02
71	3.0	3.80382E-02			
72	3.1	2.98215E-02	8.15486E-01	-4.30422E-01	5.70911E-02
73	3.2	2.27466E-02			
74	3.3	1.67462E-02	8.59250E-01	-4.56707E-01	6.10313E-02
75	3.4	1.19665E-02			
76	3.5	8.33869E-03	7.18858E-01	-3.74637E-01	4.90375E-02
77	3.6	5.69164E-03			
78	3.7	3.73771E-03	4.65457E-01	-2.32962E-01	2.92360E-02
79	3.8	2.36851E-03			
80	3.9	1.49193E-03	2.48193E-01	-1.19181E-01	1.43397E-02
81	4.0	9.02138E-04			
82	4.1	6.00119E-04	1.11179E-01	-5.15193E-02	5.98754E-03
83	4.2	4.17853E-04			
84	4.3	3.14420E-04	2.21167E-02	-9.20234E-03	9.60942E-04
85	4.4	2.30205E-04			
86	4.5	1.90961E-04	1.55411E-02	-6.49844E-03	6.86068E-04
87	4.6	1.65438E-04			
88	4.7	1.41558E-04	2.89060E-03	-9.38525E-04	7.52387E-05
89	4.8	1.19182E-04			
90	4.9	9.85499E-05	3.94784E-03	-1.37689E-03	1.20678E-04
91	5.0	8.03319E-05			
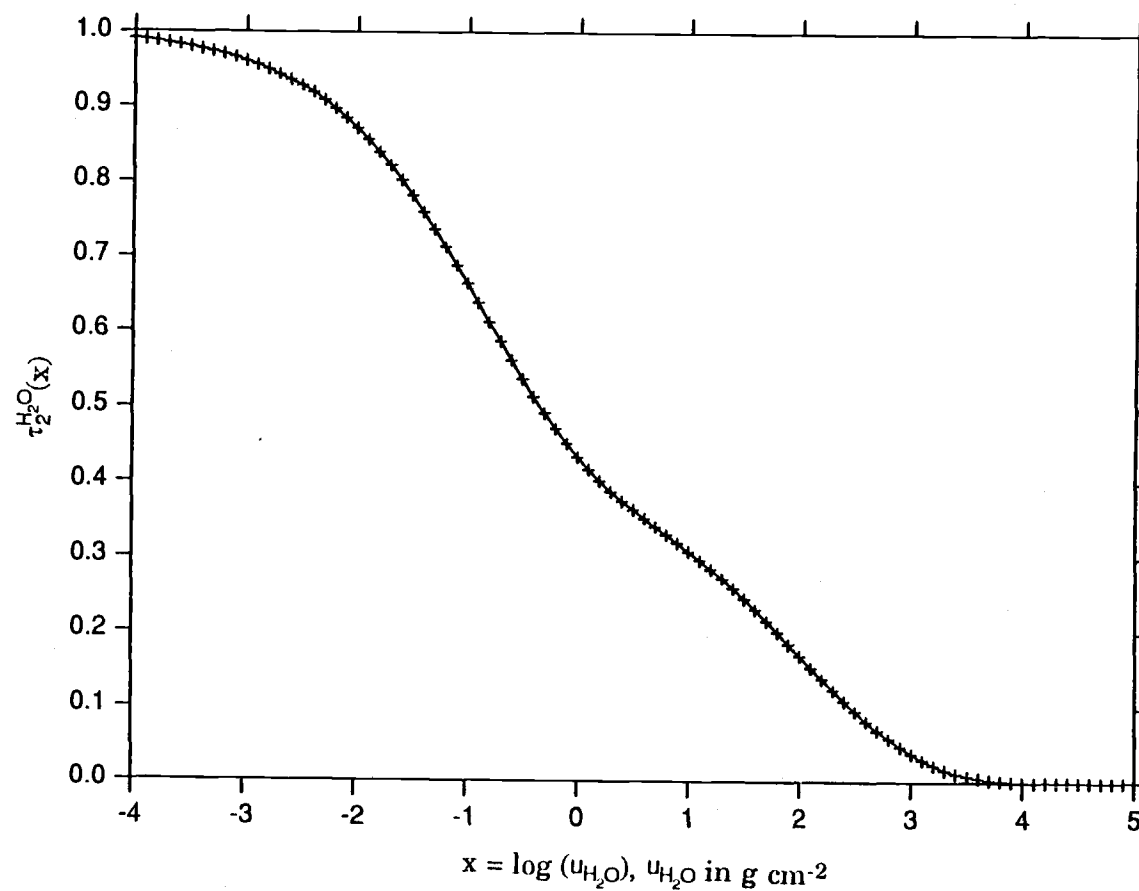
Fig. 7. Comparison of the actual (crosses) and fitted (solid line) values of the transmission function $\tau_2^{H_2O}$ due to the wings of the water vapor bands.

3.1.4. Continuum

As shown in Fig. 4, the water vapor continuum occurs in spectral bands 2 - 4. For this study, only the self-broadened water vapor continuum is considered since the foreign-broadened water vapor continuum is relatively small (Roberts et al., 1976)

a. *Spectral interval 2*

The transmission function of the water vapor continuum in spectral interval 2 has been calculated with the LOWTRAN 6 code for the range of the diffusive water vapor amount $u_{cont.}$ defined by Eq. (106) from 10^{-8} to 1 g cm^{-2}. The calculated transmission function and coefficients of the fitted quadratic polynomials are presented in Table 5 and the actual and fitted transmission functions are compared in Fig. 8. The error of the fitted function is less than 4.9×10^{-4} % for values of the transmission functions greater than 0.01.

b. *Spectral intervals 3 and 4*

The transmission functions of water vapor continuum in spectral intervals 3 and 4 have been calculated by Chou (1984) as

$$\tau_3^{H_2O \ cont.}(u_{cont.}) = \exp\left[-27 \ (u_{cont.})^{0.83}\right] , \tag{89}$$

and

$$\tau_4^{H_2O \ cont.}(u_{cont.}) = \exp\left[-9.79 \ u_{cont.}\right] . \tag{90}$$

3.2. Carbon dioxide

The transmission function for spectral interval 3 due to CO_2 has been calculated by in Chou and Peng (1983) from

Table 5. Transmission function for spectral band 2 due to the water vapor continuum together with the coefficients of their fitted quadratic polynomials $\tau_2^{H_2O\ cont.}(x) = a_i + b_i\,x + c_i\,x^2$.

i	x	$\tau_2^{H_2O\ cont.}$	a_i	b_i	c_i
1	-8.0	9.99999E-01			
2	-7.9	9.99998E-01	9.99960E-01	-4.76838E-06	0.00000E+00
3	-7.8	9.99998E-01			
4	-7.7	9.99997E-01	9.98882E-01	-2.82528E-04	-1.78815E-05
5	-7.6	9.99996E-01			
6	-7.5	9.99995E-01	9.98565E-01	-3.69550E-04	-2.38419E-05
7	-7.4	9.99994E-01			
8	-7.3	9.99992E-01	9.98113E-01	-4.96797E-04	-3.27820E-05
9	-7.2	9.99990E-01			
10	-7.1	9.99988E-01	9.97533E-01	-6.63103E-04	-4.47036E-05
11	-7.0	9.99984E-01			
12	-6.9	9.99980E-01	9.97393E-01	-7.03932E-04	-4.76838E-05
13	-6.8	9.99975E-01			
14	-6.7	9.99969E-01	9.96275E-01	-1.03058E-03	-7.15271E-05
15	-6.6	9.99961E-01			
16	-6.5	9.99951E-01	9.93663E-01	-1.81973E-03	-1.31130E-04
17	-6.4	9.99938E-01			
18	-6.3	9.99922E-01	9.90970E-01	-2.66009E-03	-1.96690E-04
19	-6.2	9.99901E-01			
20	-6.1	9.99876E-01	9.85918E-01	-4.28797E-03	-3.27826E-04
21	-6.0	9.99844E-01			
22	-5.9	9.99803E-01	9.78746E-01	-6.68139E-03	-5.27502E-04
23	-5.8	9.99752E-01			
24	-5.7	9.99688E-01	9.69034E-01	-1.00324E-02	-8.16564E-04
25	-5.6	9.99608E-01			
26	-5.5	9.99506E-01	9.52991E-01	-1.57678E-02	-1.32919E-03
27	-5.4	9.99378E-01			
28	-5.3	9.99217E-01	9.31326E-01	-2.38032E-02	-2.07425E-03
29	-5.2	9.99015E-01			
30	-5.1	9.98760E-01	8.98827E-01	-3.63141E-02	-3.27831E-03
31	-5.0	9.98440E-01			
32	-4.9	9.98037E-01	8.51155E-01	-5.53999E-02	-5.18860E-03
33	-4.8	9.97530E-01			
34	-4.7	9.96892E-01	7.81834E-01	-8.43176E-02	-8.20438E-03
35	-4.6	9.96090E-01			
36	-4.5	9.95083E-01	6.82940E-01	-1.27368E-01	-1.28895E-02
37	-4.4	9.93818E-01			
38	-4.3	9.92230E-01	5.41920E-01	-1.91545E-01	-2.01911E-02
39	-4.2	9.90238E-01			
40	-4.1	9.87741E-01	3.44308E-01	-2.85762E-01	-3.14212E-02
41	-4.0	9.84616E-01			
42	-3.9	9.80710E-01	7.42213E-02	-4.20975E-01	-4.83441E-02
43	-3.8	9.75838E-01			
44	-3.7	9.69773E-01	-2.82433E-01	-6.08912E-01	-7.31023E-02
45	-3.6	9.62247E-01			
46	-3.5	9.52940E-01	-7.26536E-01	-8.55892E-01	-1.07441E-01
47	-3.4	9.41485E-01			
48	-3.3	9.27465E-01	-1.22916E+00	-1.15174E+00	-1.50976E-01
49	-3.2	9.10425E-01			
50	-3.1	8.89895E-01	-1.70083E+00	-1.44643E+00	-1.97006E-01
51	-3.0	8.65425E-01			
52	-2.9	8.36639E-01	-1.97286E+00	-1.62703E+00	-2.26978E-01

Table 5. Continued.

| i	x	$\tau_2^{H_2O\ cont.}$	a_i	b_i	c_i
53	-2.8	8.03314E-01			
54	-2.7	7.65467E-01	-1.83197E+00	-1.52472E+00	-2.08408E-01
55	-2.6	7.23452E-01			
56	-2.5	6.78027E-01	-1.18484E+00	-1.02486E+00	-1.11884E-01
57	-2.4	6.30364E-01			
58	-2.3	5.81959E-01	-2.91174E-01	-2.79546E-01	4.35117E-02
59	-2.2	5.34424E-01			
60	-2.1	4.89196E-01	2.92467E-01	2.48622E-01	1.63001E-01
61	-2.0	4.47227E-01			
62	-1.9	4.08773E-01	2.51481E-01	2.03889E-01	1.50881E-01
63	-1.8	3.73335E-01			
64	-1.7	3.39816E-01	-1.48137E-01	-2.41545E-01	2.67565E-02
65	-1.6	3.06832E-01			
66	-1.5	2.73146E-01	-3.97674E-01	-5.50665E-01	-6.89679E-02
67	-1.4	2.38080E-01			
68	-1.3	2.01769E-01	-2.97903E-01	-4.04102E-01	-1.51832E-02
69	-1.2	1.65155E-01			
70	-1.1	1.29748E-01	-6.71913E-02	-1.85862E-02	1.45863E-01
71	-1.0	9.72578E-02			
72	-0.9	6.91962E-02	5.97585E-02	2.32631E-01	2.70130E-01
73	-0.8	4.65370E-02			
74	-0.7	2.95347E-02	5.66409E-02	2.21377E-01	2.60934E-01
75	-0.6	1.77509E-02			
76	-0.5	1.02617E-02	2.01837E-02	9.87904E-02	1.57893E-01
77	-0.4	5.93042E-03			
78	-0.3	3.64996E-03	3.68437E-03	1.73041E-02	5.72982E-02
79	-0.2	2.51546E-03			
80	-0.1	1.91459E-03	1.52124E-03	-2.89599E-03	1.03758E-02
81	0.0	1.52124E-03			
82	0.1	1.20792E-03	1.52124E-03	-3.36405E-03	2.30878E-03
83	0.2	9.40779E-04			
84	0.3	7.13707E-04	1.50949E-03	-3.22545E-03	1.90950E-03
85	0.4	5.24827E-04			
86	0.5	3.71897E-04	1.46682E-03	-3.01551E-03	1.65134E-03
87	0.6	2.51992E-04			
88	0.7	1.61632E-04	1.33151E-03	-2.56683E-03	1.27940E-03
89	0.8	9.68591E-05			
90	0.9	5.33194E-05	1.04301E-03	-1.84694E-03	8.30319E-04
91	1.0	2.63863E-05			
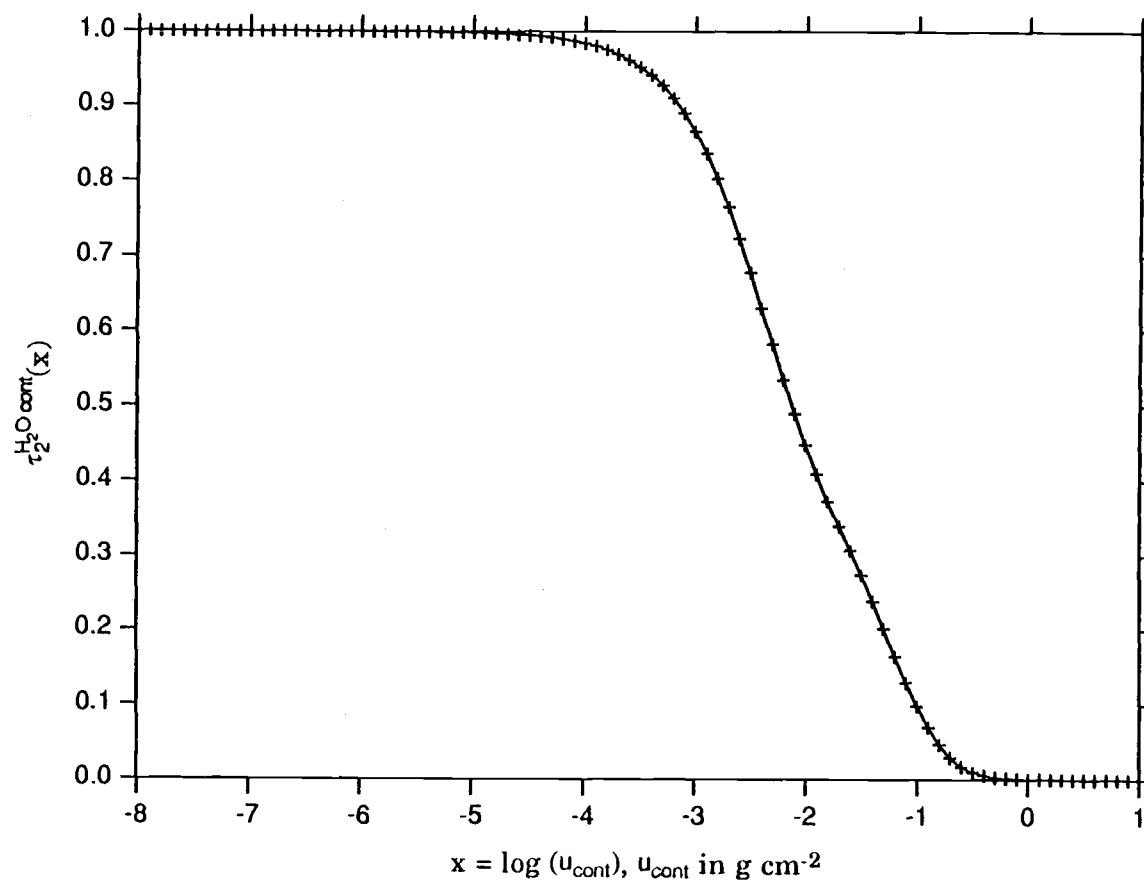
Fig. 8. Comparison of the actual (crosses) and fitted (solid line) values of the transmission function $\tau_2^{H_2O\ cont.}$ of the water vapor continuum in spectral interval 2.

$$\tau_3^{CO_2} = \frac{1}{\Delta v_i} \int_{\Delta v_i} \tau_{CO_2,\Delta v_i} \, dv \,, \tag{91}$$

where Δv_i is the spectral sub-band for CO_2 in spectral interval 3 and

$$\tau_{CO_2,\Delta v_i} = \exp\left[-\frac{a \, u_{CO_2}}{1 + b \, u_{CO_2}^n} \right]. \tag{92}$$

In Eq. (92), a, b and n are coefficients which depend upon Δv_i, and u_{CO_2} is the scaled absorber amount in atm-cm defined in Eq. (107). The values of a, b and n are given in Table 6.

Table 6. Parameters for the center and wing regions of the 15 µm spectral band from Chou and Peng (1983).

Parameter	Band Center	Band Wings
Δv (cm^{-1})	620 - 720	540 - 620
		720 - 800
P_r (mb)	30	300
P_c (mb)	1	1
m	0.85	0.50
n	0.56	0.57
a	3.1	0.04
b	15.1	0.9
T_r (K)	240	240
R(200,240)	0.74	0.36
R(280,240)	1.51	2.66

3.3. Ozone

The transmission function for spectral interval 4 due to O_3, $\tau_4^{O_3}$, has been calculated with the LOWTRAN 6 code in the range of ozone amounts from 10^{-4} to 10 atm-cm (see Eq. (109)). The calculated transmission function and coefficients of the fitted quadratic polynomials are presented in Table 7 and these data are compared in Fig. 9. The error of the fitted ozone transmission function is less than 2.8×10^{-4} %.

4. Cloud Emissivity

Stephens (1978) parameterized the effective emissivity of a cloud for IR radiation in terms of the liquid water path, W (g m^{-2}), as

$$\varepsilon_\ell^{\uparrow,\downarrow} = 1 - \exp\left(-a_0^{\uparrow,\downarrow} W_\ell\right), \tag{93}$$

where $a_0^{\uparrow,\downarrow}$ defines a mass absorption coefficient for the total infrared flux. The values of $a_0^{\uparrow,\downarrow}$ for the liquid water cloud were obtained as

$$a_0^{\uparrow} = 0.130 \text{ m}^2\text{g}^{-1} \tag{94}$$

and

$$a_0^{\downarrow} = 0.158 \text{ m}^2\text{g}^{-1} \tag{95}$$

from the empirical fir of eight different cloud types. For cirrus cloud, the values of $a_0^{\uparrow,\downarrow}$ are given as

$$a_0^{\uparrow} = 0.05 \text{ m}^2\text{g}^{-1} \tag{96}$$

and

$$a_0^{\downarrow} = 0.06 \text{ m}^2\text{g}^{-1} \tag{97}$$

in Starr and Cox (1985). However, based on Griffith *et al.* (1980) the values of $a_0^{\uparrow}$ and $a_0^{\downarrow}$ are chosen as 0.096 m^{2}g^{-1} for the tropical region.

Table 7. Transmission function for spectral band 4 due to O_3 together with the coefficients of their fitted quadratic polynomials

$$\tau_4^{O_3}(x) = a_i + b_i\, x + c_i\, x^2.$$

| i	x	$\tau_4^{O_3}$	a_i	b_i	c_i
1	-4.0	9.99231E-01			
2	-3.9	9.99036E-01	9.39406E-01	-2.82956E-02	-3.33485E-03
3	-3.8	9.98774E-01			
4	-3.7	9.98448E-01	9.21658E-01	-3.77905E-02	-4.60441E-03
5	-3.6	9.98030E-01			
6	-3.5	9.97518E-01	8.93492E-01	-5.36398E-02	-6.83368E-03
7	-3.4	9.96870E-01			
8	-3.3	9.96050E-01	8.25541E-01	-9.38608E-02	-1.27853E-02
9	-3.2	9.94974E-01			
10	-3.1	9.93582E-01	8.01587E-01	-1.08451E-01	-1.50056E-02
11	-3.0	9.91891E-01			
12	-2.9	9.89869E-01	7.47095E-01	-1.45095E-01	-2.11653E-02
13	-2.8	9.87424E-01			
14	-2.7	9.84401E-01	6.27298E-01	-2.30655E-01	-3.64424E-02
15	-2.6	9.80650E-01			
16	-2.5	9.76108E-01	5.94123E-01	-2.56038E-01	-4.12976E-02
17	-2.4	9.70740E-01			
18	-2.3	9.64075E-01	4.45360E-01	-3.77783E-01	-6.61978E-02
19	-2.2	9.56086E-01			
20	-2.1	9.46796E-01	4.18434E-01	-4.03091E-01	-7.21382E-02
21	-2.0	9.36064E-01			
22	-1.9	9.23941E-01	3.60018E-01	-4.63603E-01	-8.77903E-02
23	-1.8	9.10063E-01			
24	-1.7	8.94273E-01	2.80570E-01	-5.52817E-01	-1.12833E-01
25	-1.6	8.76226E-01			
26	-1.5	8.55663E-01	1.80548E-01	-6.79250E-01	-1.52782E-01
27	-1.4	8.32045E-01			
28	-1.3	8.05785E-01	1.70836E-01	-6.98116E-01	-1.61302E-01
29	-1.2	7.76299E-01			
30	-1.1	7.43735E-01	1.23731E-01	-7.81803E-01	-1.98330E-01
31	-1.0	7.07204E-01			
32	-0.9	6.67934E-01	2.56227E-01	-5.15727E-01	-6.47504E-02
33	-0.8	6.27369E-01			
34	-0.7	5.86352E-01	3.30439E-01	-3.26585E-01	5.57203E-02
35	-0.6	5.46450E-01			
36	-0.5	5.07968E-01	3.33577E-01	-3.18753E-01	6.00577E-02
37	-0.4	4.70688E-01			
38	-0.3	4.34266E-01	3.35850E-01	-3.00931E-01	9.04070E-02
39	-0.2	3.99653E-01			
40	-0.1	3.65438E-01	3.32912E-01	-3.16816E-01	8.44424E-02
41	0.0	3.32912E-01			
42	0.1	3.01129E-01	3.32912E-01	-3.23236E-01	5.40345E-02
43	0.2	2.70426E-01			
44	0.3	2.41096E-01	3.33922E-01	-3.33600E-01	8.05946E-02
45	0.4	2.13377E-01			
46	0.5	1.86591E-01	3.35641E-01	-3.35900E-01	7.55989E-02
47	0.6	1.61317E-01			
48	0.7	1.38467E-01	3.46177E-01	-3.76328E-01	1.13715E-01
49	0.8	1.17892E-01			
50	0.9	9.99388E-02	3.59811E-01	-4.11617E-01	1.36522E-01
51	1.0	8.47164E-02			
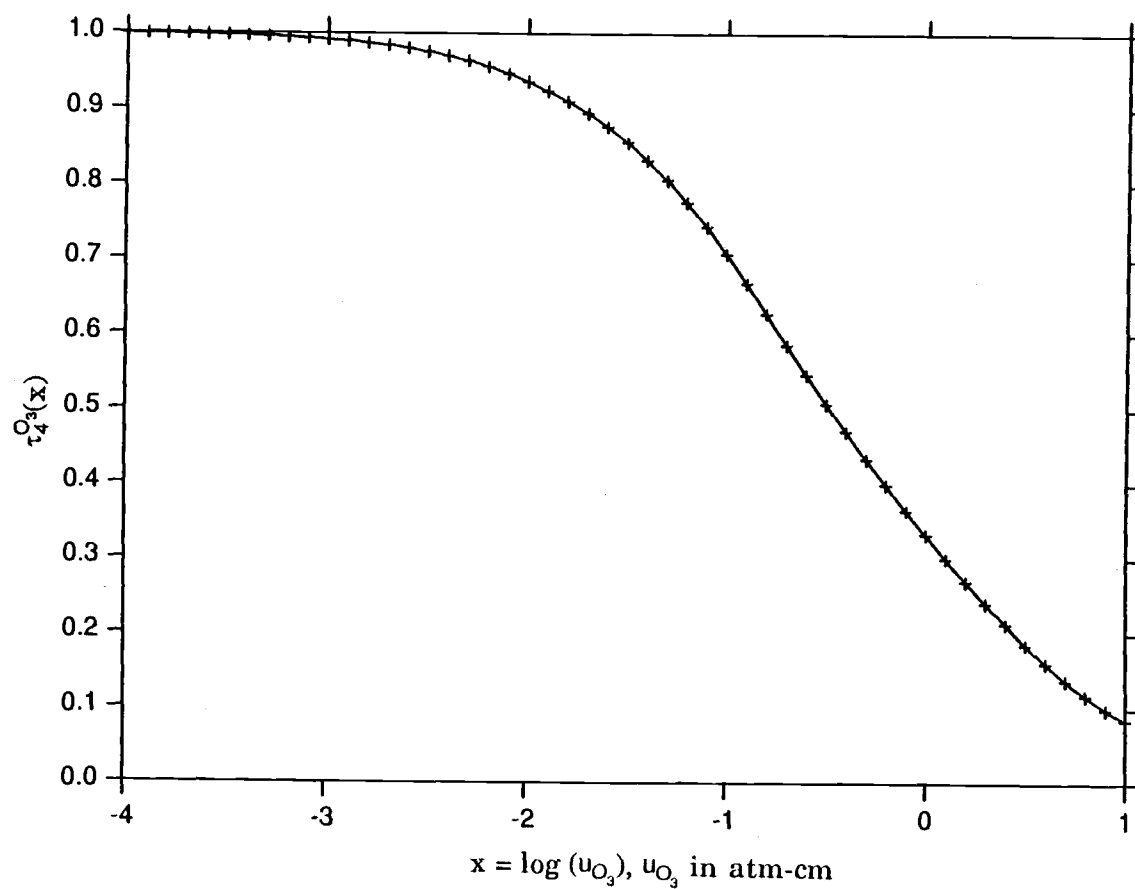
Fig. 9. Comparison of the actual (crosses) and fitted (solid line) values of the transmission function $\tau_4^{O_3}$ of ozone in spectral interval 4.

5. Effective absorber amounts

5.1. Water vapor

5.1.1. Line absorption

The scaled water vapor amount, u_{H_2O}, is determined from the water vapor mixing ratio, q_{H_2O}, by

$$u_{H_2O} = \int_p \left(\frac{p}{p_0}\right)^n q_{H_2O}(p) \frac{dp}{g} \tag{98}$$

where $p_0 = 1000$ mb and the scaling factor $n = 0.9$ as in McClatchey *et al.* (1973).

In general, the moisture profile is assumed to have the following form

$$q_{H_2O}(p) = a \left(\frac{p}{p_0}\right)^b . \tag{99}$$

However, the model atmosphere is limited to the troposphere and

$$q_{H_2O}(p) = \begin{cases} a \left(\dfrac{p}{p_0}\right)^b, & \text{for } p \geq p_{TROP}, \\[2ex] q_{st}\left(\dfrac{p}{p_{st}}\right)^{b'}, & \text{for } p_{st} \leq p \leq p_{TROP}, \\[2ex] q_{st} = 2.5 \times 10^{-6}, & \text{for } \leq p_{st} \equiv 100 \text{ mb}, \end{cases} \tag{100}$$

where p_{TROP} is the pressure at the model tropopause (200 mb). In general, a and b are determined from Eq. (99) evaluated at p_ℓ and $p_{\ell+1}$, to obtain

$$a_{\ell+1/2} = q_\ell \left(\frac{p_\ell}{p_0}\right)^{-\frac{\log(q_{\ell+1}/q_\ell)}{\log(p_{\ell+1}/p_\ell)}} , \tag{101}$$

and

$$b_{\ell+1/2} = \frac{\log(q_{\ell+1}/q_\ell)}{\log(p_{\ell+1}/p_\ell)} . \tag{102}$$

When the model atmosphere is limited to the troposphere, q at the tropopause, q_{TROP}, is

$$q_{TROP} = a_{1/2}\left(\frac{p_{TROP}}{p_0}\right)^{b_{1/2}} , \tag{103}$$

and $a_{1/2}$ and $b_{1/2}$ given in Eqs. (101) and (102), are respectively

$$a_{1/2} = q_{st}\left(\frac{p_{st}}{p_0}\right)^{-\frac{\log(q_1/q_{st})}{\log(p_1/p_{st})}} , \tag{104}$$

and

$$b_{1/2} = \frac{\log(q_1/q_{st})}{\log(p_1/p_{st})} . \tag{105}$$

5.1.2. Continuum absorption

The scaled water vapor amount for the continuum absorption, as calculated by Kneizys *et al.* (1980, 1983), is

$$u_{cont.}(p_1,p_2) = \int_{p_1}^{p_2} q^2(p)\left(\frac{T_s}{T}\right)\left(\frac{p}{p_s}\right)\exp\left\{1800\left[\frac{1}{T}-\frac{1}{T_s}\right]\right\}\frac{dp}{g} , \tag{106}$$

where p_s is 1013 mb and T_s = 296 K.

5.2. Carbon dioxide

The scaled CO_2 amount can be calculated as

$$u_{CO_2}(p_1,p_2) = \int_{p_1}^{p_2} C(p)\, f(p,T)\, \frac{dp}{g}\, , \qquad atm\text{--}cm, \tag{107}$$

where $C(p)$ $(g^{-1}\, cm^3)$ is the absorber concentration and $f(p,T)$ is the scaling function, given by Chou and Peng (1983) as

$$f(p,T) = \left(\frac{p}{p_r}\right)^m R(T,T_r)\, . \tag{108}$$

The values of p_r, T_r and m are provided in Table 6, and $R(T,T_r)$ is linearly interpolated from the values of $R(200,240)$ and $R(280,240)$.

5.3. Ozone

The scaled amount of O_3 is given as

$$u_{O_3} = \frac{1}{\rho_{O_3,NTP}} \int q_{O_3}(p) \left(\frac{p}{p_0}\right)^n \frac{dp}{g}\, , \tag{109}$$

where $\rho_{O_3,NTP} = 2.133 \times 10^{-3}$ g cm^{-3}, q_{O_3} is the ozone mixing ratio, and the scaling factor n is taken as 0.3 following Manabe and Möller(1961).

6. Comparison with other Models and Observations

6.1. Intercomparison with other Models

The proposed longwave radiation scheme is compared with both current

scheme (Ghan *et al.*, 1982) and other models reported in the ICRCCM (Luther *et al.*,1988) for various sky conditions.

Figure 10 shows the relative net flux absorbed by the atmosphere for the case of CO_2 only. The new longwave radiation scheme simulates the net absorbed flux within 25% - 50% of the values of the ICRCCM models for both $CO_2 = 300$ ppm and 600 ppm case except the subarctic winter case.

Figure 11 shows the relative net absorbed fluxes for the case of H_2O only. The new scheme simulates the net absorbed flux reasonably well for the H_2O continuum that the current longwave radiation scheme ignored. In the absence of the H_2O continuum, the new scheme underestimated the net absorbed flux by the atmosphere, while the current scheme somewhat overestimates.

Figure 12 shows all constituents cases. The new scheme is within 25 - 75% boxes while the current scheme is near the extreme low for both $CO_2 = 300$ ppm and 600 ppm cases. This significant underestimation of current scheme may be partly due to the current scheme ignored H_2O continuum and due to the transmission functions of current scheme are using single band model as well as out of date.

6.2. Comparison with Observations

The calculated longwave flux profiles with new scheme have been compared with both those calculated with current scheme (Ghan *et al.*, 1982) and the data observed on board the NASA 990 aircraft under clear conditions on May 18, 1979 (Ackerman and Cox, 1982; Luther *et al.*,1988), and the data measured on board the NCAR Electra under near homogeneous cloud conditions on June 21, 1979 (Ellingson and Serafino, 1984:Luther *et al.*,1988). Figures 13 and 14 show that the comparisons of the calculated flux profiles with new scheme with those measured with ±5% estimated error bars and with those calculated with current scheme.

The left panel of Fig. 13 shows that the calculated upward fluxes with new scheme under clear conditions are within a +5% error range for the entire layer, with exception of those above 300 mb, while the downward fluxes are in a +5% error range below 600 mb. The underestimation of the
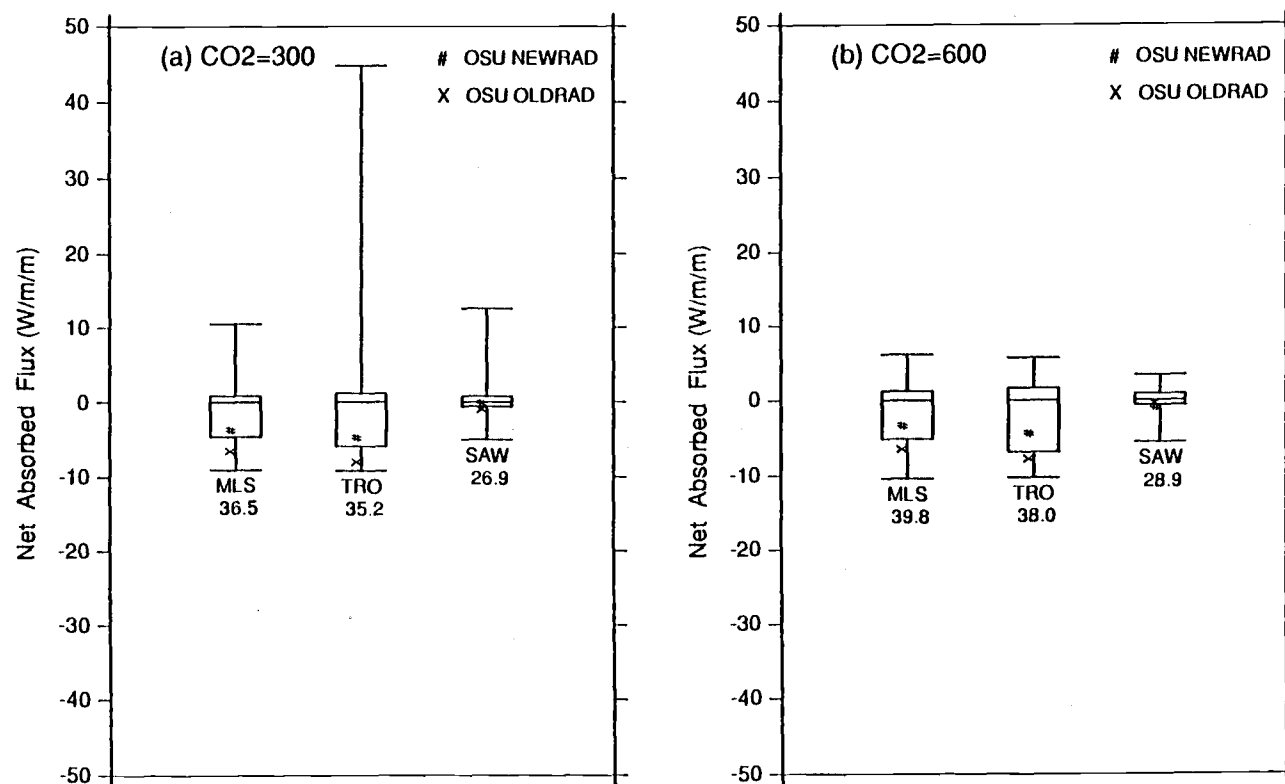
Fig. 10. The relative net flux absorbed by the ICRCCM models (Luther *et al.*, 1988) for the CO_2 only case. MLS, TRO and SAW represent the midlatitude summer, tropical and subarctic winter cases of McClatchey *et al.*, (1973) The bottom and top of each box denote the 25th and 75th percentile values, respectively; the horizontal line within the box represents the median value, and the horizontal lines outside the rectangle are the extreme values. The number under the box is the median value, which has been subtracted from all values. The results for the present parameterization are shown by # and those for its predecessor (Ghan,*et al.*, 1982) by x.
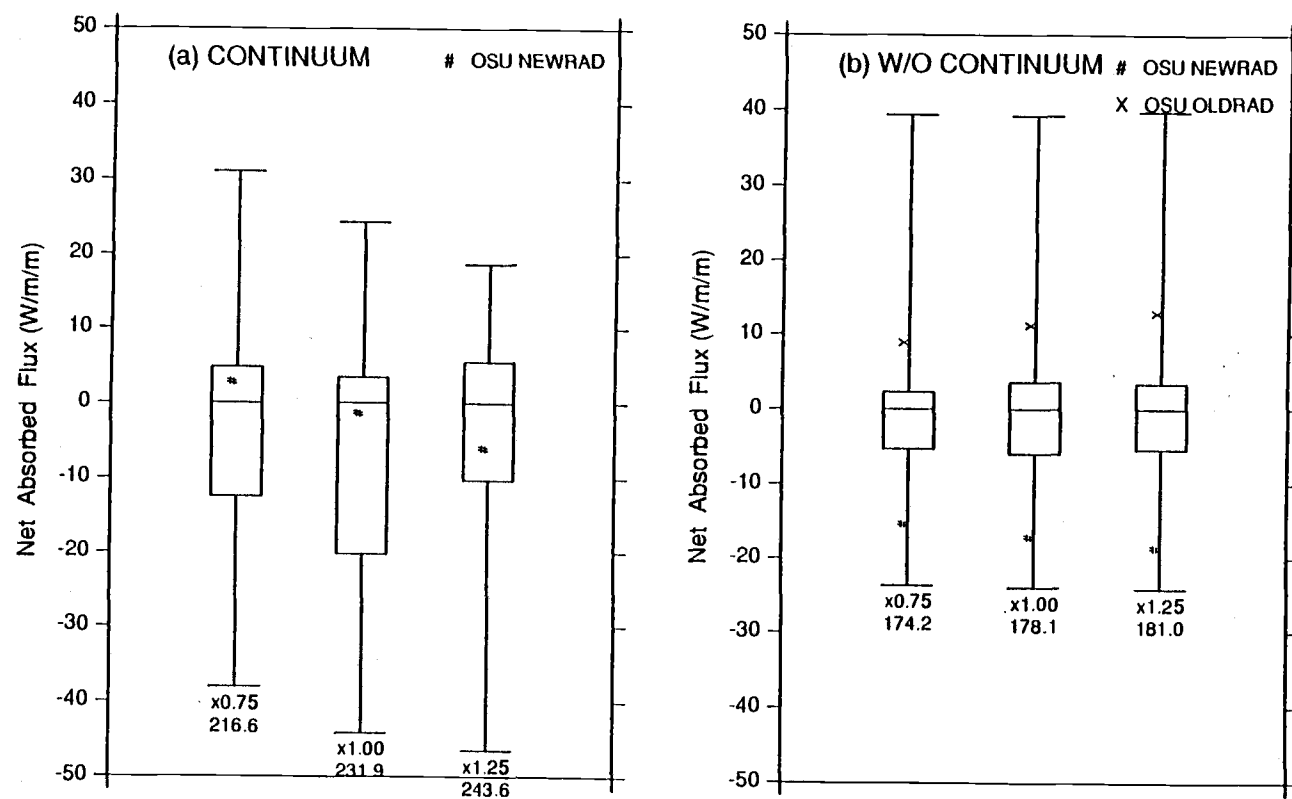
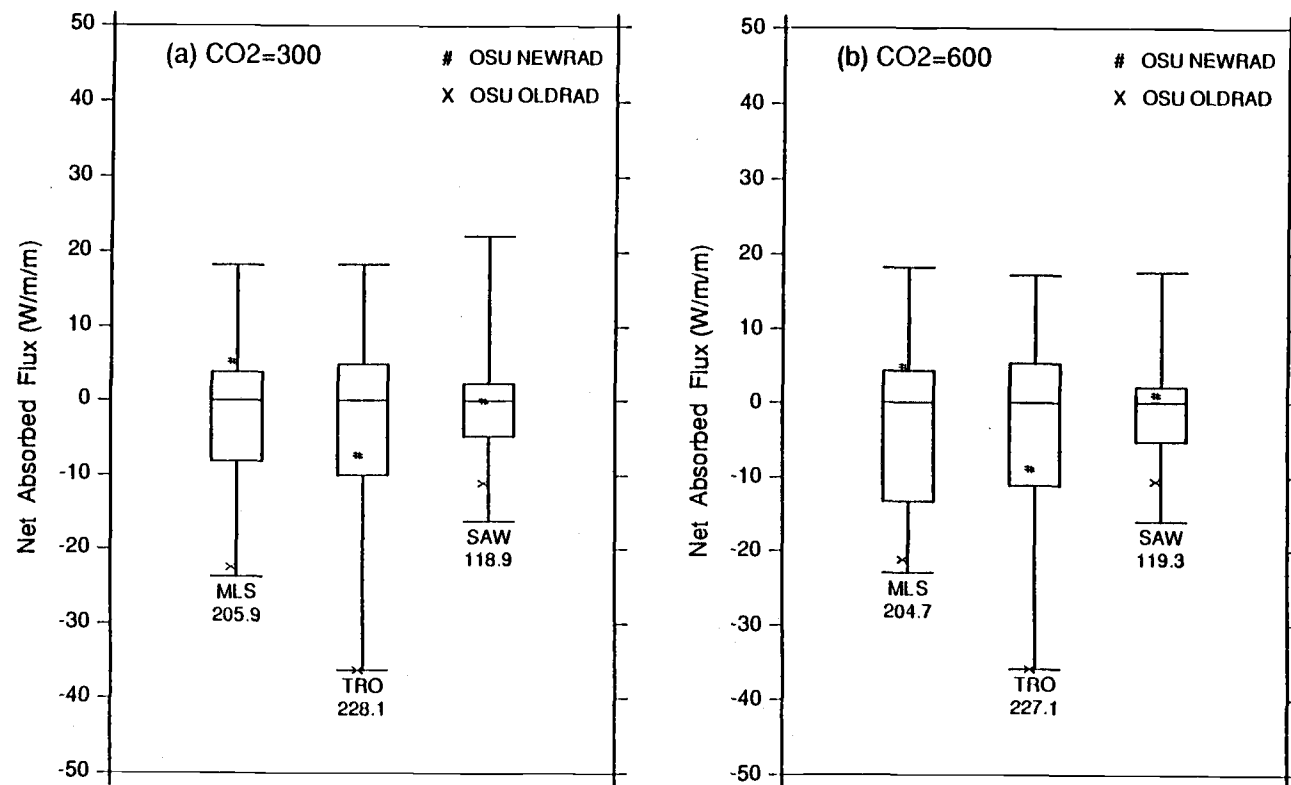Fig. 11. As in Fig. 10, except for H_2O only.

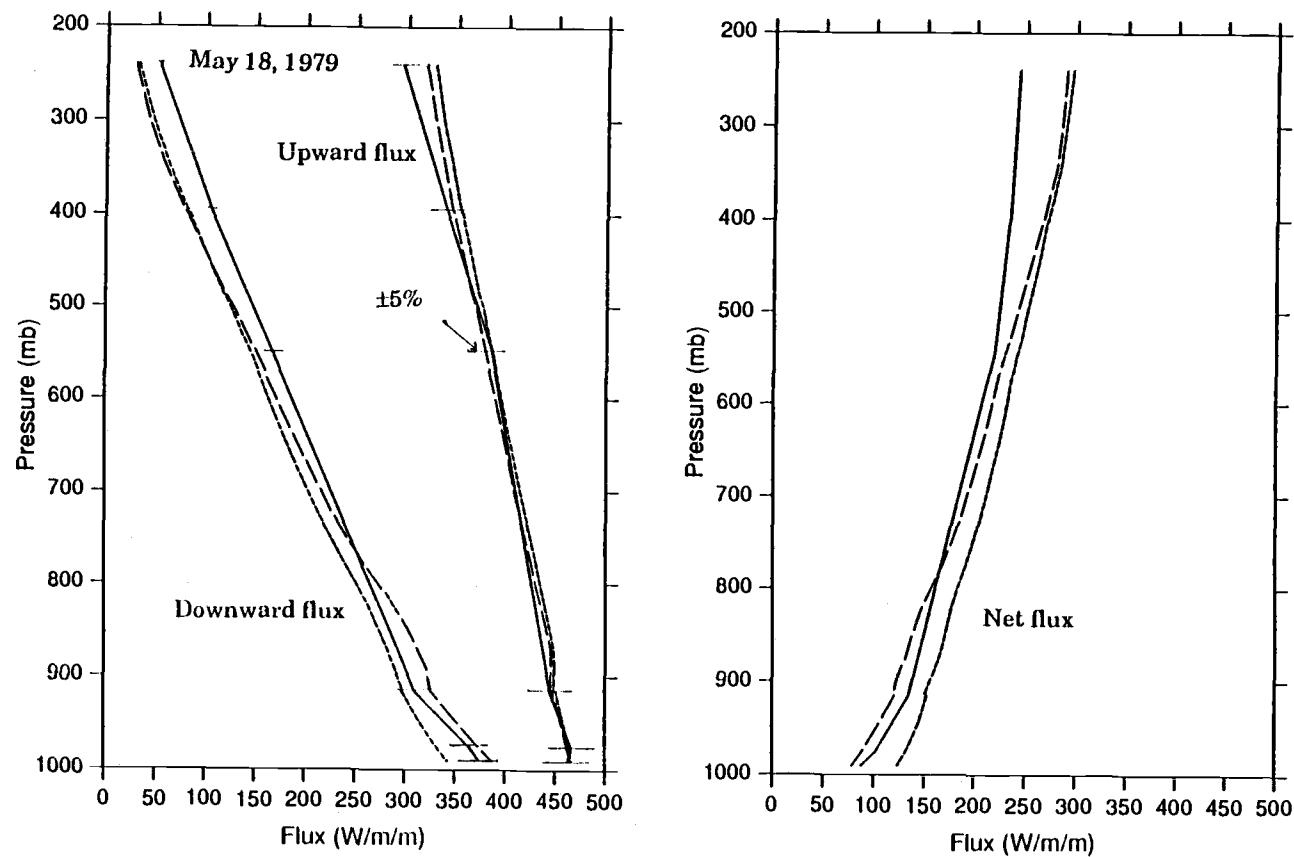Fig. 12. As in Fig. 10, except for all constituents.

Fig. 13. Observed flux profiles (solid line), those calculated with new scheme (dashed line), and those calculated with current scheme (dotted line) for a clear sky conditions on May 18, 1979 over the Arabian Sea. Horizontal bars indicate the estimated observational error(±5%).
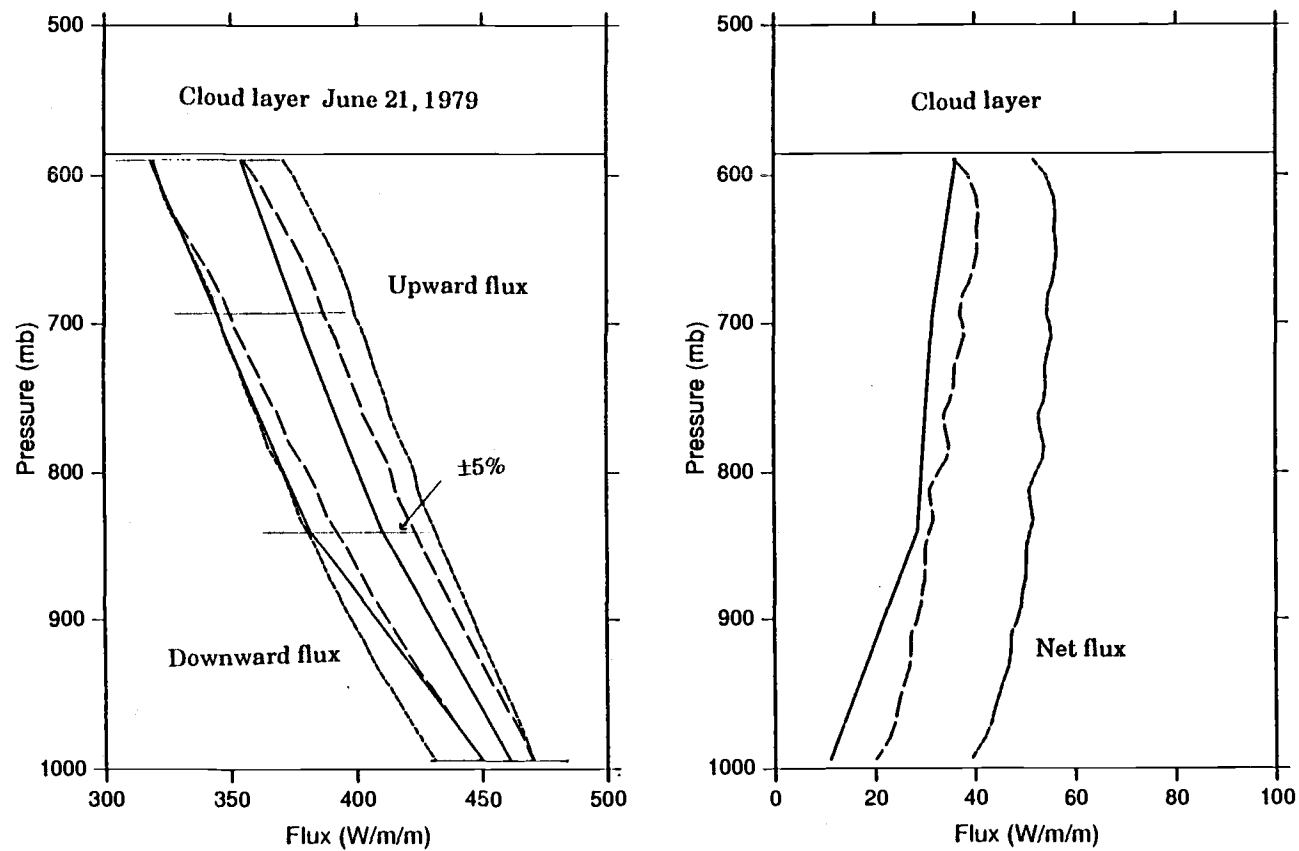
Fig. 14. As in Fig. 13, except for the cloudy case on June 21, 1979.

fluxes calculated with the new scheme are lager than the 5% error of the observations above 600 mb. The right panel of Fig. 13 shows that the net fluxes calculated with the new scheme are a significant improvement for a range, under 600 mb, when compared to those with current scheme.

The left panel of Fig. 14 shows that the both downward and upward fluxes calculated with the new scheme are in an error range of ±5% of the observations for the entire cloud layer below. The right panel of the Fig. 14 shows the net radiation calculated with the new scheme are overestimated by less than 10 w/m^2, while those with current scheme are about 30 w/m^2 for the entire cloud layer below.

REFERENCES

Ackerman, S. A., and S. K. Cox, 1982: The Saudi Arabian heat low: Aerosol distributions and thermodynamic structure. *J. Geophys. Res.*, **87**, 8991-9002.

Chou, M.-D., 1984: Broadband water vapor transmission functions for atmospheric IR flux computation. *J. Atmos. Sci.*, **41** 1775-1778.

Chou, M.-D. and L. Peng, 1983: A parameterization of the absorption in 15 μm CO_2 spectral region with application to climate sensitivity studies, *J. Atmos. Sci.*, **40**, 2183-2192.

Ellingson, R. G., and G. N. Serafino, 1984: Observations and calculations of aerosol heating over the Arabian Sea during MONEX. *J. Atmos. Sci.*, **41**, 575-589.

Ghan, S. J., J. W. Lingaars, M. E. Schlesinger, R. L. Mobley and W. L. Gates, 1982: A documentation of the OSU two-level atmospheric general circulation model. Report No. 61, Climatic Research Institute, Oregon State University, 391pp.

Griffith, K.T., S.K. Cox and R.C. Knollenberg, 1980: Infrared radiative properties of tropical cirrus clouds inferred from aircraft measurements. *J. Atmos. Sci.*, **37**, 1073-1083.

Kneizys, F. X., E. P. Shettle, W. O. Gallery, J. H. Chetwynd, Jr.,L. W. Abreu, J. E. A. Selby, R. W. Fenn and R. A. McClatchey, 1980: Atmospheric transmittance/Radiance: Computer code LOWTRAN 5. Optical Physics Div., 7670, Hanscom AFB, Bedford, MA, 233pp.

Kneizys, F. X., E. P. Shettle, W. O. gallery, J. H. Chetwynd, Jr.,L. W. Abreu, J. E. A. Selby, S. A. Clough and R. W. Fenn, 1983: Atmospheric transmittance/Radiance: Computer code LOWTRAN 6. Optical Physics Div., 7670, Hanscom AFB, Bedford, MA, 200pp.

Liou, K.-N., 1980: *An introduction to atmospheric radiation.* Academic press Inc., London, England, 392pp.

Luther, F. M., R. G. Ellingson, Y. Fouquart, S. Fells, N. Scott and W. J. Wiscomb, 1988: Intercomparison of radiation codes in climate models (ICRCCM): Longwave clear-sky results. Bull. Amer. Meteor. Soc., 69, 40-48.

McClatchey, R. A., R. W. Fenn, J. E. A. Selby, J. S. Garing, and F. E. Volz, 1973: *Optical properties of the atmosphere.* AFCRL-70-0527, Air Force Cambridge Research Laboratories, Bedford, MA, pp85.

Manabe, S., and F. Möller, 1961: On the radiative equilibrium and heat balance of the atmosphere. *Mon. Wea. Rev.*, **89**, 503 - 532.

Roberts, R. E.,J. E. A. Selby and L. M. Bidlerman, 1976: Infrared continuum absorption by atmospheric water vapor in the 8 - 12 μm window. *Applied Optics*, **15**, 2085 - 2090.

Starr, D.O'C., and S.K. Cox, 1985: Cirrus clouds, Part II: Numerical experiments on the formation and maintenance of cirrus. *J. Atmos. Sci.*, **42**, 2682-2694.

Stephens, G. L., 1978: Radiation profiles in extended water clouds. II. Paramerization schemes. *J. Atmos. Sci.*, **35**, 2123-2132.